

PLASTIC DEFORMATION AND WORK HARDENING

PLASTIC DEFORMATION AND WORK HARDENING OF
AL AND AA5754 AL ALLOYS

By
DONG-YEOB PARK, PH.D, M.SC., B.ENG.

A Dissertation
Submitted to the School of Graduate Studies
in Partial Fulfilment of the Requirements
for the Degree
Doctor of Philosophy

McMaster University
©Copyright by Dong-Yeob Park, December 2007

DOCTOR OF PHILOSOPHY (2007)
Department of Materials Science and Engineering

McMaster University
Hamilton, Ontario

TITLE: Plastic Deformation and Work Hardening
of Al and AA5754 Al Alloys

AUTHOR: Dong-Yeob Park, Ph.D, M.Sc., B.Eng.

SUPERVISOR: M. Niewczas

NUMBER OF PAGES: xxv, 212

Abstract

This research has been carried out to understand the relation between work hardening, deformation behaviour, dislocation substructure and crystallographic texture developed during plastic flow in pure Al and continuous cast and direct chill cast AA5754 Al-Mg alloys. Tensile and strain rate sensitivity tests are performed in the temperature range 4.2K-295K; details of the process of dislocation accumulation, the dislocation substructure development and texture evolution are followed using a range of techniques such as TEM, in-situ resistivity measurements and X-ray diffraction. The tensile deformation results show an unprecedented level of strength and unusual work hardening behaviour of Al-alloys at 4.2K. The electrical resistivity data suggest that fracture is initiated by the collapse of the dislocation network at places where dislocations develop a critical spacing for spontaneous annihilation. This spacing is estimated at approximately 8nm at 4.2K for both pure Al and Al alloys and ~ 12 nm at 78K for pure Al. Strain rate sensitivity measurements suggest that deformation of high purity Al is governed by dislocation-dislocation interactions in a broad range of temperatures, whereas Al alloys exhibit a larger thermal component of flow stress due to the presence of solute atoms in the matrix. The texture studies show that, independently of initial texture, the tensile axis of deformed samples rotates to $\langle 111 \rangle$ stable end orientation, and the intensity of the $\langle 111 \rangle$ peak increases parabolically with the flow stress, also strongly affected by the temperature. The experiments carried out on samples oriented at different angles to the rolling direction indicate that the crystallographic texture is the major factor responsible for the anisotropy of the alloys' mechanical properties. This is attributed to the effect of the operating slip systems activated during tensile deformation. The Visco-Plastic Self Consistent modeling has been carried out to predict mechanical behaviours of AA5754 alloys and to provide insight into operating mechanisms of plastic flow as well as the origin of the

anisotropy of mechanical properties. These results indicate that the more effective dislocation storage in the substructure at a low temperature significantly increases the work hardening rate at the later stage of deformation, and the crystallographic texture is the major cause of the anisotropy in the flow stress behaviour.

Acknowledgements

The author would like to express his deepest gratitude to his major advisor Dr. Marek Niewczas for his patience and guidance throughout this research. Gratitude is also expressed to the supervisory committee members Dr. David Wilkinson and Dr. Mukesh Jain for their valuable advice. The author wishes to thank Dr. Raja Mishra of GM and Dr. Bjorn Holmedal of the Norwegian University of Science and Technology for comments on a part of this work. Special thanks are expressed to many others who made contributions: Dr. Jim Britten for helping to measure texture, Mr. Fred Pearson for helping with TEM, and Mr. Steve Koprach for helping with SEM.

The author wishes to thank the Centre for Automotive Materials and Manufacturing (CAMM) for financial support. Dr. Olaf Engler of Hydro Aluminium GmbH is gratefully acknowledged for providing the high purity aluminum used in this work. AA5754 alloys were kindly supplied by Novelis.

Table of Contents

Abstract	iii
Acknowledgements	v
List of Figures	x
List of Tables	xxv
Chapter 1 Introduction	1
1.1 Motivation and Background	1
1.2 Organization and Synopsis of Thesis	3
Chapter 2 Plastic Deformation: A Review	5
2.1 Characterization of Plastic Deformation	5
2.1.1 Flow Curves of Single Crystals and Polycrystals	5
2.1.2 Kocks-Mecking Analysis - Athermal Hardening	9
2.1.3 Kinetics of Plastic Flow	13
2.1.4 Effect of Temperature and Strain Rate	14
2.1.5 Dislocation Density Measurement using Electrical Resistivity .	18
2.2 Deformation Characteristics of Pure Al and Al-Mg Alloys	20
2.2.1 Mechanical Properties and Deformation Behaviour	20
2.2.1.1 Work Hardening Behaviour of Pure Al	20
2.2.1.2 Effect of Mg on Mechanical Properties of Al-Alloys . .	23
2.2.2 Microstructure Evolution during Plastic Deformation	32

2.2.2.1	Pure Al	32
2.2.2.2	Effect of Mg on Microstructure	37
2.3	Effect of Thermomechanical Process on Material Properties	40
2.3.1	Mechanical Properties and Microstructure	41
2.3.2	Texture	43
2.4	Anisotropic Deformation of Sheet Materials	47
2.4.1	Factors Causing Anisotropy	48
2.4.2	Texture	52
2.5	Summary	58
2.6	Research Objective and Methodology	58
Chapter 3	Experimental Procedure and Techniques	60
3.1	Tensile and Strain Rate Sensitivity Tests	60
3.2	Structural Studies	63
Chapter 4	Results	68
4.1	Continuous Deformation	68
4.1.1	Deformation Behaviour and Fracture	68
4.1.2	Strain Rate Sensitivity Measurements	75
4.1.3	Electrical Resistivity	78
4.1.4	Intermittent Annealing Experiments	81
4.1.5	Structural Studies	95
4.1.6	Texture	98

4.2	Anisotropic Deformation	108
4.2.1	Tensile Behaviour	108
4.2.2	Strain Rate Sensitivity	112
4.2.3	Texture	115
4.2.3.1	Texture Evolution in Anisotropic Deformation	115
4.2.3.2	Effect of Texture on Mechanical Anisotropy	122
Chapter 5	Discussion	125
5.1	Continuous Deformation	125
5.1.1	Mechanical Properties	125
5.1.2	Mechanism of Plastic Deformation	132
5.1.3	Electrical Resistivity and Microstructure	134
5.1.3.1	Continuous Deformation	134
5.1.3.2	Fracture	141
5.1.3.3	Intermittent Annealing	143
5.1.4	Texture	147
5.1.4.1	Initial Texture	147
5.1.4.2	Texture Evolution	148
5.1.4.3	Stable End Orientation	156
5.1.5	Texture Modeling	159
5.2	Anisotropic Deformation	168
5.2.1	Mechanical Properties	168

5.2.2	Texture	171
5.2.2.1	Rotation Path of the TA	171
5.2.2.2	Stable End Orientation	173
5.2.3	Modeling	180
Chapter 6	Summary and Conclusions	182
	Bibliography	186
	Appendix A Anova Analysis	198
	Appendix B Roughness	201
	Appendix C Methodology of VPSC Modeling	204
	Appendix D Resistivity Measurement	207
	Appendix E Mean Free Path	209
	Appendix F Strain Rate Sensitivity - Haasen plot	210

List of Figures

2.1	Schematics of (a) flow curve and (b) work hardening rate (θ) vs. flow stress for a fcc single crystal deformed in a single slip	6
2.2	Schematics of (a) flow curve and (b) work hardening rate (θ) vs. flow stress for fcc polycrystals	8
2.3	Dislocation storage rate when the mean free path Λ is constant (dots); when it is proportional to the dislocation spacing (dashes); and when both superpose (solid) (After Kocks and Mecking [38])	11
2.4	Typical experimental observations of the dislocation storage rate (After Narutami and Takamura [43])	11
2.5	Strain hardening of silver single crystal (a) and copper polycrystals (b) (After Mecking and Kocks [45])	12
2.6	Strain rate sensitivity test	17
2.7	Schematic Haasen plot (After Diak et al [51])	18
2.8	Work hardening rates of pure Al at different deformation temperatures, as indicated on the graph (After Gil-Sevillano [36])	21
2.9	Schematic diagram illustrating the $\theta - \sigma$ behaviour in terms of the effect of the contribution of different structural elements on work hardening: (i) contribution of particles which are elastically loaded (primarily affects the low strain region and the elastic-plastic transition), (ii) contribution of solute atoms which affect dynamic recovery and (iii) contribution of strain induced obstacle generation due to phase transitions, e.g., dynamic precipitation during deformation. (After Embury et al. [64]).	23

2.10	Effect of the addition of Mg to pure Al on tensile properties (After Vasudevan and Doherty [67])	24
2.11	Effect of the addition of Mg on frictional stress, σ_0 (After Burger et al. [69])	25
2.12	Influence of test temperature on yield stress and UTS in AA110 alloys (After Lloyd [73])	27
2.13	Work hardening at different temperatures for AA1100 (After Lloyd [73]) .	28
2.14	Variation in dynamic recovery rate with temperature (After Lloyd [73]) .	29
2.15	Temperature dependence of the yield stress, σ_y , and ductility, ϵ_F , in AA5154 and AA5052 (After Lloyd [74])	30
2.16	Strain rate sensitivity, m , as a function of temperature in different AA5xxx (After Lloyd [74])	31
2.17	The microstructure of high purity Al cold-rolled 10% (above) is subdivided by extended (Dense dislocation walls: DDWs) and sharp (Microbands: MBs) dislocation boundaries, which form a cell block structure. The cell blocks are subdivided by ordinary dislocation cells. The figure below shows Geometrically Necessary Boundaries (GNBs) marked A, B, C, etc. and Incidental Dislocation Boundaries (IDBs) marked a, b, c, etc. (After Liu et al. [82])	35
2.18	Spatial arrangement of the dislocation of Al-2.5%Mg alloys (After Verdier et al. [96])	38
2.19	A uniform distribution of dislocation tangles (a) and the organized dislocation tangles called a Taylor lattice (b) of Al + 5.5at.%Mg. Dashed lines in (b) are the trace of $\{111\}$ planes. (After Hughes [78])	38
2.20	Schematic of the CC and DC processes	40

2.21 Particle structure of (a) the DC and (b) CC AA5182 alloys (After Yu et al. [4])	41
2.22 The (111) pole figures of as-received hot band SC and DC materials (After Cheng and Morris [6])	44
2.23 The (111) pole figures of annealed hot band SC and DC materials (After Cheng and Morris [6])	45
2.24 Microtexture: IPF maps of completely recrystallized AA5052 for (a) CC and (b) DC hot bands. IPF maps are overlapped by corresponding crystal orientation maps in which character “C” indicates the grain with Cube orientation (After Liu and Morris [3])	46
2.25 Stress-strain curve for annealed Al-3%Mg alloy (After Johnson and Lloyd [115])	47
2.26 Anisotropy: (a) yield strength and (b) tensile elongation in O-temper AA5754 and AA5454 (After Johnson and Lloyd [115]).....	48
2.27 {111} pole figure for pure Al after pre-rolling in the RD direction and subsequent shear deformation up to $\gamma=1.0$ at 90° from the rolling direction (After Lopes et al [119])	50
2.28 True stress, σ , and work hardening, θ , characteristics as a function of strain for AA1200 rolled to a strain of 0 and 0.2 measured at 0° , 45° , and 90° from the rolling direction (After Eardley et al. [17])	51
2.29 Orientation distributions of commercially pure Al strained 0, 9, 18, 27, and 36% (After Ohtani and Inagaki [124])	53
2.30 Evolution of intensities of (111) axis parallel to TA for commercially pure Al and Al-Mg alloys (After Ohtani and Inagaki [124])	53

2.31	(111) pole figures of 95% cold rolled fcc metals; (a) copper and (b) 70:30 brass (After Hirsch and Lucke [125])	54
2.32	(111) pole figures of Al-5%Ca-5%Zn: prior to tensile deformation (a) and samples deformed with the tensile axis in the rolling direction (b), perpendicular to the rolling direction (c), and at 45° from the rolling direction (d) (After Ruano and Gonzalez [126])	56
2.33	Standard (001) stereographic projection showing rotation of the tensile axis of samples during uniaxial deformation (Modified from Ruano and Gonzalez [126]). Relative TA directions to the RD are marked TA with subscripts of 0, 45 and 90 depending on the angle to the RD; transverse direction, TD; and normal direction, ND.	57
3.1	An example of strain rate sensitivity measurements of CC alloy at 78K . .	61
3.2	Schematics of the orientation of the tensile direction of the samples adopted for the studies of the anisotropic deformation	62
3.3	Schematic of major device units in a GADDS system (After Bruker AXS inc. [127])	65
3.4	Sample rotation and translation in the X-ray system: (a) relationship between rotation axes ($\omega\chi_g\phi$) and $X_L Y_L Z_L$ coordinates and (b) relationship between rotation axes and translation axes XYZ (After Bruker AXS inc. [127])	65
3.5	Relationship between a sample and detector positions; D is the distance from the sample to the detector and α is the swing angle of the detector (After Bruker AXS inc. [127])	66

3.6	A typical example of the diffraction pattern of X-rays used for the processing of the texture of deformed materials: (a) an area detector reflection for a specimen tested at 295K and (b) a reflection coverage in a pole figure	67
4.1	True stress vs. true strain characteristics at the initial strain rates of (a) 1.6×10^{-4} , (b) $1.6 \times 10^{-5} s^{-1}$ for the CC alloy (CC) and pure Al (Al) and (c) 1.6×10^{-4} for the DC alloy (DC) at temperatures 4.2K, 78K and 295K (cont'd)	69
4.1	(cont'd)	70
4.2	The effect of heat-treatment on mechanical properties of CC specimens heat-treated for two hours at 350°C and 450°C, respectively. Tensile tests were conducted at 295K and a strain rate of $1.6 \times 10^{-4} s^{-1}$	71
4.3	SEM observations of the fracture surface of CC alloys deformed at (a) 295K, (b) 78K and (c) 4.2K.	72
4.4	SEM observations of the fracture surface of pure Al deformed at (a) 295K and (b) 4.2K.	73
4.5	Normalized by temperature dependent shear modulus work hardening characteristics as a function of reduced flow stress. CC and Al denote the CC alloy and pure Al, respectively. NA and AQ denote the natural aged and the as-quenched Al-Zn-Mg alloys, respectively, for comparison from the literature [133]	74

4.6	Haasen plot characteristics obtained from strain rate sensitivity tests with rate changes between 10^{-4} and $10^{-5}s^{-1}$. CC and CC4 denote continuous cast alloys annealed for 2 hours at 350°C and 450°C, respectively; DC, direct chill cast alloy; Al, pure Al. For comparison with the present data, strain rate sensitivity results for AA6111 are replotted from Esmacili et al [134]. A6(1h) represent AA6111 material aged for 1 hour at 180°C, and A6(SS) represents the supersaturated solid solution AA6111.	76
4.7	Activation volume as a function of the effective flow stress on a log scale for the CC alloy and pure Al. Activation area is given on the right axis.	78
4.8	Evolution of defect induced resistivity change during deformation as a function of (a) true strain and (b) the effective flow stress for the CC alloy and pure Al	79
4.9	True tensile stress vs. true strain of continuously deformed and annealed samples of pure Al: (a) four intermittent anneals and (b) two intermittent anneals	82
4.10	Yield stress drop induced by annealing during deformation	83
4.11	Increase in resistivity as a function of tensile strain: (a) four intermittent anneals and (b) two intermittent anneals	84
4.12	Increase in resistivity as a function of true stress: (a) four intermittent anneals and (b) two intermittent anneals	85
4.13	Changes in recoverable and unrecoverable resistivity as a function of true strain for intermittently annealed samples	87

4.14	Changes in recoverable and unrecoverable resistivity as a function of true stress for intermittently annealed samples	88
4.15	Isochronal annealing curve for pure Al deformed 37% (380MPa) at 4.2K. Open symbols represent the fraction of deformation-induced resistivity remaining in the structure as a function of anneal temperature. The closed symbol shows the resistivity remaining when an equivalently deformed sample is annealed by warming directly to a given temperature.	89
4.16	True tensile stress vs. true strain characteristics continuously deformed and annealed samples of pure Al at anneal temperature of 100K.	90
4.17	True tensile stress vs. true strain characteristics continuously deformed and annealed samples of pure Al at anneal temperature of 200K	90
4.18	True tensile stress vs. true strain characteristics continuously deformed and annealed samples of pure Al at anneal temperature of 260K	91
4.19	Increase in resistivity as a function of true strain at anneal temperature of 100K	91
4.20	Increase in resistivity as a function of true strain at anneal temperature of 200K	92
4.21	Increase in resistivity as a function of true strain at anneal temperature of 260K	92
4.22	Increase in resistivity as a function of true stress at anneal temperature of 100K	93
4.23	Increase in resistivity as a function of true stress at anneal temperature of 200K	93

4.24 Increase in resistivity as a function of true stress at anneal temperature of 260K	94
4.25 TEM observations of the microstructure of CC alloys: (a) prior to deformation, (b) the substructure developed after 10% of deformation at 295K at the flow stress of 130MPa, (c) dislocation substructure developed after 17% of deformation at 4.2K corresponding to the flow stress of 320MPa and (d) dislocation substructure developed in the CC sample deformed till fracture, i.e. after 33% of deformation at 4.2K corresponding to the flow stress of 520MPa (TA denotes the tensile direction.). (cont'd)	96
4.25 (cont'd)	97
4.26 TEM observations of the microstructure of pure Al deformed till fracture at different temperatures, i.e., (a) 35% of deformation at 295K corresponding to a flow stress of 50MPa, (b) 30% of deformation at 78K at the flow stress of 150MPa, (c) 43% of deformation at 4.2K corresponding to a flow stress of 415MPa.	99
4.27 {111} pole figures of: (a) the as-received CC alloy, (b) the CC alloy after annealing at 350°C for 2hrs, (c) the CC alloy after annealing at 450°C for 2hrs and (d) {111} pole figures of the as-received DC alloy. RD represents the previous rolling direction of the samples.	100
4.28 {111} pole figures for (a) CC and (b) DC samples deformed at 4.2K to different strains given in the figure. Tensile axis is denoted as TA. . . .	101
4.29 {111} pole figures of CC specimens annealed at (a) 350°C and (b) 450°C after fracture (about 19% of strain) at room temperature.	102

4.30	Selected sections of orientation distribution for the CC specimen deformed till fracture at 4.2K (32% of strain) at different Φ angels of 25° , 45° , 65° and 90°	104
4.31	Orientation distributions function at a constant $\Phi = 65^\circ$ for CC samples deformed to different strains at temperature of (a) 295K, (b) 78K and (c) 4.2K	105
4.32	(cont'd)	106
4.32	Orientation distributions of the CC material at $\Phi = 65^\circ$ and $\Theta = 35^\circ$ deformed at (a) 295K, (b) 78K and (c) 4.2K with the strain rate of $10^{-4}s^{-1}$. Figures show orientation distributions for the specimen annealed at 350°C and deformed to a given strain indicated on the graph; figure (a) shows the data for the specimen annealed at 450°C . Data for the samples deformed at the strain rate of $10^{-5}s^{-1}$ are included on the graphs for comparison. (cont'd)	107
4.33	True stress vs. true strain curves for the (a) CC and (b) DC. Note: 0° , 45° and 90° are angles of the tensile axis to the rolling direction of the sheet.	109
4.34	Behaviour of the work hardening rate for (a) CC and (b) DC alloys as a function of true strain.	110
4.35	Work hardening (WH) rates at the early stage of deformation for (a) CC and (b) DC samples deformed to 3% of strain at 295K and 9% of strain at 78K and 4.2K	111
4.36	Haasen plot obtained from strain rate change tests at the test temperature of 78K for CC and DC alloys	112

4.37	Activation area obtained from the rate sensitivity data at 78K for the (a) CC and (b) DC. 450°C denotes the CC material heat-treated at 450°C for 2 hours	114
4.38	{111} pole figures of CC samples undeformed (a) and deformed at 4.2K with the tensile axis TA at (b) 0°, (c) 45° and (d) 90° to the previous rolling direction RD	117
4.39	Evolution of {111} pole figure during deformation at 4.2K for the (a) CC and (b) DC for the tensile axis at 90° to the previous RD	118
4.40	Selected sections ($\Phi = 25, 65$ and 90) of orientation distribution for the CC specimen after 31% deformation at 4.2K for the tensile axis at 0° and 90° to the previous RD	119
4.41	Orientation distributions at $\Phi = 90$ and $\Theta = 45$ for the tensile axis at (a) 0° and (b) 90° to the previous RD for CC specimens deformed at 4.2K	120
4.42	Selected sections ($\Phi = 25, 45, 65$ and 90) of orientation distribution for the tensile axis at 45° to the previous RD for CC specimens deformed 32% at 4.2K	121
4.43	Evolution of Taylor factor during deformation for the CC at 0°, 45° and 90° angles to the previous rolling direction RD, respectively	123
4.44	Effect of the preferred crystallographic orientation on the flow stress: (a) angular variation of the flow stress σ and (b) the flow stress normalized by the corresponding Taylor factor (σ/M) at strain of approximately 20% for the CC alloy	124

5.1	The effect of dislocation storage on the strain hardening of the CC alloy and pure Al, respectively. θ_o is defined as the slope of a straight line though the origin in the region of linearity (see text for details).	128
5.2	Flow stress as a function of the total dislocation density for Al, CC and DC alloys. Slopes of these relationships give values of the exponent n in relationship given by equation (5.5). The n values are 0.54, 0.5, 0.34, 0.29 for Al deformed at 78K and 4.2K, the CC alloy deformed at 4.2K and the DC alloy deformed at 4.2K, respectively (see the text for details). Linear regression lines are also included in the figure.	135
5.3	Evolution of the dislocation mean free path for CC and DC alloys deformed at 4.2K and Al deformed at 4.2K and 78K. Al(Ref) denotes the mean free path for nominally pure Al deformed at 78K, taken from the literature [147].	138
5.4	Rate of the dislocation density change with the strain $\frac{d\rho}{d\epsilon}$ as a function of the dislocation density ρ . The characteristics are fitted to the rate equation $\frac{d\rho}{d\epsilon} = k_1\sqrt{\rho} - k_2\rho$ with k_1 and k_2 constants given in Table 5.1. Both the experimental data points (symbols) and the fitting curves (lines) are shown in the graph.	140
5.5	Microstructure of the two intermittent annealed sample of pure Al (after fracture)	145
5.6	Inverse pole figures for tensile axis of the CC specimen deformed at 4.2K after different amount of deformation, revealing a rotation of tensile axis to either $\langle 111 \rangle$ or $\langle 001 \rangle$ orientation.	149

5.7	Effect of temperature on intensities of (a) $\langle 111 \rangle$ and (b) $\langle 001 \rangle$ peaks parallel to the tensile axis of CC and DC samples as a function of true strain (cont'd)	152
5.7	(cont'd)	153
5.8	Effect of temperature on intensities of (a) $\langle 111 \rangle$ and (b) $\langle 001 \rangle$ peaks parallel to the tensile axis of CC and DC samples as a function of effective stress. The fitting curves are also included on the graphs (cont'd)	154
5.8	(cont'd)	155
5.9	Comparisons of experiments (lines) and simulations (symbols) of deformation at room temperature for CC materials annealed for 2 hours at 350°C and 450°C	161
5.10	Comparisons of experimental (lines) and simulated (symbols) true stress - true strain curves for CC (a) and DC (b) alloys	162
5.11	$\{111\}$ pole figure obtained from deformation simulation for CC materials: 18% strain at room temperature with CC materials annealed at 450°C (a) and 350°C (b) and 33% strain at 4.2K for CC (c) and DC (d) materials	163
5.12	Simulated inverse pole figures for tensile axis of CC specimen deformed at 4.2K after different amount of deformation, revealing a rotation of tensile axis to either $\langle 111 \rangle$ or $\langle 001 \rangle$ orientation.	164
5.13	Simulated intensities of $\langle 111 \rangle$ axes lying parallel to the tensile axis as a function of effective stress (a) and true strain (b) (cont'd)	166
5.13	(cont'd)	167

5.14	Misorientation across the banded structure for the CC material tested at 78K. Kikuchi diffractions reveal misorientations across bands	172
5.15	Inverse pole figures of the TA perpendicular to the previous RD for the CC specimen tested at 4.2K	175
5.16	Behaviour of the stable end orientation as a function of effective flow stress for the tensile axes at 0°, 45° and 90° to the previous RD for the CC (a) and DC (b). The y-axis represents the intensity of <111> axis parallel to the tensile direction.	176
5.17	Behaviour of the stable end orientation as a function of strain for the tensile axes at 0°, 45° and 90° to the previous RD for the CC alloy. The y-axis represents the intensity of <111> axis oriented parallel to the tensile direction.	177
5.18	Comparisons of simulated and experimental {111} pole figures after 33% straining of CC specimens at 4.2K	178
5.19	Simulated results of the stable end orientation as a function of effective flow stress for the tensile axes at 0°, 45° and 90° to the previous RD for the CC alloy	179
5.20	Simulation of the flow stress for (a) CC and (b) DC alloy samples with different orientations marked on the graphs. In the analysis, initial experimental texture corresponding to the respective tensile directions was used.	181
6.1	Surface observation with stereoscopes. Lüders-like bands are clearly visible at temperature 295K. The picture has been enlarged.	202
6.2	Roughness measurements for CC materials	203

6.3	Schematic of the strain hardening model incorporated in VPSC code: (a) parameters of the empirical Voce law for a single crystal on the critical stress τ vs. the microscopic shear Γ curve and (b) their relation with a macroscopic stress-strain (S-E) curve (after Tome et al [155]) (see section 5.1.5 for detailed descriptions of parameters and relations.) . . .	206
6.4	Schematic of the <i>in-situ</i> resistivity measurement setup. l represents the length of the specimen across which the potential difference is measured. l and the cross-section area (s) of the sample are used to compute the resistivity (ρ) as described in Equation 2.20.	208
6.5	Evolution of the dislocation mean free path for CC and DC alloys deformed at 4.2K and Al deformed at 4.2K and 78K: Log(mean free path) vs. Log($\sigma - \sigma_y$). Al(Ref) denotes mean free path data for pure Al deformed at 78K taken from the literature [147]. Details are found in Figure 5.3 and section 5.1.	209
6.6	Haasen plot characteristics obtained from strain rate sensitivity tests for CC tested at 78K. Open symbols represent data obtained by an increase of strain rate, and closed symbols represent data obtained by a decrease of strain rate.	210
6.7	Haasen plot characteristics obtained from strain rate sensitivity tests for DC tested at 78K. Open symbols represent data obtained by an increase of strain rate, and closed symbols represent data obtained by a decrease of strain rate.	211

6.8	Haasen plot characteristics obtained from strain rate sensitivity tests for pure Al tested at 295K. Open symbols represent data obtained by an increase of strain rate, and closed symbols represent data obtained by a decrease of strain rate.	211
6.9	Haasen plot characteristics obtained from strain rate sensitivity tests for pure Al tested at 78K. Open symbols represent data obtained by an increase of strain rate, and closed symbols represent data obtained by a decrease of strain rate.	212
6.10	Haasen plot characteristics obtained from strain rate sensitivity tests for pure Al tested at 4.2K. Open symbols represent data obtained by an increase of strain rate, and closed symbols represent data obtained by a decrease of strain rate.	212

List of Tables

2.1	Compositions of the commercial alloys studied by Lloyd [73]	27
3.1	Composition of the Al alloy (in wt. %)	60
4.1	Fitting parameters for recoverable defects with $y = a \cdot x^b$ equation	86
4.2	Fitting parameters for unrecoverable defects with linear equation $y = c \cdot x$	87
5.1	Values of the fitting parameters n , k_1 , and k_2 to equations (5.5) and (5.6)	135
5.2	I_o , β , and w values in equation (5.7) used to fit experimental data in Figure 5.8	156
5.3	Single crystal hardening parameters of the modified Voce hardening equa- tion used to fit experimental data with VPSC methodology (units of MPa)	160
5.4	I_0 , β , and w values in equation (5.7) and the fitting curves are shown in Figure 5.16	174
6.1	Anova analysis results with $\alpha = 0.05$ for Figure 4.44 (a): comparisons of flow stresses between difference tensile directions at strain of 20%	199
6.2	Anova analysis results with $\alpha = 0.05$ for Figure 4.44 (b): comparisons of flow stresses normalized by corresponding Taylor factors between difference tensile directions at strain of 20%	200

Chapter 1

Introduction

1.1 Motivation and Background

The applications of aluminum alloys are increasing, especially in the automotive industry due to the relatively high ratio of strength to weight. Aluminum alloys of the 5000 series are considered for structural and closure (panel) applications in the automotive industry and also for inner panels because of the better deep drawing behaviour. The AA5754 (Al-3 wt.% Mg) alloy has been used for the majority of the prototype structures produced from sheet materials [1, 2].

Commercial sheet materials are generally produced by either continuous casting (CC) technology or more traditional direct chill (DC) casting technology for fabrication of thin sheet products. The DC process involves ingot casting, homogenization, hot and cold rolling, followed by annealing. During continuous casting, a thin slab of an alloy is produced directly from a molten state by over-passing the hot rolling stage. A higher cooling rate during continuous casting induces small intermetallic particles and precipitates in CC alloys after hot rolling and allows for the preservation of components of a deformation texture with a β fiber texture that extends from the Copper to Brass components having an S component at the center. DC alloys contain more uniform microstructure with larger particles [3, 4].

These differences in microstructure and texture affect the mechanical behaviour during subsequent thermomechanical processes, as mechanical properties are closely

related to the microstructure and texture of aluminum alloys. It is recognized that the microstructure developed during the CC process makes it difficult to obtain a full recrystallization texture containing a cube texture component [3,5]. As a result, CC products exhibit an inferior formability and a larger mechanical anisotropy than DC materials in the following deformation processes [4–6].

The anisotropy of deformation behaviour, therefore, is a significant factor to be considered in the forming process of a rolled aluminum sheet. The anisotropy in a polycrystal material is mainly attributed to the non-uniform crystal orientation distribution. For example, tensile testing of materials containing a strong initial cube texture material (AA1200) showed 4-fold anisotropy in strain hardening and ductility [7]. Some polycrystal models have proved to be able to successfully predict the anisotropic behaviour of the material, e.g. the Taylor model [8–11] and the self-consistent model [12,13]. The anisotropic deformation can be also influenced by other factors such as: (1) grain structure, (2) mechanical fibering, and (3) microstructure [14–16]. For instance, recovery [17] or stacking faults [7] can cause significant differences in the magnitude of directional internal stresses in the microstructure and may influence the anisotropy. Other variables, such as solutes [18] or microbands [9], influencing the evolution of the deformation substructure are also associated with the anisotropy in a similar way. Manufacturing processes such as CC and DC can cause the directionality of the flow stress or the work hardening behaviour due to the effect of thermomechanical process on microstructure; this will be discussed in more details in Chapter 2.

Previous studies of other researchers on AA5754 Al alloy have dealt with mechanical behaviour and microstructure [6,19–24], the texture evolution during cold rolling [25,26], the earing behaviour [6,27,28] and the anisotropy of mechanical behaviour [28,29]. Most results available in the literature have been carried out at room or

elevated temperatures. However, there is an interest in understanding the work hardening behaviour of commercial alloys at lower temperatures not only because of the fundamental nature of such studies but also from the practical side, as many of these systems are restricted from being used at elevated temperatures [30–32]. Furthermore, only few researchers have addressed the interrelation between work hardening, microstructure and crystallographic texture.

The present work attempts to fill this gap and is focused on plastic deformation of cold rolled sheets of CC and DC AA5754 materials at a low temperature range. Through the study of deformation behaviour of samples oriented at various tensile directions with respect to the previous rolling direction and at different temperatures, one can obtain an insight into underlying mechanisms of the plastic flow, the work hardening, and the anisotropy of these properties. This knowledge will help in alloy design and in prediction of formability and workability of these materials.

1.2 Organization and Synopsis of Thesis

The thesis consists of five main parts: (1) a literature review, (2) experiment methods, (3) experimental results, (4) discussion of results and (5) conclusions.

The first chapter, “Introduction,” addresses the motivation and the background of why the plastic deformation study of Al and AA5754 Al Alloys at low temperatures is pursued as a research topic.

The second chapter, “Plastic Deformation: A Review,” describes previous studies carried out by other authors on these alloy systems and the fundamental background of some concepts used to explain the results in the subsequent chapters. The chapter concludes with the objectives of the present research and the research approach.

The third chapter, “Experimental Procedure and Techniques,” deals with materials, material preparation and experiment methods.

The fourth and the fifth chapters cover “Results and Discussion.” These chapters address: (1) deformation characteristics of pure Al and AA5754 Al alloys at 4.2K, 78K and 295K such as work hardening behaviour, microstructure, *in-situ* electrical resistivity measurement and strain rate sensitivity, (2) behaviours and characteristics of the crystallographic orientation of the alloys during deformation and (3) the anisotropic characteristics including the mechanical behaviour and texture of the alloys when the tensile axis is oriented at 0, 45 and 90 angles from the previous rolling direction. These chapters also present the simulation results of the tensile tests using the viscoplastic self-consistent (VPSC) code [13] with experimentally measured texture as input. The work hardening parameters used in the VPSC code are correlated to the work hardening behaviour observed in experiments.

Finally, the thesis finishes with conclusions and a set of appendices. The appendices include the supplemental data and experimental results obtained during the study, which are important, but not within the scope of the research.

Chapter 2

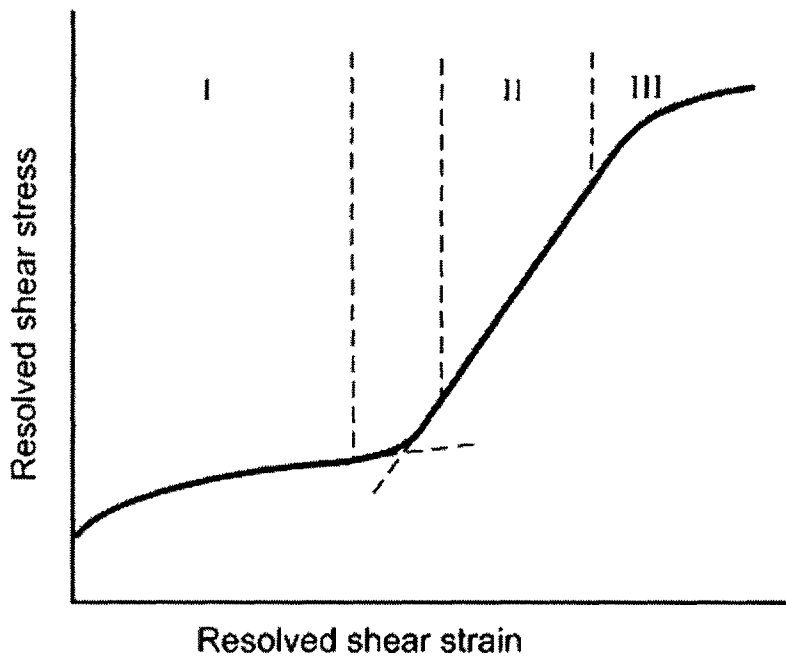
Plastic Deformation: A Review

2.1 Characterization of Plastic Deformation

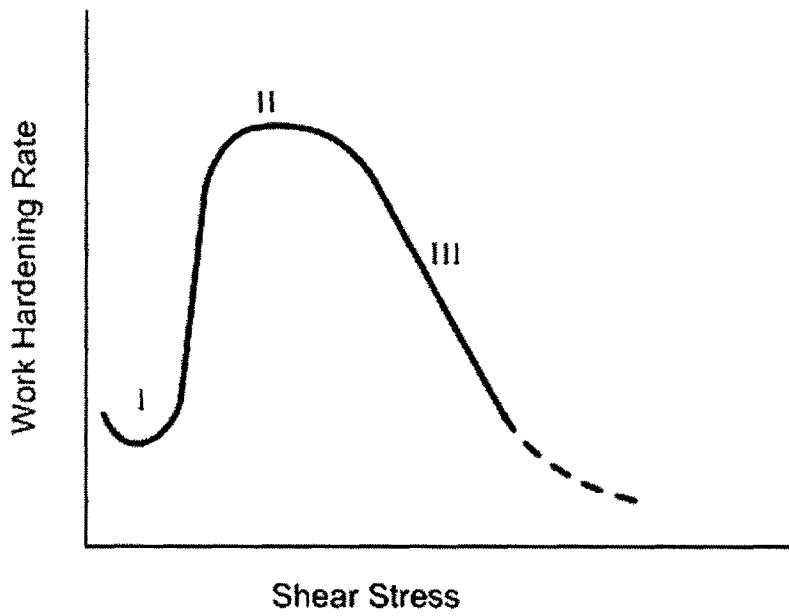
2.1.1 Flow Curves of Single Crystals and Polycrystals

One of the main deformation characteristics of metals is that the required shear stress to continue the movement of dislocation increases with increasing shear strain, due to strain hardening or work hardening. The theory of work hardening is helpful to explain the experimentally observed stress-strain behaviours. Strain hardening is caused by dislocation interactions with other dislocations and/or obstacles. Since the structure of a polycrystalline material includes an aggregate of single crystals, it is desirable first to understand the behaviour of single crystals.

Generally, the flow curve of a single crystal can be divided into three stages of strain hardening (Figure 2.1). Stage I, *easy glide*, is a stage whose occurrence strongly depends on the orientation of the crystal. The crystal exhibits little strain hardening in this stage. Stage II displays linear characteristic with the steepest rate of strain hardening. This stage is insensitive to strain rate or temperature. Stage III is a region that shows a decreasing slope and that is sensitive to both temperature and the rate of deformation. This stage is accompanied by a dynamic recovery. The occurrence of stage III limits the extent of stage II. For example, metals such as aluminum with high



(a)



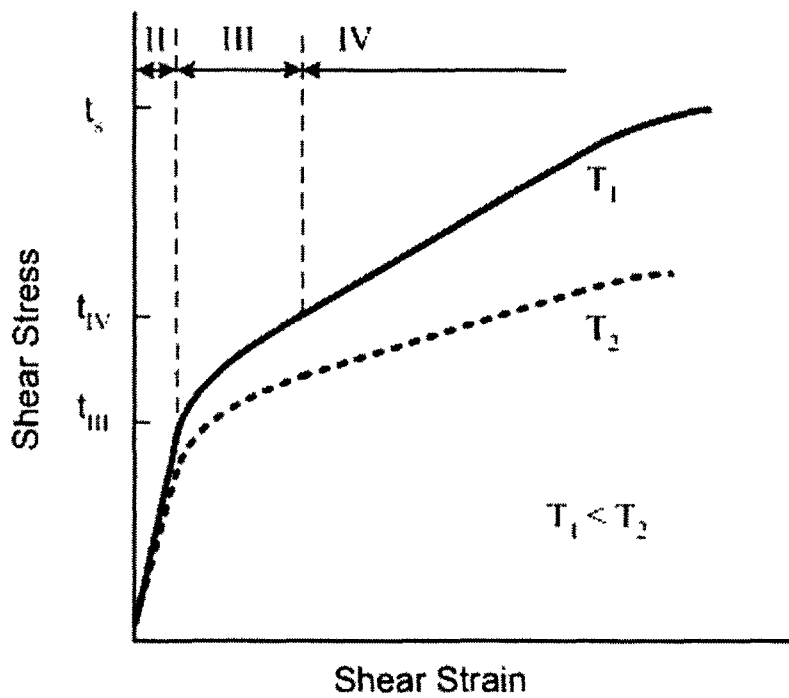
(b)

Figure 2.1: Schematics of (a) flow curve and (b) work hardening rate (θ) vs. flow stress for a fcc single crystal deformed in a single slip

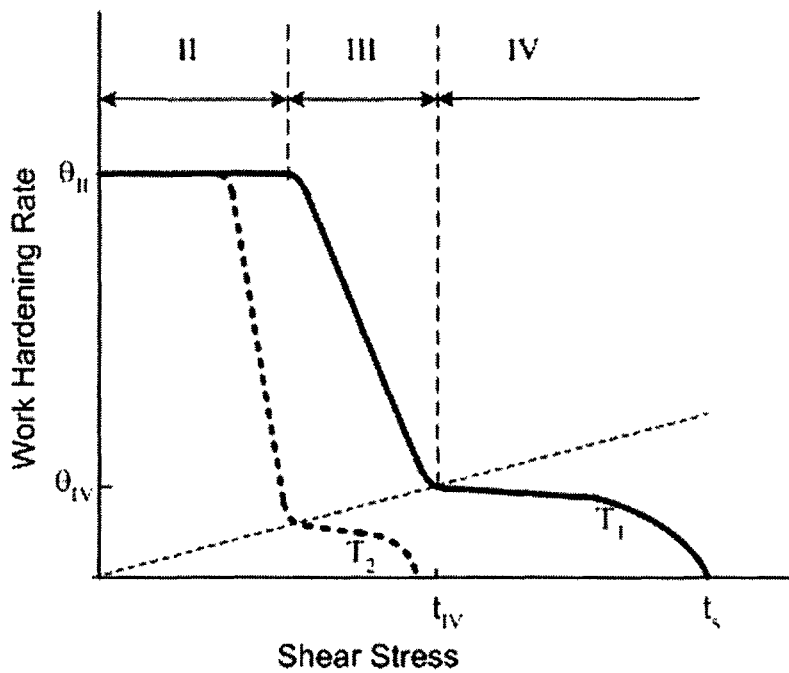
staging-fault energy (SFE) usually exhibit a very small region of stage II, especially at high temperatures, because they activate the cross slip, which acts as a relaxation mechanism that decreases the rate of work hardening.

These characteristic stages are also found in polycrystals. The flow curve of polycrystals at relatively low temperatures can be divided into four stages (Figure 2.2(a)). These four stages are clearly distinguished in the plot of work hardening rate, $\theta = \partial\tau/\partial\gamma$, versus flow stress (Figure 2.2(b)). In polycrystals, stage I is suppressed due to the fact that multiple slip systems operate right from the beginning of deformation. The initial slope of flow curves of polycrystals is similar to that of the single crystals in stage II which is characterized by a linear work hardening rate.

Stage III is strongly dependent on temperature and the strain rate in single crystals, which is also true for polycrystals, and can be described by a parametric scaling law involving both temperature and strain rate. The stage IV starts when the athermal storage of dislocations is balanced by dynamic recovery at the end of the stage III. The stage IV was introduced by Gil Sevillano et al. [33]. It was argued that this stage usually occurs only for two phase alloys at a large strain [34]. However, it was later shown by others [35] that it is common also for pure metals and alloys. This stage is characterized by a linear work hardening rate, although deviation from the linearity is also often found. Another characteristic of the stage IV is that the onset of work hardening rate, θ_{IV} , (Figure 2.2(b)) depends on the stress, τ_{IV} : $\theta_{IV} = C_{IV}\tau_{IV}$ (the typical value of C_{IV} is 0.1) [34,36,37]. This means that the stage IV also depends on temperature and strain rate similarly to the Stage III. In this stage, it is difficult to identify the work hardening mechanism due to competition between the low work hardening rate and the geometrical and structural instability. Furthermore, this stage is not detectable in a tensile test where necking is initiated at the Considere point, before the beginning of the stage IV [38]. Before reaching the saturation stress, τ_s , a



(a)



(b)

Figure 2.2: Schematics of (a) flow curve and (b) work hardening rate (θ) vs. flow stress for fcc polycrystals

stage V was introduced by Zehetbauer and Seumer [35]. The beginning of the Stage V is defined by the appearance of a sharp kink in the work hardening rate vs. flow stress curve (Figure 2.2(b)). It is argued that a stage V seems to be redundant in most materials [39].

2.1.2 Kocks-Mecking Analysis - Athermal Hardening

When the flow stress is dominated by dislocation-dislocation interactions, the resolved shear stress τ is related to the total dislocation density stored in the material according to the well known empirical equation [38, 40, 41]:

$$\tau - \tau_0 = \alpha\mu b\sqrt{\rho} \quad (2.1)$$

where τ_0 is the friction stress, b is the magnitude of the Burgers vector of the dislocation, μ is the shear modulus, ρ is the dislocation density and α is a number between 0.2 - 0.35.

In terms of externally applied stress, this equation can be rewritten as:

$$\sigma - \sigma_0 = M\alpha\mu b\sqrt{\rho} \quad (2.2)$$

where M is the Taylor factor and σ_0 is the yield stress of the material.

As the flow stress is determined by Eq. 2.1, the rate of accumulation of dislocations can be expressed in terms of the mean free path of the dislocation, Λ , which is proportional to $\rho^{-1/2}$ [38, 42]:

$$\frac{d\rho}{d\gamma} = \frac{dL}{bda} = \frac{1}{b\Lambda} = \frac{\sqrt{\rho}}{\beta b} \quad (2.3)$$

where γ is the shear strain, dL is the length of dislocation stored per area swept da , and β is constant.

By differentiating Eq. (2.1) and inserting Eq. (2.3):

$$(\tau - \tau_0)\frac{d\tau}{d\gamma} = \frac{(\alpha\mu b)^2}{2} \frac{d\rho}{d\gamma} \quad (2.4)$$

By combining Eq. (2.3) with the definition $\theta = d\tau/d\gamma$, one may write this as:

$$(\tau - \tau_0)\theta = \frac{(\alpha\mu)^2 b}{2 \Lambda} \quad (2.5)$$

Rearrangement of Eqs. (2.1), (2.3) and (2.4) leads to

$$\frac{\theta}{\mu} = \frac{\alpha}{2 \Lambda \sqrt{\rho}} = \frac{\alpha}{2\beta} \quad (2.6)$$

Eqs. 2.5 and 2.6 explicitly introduce the concept of “similitude” [38]. If all dislocations generated during deformation are stored not in the interior of grains but at grain boundaries, mean free path Λ will be constant, which makes Λ the grain size and $\tau\theta$ should be constant according to Eq. 2.5 and illustrated in Figure 2.3 (horizontal dotted line). For ‘similitude’, the mean free path is proportional to the dislocation spacing which is the inverse square-root of the dislocation density; then θ would be a constant according to Eq. 2.6 and $(\tau - \tau_0)\theta$ should be proportional to $\tau - \tau_0$ (dashed line in Figure 2.3). In reality, both a constant Λ and the proportionality to the dislocation spacing contribute to dislocation accumulation (solid line in Figure 2.3).

However, experimental observations show that the lines tend to start out straight and then curve downward (e.g., Figure 2.4). This is attributed to the effect of dynamic recovery which breaks the similitude. In this regime, the dynamic recovery strongly depends on temperature and strain rate. The mean free path Λ is related to the athermal storage mechanism, while $d\rho/d\gamma$ remains as the net accumulation rate:

$$d\rho = \frac{d\gamma}{b\Lambda} - d\rho_r \quad (2.7)$$

where $d\rho_r$ is the density of dislocation annihilation.

The strain hardening rate is, then, expressed in terms of these two mechanisms [38]:

$$\theta = \theta_0 - \theta_r(\dot{\gamma}, T) \quad (2.8)$$

where θ_0 is the athermal storage term of the strain hardening rate, θ_r is the dynamic recovery term, $\dot{\gamma}$ is the crystallographic shear rate, and T is temperature.

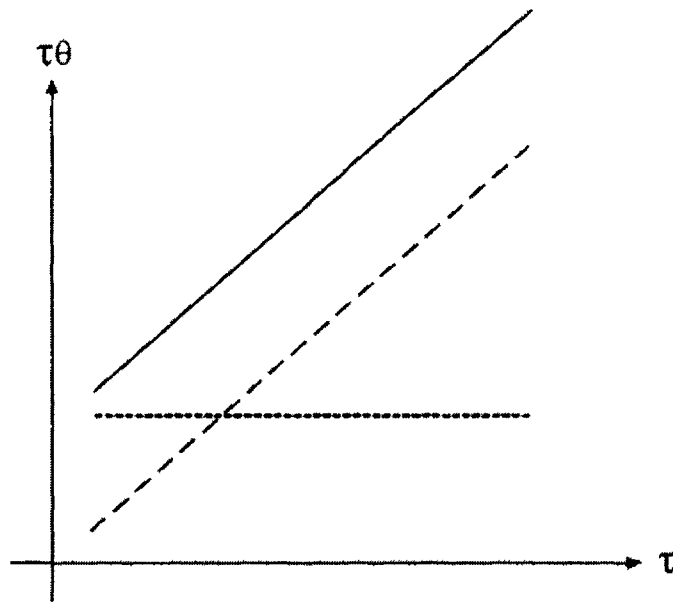


Figure 2.3: Dislocation storage rate when the mean free path Λ is constant (dots); when it is proportional to the dislocation spacing (dashes); and when both superpose (solid) (After Kocks and Mecking [38])

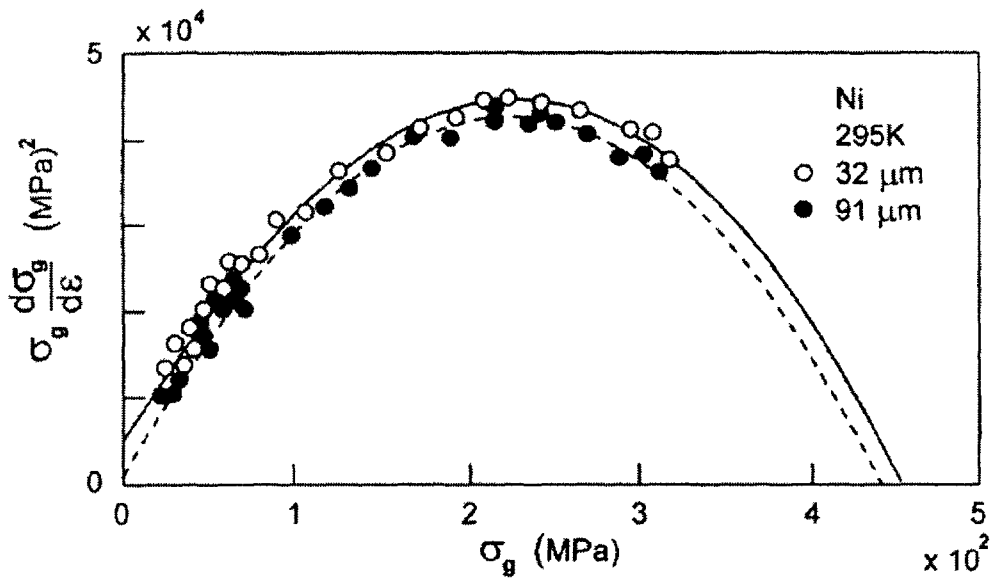


Figure 2.4: Typical experimental observations of the dislocation storage rate (After Narutami and Takamura [43])

This can be written for the polycrystal strain hardening rate if the appropriate Taylor factor is applied [38,44]:

$$(\sigma - \sigma_y)\dot{\theta} = (\sigma - \sigma_y)[\theta_0 - \theta_r(\sigma, \dot{\epsilon}, T)] \tag{2.9}$$

where σ is the flow stress, σ_y is the yield stress, and $\dot{\epsilon}$ is the strain rate.

Eqs. 2.7 and 2.8 convey two mechanisms; they do not involve a concept of stages. Both these mechanisms occur from the beginning to the end of the plastic deformation. The athermal term dominates at a low strain region and is compensated by the dynamic recovery term at a large strain region.

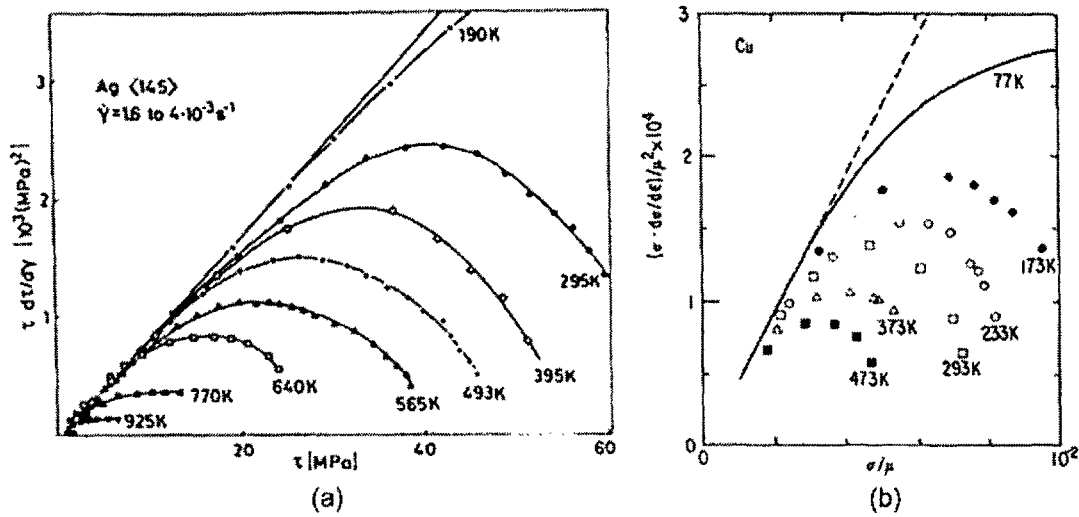


Figure 2.5: Strain hardening of silver single crystal (a) and copper polycrystals (b) (After Mecking and Kocks [45])

The influence of temperature on the athermal hardening is shown in Figure 2.5. For silver single crystal, the data show a straight line through the origin for a finite range of flow stress, especially up to about half the melting point, which confirms the existence of the athermal hardening rate θ_0 and stage II hardening. At high temperatures, the initial slope is close to θ_0 but deviates from it at the beginning of deformation. Copper polycrystals also exhibit the same behaviour; the initial

hardening rate is identical for all temperatures, but deviation from the initial slope occurs earlier at the higher temperature. This athermal hardening rate, θ_o , is always of a factor of 2 of the value $\mu/200$ on a resolved stress basis and allows one to define a dynamic recovery rate, θ_r , as the deviation of the actual net slope of the stress strain curve from θ_o . The dynamic recovery term is dominated by the temperature and strain rate sensitivity of strain hardening [45].

2.1.3 Kinetics of Plastic Flow

The relation between flow stress at the absolute zero temperature, $\hat{\sigma}$, and dislocation density, ρ , is generally expressed as:

$$\hat{\sigma} = \hat{\sigma} \mu b \sqrt{\rho} \quad (2.10)$$

where b is the magnitude of the Burgers vector, μ is the shear modulus, and $\hat{\sigma}$ is a constant associated with the strength of the dislocation/dislocation interaction. That is, the flow stress is proportional to the square root of the dislocation density for the contribution from dislocation-dislocation interactions. As temperature increases, the obstacles can be more easily overcome with the help of thermal activation, and the work hardening state cannot be described by a single parameter such as the density of dislocation as in Eq. 2.10. Additional parameters need to include, for example, the distribution of dislocations at a given temperature and rate of straining. Then the flow stress becomes:

$$\sigma = s(\dot{\epsilon}, T) \hat{\sigma} \mu b \sqrt{\rho} \equiv \alpha \mu b \sqrt{\rho} \quad (2.11)$$

where $s(\dot{\epsilon}, T)$ is a function of rate sensitivity and becomes 1 as T goes toward 0. The above two equations take account of only resistance to dislocation motion that arises from other (forest) dislocations. However, in most cases, there are additional obstacles

to dislocation motion such as intrinsic lattice resistance, solution hardening, grain size effect and precipitates. These contributions can be added to the above constitutive equation:

$$\sigma = s(\dot{\epsilon}, T)\hat{\sigma}\mu b\sqrt{\rho} + \sigma_0(\dot{\epsilon}, T) \quad (2.12)$$

The rate dependence of σ_0 is more sensitive than that of s .

2.1.4 Effect of Temperature and Strain Rate

It was mentioned earlier that the flow curve of a polycrystal deviates from the linearity when the onset of stage III begins during plastic deformation. This is attributed to the fact that the flow stress is strongly dependent upon temperature and strain rate. In general, the strength of the material decreases and ductility increases as temperature increases. Cottrell and Stokes [46] found out that the temperature-dependent portion of the flow stress is proportional to the total flow stress. These researchers pointed out that divergence from this proportionality can occur if either (i) the internal structure (such as the density and configuration of dislocations, dislocations tangles, cell and substructure, etc.) developed during plastic deformation or (ii) the flow stress depends on temperature. An important relationship that referred to Cottrell and Stokes law was deduced from experiments with fcc crystals:

$$\left(\frac{\sigma_j}{\sigma_k}\right)_u \left(\frac{\sigma_k}{\sigma_i}\right)_v = \left(\frac{\sigma_j}{\sigma_i}\right)_w = constant \quad (2.13)$$

where σ_j/σ_k is the ratio of flow stress measured at a constant strain rate when its temperature is changed abruptly from T_k to T_j . The subscripts, u , v , and w , represent the temperature change when the strain of the specimen is u , v , and w , respectively. That is, it is independent of the actual strain of the specimen. This relationship is valid once the strain exceeds a small percentage, i.e. beyond stage I, in the stress-strain curve.

The flow stress change, $\Delta\sigma$, with a sudden change in temperature and strain rate during a tensile test provides an insight into the nature of interactions between mobile dislocations and obstacles responsible for work hardening. Cottrell and Stokes [46] showed that the total flow stress consists of two parts: (1) the irreversible part produced by the interaction of the current dislocation configuration with long range obstacles and (2) the reversible part ($\sigma_r = \Delta\sigma$), which is associated with thermal fluctuations and assists dislocations to overcome short range obstacles. The reversible part is reproducible and proportional to the total flow stress, σ . The Cottrell-Stokes relationship can be rewritten as following:

$$\frac{\Delta\sigma}{\sigma} = \text{constant} \quad (2.14)$$

where $\Delta\sigma$ is the change in flow stress with a change in temperature or strain rate during a tensile test, and σ is the stress before or after the sudden change.

Basinski [47] reported a gradual increase of the Cottrell-Stokes ratio with increasing deformation of copper single crystal at room temperature and argued that the reversible and irreversible parts of the flow stress originate invariably from the same kind of obstacles (forest dislocations), although they depend in different degrees on the forest dislocation density. Mecking and Kocks [45] examined single crystals of various orientation over the wide range of temperatures and reported possibilities for the separation of two regimes of the Cottrell-Stokes law: (1) the change in flow stress with the change in strain rate is proportional to the flow stress during athermal hardening (i.e. stage II), and (2) an increase initiates from a linear relation of the rate sensitivity of the resolved shear stress ($\Delta\sigma/\Delta\ln\dot{\epsilon}$) versus the resolved shear stress due to dynamic recovery process. The validity of the Cottrell-Stokes law was examined by Saimoto and Sang [48]. These authors concluded that the Cottrell-Stokes law is fulfilled at low stresses, while a deviation from it is observed at high stresses. Bochniak [49] carried out the Cottrell-Stokes law studies on copper, aluminum and

silver single crystals deformed at low temperatures and concluded that the increasing deviation from the Cottrell-Stokes law at the beginning of plastic flow can testify that, at least at a low temperature regime, the plastic flow in stages II and III is controlled by the same mechanism and that the deformation mechanism systematically changes throughout the deformation.

The strain rate sensitivity data can be conveniently represented in terms of a ‘Haasen plot’ in which rate sensitivity is plotted as a function of the (effective) stress. The Haasen plot is derived from a general relationship between flow stress, σ , and strain rate, $\dot{\epsilon}$, at a given structure, Σ , and temperature, T :

$$\sigma = C (\dot{\epsilon})^m \Big|_{\Sigma, T} \quad (2.15)$$

where m is known as the strain-rate sensitivity in the engineering definition. The exponent m can be obtained from the slope of a plot of $\log \sigma$ vs. $\log \dot{\epsilon}$. However, m is determined from a strain-rate change test by measuring the change in flow stress resulting from a change in strain rate at a constant strain and temperature (Figure 2.6) as following:

$$m = \left(\frac{\partial \ln \sigma}{\partial \ln \dot{\epsilon}} \right)_{\Sigma, T} = \frac{\Delta \log \sigma}{\Delta \log \dot{\epsilon}} = \frac{\log \sigma_j - \log \sigma_i}{\log \dot{\epsilon}_j - \log \dot{\epsilon}_i} \quad (2.16)$$

The value of m is low for metals but increases with temperature: $m < 0.1$ at room temperature and $m \sim 0.1-0.2$ at $0.5T_m$ (T_m is the melting point) [50]. High strain-rate sensitivity of the material tends to decrease rates of strain-hardening and therefore, becomes the indicator of superplasticity.

The slope of Haasen plot, S , is the thermodynamic strain rate sensitivity:

$$\frac{1}{T} \left(\frac{\partial \ln \sigma}{\partial \ln \dot{\epsilon}} \right)_{\Sigma, T} = \frac{m}{T} = S \quad (2.17)$$

The (thermodynamic) strain rate sensitivity, S , and the intercept to the ordinate of the Haasen plot are a measure of the relative thermally activatable species. A

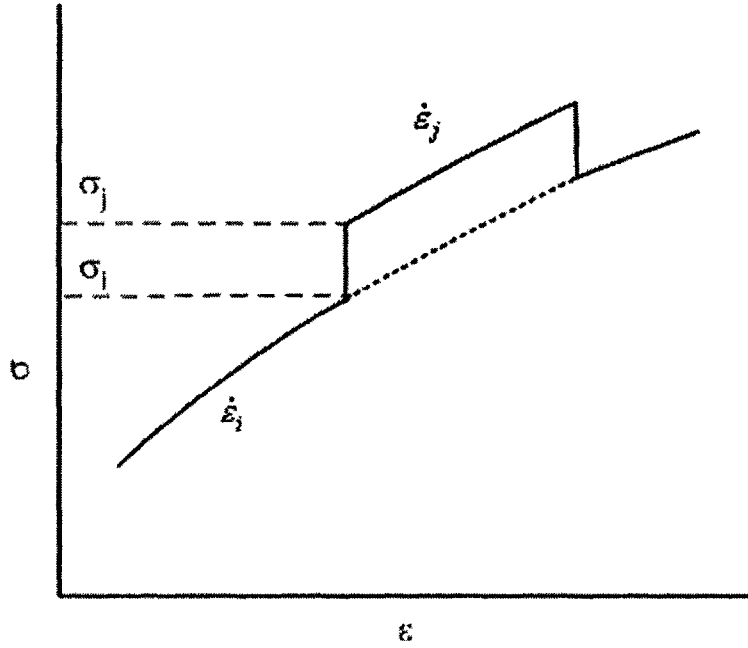


Figure 2.6: Strain rate sensitivity test

positive intercept indicates that a set of obstacles exists where thermal activation is easier than the forest dislocation contribution. On the other hand, a negative intercept indicates the existence of an athermal contribution. When the flow stress is determined solely by dislocation-dislocation interactions, i.e. Eq. 2.11 is valid, the Haasen plot intercepts the origin (Figure 2.7). For a multi-component system, Eq. 2.17 can be rewritten:

$$\frac{1}{T} \left(\frac{\partial \sigma}{\partial \ln \dot{\epsilon}} \right)_{\Sigma, T} = \frac{1}{T} [\sigma_d m_d + \sigma_s m_s + \sigma_t m_t] \quad (2.18)$$

The subscripts d , s , and t stand for dislocations, solutes and other thermally activatable species, respectively. This equation can be re-expressed for polycrystalline material [51],

$$\frac{1}{T} \left(\frac{\partial \sigma}{\partial \ln \dot{\epsilon}} \right)_{\Sigma, T} = \frac{1}{T} [(\sigma - \sigma_0) m_d + \sigma_s m_s + \sigma_t m_t] \quad (2.19)$$

where σ_0 represents the yield stress.

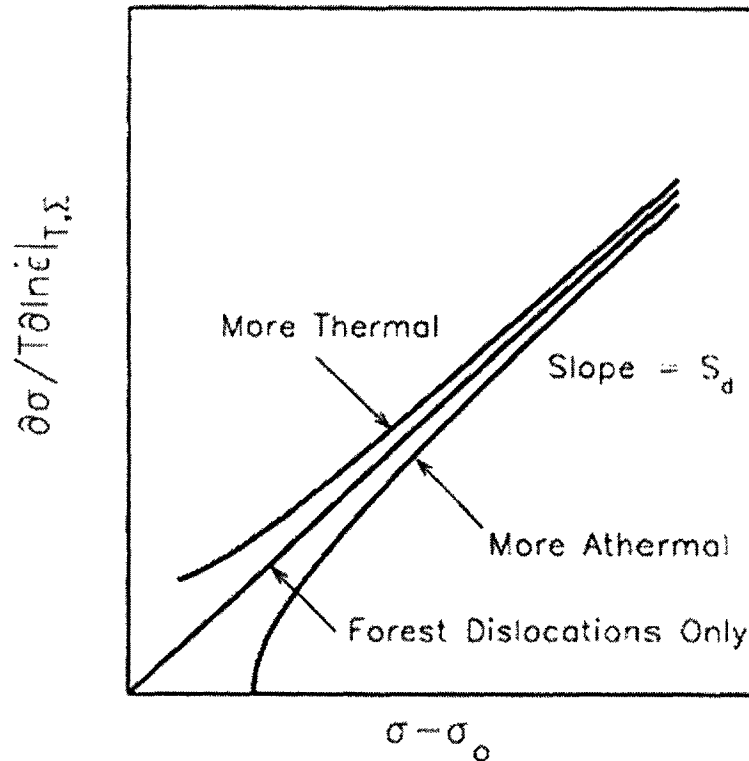


Figure 2.7: Schematic Haasen plot (After Diak et al [51])

2.1.5 Dislocation Density Measurement using Electrical Resistivity

The variation of dislocation density during deformation can be determined by several methods other than by direct counting using etch pits or electron microscopy. They are: (1) solution calorimetry, in which the heat of solution on dissolving deformed and annealed specimens is compared, (2) differential calorimetry, in which the difference between the power supplied to warm up deformed and annealed specimens is measured and (3) technique involving measurements of the difference between the heat evolved during the deformation and the work done on the specimen [52]. Electrical resistivity is another method used for determination of dislocation density in deformed crystals. Measurement of the resistivity change during deformation at low

temperature provides information about changes in the internal structure of the specimen, such as dislocations, point defects, grain boundaries etc. The resistivity caused by dislocations has been determined with some accuracy [53–56].

Dislocation density can be determined by using Matthiessen rule (1862):

$$R = \rho \frac{l}{s} \quad (2.20)$$

$$\begin{aligned} \rho &= \rho_T(T) + \rho_d + \rho_v + \rho_i + \rho_{gb} + \rho_{imp} \\ &= \rho_T(T) + C_d d_d + C_v d_v + C_i d_i + C_{gb} d_{gb} + C_{imp} d_{imp} \end{aligned} \quad (2.21)$$

where R is the resistance in $[\Omega]$, l is the length of the specimen in $[cm]$, s is the cross area of the specimen in $[cm^2]$, ρ is the total measured resistivity in $[\Omega cm]$, $\rho_T(T)$ is the resistivity caused by the lattice vibration, i.e. phonon scattering, and C refers to the scattering factor. The subscripts d, v, i, gb and imp represent dislocation, vacancy, interstitial, grain boundary and impurity, respectively. $\rho_T(T)$ is a function of temperature. At high temperatures, resistivity cannot provide information about the defect content, because phonon scattering which increases with rising temperature is the order of magnitudes higher than dislocation scattering. However, at very low temperatures, lattice vibration becomes insignificant and the scattering from lattice defects can be measured. Phonon scatterings at 300K and 4.2K are 10^{-6} and $10^{-12} \Omega cm$, respectively. $C_{v(i)}$ for one vacancy (interstitial) is $10^{-12} \Omega cm^4$, and C_d for $1cm$ of dislocation line in $1cm^3$ volume is $10^{-19} \Omega cm^3$. The resistivity increase during deformation is caused by the change in dislocation density and/or the concentration of point defects. By measuring resistance and using the Matthiessen rule with known scattering factors, the stored dislocation density can be calculated. The electrical resistivity method is suitable for the measurement of high dislocation densities for the heavily deformed materials, especially where the resolution of available electron microscopy techniques is insufficient. Errors can arise during the measurement of the resistivity due to the difference of the resistivity between the surface and the interior

of the specimen [57] and the generation of thermal electromotive force (EMF) between junctions at different temperatures. These errors, however, can be reduced by using a low current to reduce specimen heating and by reversing the current during the measurement and then taking the average of two readings.

By measuring the change of resistivity of copper single crystals deformed in stages II and III, it was found that the resistivity due to dislocations increases quadratically with resolved shear stress [55, 58, 59].

2.2 Deformation Characteristics of Pure Al and Al-Mg Alloys

2.2.1 Mechanical Properties and Deformation Behaviour

2.2.1.1 Work Hardening Behaviour of Pure Al

A comprehensive review of the general features of the work hardening behaviour and microstructure in various materials deformed to large strains was given in 1980's by Gil-Sevillano et al. [33] and Gil-Sevillano in a subsequent paper [36]; the reader is referred to these articles for references on the work carried out before 1993. The relationship between mechanical properties and dislocation substructure produced during plastic deformation in pure aluminum and Al-alloys has also been studied quite extensively, and there is a large volume of published data available. However, most of these studies have targeted relatively high temperatures, usually above room temperature, where thermally activated processes play an important role in the plastic flow, and phenomena such as dynamic recovery and/or dynamic recrystallization add to the complexity of deformation behaviour of this metal, e.g. [60–63]. There has been

very little research carried out at a low or very low temperature regime, where these processes are suppressed, which also simplifies the interpretation of results. Below, we review experimental work carried out by other researchers on mechanical properties of Al and Al alloys pertinent to the present study, together with the basis of relevant theoretical foundation.

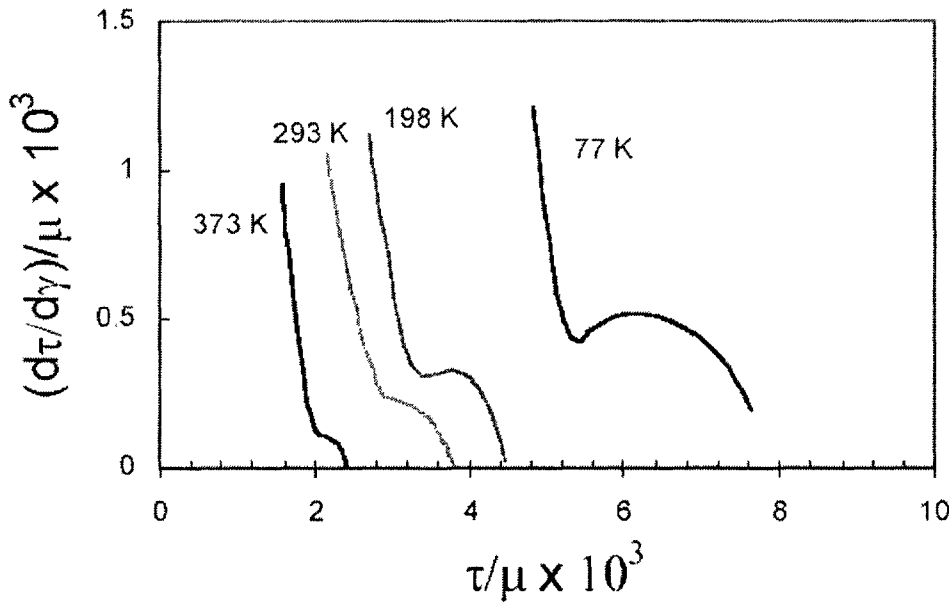


Figure 2.8: Work hardening rates of pure Al at different deformation temperatures, as indicated on the graph (After Gil-Sevillano [36])

Gil-Sevillano [36] provided a thorough description of the approaches for modeling of dislocation accumulation and annihilation in single phase material utilizing the relationship between work hardening rate and flow stress. Figure 2.8 shows the work hardening characteristics for pure Al re-plotted from work of Gil-Sevillano [36], which reveals the different stages of work hardening in this metal. At small strains, one observes a linear decrease of hardening rate with flow stress, which subsequently stabilizes at a certain stress level depending upon deformation temperature. The work hardening may or may not increase at higher strains and again decreases to the

low hardening levels, characteristic for stage IV work hardening (Figure 2.8). The linear decrease in hardening rate at low strains is described by:

$$\frac{\partial \sigma}{\partial \varepsilon_p} = \theta = \theta_0 \left(1 - \frac{\sigma}{\sigma_v} \right) \quad (2.22)$$

where θ is the hardening rate at the stage II work hardening (typically $\mu/20$ for high purity FCC metals), and σ is a scaling parameter to characterize the rate of decrease in work hardening rate with the stress. Assuming that the Taylor relationship between flow stress and dislocation density is satisfied, the flow stress is given by:

$$\sigma = \alpha M G b \sqrt{\rho} \quad (2.23)$$

where α is a geometric constant about 0.33, M is the Taylor factor, G is the shear modulus, b is the magnitude of the Burgers vector and ρ is the dislocation density. The equation for the work hardening can be re-written in terms of the evolution of dislocation density with strain, such that:

$$\frac{\partial \rho}{\partial \varepsilon_p} = (k_1 \sqrt{\rho} - k_2 \rho) \quad (2.24)$$

In this description the slope of the $\theta - \sigma$ is proportional to the rate of dynamic recovery, k_2 . Further integration of first equation or rearrangement of second and third equations leads to the well-known Voce equation:

$$\sigma = \sigma_v - \sigma_v \exp \left(-\frac{\theta_0}{\sigma_v} \varepsilon_p \right) \quad (2.25)$$

which provides a good description of the flow stress as a function of strain in a lower strain region, i.e. ignoring the Stage IV of work hardening.

Embury, Poole and Lloyd [64] provided a general description of the work hardening behaviour in terms of three regimes in which different processes are predominant during plastic deformation. The authors argue that this description should apply to both single phase and multi-phase materials. According to Embury and co-workers,

the work hardening behaviour at low strains is determined by (i) the ability to spread deformation through the metal and processes which involve spring-back actions during forming operations in practical conditions, (ii) the rate of decrease in work hardening rate in which the processes of defect removal take over the processes of defect storage, and finally (iii) the behaviour at large strains which is relevant to large strain operations such as foil rolling. The schematic representation of these processes on the work hardening as a function of stress is shown in Figure 2.9.

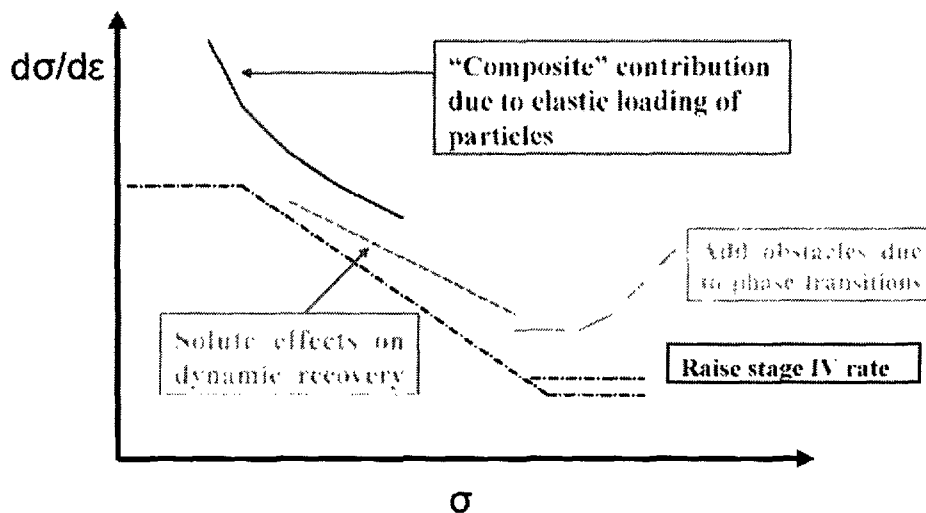


Figure 2.9: Schematic diagram illustrating the $\theta - \sigma$ behaviour in terms of the effect of the contribution of different structural elements on work hardening: (i) contribution of particles which are elastically loaded (primarily affects the low strain region and the elastic-plastic transition), (ii) contribution of solute atoms which affect dynamic recovery and (iii) contribution of strain induced obstacle generation due to phase transitions, e.g., dynamic precipitation during deformation. (After Embury et al. [64])

2.2.1.2 Effect of Mg on Mechanical Properties of Al-Alloys

Impurities or alloying additions increase athermal component of the yield strength more than the thermal component in pure aluminum [65]. It is seen in Figure 2.10 that addition of Mg to Al increases its yield strength and the ultimate tensile strength

(UTS), whereas it decreases the homogeneous elongation in the range up to about 2wt% of Mg. The research studies done by Takaai and coworkers [65] show that UTS of dilute Al-Mg alloys significantly increases with decreasing temperature down to 7K. For other Al-Mg alloys, UTS also increases with decrease in temperature to about 25K in 5083-O Al alloy and to about 40K in Al-5.3% Mg alloy, and it becomes nearly constant below those temperatures. The yield stress in those two alloys increases very slowly with decrease in temperature [66].

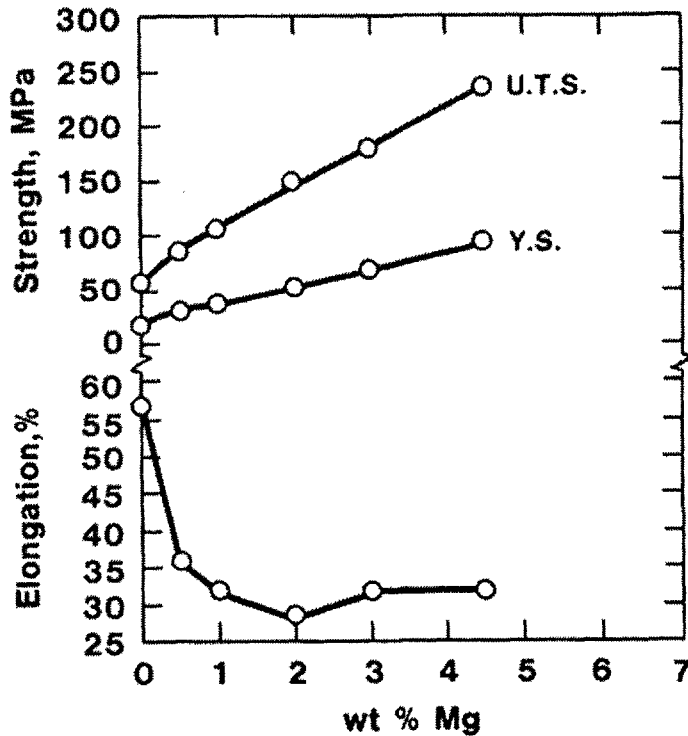


Figure 2.10: Effect of the addition of Mg to pure Al on tensile properties (After Vasudevan and Doherty [67])

For commercially pure aluminum, strain rate dependence of the flow stress, $(\Delta\sigma)_T$, at 77K is larger than that of 4K in contrast with the results for bcc metals Nb and Nb alloys [65]. The addition of Mg to pure Al generally decreases the strain-hardening exponent, n , and increases K in the Holloman equation, $\sigma = K\varepsilon^n$. This indicates

that the strength including work hardening capability is increased and the ductility is decreased by the addition of Mg. With further increasing Mg content, n remains constant, but K continues to increase [67]. At large strains such as stage IV of the work hardening, the work hardening rate becomes independent of the solute content. This is attributed to an increased shear band formation and dislocation storage patterns in subgrain boundaries and interior [68]. The addition of Mg strengthens the material more efficiently in the very dilute range (<1 at%Mg) than in the more concentrated alloys. At Mg levels less than 1at%, the yield strength change (ΔYS) is proportional to $(\text{at}\% \text{ Mg})^{2/3}$, whereas ΔYS is linear to $(\text{at}\% \text{ Mg})^{1/3}$ at Mg levels higher than 1 at% [67]. The Mg also increases the frictional stress, σ_o , in the Hall-Patch equation ($\sigma_y = \sigma_o + kd^{-1/2}$) as shown in Figure 2.11 [69].

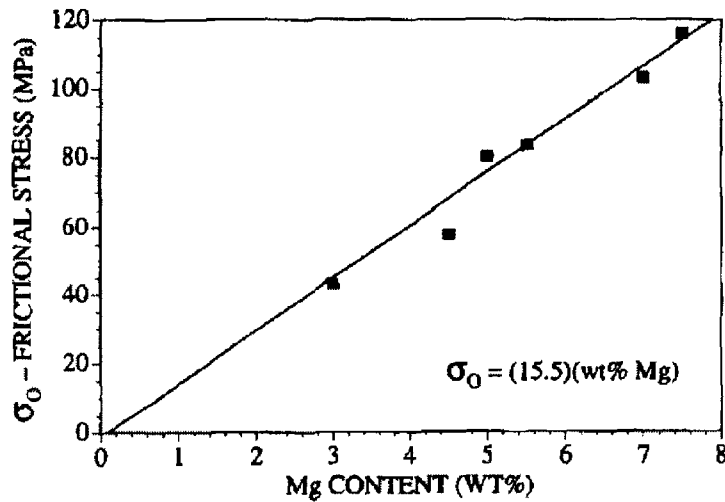


Figure 2.11: Effect of the addition of Mg on frictional stress, σ_0 (After Burger et al. [69])

Ductility of pure Al increases with decreasing temperature due to the increasing uniform deformation caused by the higher work hardening capacity [66]. Ductility decreases with increase in Mg content at high temperature ranges between 300K and 700K [70]. However, Rollet and co-workers [71] showed, by performing torsion tests

at temperatures between 77K - 473K, that Al-1%Mg alloy exhibits a clear stage IV of work hardening at all temperatures except the highest temperature, although the commercial pure Al shows a distinct stage IV only at the lowest temperature. These authors argue that small differences in yield strength caused by solute hardening are magnified by strain hardening behaviour.

More systematic studies on the effect of various alloying elements on properties of Al-based alloys have been carried out recently by Lloyd and Court [72] and Lloyd [73]. Lloyd and Court studied the effect of Mg addition in alloys containing up to 3 wt%Mg and argued that Mg does not influence the glide process of dislocations in these alloys. As a result, the free slip distance is strain-dependent as expected from dislocation-dislocation interactions in these alloys. On the other hand, in an Al-5wt%Mg alloy, the analysis indicates that solute atoms are controlling the dislocation mean free path. If Mn is added to the Al-5 wt%Mg alloy, as it is in commercial alloys, it has little influence on the grain size dependence, but it does increase the frictional stress at the highest Mn level of 0.7 wt% [72].

Lloyd [73] has carried out the analysis of the work hardening behaviour of commercial 1000, 3000 and 5000 series Al alloys in the temperatures ranging from room temperature down to 85K. Table 2.1 shows composition of Al-alloys studied by Lloyd [73]. Figure 2.12 shows the effect of the temperature on both yield stress (YS) and ultimate tensile strength (UTS) in AA1100 series containing 0.1wt%Si and 0.33wt%Fe, whereas Figure 2.13 shows the work hardening for this system as a function of flow at different temperatures.

Lloyd argued that, in the low solute alloys such as AA1100 and AA3003, the dislocation structure develops cells that are sharp and that the cell size decreases with the strain. The generation of cells requires dislocation rearrangement and annihilation, lowering the stored energy of the material, which is reflected in the high dynamic

Table 2.1: Compositions of the commercial alloys studied by Lloyd [73]

Alloy	Mg(wt%)	Si(wt%)	Mn(wt%)	Fe(wt%)
AA1100	-	0.1	0.05	0.33
AA3003	0.8	0.21	1.04	0.5
AA5005	0.8	0.13	0.03	0.5
AA5052	2.27	0.1	0.06	0.22
AA5754	3.15	0.08	0.2	0.18
AA5182	4.7	0.05	0.3	0.2

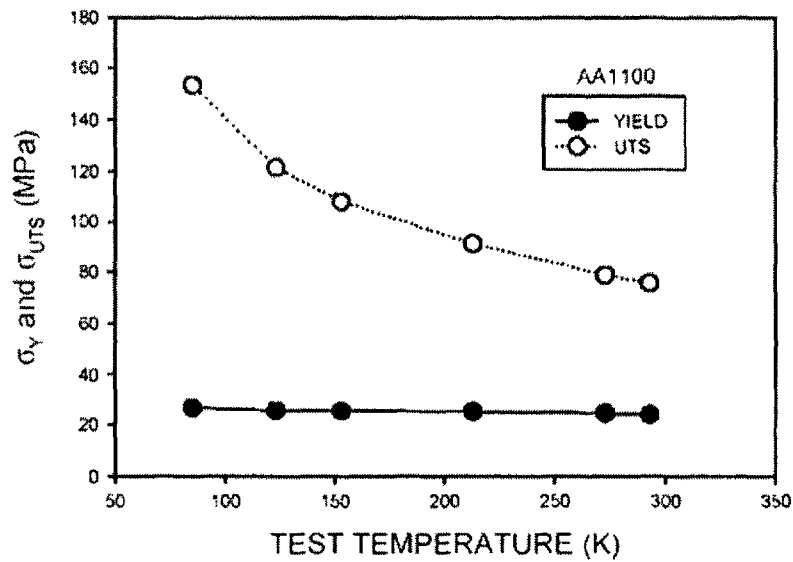


Figure 2.12: Influence of test temperature on yield stress and UTS in AA1100 alloys (After Lloyd [73])

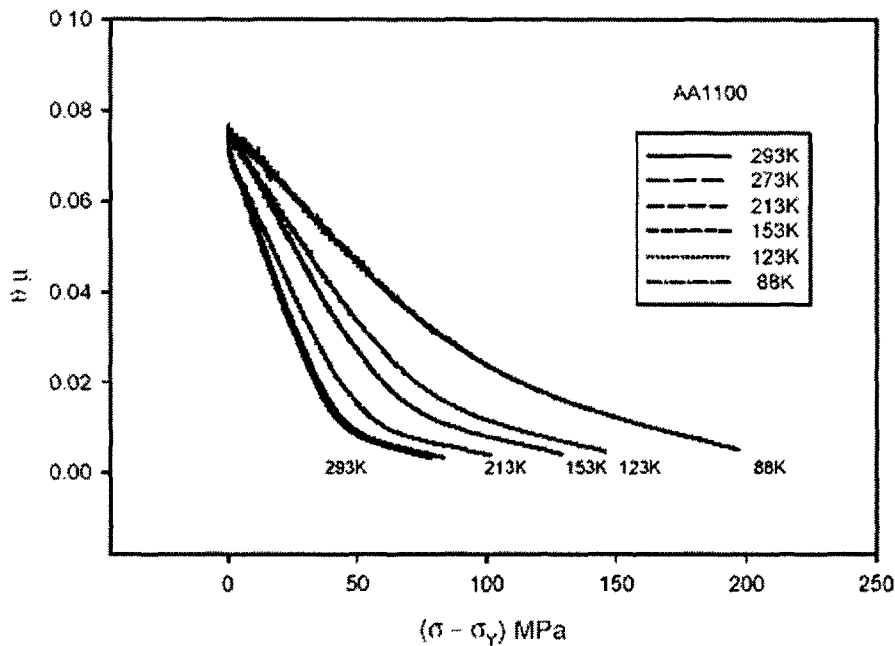


Figure 2.13: Work hardening at different temperatures for AA1100 (After Lloyd [73])

recovery rates exhibited by such systems at room temperature. When Mg is present in the alloy, the Mg atoms segregate to dislocations, forming solute atmospheres that exert a drag on dislocations and inhibiting dislocations to glide, cross slip and climb. The extent of the solute drag increases with increasing Mg content, and this is reflected in a decrease in dynamic recovery rate with increasing Mg level [73]. Figure 2.14 shows variations in dynamic recovery rate with a temperature for all alloys tested by Lloyd [73]. According to this researcher, the dynamic recovery rate, as measured from the saturation stress σ_s , scales with the Mg level as: $[\sigma_s = 50 + 40(\text{wt}\% \text{Mg})]$. Solution hardening is also linear with Mg level, but in this case, the strengthening coefficient is about 16. In the conclusions, Lloyd argues that Mg atoms have a larger effect on work hardening than solution strengthening. The solute drag effects caused by the addition of alloying elements to these alloys inhibit dislocation rearrangement and increase the work hardening rate. Decreasing the temperature has a similar ef-

fect, but the temperature sensitivity is higher in the low solute alloys, which reflects the competition between the reduced thermal effects decreasing dynamic recovery, while a reduced solute drag would have the opposite effect [73].

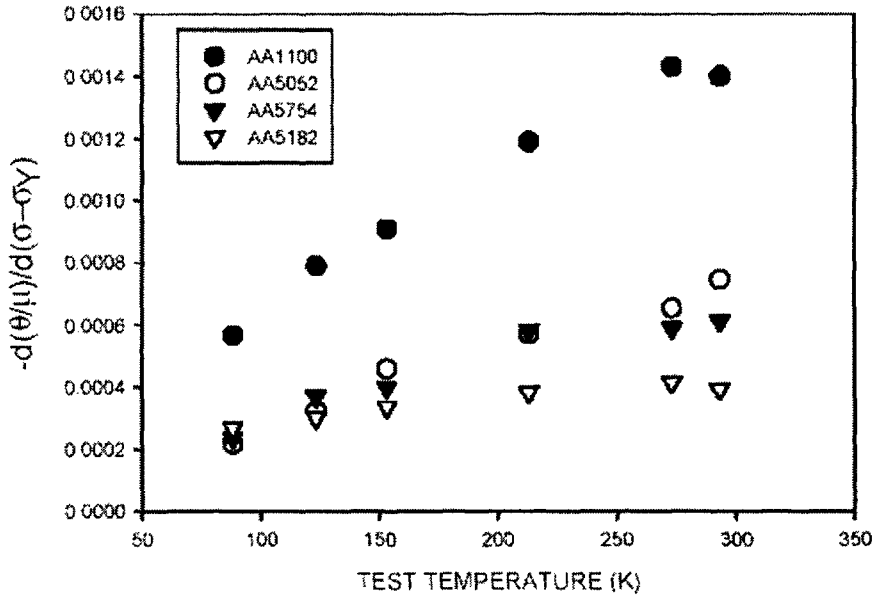


Figure 2.14: Variation in dynamic recovery rate with temperature (After Lloyd [73])

Earlier work of Lloyd on 5xxx Aluminum Alloys revealed that the temperature dependence of ductility (Figure 2.15) is generally associated with strain rate sensitivity, m (Figure 2.16) [74]. The author argues that the high positive strain rate sensitivities restrict the growth of any localized necks formed during the deformation of Al-Mg alloys and thus result in a large increase in ductility; e.g. the ductility at high temperatures shown in Figure 2.15 can be related to the high strain rate sensitivity of the material seen in Figure 2.16.

Impurities or low amount of solute not only affect the mechanical properties but also influence the evolution of deformation textures. Jin and Saimoto [19] reported that the rolling texture in AA5754 Al-Mg alloy containing a very low amount of Fe solute produces reduced texture intensity with detectable amounts of a hot rolling

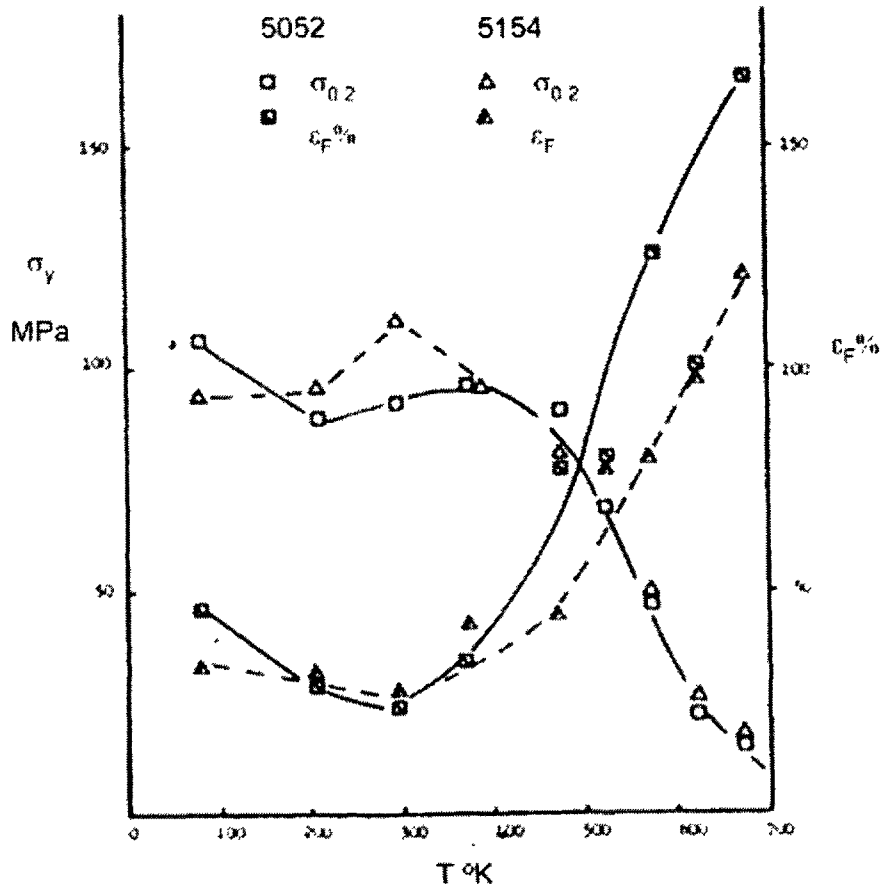


Figure 2.15: Temperature dependence of the yield stress, σ_y , and ductility, ϵ_F , in AA5154 and AA5052 (After Lloyd [74])

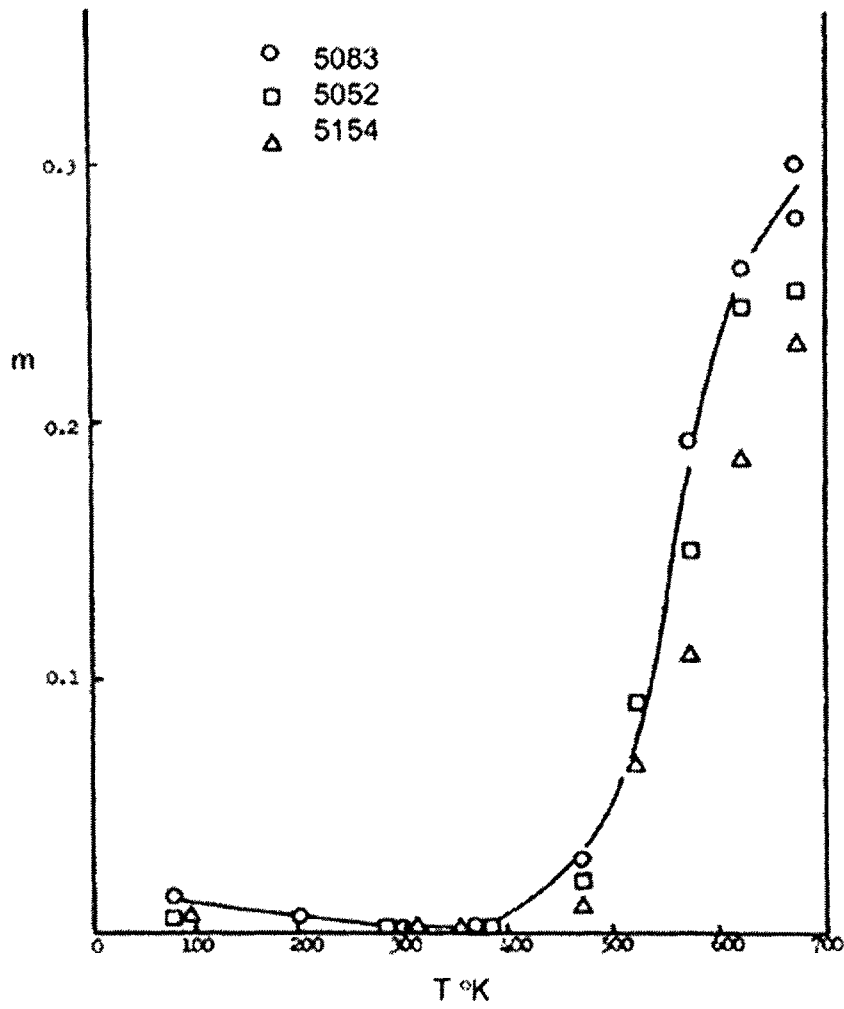


Figure 2.16: Strain rate sensitivity, m , as a function of temperature in different AA5xxx (After Lloyd [74])

component near the surface of the sheet. These authors argue that these effects result from the intrinsic change in the nature of dislocation mobility once the strong dislocation pinning solutes are removed. The size and distribution of precipitates also affect the annealing texture. Coarse (above $1\mu\text{m}$) and sparse precipitates result in discontinuous recrystallization due to the particle stimulated recrystallization, while fine and dense precipitates have an opposite effect, due to the strain induced recrystallization [6, 75]. These texture changes eventually affect the formability; in general, a strong recrystallization texture increases the ductility, improves the workability and eventually results in the higher formability [6].

2.2.2 Microstructure Evolution during Plastic Deformation

2.2.2.1 Pure Al

Previous studies have revealed that the distribution of dislocations induced by plastic deformation is generally heterogeneous [76–79]. For materials with medium or high stacking fault energy (SFE), including pure Al and Al alloys with a low solute content, “tangled” dislocations are formed in the initial stage of deformation, and with increasing strain such a substructure is eventually transformed into a structure consisting of cells by the process involving the formation and the linkage of “tangled walls.” That is, instead of forming a random and uniform distribution of dislocations, the substructure in single-phase materials is organized in a special configuration consisting of deformation induced dislocation boundaries and high angle boundaries separating volumes of relatively low dislocation density in a three-dimensional cell-like dislocation arrangement [33]. The dimensions of the cell structure are temperature

dependent; for example, pure aluminum develops a cell structure the size of which decreases as temperature decreases [77].

It is important to emphasize that generally the type of the cell structure is influenced by several material and process parameters, such as SFE, grain size, initial texture and amount of plastic strain. SFE of the material influences the type of the dislocation substructure and dislocation arrangements, which are produced due to the enhanced cross-slip events and perhaps also other important properties such as dislocation core structure affecting cross-slip tendency and/or strain localization. For example, it is known that increasing SFE leads to the appearance of the second generation microbands in close to $\{111\}$ orientation, which do not always produce localized shear flow in the material [77]. For polycrystalline copper, materials with larger grain size exhibit more heterogeneous deformation behaviour than small grain materials, and the subdivision of their cell structure into subgrains is more pronounced [77].

For pure aluminum, one does not observe a significant effect of the grain size on the deformation microstructure. However, a faster rate of structural development has been observed in the fine-grain samples compared to the coarse-grained materials [80]. Furthermore, microbands are less frequently observed in fine-grained aluminum ($35\mu\text{m}$), whereas well-developed microbands are formed in the medium and large grain size ($80\mu\text{m}$ and $400\mu\text{m}$) specimens [9]. The microstructure development is affected by the crystallographic orientation (texture) of the grains through the various forms of dislocation interactions [81]. The difference in grain misorientations across the grain boundaries enhances the microstructural heterogeneities as the strain increases [82]. The amount of strain influences the cell size and the cell misorientation. With increasing strain, the homogeneous rotation of the individual cells within the cell blocks becomes increasingly difficult, and thus the size of a cell block decreases. It has been reported that when the pure Al is strained from 10% to 30%, the cell size

is reduced from $2\mu\text{m}$ to $1.3\mu\text{m}$ [83]. These results are in agreement with the earlier work of Young and co-workers [84]. Meanwhile, Hansen [85] argued that the strain has little effect on the subgrain size.

With further straining, dislocations accumulated within individual cells are arranged in lower energy configuration subgrains. Additionally, a number of larger inhomogeneities may be superimposed on this structure, such as dense dislocation walls, microbands and shear bands [76, 77]. The local misorientations of subgrains increase with deformation, leading to cell subdivision and further refinement of the structure. The process of grain subdivision is characterized by the formation of cell blocks bounded by extended dislocation boundaries. Typical structural features of the highly deformed microstructure of pure aluminum polycrystals are cells, dense dislocation walls (DDWs), microbands and subgrains. Dense dislocation walls (DDWs) and microbands (MBs) are called sometimes geometrically necessary boundaries (GNBs). The boundaries confining the ordinary dislocation cells are called incidental dislocation boundaries (IDBs) (Figure 2.17); for more details on the definition and description of these structures, the reader is referred to the work of Kuhlmann-Wilsdorf and Hansen [86], Bay and co-workers [76] and Liu and Hansen [87].

This general subdivision pattern by dislocation boundaries applies to both single and polycrystals [76, 88, 89]. The mechanism of grain subdivision depends on the stacking fault energy of the material, which in turn depends on the nature of the dislocation interactions that are taking place and the nature of dislocation debris that constitutes the dislocation walls. In high stacking fault energy fcc metals such as aluminum, the microstructure evolves in such a way that well-defined subgrain boundaries are formed as a result of dynamic recovery. Generally, bands of high misorientation are observed in the interior of the grains and at the grain boundaries [80]. The cell structure which develops at a high temperature is more homogeneous

and more equiaxed [85]. It appears that grain subdivision is a common feature of many crystalline systems and occurs both on the macroscopic (tens of grains) and microscopic (individual grains or subgrains) level [76].

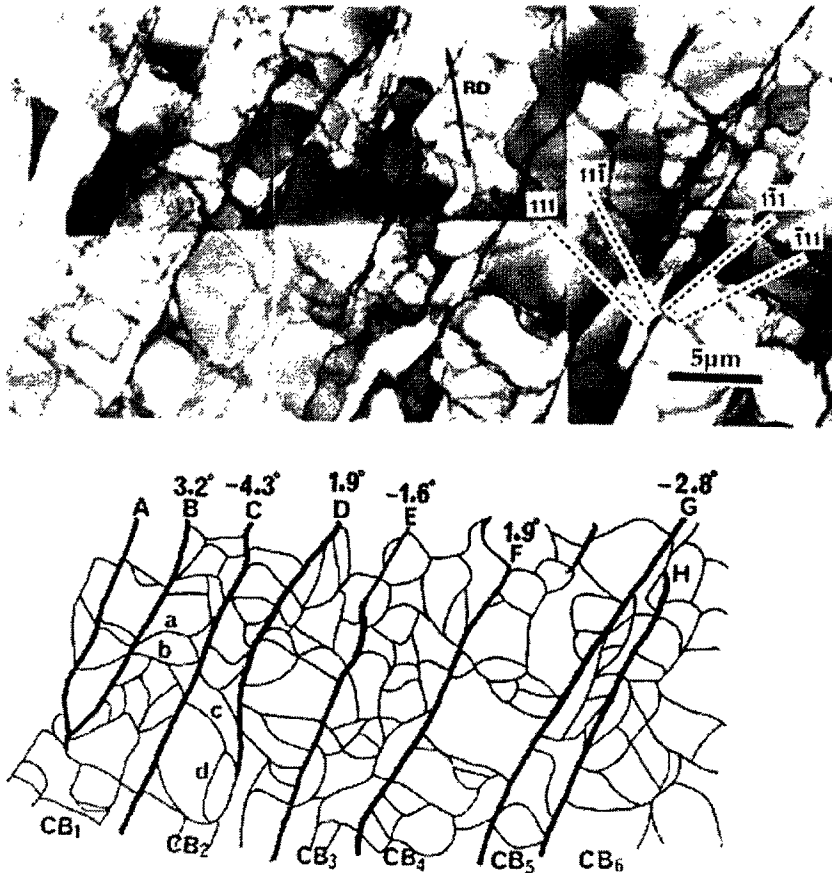


Figure 2.17: The microstructure of high purity Al cold-rolled 10% (above) is subdivided by extended (Dense dislocation walls: DDWs) and sharp (Microbands: MBs) dislocation boundaries, which form a cell block structure. The cell blocks are subdivided by ordinary dislocation cells. The figure below shows Geometrically Necessary Boundaries (GNBs) marked A, B, C, etc. and Incidental Dislocation Boundaries (IDBs) marked a, b, c, etc. (After Liu et al. [82])

It is currently believed that grain subdivision is controlled by the efficiency of the recovery processes that are taking place within the dislocation boundaries. However, details of these processes are unclear. It has been shown that dynamic recovery

operates effectively during the plastic deformation of a material even at lower temperatures, resulting in a decrease of the flow stress as the temperature increases [76,90]. At larger deformations, energy stored in defects accumulated in the material may be released by nucleation of dynamic recrystallization, which under appropriate conditions may lead to a sudden decrease in flow stress, premature flow localization, and fracture of the material, e.g., [90] and references available therein. The subgrain size decreases with increasing strain until it reaches a steady-state size. At the same time, the misorientation between subgrains and microbands also increases with strain to a steady-state [91].

The influence of microstructure on the work hardening behaviour of pure aluminum deformed at 77K was studied by Chu and Moris [92]. These authors show that a recrystallized or well-annealed microstructure, free of subgrains, develops well-defined dislocation cells when deformed, and has a work hardening rate that decreases rapidly with increasing stress. In contrast, when the test sample is recovered, subgrains hinder the formation of dislocation cells. As an apparent consequence, a high rate of work hardening is retained at high stress, which leads to an improved combination of strength and elongation.

Both the recrystallized and recovered microstructures obey constitutive relations of the Kocks-Mecking form: $\theta = \theta_0 - K\sigma$, where θ is the work hardening rate and σ is the flow stress. However, the values of the initial work hardening rate, θ_0 , and slope, K , depend on the microstructure. The values determined for the recrystallized microstructure are close to those found for aluminum. In comparison, the values of θ_0 and K for the recovered microstructure are significantly lower but are compatible with the Kocks-Mecking model if it is assumed that approximately 60% of the total dislocation density is used to maintain geometric compatibility and is unavailable for hardening. The authors argue that the interpretation is at least quantitatively con-

sistent with TEM observations, which show significant localized dislocation activity along the subgrain boundaries.

2.2.2.2 Effect of Mg on Microstructure

The solute atoms both inhibit the process of dynamic recovery, by making cross-slip and climb difficult, and enhance the work hardening. Kral [93] argued that the climb of dislocations is not critical for the dynamic recovery to operate effectively due to easy cross-slip for Al-Mg alloys at high temperatures. Thus, in contrast to the substructure developed in pure Al, the addition of a solute, such as Mg, inhibits the cell formation by increasing the friction stress and the effect on SFE. It is known that Mg decreases stacking fault energy of Al-Mg systems. As a result, the dislocation substructure consists of a uniform distribution of dislocation tangles organized along the $\{111\}$ slip planes [78, 94, 95]. Assuming that the dislocations are preferentially stored along $\{111\}$ planes and the misorientations occur from the wavy types of $\{111\}$ planes ($(\bar{1}\bar{1}1)$ and (111) planes), the traces of their intersection become parallel to $[01\bar{1}]$ as shown in Figure 2.18 [96]. This organized structure is defined as a Taylor lattice (Figure 2.19) [79]. At larger strains, the microstructure shows sharp microbands, which cut through the dislocation tangles [94, 97, 98].

Due to the relatively high diffusivity of the Mg solute at room temperature, common characteristic processes observed in Al-Mg alloys are dynamic strain aging and non-uniform plastic deformation, which result in discontinuities (serrations) in the stress-strain curve known as the Portevin-Le Chatelier (PLC) effect. The solute associated with the PLC effect is known to prohibit the dynamic recovery process by restricting cross-slip [99, 100].

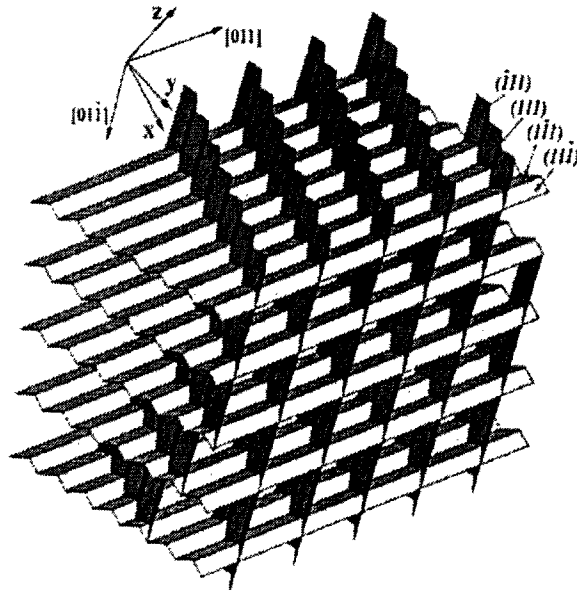


Figure 2.18: Spatial arrangement of the dislocation of Al-2.5%Mg alloys (After Verdier et al. [96])

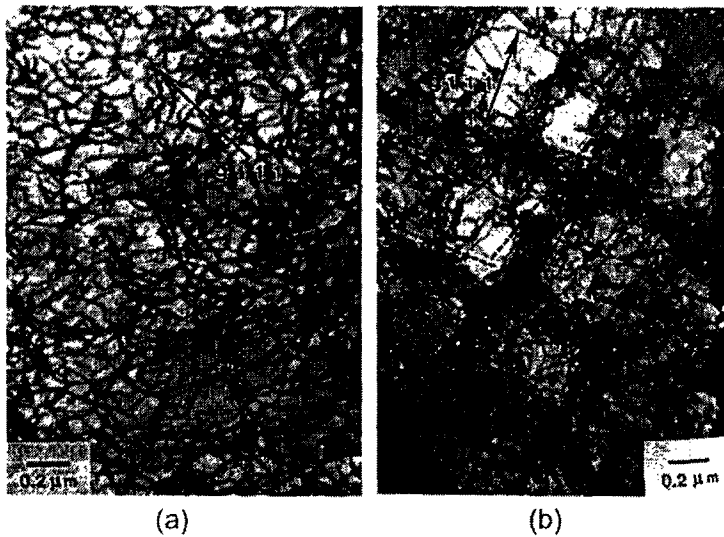


Figure 2.19: A uniform distribution of dislocation tangles (a) and the organized dislocation tangles called a Taylor lattice (b) of Al + 5.5at.%Mg. Dashed lines in (b) are the trace of $\{111\}$ planes. (After Hughes [78])

This increases dislocation density significantly; the microstructure developed in materials of pronounced PLC-type deformation is generally characterized by uniform and rapid accumulation of dislocations, with no evidence of dynamic recovery or dislocation cell formation [101].

The dislocation microstructure which is being developed influences the texture evolution during deformation. Endou and Inagaki [102] observed a remarkable development of S and Copper orientations in pure Al in which well-defined elongated cell structures were formed. The development of these main rolling texture components is strongly suppressed in the Al-5%Mg alloy in which only dense dislocation tangles and ill-defined small cells are formed. Endou and Inagaki argue that the elongated cell structures provide the necessary boundary conditions for the development of the strong rolling textures. The grain establishes a dynamic equilibrium and arrives at its stable end orientation if elongated cell structures are fully developed in a grain. Field and Weiland [103] and Hansen and co-workers [104] reported the effect of cell size on crystallographic orientation (texture) in pure Al and pure nickel, respectively. This has been further accounted by Field and Weiland [103] who provided a modified relation between dislocation density and mean free path (Eq. 2.26) as well as included a description of the distribution of crystallite orientations (Eqs. 2.27 and 2.28).

$$\sigma - \sigma_y = M\alpha_1\mu b\rho^{1/2} \quad \text{and} \quad \sigma - \sigma_y = \alpha_2\mu \left(\frac{b}{\lambda}\right)^m \quad (2.26)$$

where ρ , λ , μ and b are the dislocation density, average cell size, shear modulus, and Burgers vector, respectively.

$$\sigma - \sigma_y = \alpha_1(\dot{\epsilon}, T)\mu(T)b \left[\frac{1}{8\pi^2} \oint_{g \in so(3)} f(g)\rho_t(g)dg \right]^{\frac{1}{2}} \quad (2.27)$$

and

$$\sigma - \sigma_y = \alpha_1(\dot{\epsilon}, T)\mu(T)b \left[\frac{1}{8\pi^2} \oint_{g \in so(3)} \left(\frac{f(g)}{\lambda(g)}\right) dg \right]^m \quad (2.28)$$

$f(g)$ in the above equations is the normalized crystallite orientation distribution function (ODF); $\rho(g)$, dislocation density; $\lambda(g)$ is the cell size (mean free path for dislocation motion).

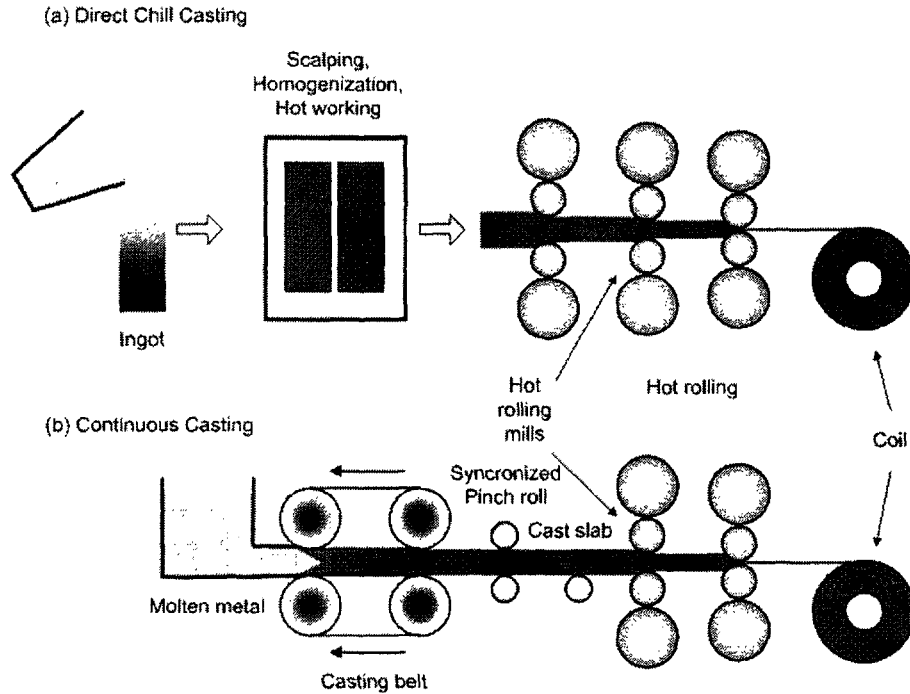


Figure 2.20: Schematic of the CC and DC processes

2.3 Effect of Thermomechanical Process on Material Properties

In North America, the 5000 series of Al alloys have been considered for structural applications in the automotive industry as mentioned earlier. However, the main barrier to replacing the current conventional materials is the high cost of producing aluminum sheets. In this regard, the continuous casting (CC) process is more economical production process because it reduces some processing steps compared to direct chill casting (DC) as schematically illustrated in Figure 2.20. Unfortunately,

materials produced by CC generally have an inferior formability due to the different thermomechanical process.

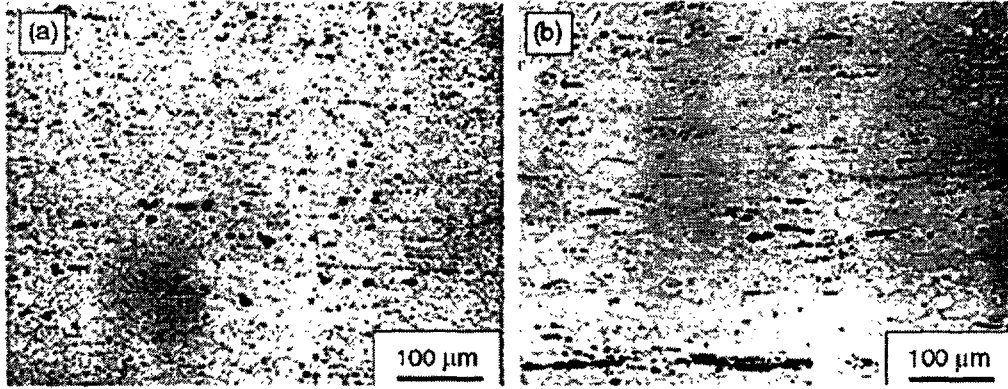


Figure 2.21: Particle structure of (a) the DC and (b) CC AA5182 alloys (After Yu et al. [4])

2.3.1 Mechanical Properties and Microstructure

Generally, DC alloys contain relatively large precipitates ($>10 \mu\text{m}$) whereas CC materials contain fine ones ($<1 \mu\text{m}$) due to the high cooling rate during the CC process. For example, Figure 2.21 shows much smaller dispersoids in the as-received CC AA5182 hot band. There are two main intermetallic phases that form during solidification: (1) the insoluble and (2) the soluble phases (e.g., Mg_2Al_4). The insoluble phases are usually iron/silicon-bearing precipitates such as Al_mFe . In a large ingot, the metastable phases Al_6Fe and Al_mFe are found near the surface where cooling rates are high, and Al_3Fe is found close to the center where the material cools more slowly [105, 106]. These large particles are generally brittle, and the fracture of particles leads to the presence of voids in the microstructure during the deformation or thermomechanical processing. Uncracked large particles cause extensive matrix flow between the (soft) matrix and the (hard) particle to maintain the compatibility.

Hence, high dislocation densities and large lattice misorientation (>10 deg.) are often observed near the particles, which becomes a favorable site for nucleation of recrystallization [107], which results in discontinuous recrystallization and eventually affects the deformation behaviour. A dispersion of particles with diameters larger than η_c accelerates recrystallization and leads to a finer grain size [108]. Smaller particles hinder the grain boundary migration by particle dispersion, which exert a drag pressure (P_z) on recrystallization fronts sweeping through the deformed structure [109].

$$P_z = \frac{3}{2}\beta\gamma(f/r) \quad (2.29)$$

where γ is the specific grain-boundary energy (about 0.3 J/m^2 for Al), f is the volume fraction of particles, r is the average particle radius, and β is a constant having a value near $\frac{1}{2}$.

During deformation, when (large) particles are cut by mobile dislocations, deformation localizes in persistent slip bands formed in the microstructure by the passage of dislocations through precipitates. This eventually reduces work hardening and leads to a premature shear failure. However, uncracked and non-deformable particles increase work hardening by formation of dislocation debris around particles [110]. At the same time, this local plastic strain concentration near the particles initiate fracture by decohesion or cracking of particles. In contrast, fine particles result in a low work hardening rate and tend to form intensive slip bands and shear bands, which induce shear mode failure. Therefore, from the point of view of formability, it may be desirable to develop duplex particle structure of fine and large particles for strength and ductility; small particles ($\approx 0.01 \mu\text{m}$) for strength and large particles ($>1 \mu\text{m}$) to break up the slip pattern and prevent the formation of persistent slip bands [111,112]. Therefore, the DC alloy shows better formability. Yu and co-workers [4] reported that the as-received CC hot band showed an inferior bendability and failed at angles of less than 90° , while the DC hot band showed a maximum bending of 180° . The bend-

ability of the annealed CC hot bands was improved greatly from below 90° to 150° but still inferior to that (180°) of the DC hot band.

2.3.2 Texture

It was reported that CC materials generally do not develop strong recrystallization textures after annealing [4, 5, 113]. Since CC materials are usually free from coarse particles ($>1 \mu\text{m}$), they undergo strain-induced recrystallization that resembles the current texture, hence the so-called continuous recrystallization. The occurrence of continuous recrystallization is determined by various parameters, mainly by the solute Fe level in the aluminum matrix, but also by the initial grain size, the local strain state, the specific orientation of each individual crystallite and the misorientation at the grain boundaries [114]. On the contrary, DC materials contain large particles which induce the particle-stimulated recrystallization, which changes the deformation texture to an annealing texture such as a cube or R-Cube texture, the so-called discontinuous recrystallization. Figures 2.22 and 2.23 show examples of textures of strip cast (SC) and DC materials after annealing [6].

All as-received SC and most of as-received DC hot bands have typical deformation textures with a β fiber extending from the copper orientation $\{112\}\langle 111 \rangle$ through the S orientation $\{123\}\langle 634 \rangle$ and ending at the brass orientation $\{011\}\langle 211 \rangle$; the thinner DC hot band (2.6mm) already has a typical recrystallization texture (Figure 2.22). After annealing, the thinner DC (2.6mm) shows a strong R-cube texture $\{124\}\langle 211 \rangle$ and the thick DC hot band (4.5mm) contains a typical recrystallization texture, although the texture is weak. SC hot bands show the recrystallization texture (cube component $\{100\}\langle 001 \rangle$), but weak deformation textures are still observed in SC 5182 (Figure 2.23). These different textures affect the properties of the subsequent

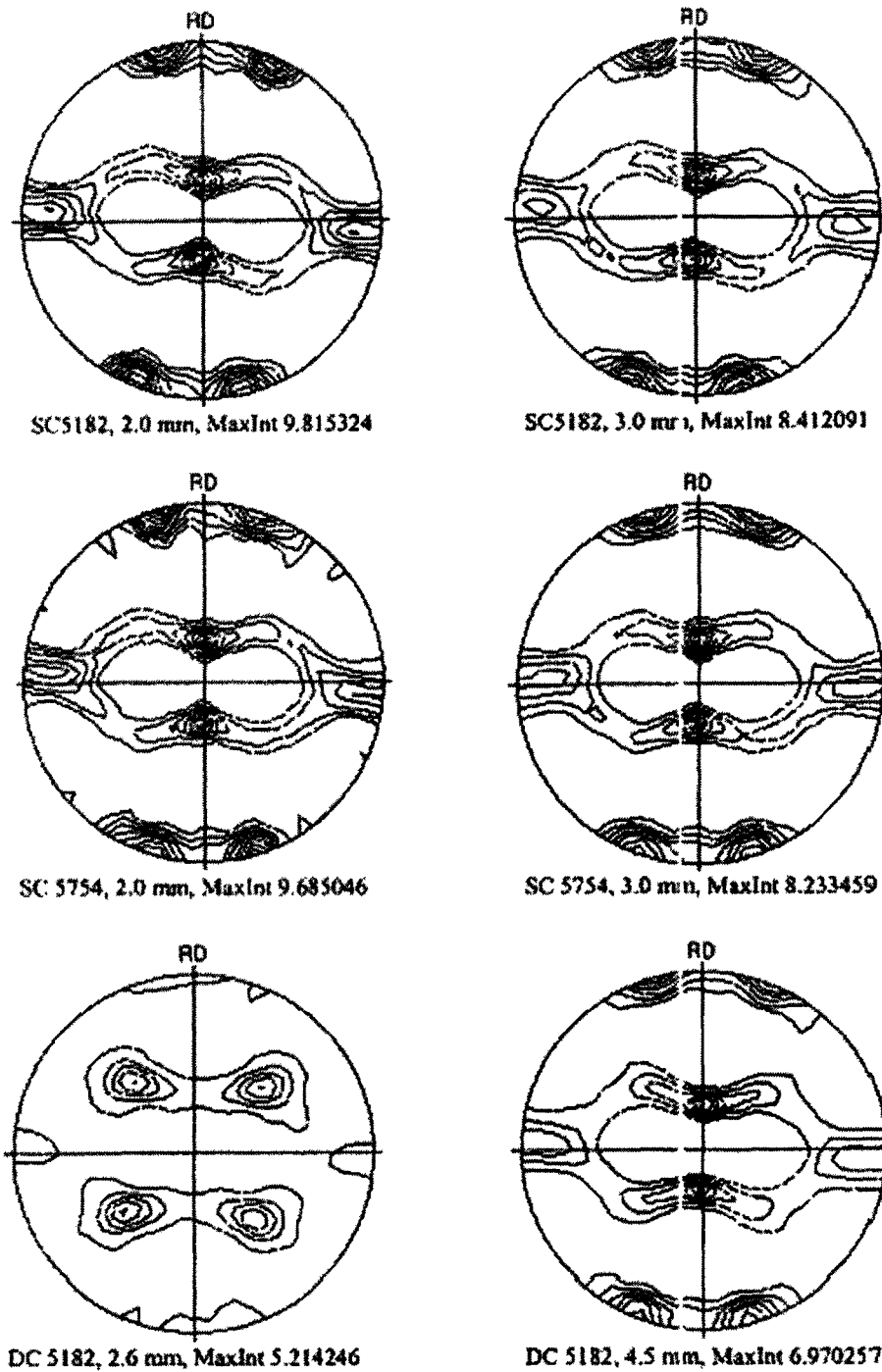


Figure 2.22: The (111) pole figures of as-received hot band SC and DC materials (After Cheng and Morris [6])

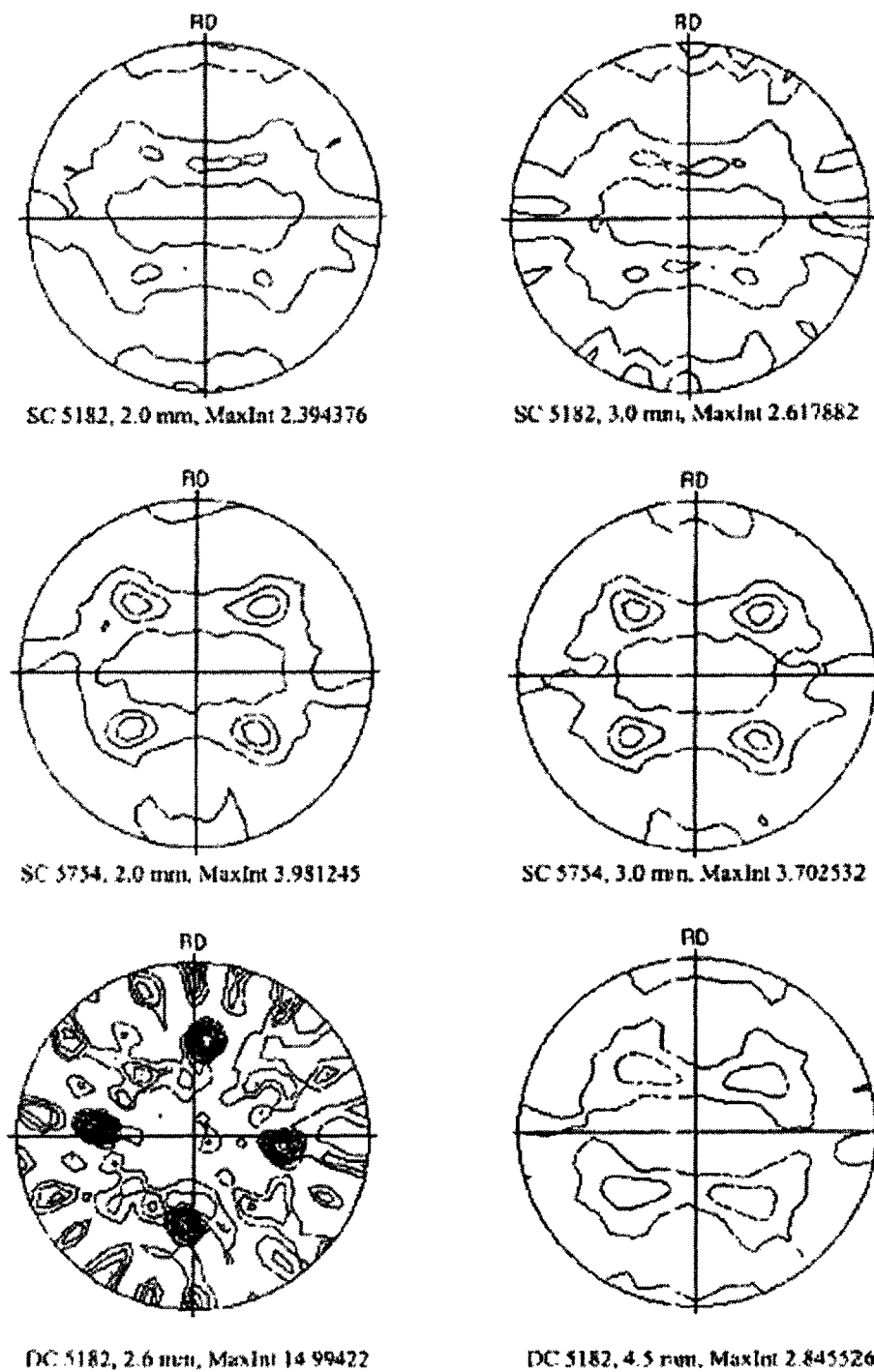


Figure 2.23: The (111) pole figures of annealed hot band SC and DC materials (After Cheng and Morris [6])

deformation. Annealed SC 5754 hot bands develop a 90° earing during cup testing, while annealed SC 5182 hot bands develop both a 90° and 45° earing as a result of the combined effects of recrystallization texture producing a 90° earing and deformation texture producing a 45° earing [6].

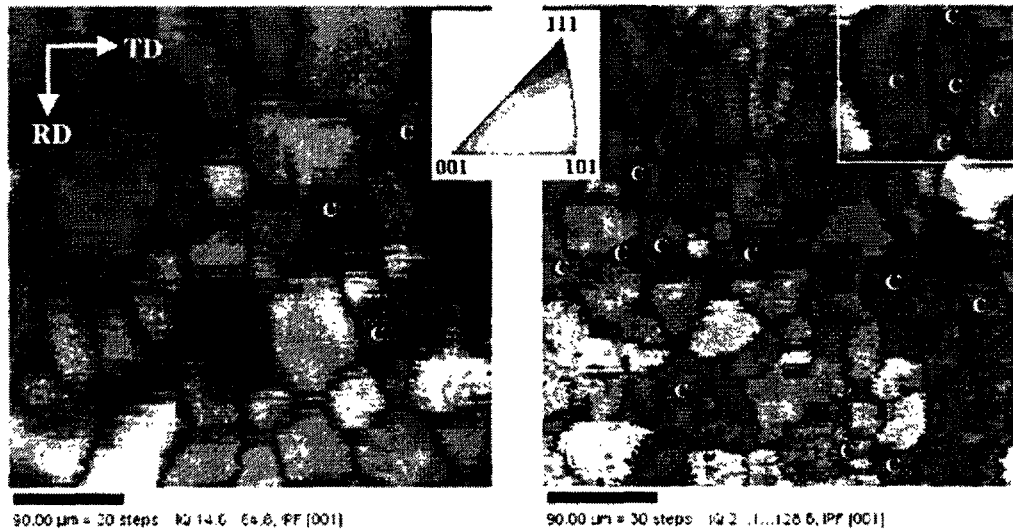


Figure 2.24: Microtexture: IPF maps of completely recrystallized AA5052 for (a) CC and (b) DC hot bands. IPF maps are overlapped by corresponding crystal orientation maps in which character “C” indicates the grain with Cube orientation (After Liu and Morris [3])

The difference of the annealing texture between CC and DC alloys is also observed from microtexture measurements when using the electron backscatter diffraction (EBSD) technique. Liu and Morris [3] reported the inverse pole figure (IPF) with respect to the normal direction (ND) of completely recrystallized AA 5052 (Figure 2.24). Corresponding crystal orientation (CO) maps are overlapped on IPF maps to indicate the grains with Cube orientation, which is indexed with a white character “C” on the maps. It is seen that more Cube oriented grains are observed in the recrystallized DC hot band. The fraction of Cube oriented grains is 3.0 and 18.9 pct for recrystallized CC and DC hot bands, respectively. This Cube component is observed in the DC material even after 90 pct cold rolling, although the α and β

fibers become well developed beyond 60 and 70 pct cold rolling reduction in both CC and DC materials, respectively [3].

2.4 Anisotropic Deformation of Sheet Materials

The majority of Al alloys, especially in the form of sheet, are quite anisotropic. In terms of tensile properties, the tensile yield strength and tensile elongation are a function of orientation in the sheet (e.g., Figure 2.25). Figure 2.26 shows that the yield strength and tensile elongation in 1 mm gauge O-temper AA5754 and AA5454 are a function of the testing orientation [115]. The main factor for the plastic anisotropy is the non-uniformity of crystal orientation distribution in polycrystals materials, especially annealed materials. However, other aspects of the microstructure or of the deformation behaviour may be the cause of the anisotropic mechanical properties.

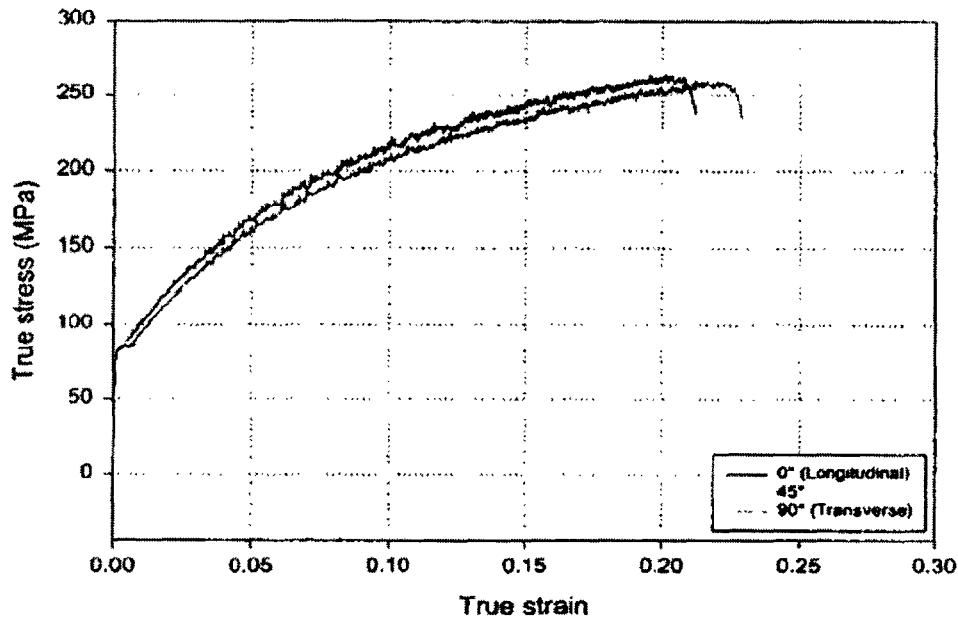


Figure 2.25: Stress-strain curve for annealed Al-3%Mg alloy (After Johnson and Lloyd [115])

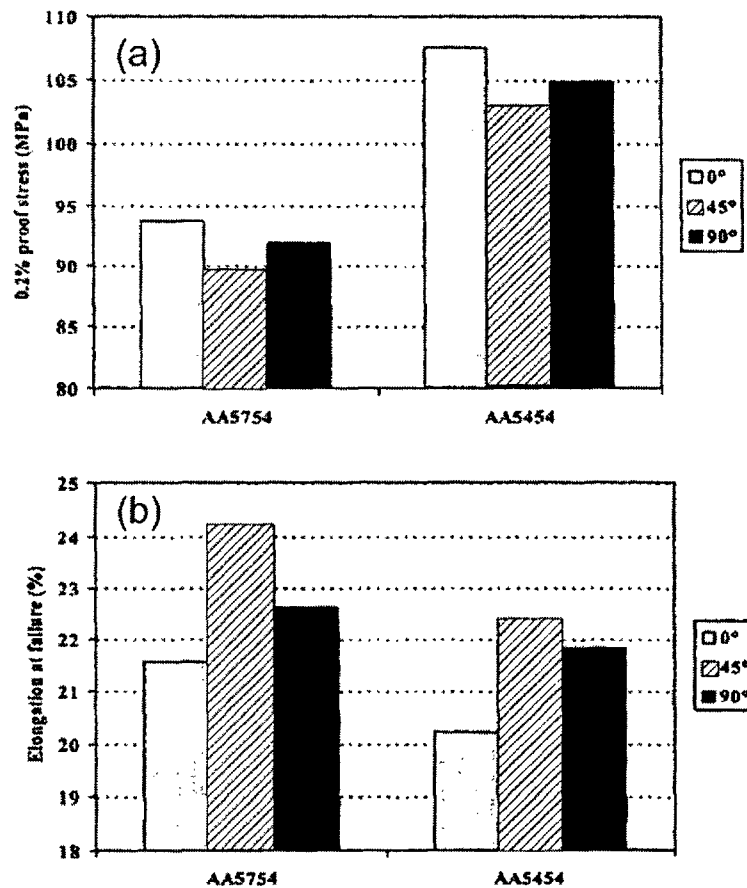


Figure 2.26: Anisotropy: (a) yield strength and (b) tensile elongation in O-temper AA5754 and AA5454 (After Johnson and Lloyd [115])

2.4.1 Factors Causing Anisotropy

Johnson and Lloyd [115] investigated the factors controlling anisotropy of the properties in the annealed Al-Mg (5xxx series) alloys: (1) grain structure, (2) alloy composition, (3) nature of the plastic deformation (inhomogeneous deformation) and (4) crystallographic texture. They concluded that the anisotropy observed in Al-Mg alloys is not attributed to microstructural anisotropy, but rather to the influence of the crystallographic texture. Although the texture evolution was not correlated to the behaviour of work hardening in detail, these authors argue that the starting texture

of the initial sheet determines the work hardening rate and affects the homogeneous deformation behaviour up to plastic instability. In subsequent chapters, the present work will attempt to elucidate the relation between the behaviour of work hardening and the texture evolution in detail.

The crystallographic texture is often considered as a major factor of the anisotropy of mechanical properties of annealed metals without large fractions of secondary phases. However, when alloys are plastically deformed, the prior deformation substructure becomes another source of plastic anisotropy. Various studies about the effect of the pre-strained substructure on the subsequent deformation behaviour have been carried out by many researchers, e.g. [9, 14–18, 116–119]. Under such conditions materials may exhibit different behaviours and properties; experiments which probe such behaviour are often classified as a strain-path change. One well known phenomena in this class is the Bauschinger effect. However, in the practical forming of rolled sheet or in multi-stage pressing, ‘orthogonal’ path change is more important than reversal straining [18]. The present work is focused on the plastic deformation of annealed Al alloys, but the strain-path change effects will also be covered because the underlying mechanisms of the anisotropy caused by a strain-path change can provide insight into the factors which determine the behaviour of these materials during forming operations.

Under the condition of “orthogonal” path changes, one observes a transient “latent” hardening effect. The flow stress in the second stage of deformation is higher than that which is expected with “isotropic” hardening, and a relatively low work hardening regime appears afterward, which eventually influences strain distribution and ductility [18]. Lopes and co-workers [119] reported that the mechanical response of aluminum could be addressed solely by using textures and Taylor factor evolutions. They carried out the study with low carbon steel and pure Al and showed that, for

aluminum, the texture after shearing is rather similar to the previous one except for a definite rotation of the main orientation components (Figure 2.27). Shearing results in a crystallographic rotation mainly around the normal direction to the sheet plane.

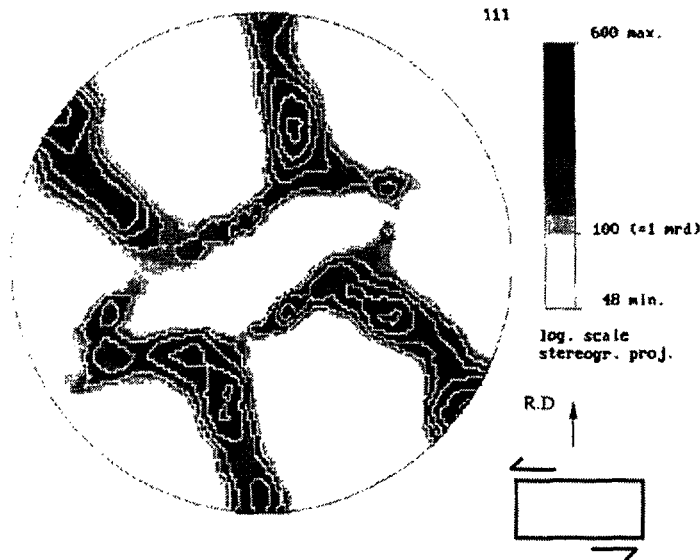


Figure 2.27: $\{111\}$ pole figure for pure Al after pre-rolling in the RD direction and subsequent shear deformation up to $\gamma=1.0$ at 90° from the rolling direction (After Lopes et al [119])

However, Eardley and co-authors [17] argue that the strain induced anisotropy of a strong cube texture of commercially pure Al is related to the substructure created during pre-straining. Figure 2.28 shows the effect of both pre-strain and tensile axis direction on tensile properties. In the annealed sheet ($\epsilon=0$ in Figure 2.28), the behaviour at 0° and 90° are almost identical, but testing at 45° results in higher work hardening and greater elongation, due to the crystallographic texture of a 4-fold symmetry. The structure after the pre-strains of $\epsilon=2.0$ (Figure 2.28) has a 2-fold symmetry and shows a difference between 0° and 90° tests at the pre-strain. This indicates that the substructure created during pre-straining affects the anisotropic behaviour.

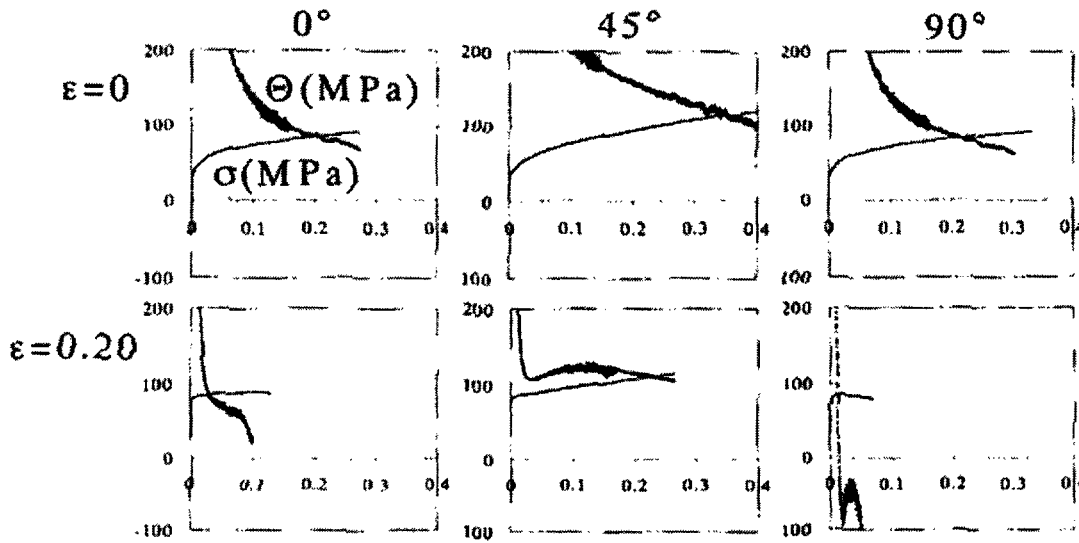


Figure 2.28: True stress, σ , and work hardening, θ , characteristics as a function of strain for AA1200 rolled to a strain of 0 and 0.2 measured at 0° , 45° , and 90° from the rolling direction (After Eardley et al. [17])

When the stacking fault energy (SFE) of cubic metals is low, the effect of the deformation substructure on the material properties is more pronounced. This is associated with the deformation substructure, especially the evolution of planar dense dislocation walls and their stability under deformation conditions. Low SFE affects dynamic recovery and consequently enhances the formation of condensed dislocation wall structures. In the early stage of plastic deformation after a strain path change, the work hardening rate is often increased. Such increase in the initial work hardening is developed more strongly in cubic metals of low SFE [7].

Solute atoms such as Mg in Al affect the development of substructure [18]. When the magnesium content is high ($\approx 5\% \text{Mg}$), the strain-induced anisotropy is low, unlike in the low magnesium alloy ($\approx 1\% \text{Mg}$) the behaviour of which is similar to pure aluminum. This is associated with the effect of solutes on dynamic recovery. Solute atoms restrict the process of dynamic recovery (cross-slip and climb) and lead to a dislocation

arrangement known as a Taylor lattice. This microstructure inhibits the anisotropy of the material behaviour [18].

2.4.2 Texture

It is known that, during the tensile test for both single crystals and polycrystals, the tensile axis rotates toward a specific crystallographic direction. When the tensile axis (TA) and the specific crystallographic direction are parallel, TA does not rotate further. This specific crystallographic direction is often defined as the stable end orientation or final stable orientation of the TA. For Al single crystals deformed in tension, $\langle 112 \rangle$ is the stable end orientation. For Al polycrystals, at least five independent slip systems should be activated to fulfill the continuity condition at grain boundaries; Taylor made calculations of lattice rotation of such a system for axisymmetric tension [120]. $\langle 111 \rangle$ and $\langle 100 \rangle$ are known as stable end orientations in the tensile test of polycrystalline material [121–123]. For example, Figure 2.29 shows the evolution of orientation distribution of commercially pure Al (A1050) whose initial texture consists of Cube texture and rolling texture that has its center at S orientation, $\{123\}\langle 634 \rangle$, under the condition of uniaxial deformation. For S orientation, Figure 2.29(a), the tensile axis clearly rotates toward $\{123\}\langle 111 \rangle$. The orientation density increases at $\{112\}\langle 111 \rangle$ (Figure 2.29(b)). Savoie and co-workers [121] also reported, with commercially pure Al (A1145) strained 30% in the rolling direction, that orientations having $\langle 111 \rangle$ and $\langle 100 \rangle$ axes in the tensile direction increased their intensities during tensile deformation. This is also clearly visible in Figure 2.30 showing that $\langle 111 \rangle // \text{TA}$ fiber textures are developed with increasing tensile strain of Al and Al-Mg alloys [124].

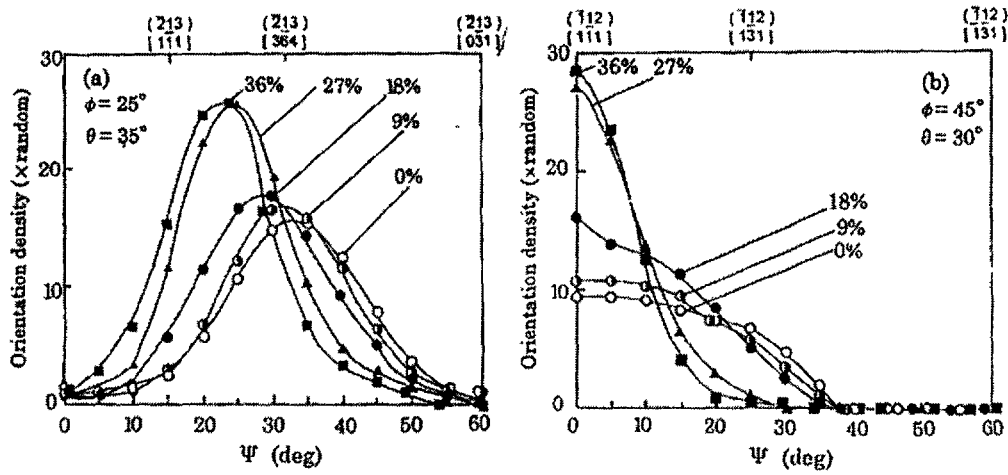


Figure 2.29: Orientation distributions of commercially pure Al strained 0, 9, 18, 27, and 36% (After Ohtani and Inagaki [124])

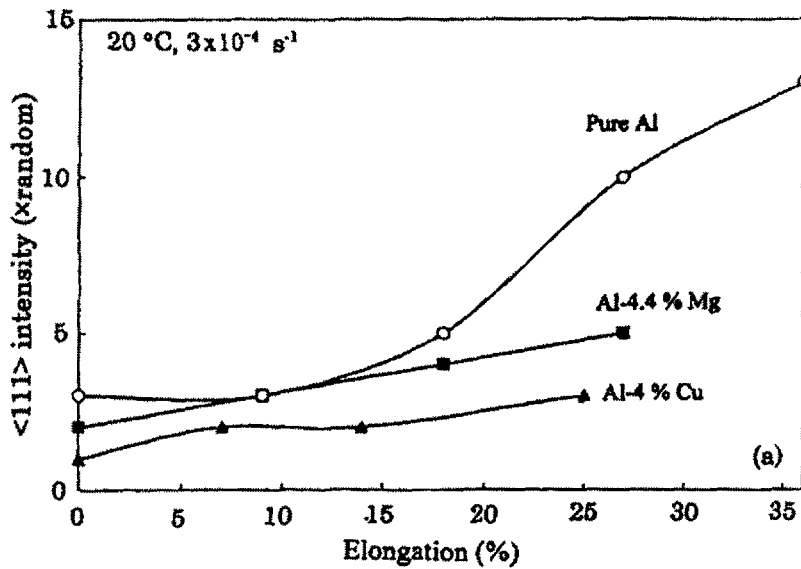


Figure 2.30: Evolution of intensities of $\langle 111 \rangle$ axis parallel to TA for commercially pure Al and Al-Mg alloys (After Ohtani and Inagaki [124])

In the rolling process, the deformation texture of fcc metals is affected primarily by stacking fault energy (SFE), γ_{SFE} . For metals with high or medium values of SFE, such as aluminum with $\gamma_{SFE} \sim 170 \text{mJm}^{-2}$ and copper with $\gamma_{SFE} \sim 70 \text{mJm}^{-2}$, the deformation texture shows a so-called “pure metal texture” (Figure 2.31(a)) in which Taylor’s condition of continuity at grain boundaries is partially satisfied. In contrast, the grains could deform like isolated single crystals for metals with low $\gamma_{SFE} < 25 \text{mJm}^{-2}$, which is called “alloy type texture” (Figure 2.31(b)). Therefore, a rolled FCC alloy with a well defined initial texture can impact the subsequent deformation behaviour and texture.

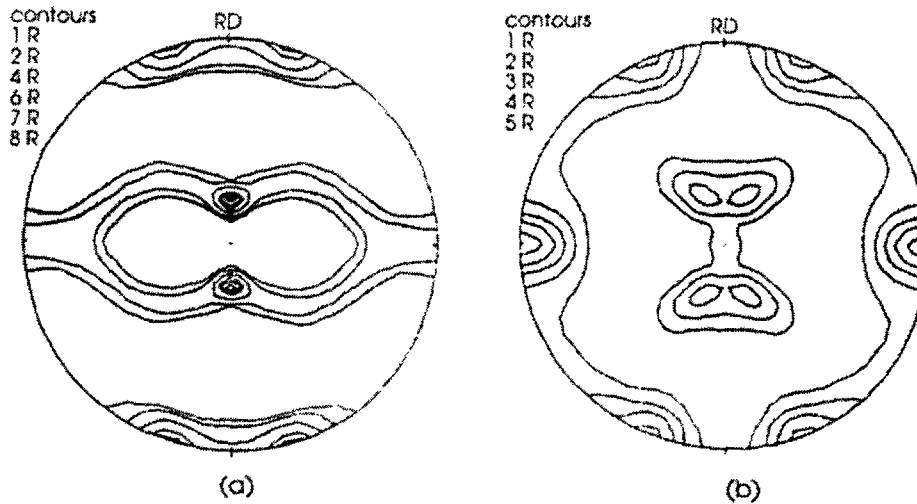


Figure 2.31: (111) pole figures of 95% cold rolled fcc metals; (a) copper and (b) 70:30 brass (After Hirsch and Lucke [125])

Ruano and Gonzalez [126] investigated the effect of initial texture (Figure 2.32(a)) on the stable end orientations of a rolled Al-5%Ca-5%Zn alloy using tensile tests at 400°C at a constant cross head speed of 10^{-2} s^{-1} where superplastic behaviour does not occur. Initial orientation in Figure 2.32(a) consisted of high intensities close to $(\bar{1}\bar{1}2)[\bar{1}11]$. When the TA is parallel to the rolling direction (RD), the TA located inside the stereographic triangle is close to $[\bar{1}11]$ (Figure 2.33). Since the TA tends

to rotate toward $[\bar{1}11]$, the grains align their $[\bar{1}11]$ direction with the TA as shown in Figure 2.32(b) and yield a “pure metal” texture. When the sample is deformed with the TA perpendicular to the RD, high intensities are observed at $(1\bar{1}0)[1\bar{1}2]$ (Figure 2.32(c)), which is known as “alloy” type texture. Based on these results, Ruano and Gonzalez [126] argued that the TA first approaches $[\bar{1}12]$ and rotates toward $[\bar{1}11]$ as shown in the path of the dotted line of Figure 2.33. For the sample deformed with the TA at 45° from the RD, the texture could not be described by low index ideal orientation, and so the path of TA could not be determined. These texture evolutions, however, were not correlated to the tensile properties or the work hardening behaviour in their study. The present work will investigate the effect of the texture evolution on the tensile and work hardening behaviour, and it will also elucidate the properties of the samples with the tensile axis 45° from RD.

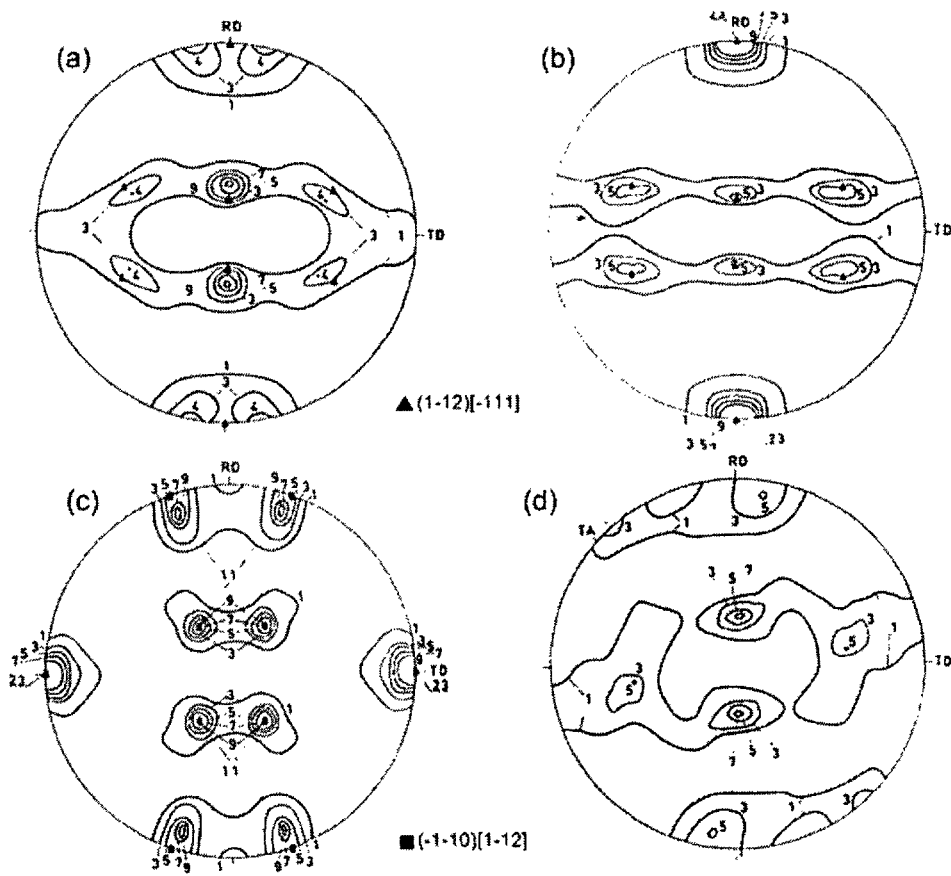


Figure 2.32: (111) pole figures of Al-5%Ca-5%Zn: prior to tensile deformation (a) and samples deformed with the tensile axis in the rolling direction (b), perpendicular to the rolling direction (c), and at 45° from the rolling direction (d) (After Ruano and Gonzalez [126])

2.5 Summary

The relationship between mechanical properties and the microstructure produced during plastic deformation of materials have been of great interest over the decades, and there is extensive literature data available on this subject. Hence, in the first part of this work, fundamental aspects of plastic deformation, work hardening and the microstructure are covered, which forms a background knowledge used in these studies.

5000 series aluminum alloys have received attention in the automotive industry due to their beneficial properties compared to the conventional materials. Aluminum alloys are usually used in the form of sheet metal; the thermomechanical process involved in the production of sheets influences the mechanical behaviour of the material during subsequent forming operations and the final product properties. Numerous factors such as microstructure, alloy composition and texture have strong impact on these properties and cause the anisotropic deformation. Until now, little work has been done to identify the relation between texture, microstructure and the work hardening behaviour of AA5754 Al alloys; the present study aims to develop a better understanding of the influence of these structural elements on the properties of materials.

2.6 Research Objective and Methodology

Various literature is available on the mechanical behaviour of AA5754 Al alloys and the factors affecting mechanical properties. Few studies, however, are found to systematically address the interrelation between the work hardening, microstructure and the crystallographic texture. Hence, the present study attempts to identify the interrelation between these factors and provide an insight into the deformation mecha-

nism of AA5754 Al alloys. The specific purposes of this research are (1) to study work hardening behaviour, microstructure and crystallographic texture developed during deformation of commercial continuous cast (CC) and direct chill cast (DC) AA5754 Al alloys and pure Al between 4.2K and 295K, (2) to study the type and the evolution of the defect structure developed in this material during plastic deformation by combination of electrical resistivity measurements and TEM, (3) to understand the anisotropy of mechanical behaviour and the effect of texture and microstructure on deformation behaviour, and (4) to model the plastic deformation of Al alloys, taking into account elements of texture and work hardening.

These objectives are achieved by performing the extensive tensile tests with CC and DC AA 5754 Al alloys and pure Al at 4.2K, 78K and 295K, from which stress-strain curves and work hardening behaviour is analyzed. The specimens are deformed to various levels of strain to investigate the evolution of their microstructure and texture by means of TEM, SEM and X-ray diffraction techniques. Combined measurements of mechanical response, changes in *in-situ* electrical resistivity during plastic deformation, studies of the dislocation substructure and crystallographic orientation of deformed samples are employed to understand the processes which control plastic deformation. The nature of obstacles to dislocation motion is investigated by means of strain rate sensitivity tests. In order to study the anisotropy of mechanical properties, tensile deformation experiments are carried out on samples with tensile axes oriented at different angles to the previous rolling direction. Plastic deformation of these materials is simulated using the existing viscoplastic self-consistent (VPSC) method with experimental results combining both texture and mechanical property data as input. Based on the simulation and experimental results, an effort is made to elucidate the underlying mechanisms of deformation behaviour observed in experiments.

Chapter 3

Experimental Procedure and Techniques

3.1 Tensile and Strain Rate Sensitivity Tests

Two major experimental tasks in this study are (1) to carry out the tension deformation encompassing strain rate sensitivity tests as well as continuous deformation of AA5754 alloys at 295K, 78K and 4.2K and (2) to study corresponding microstructure and texture. The experiments were carried out on continuous casting (CC) and direct chill casting (DC) alloys of composition given in Table 3.1 and on high-purity (99.9995%) aluminum. The as-received material was in the form of 1mm thick cold rolled CC alloy sheets, 1mm thick cold rolled and annealed DC sheets (grain size $23\mu\text{m}$) and 7mm thick pure Al. Pure Al was further cold-rolled in the laboratory to a thickness of 3.7mm.

Table 3.1: Composition of the Al alloy (in wt. %)

AA5754	Mg	Mn	Si	Fe	Cr	Cu	Ni	V	Zn	Al
SC	3.21	0.24	0.05	0.09	-	-	-	-	-	balance
DC	3.11	0.25	0.06	0.21	0.04	0.01	0.01	0.01	0.02	balance

Tensile test samples with gauge dimensions of 1 x 3.5 x 60mm were machined from the as-received alloys. Samples made of pure Al had dimensions of 2 x 3.5 x

60mm. Machined Al and CC specimens were annealed at 350°C for 30 minutes and 2 hours, respectively, followed by air cooling, to produce a recrystallized material. The average grain size of annealed samples was 600 μm and 14 μm for pure Al and the CC alloys. Some CC samples were annealed at 450°C for 2 hours in order to study the effect of grain size and annealing temperature on mechanical properties; the final grain size of these samples was 18 μm .

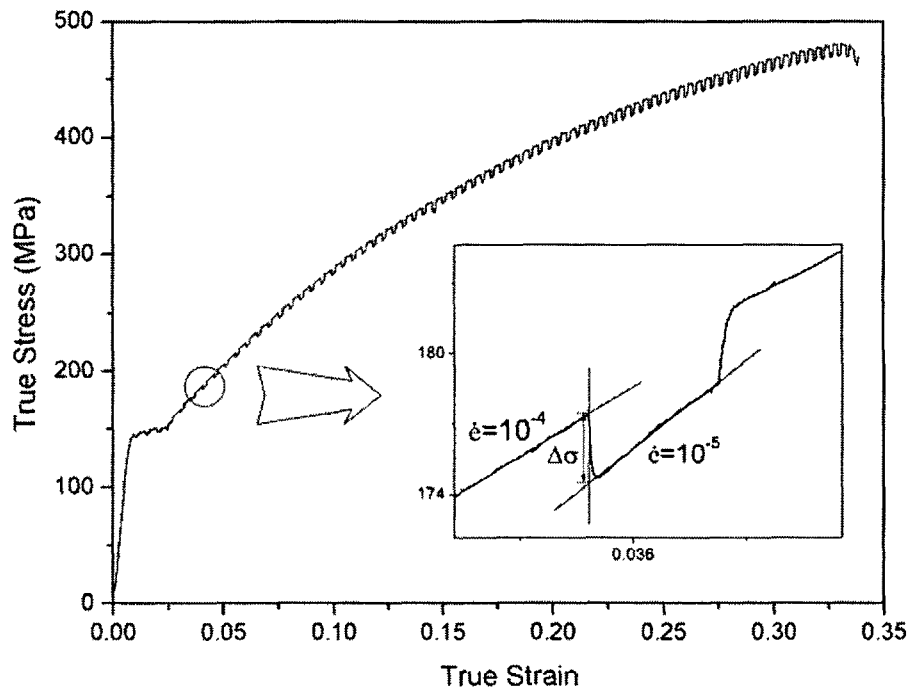


Figure 3.1: An example of strain rate sensitivity measurements of CC alloy at 78K

The specimens were deformed in a screw-driven tensile-testing machine equipped with a cryostat, at temperatures of 4.2K, 78K and 295K, at a constant cross-head velocity corresponding to an initial strain rate of $1.6 \times 10^{-4} \text{s}^{-1}$ and $1.6 \times 10^{-5} \text{s}^{-1}$. Most results presented in this thesis are based on the strain rate of $1.6 \times 10^{-4} \text{s}^{-1}$ unless otherwise indicated. The strain rate sensitivity measurements were carried at 4.2K, 78K and 295K for pure Al and at 78K for CC (annealed at 350°C/2hrs) and DC alloys by repeating the instantaneous rate change between 10^{-4} and 10^{-5}s^{-1} during

deformation and measuring consequent stress variations (Figure 3.1). Three different tensile directions, 0° , 45° and 90° from the previous rolling direction (RD) (Figure 3.2), were selected to investigate the anisotropic deformation of the materials.

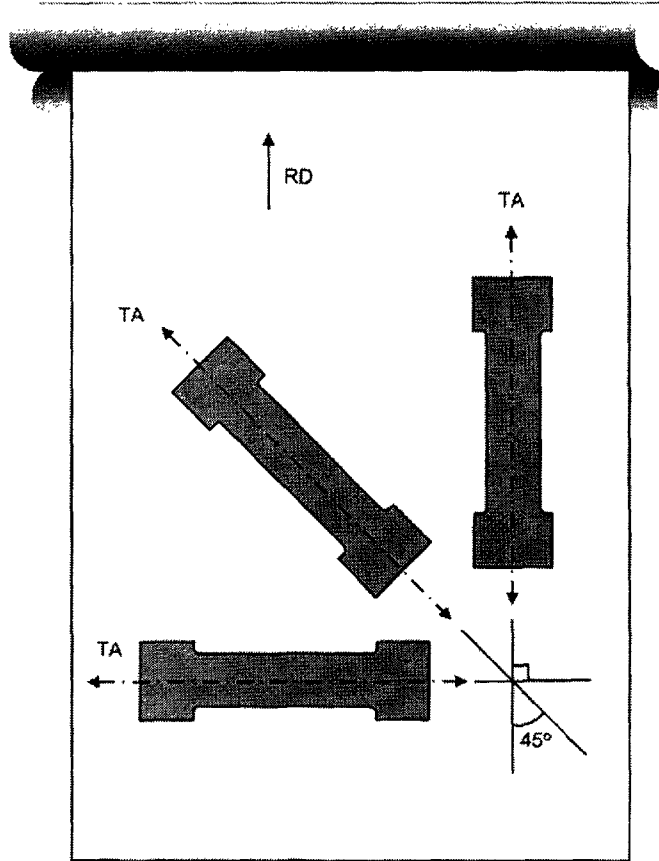


Figure 3.2: Schematics of the orientation of the tensile direction of the samples adopted for the studies of the anisotropic deformation

To investigate the evolution of deformation induced defects, the electrical resistivity measurements were carried out *in-situ* during deformation of the samples at 4.2K. Employed was the four point method for the measurement of potential drop across the sample with reversing the current flowing through the circuit (see Appendix D for the detailed resistivity measurement setup). The resistivity ratio, $RR = r_{295K}/r_{4.2K}$, i.e. ratio of the resistance at 295K over the resistance at 4.2K of pure Al, was about

2000, indicating a very low residual content of impurities and lattice defects in the material. In contrast, the alloys had a resistivity ratio of about 2. Measurements of resistivity change due to deformation induced defects in such material presents a challenge; the apparatus must be able to measure potential changes of the sample smaller than 10^{-9} V.

Annealing experiments between 4.2K and room temperature were carried out to understand nature of defects produced during plastic deformation. The samples were deformed to a given stage of deformation at 4.2K, heated to room temperature, cooled down back to 4.2K, and reloaded again. The electrical resistivity change at 4.2K during this annealing procedure provides a measure of the density of point defects that anneal out from the sample after being heated.

3.2 Structural Studies

Optical microscope observations were carried out on the polished surface of the specimens to examine the surface before and after deformation. TEM studies of the dislocation substructure were performed on selected samples with a Philips CM12 TEM electron microscope set to 120kV. Thin foils were cut in the section parallel to the wider face of the samples and were prepared by standard thinning procedures. The final polishing was carried out in a solution of 30% nitric acid in high purity methanol (HPLC) at -35°C with Tenupol-5 electropolisher. Fracture surface observations in samples deformed to failure were carried out using a Philips SEM 515 set to 20KeV and with optical microscope.

Another important characteristic of structural materials that affects mechanical properties is the orientation distribution of grains, texture. X-ray diffraction was used in this study to investigate texture evolution during the deformation and the

effect of precipitation on texture development, by using GADDS systems of Bruker Advanced X-ray Solutions (AXS) Inc. In this apparatus, the X-rays diffracted on the sample are intercepted and recorded by an area detector which acquires this data and subsequently displays the diffraction pattern into a two-dimensional image frame (Figure 3.3). Three rotational angles (ω, χ_g, ϕ) are used to describe the rotation of a sample in the diffractometer (Figure 3.4). The goniometer and sample stage are maneuvered with the geometric relationship between primary beam, sample and detector (Figure 3.5). Based on this relationship, a pole figure is constructed according to the following steps:

1. assign a reference system to the sample of interest
2. construct the projection in two dimensions which preserves the co-ordinate system chosen
3. for visualization, bin the pole (the point of the projection) density into finite areas of projection and then normalize the local intensity versus the integrated intensity.

Figure 3.6 shows an example of X-ray diffraction at a certain angle of ϕ of the specimen tested at 295K. Each arc in Figure 3.6 represents reflections of a specific plane, which is determined from Bragg's law.

For texture measurements, samples deformed to a strain level of 0, 9%, 19% and after the fracture were chemically-polished in the solution of 10% NaOH in water and were subsequently used to study texture development during plastic deformation. Texture measurements were carried out at the mid-depth of the specimens with $\text{CuK}\alpha$ radiation, a pitch of 5° and an exposure of 20 seconds. For CC materials, the texture measurements were repeated at least three times on different samples deformed to a

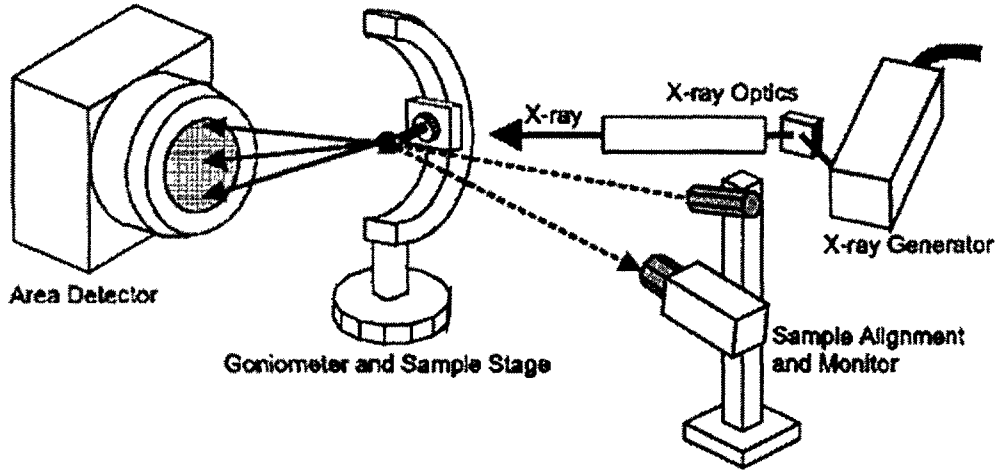


Figure 3.3: Schematic of major device units in a GADDS system (After Bruker AXS inc. [127])

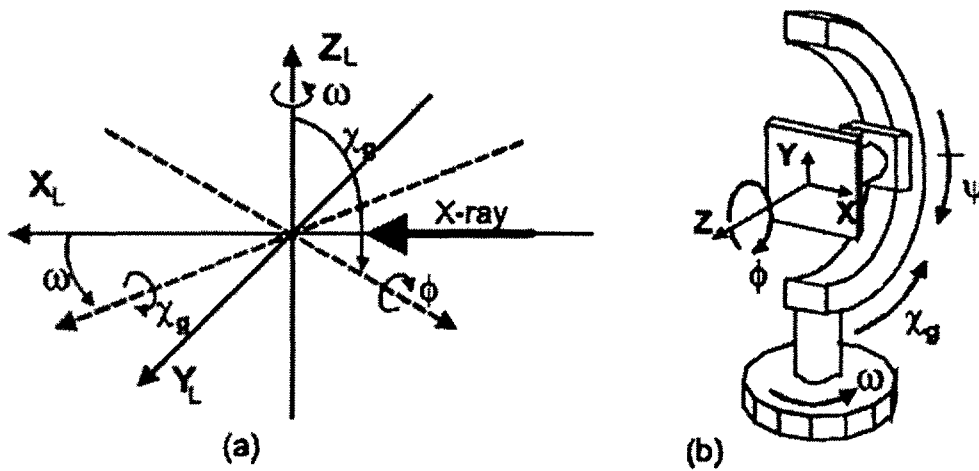


Figure 3.4: Sample rotation and translation in the X-ray system: (a) relationship between rotation axes ($\omega\chi_g\phi$) and $X_L Y_L Z_L$ coordinates and (b) relationship between rotation axes and translation axes XYZ (After Bruker AXS inc. [127])

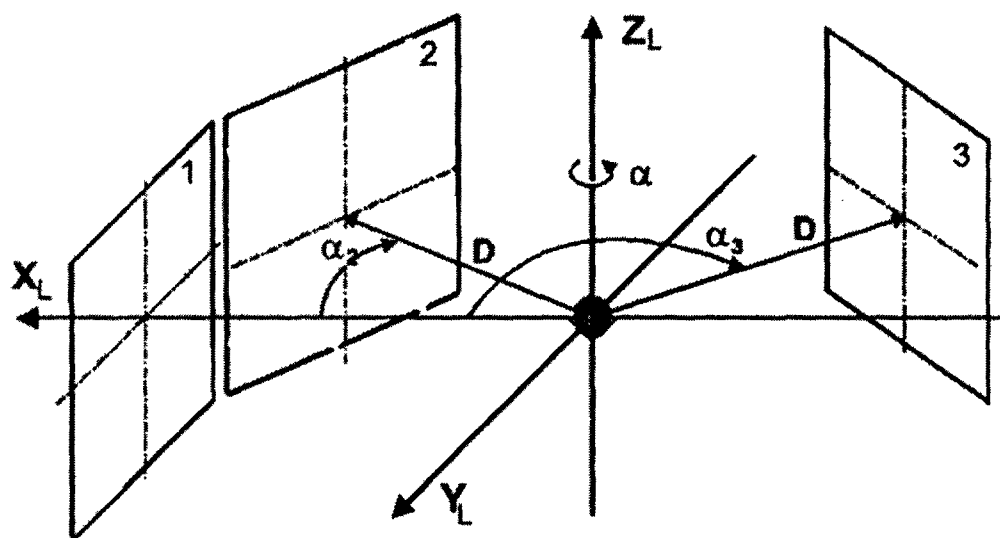
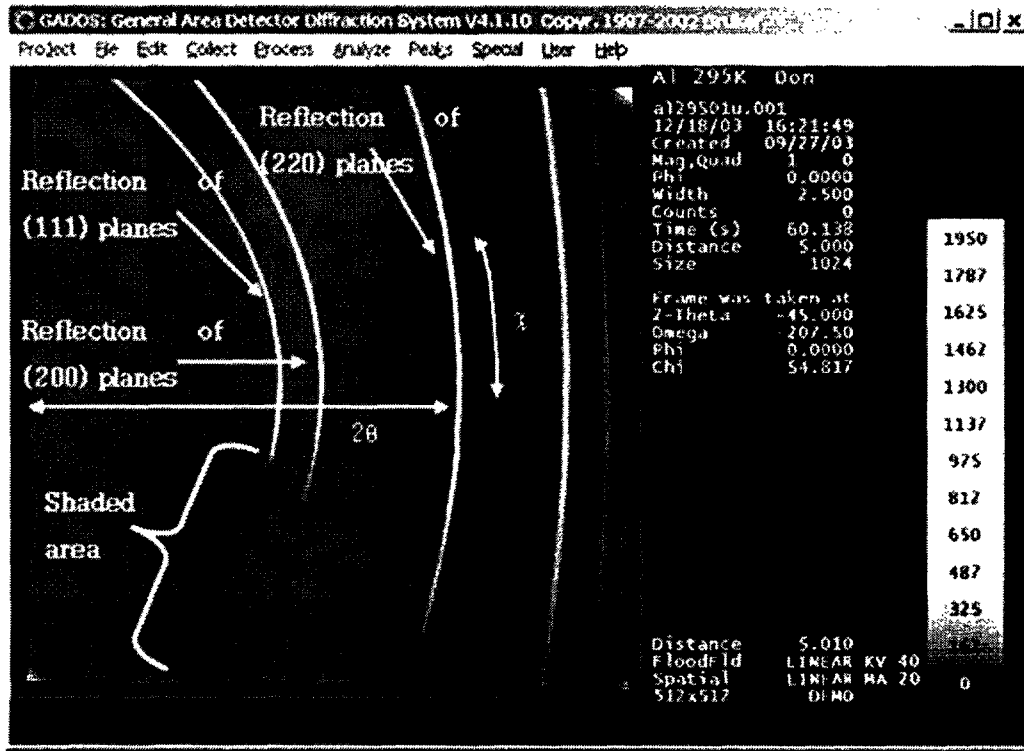


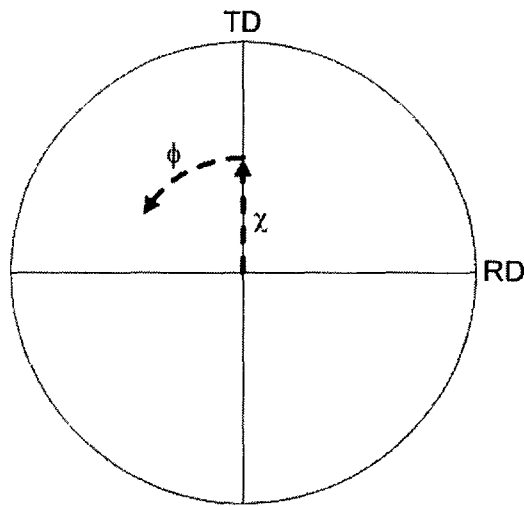
Figure 3.5: Relationship between a sample and detector positions; D is the distance from the sample to the detector and α is the swing angle of the detector (After Bruker AXS inc. [127])

given strain in order to check the consistency of the diffraction data; the scattering of peak intensities is reflected by error bars in some of the figures. Three incomplete (111), (200) and (220) pole figures were acquired in every measurement. Orientation Distribution Functions (ODF) were computed from experimental pole figures, using the popLA package with the WIMV (Williams-Imhof-Matthies-Vinel) algorithm [128]; these were subsequently used to recalculate complete pole figures.

ODF's are expressed in Kocks notation [129] and Euler angles, and ODF intensities are plotted along the contours of constant values in units of "multiples of random distribution (m.r.d)" [129].



(a)



(b)

Figure 3.6: A typical example of the diffraction pattern of X-rays used for the processing of the texture of deformed materials: (a) an area detector reflection for a specimen tested at 295K and (b) a reflection coverage in a pole figure

Chapter 4

Results

4.1 Continuous Deformation

4.1.1 Deformation Behaviour and Fracture

Figure 4.1 shows true stress-true strain characteristics of CC and DC alloys and pure Al deformed at 4.2K, 78K and 295K. Tensile curves of the alloys exhibit extensive serrations at 295K, associated with the strain aging known as Portevin-LeChatelier (PLC) effect [130]. The stress drop of the CC alloy, $\Delta\sigma$, during PLC instabilities increases with the flow stress, from approximately 6MPa at the early stage of deformation to about 8MPa at the later stages. DC alloy shows stress drops in the range 2MPa to 7MPa (Figure 4.1 (c)). The PLC effect is suppressed at 78K and samples exhibit stable plastic flow with a long onset of uniform deformation followed by fracture, as shown in Figure 4.1. At 4.2K, the material shows flow instabilities arising from the adiabatic shear deformation [131, 132], of a different nature than the ones observed at room temperature. The adiabatic deformation is accompanied by intensive acoustic emission occurring with a higher frequency and louder acoustic clicks than those observed during the PLC deformation. The sample deformed with a lower strain rate exhibits a lower frequency of adiabatic instabilities, as shown in Figure 4.1 (b). Mechanical characteristics reveal that pure Al shows substantially lower flow stress than CC alloys in the entire deformation range. The Al samples exhibit a stable

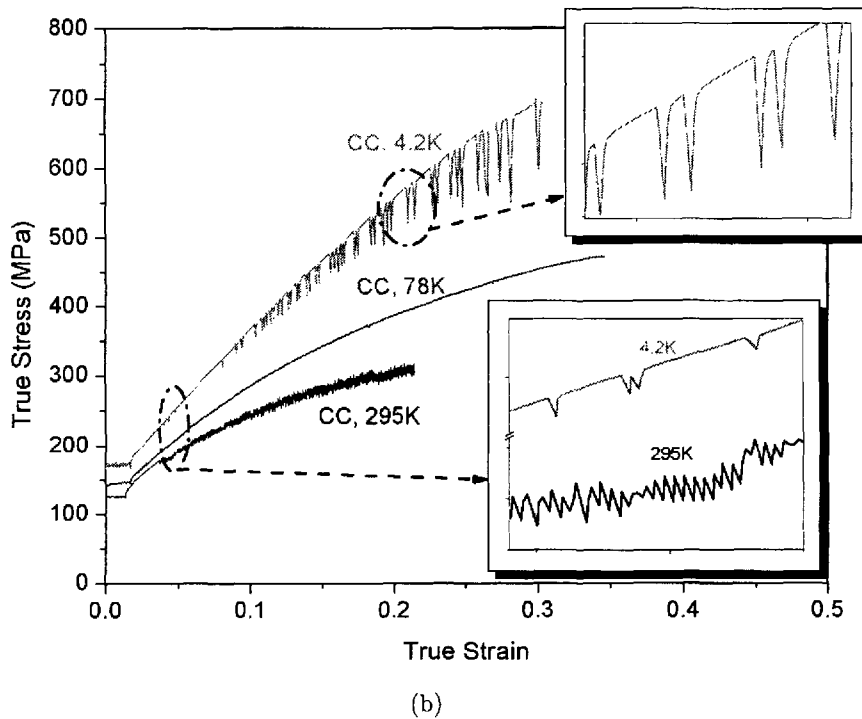
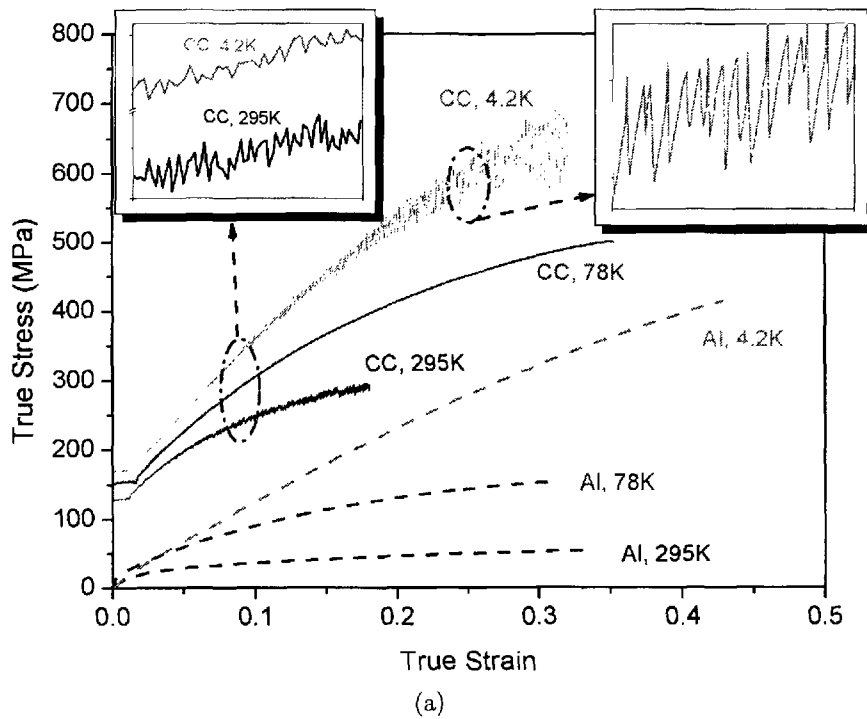


Figure 4.1: True stress vs. true strain characteristics at the initial strain rates of (a) 1.6×10^{-4} , (b) $1.6 \times 10^{-5} s^{-1}$ for the CC alloy (CC) and pure Al (Al) and (c) 1.6×10^{-4} for the DC alloy (DC) at temperatures 4.2K, 78K and 295K (cont'd)

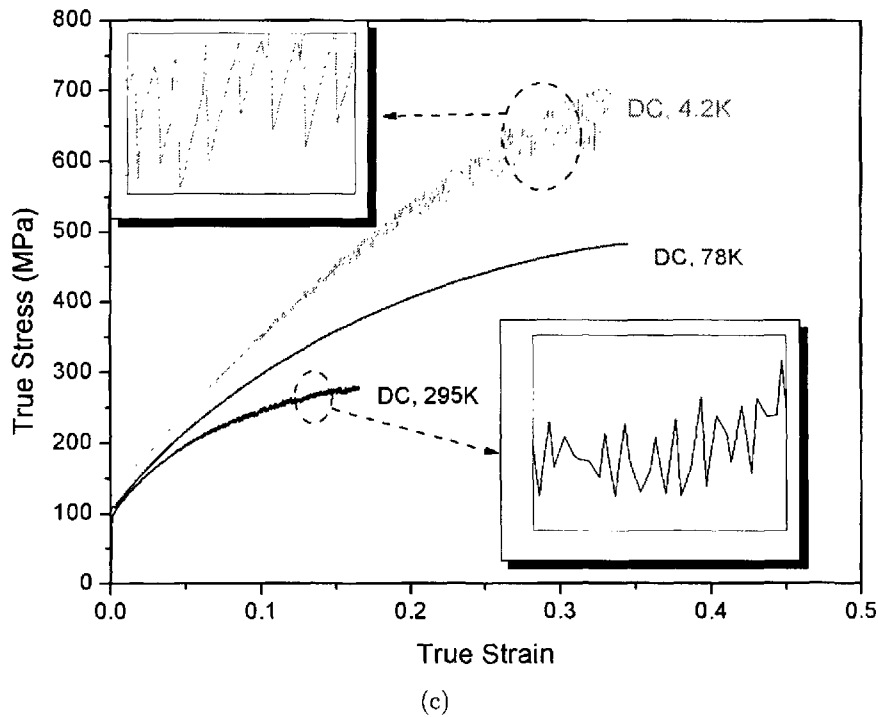


Figure 4.1: (cont'd)

plastic flow up to the point of fracture, which is initiated at the stress of approximately 50MPa, 150MPa and 410MPa at deformation temperatures of 295K, 78K and 4.2K, respectively. The fracture of the alloys occurs at much higher stresses, approximately 290MPa, 500MPa and 700MPa at corresponding temperatures of 295K, 78K and 4.2K, respectively (Figures 4.1 (a) and (c)). The alloy samples deformed at 78K show the highest uniform deformation before the fracture, which is comparable to the one observed in pure Al. Compared to CC alloys, DC alloys show very short or no Lüders deformation after yielding, as seen in Figure 4.1 (c).

Figure 4.2 shows the effect of annealing temperature on the mechanical properties of CC materials. It is seen that specimens annealed at 350°C and 450°C exhibit a qualitatively similar character of the flow curve. However, they show some differences

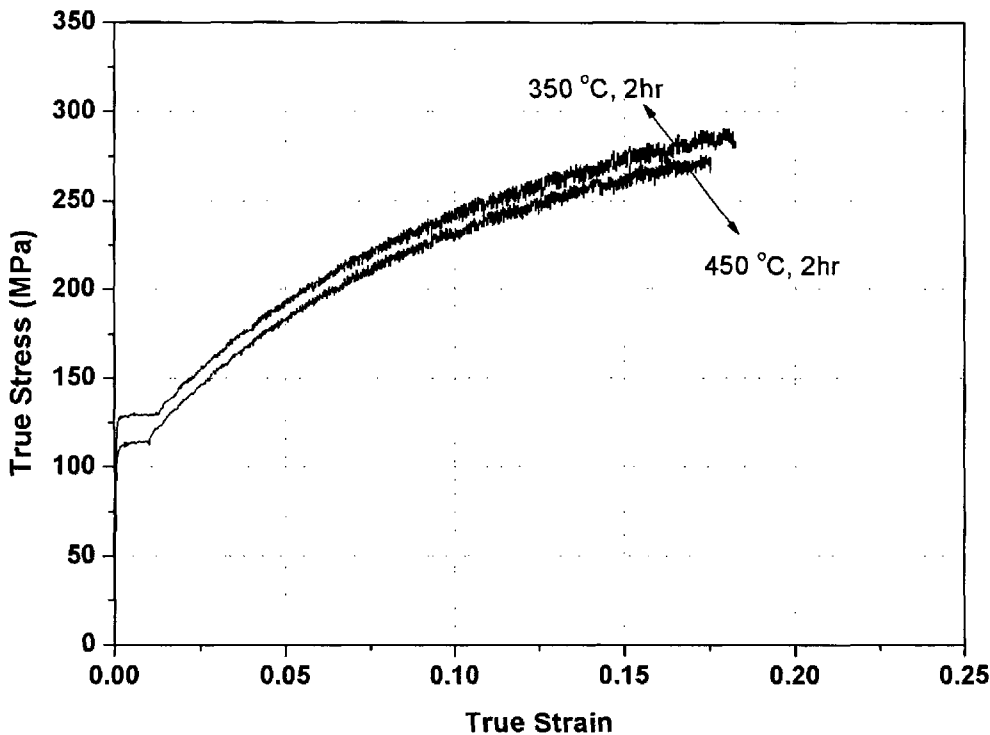


Figure 4.2: The effect of heat-treatment on mechanical properties of CC specimens heat-treated for two hours at 350°C and 450°C, respectively. Tensile tests were conducted at 295K and a strain rate of $1.6 \times 10^{-4} s^{-1}$.

in the yield stress, uniform deformation and the stress at which fracture occurs. For example, the sample annealed at 350°C has the yield stress of about 130MPa compared to 115MPa for specimens annealed at 450°C. Similarly, the fracture of the sample annealed at 450°C occurs at the stress level of about 275MPa compared to 290MPa for the sample annealed at 350°C.

Figure 4.3 shows fracture surface observations of CC samples deformed at 4.2K, 78K and 295K. The micrographs reveal an elongated dimple structure of ductile failure. Little or no particles were found on the fracture surface or within the dimples indicating that the failure is not a particle stimulated process in CC alloys. One of

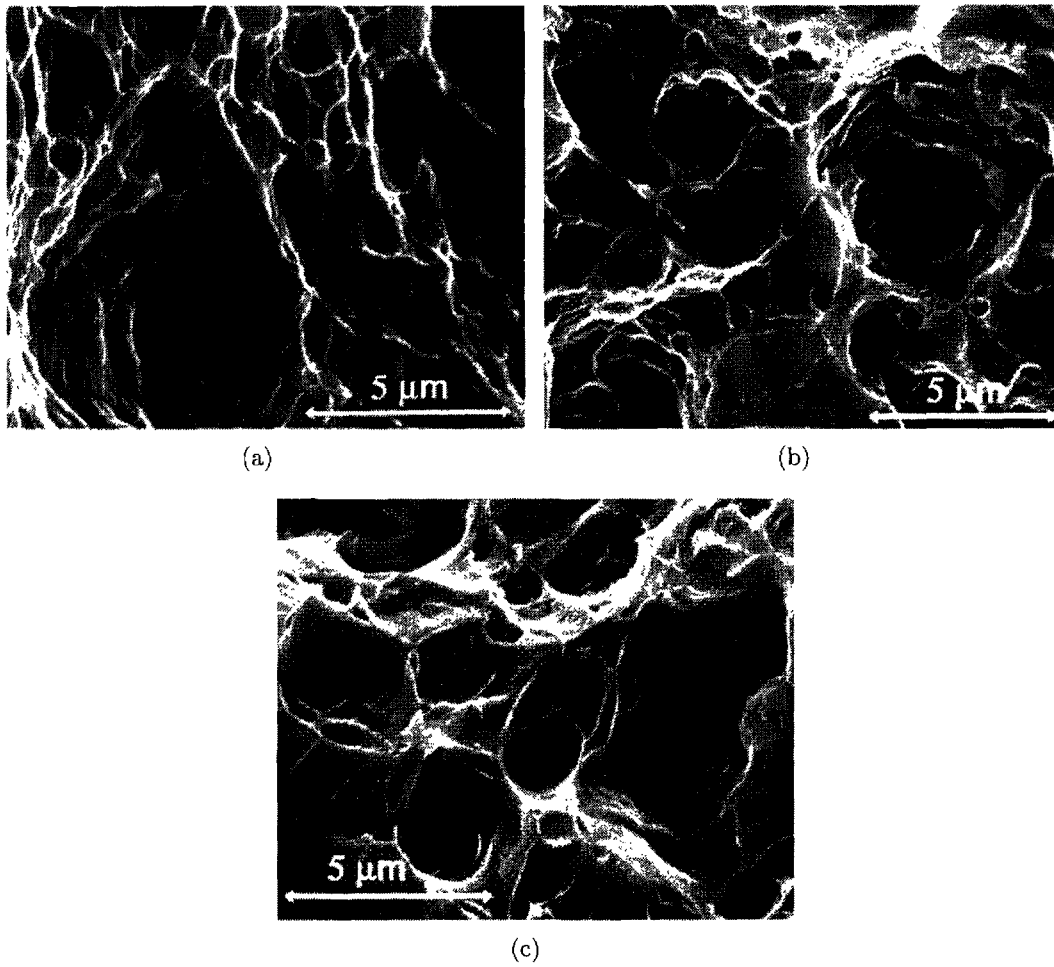


Figure 4.3: SEM observations of the fracture surface of CC alloys deformed at (a) 295K, (b) 78K and (c) 4.2K.

the characteristic features of the fracture surface in this material is the temperature dependence of the dimple size; one observes the formation of smaller dimples in samples deformed at lower temperatures. Pure Al exhibits the same trend, as shown in Figure 4.4. It is seen that, at room temperature, a few very large dimples dominate its fracture surface whereas, at 4.2K, small dimples are evenly distributed across the fracture surface. Fracture surface observations (Figures 4.3 and 4.4) indicate that the dimples formed in pure Al are much larger than these observed in Al alloys at the same deformation temperature, suggesting the higher ductility of Al, in agreement with tensile characteristics of these materials.

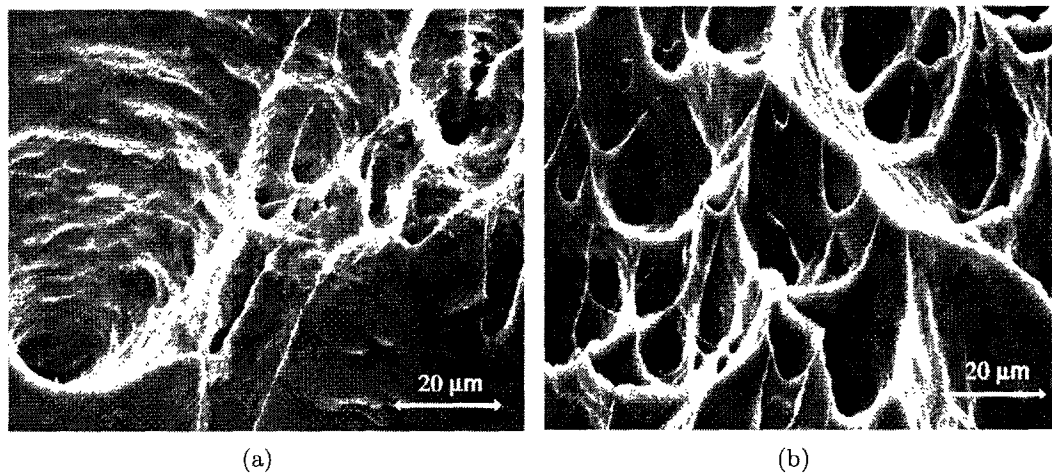


Figure 4.4: SEM observations of the fracture surface of pure Al deformed at (a) 295K and (b) 4.2K.

Figure 4.5 shows the normalized work hardening rate, θ/μ , plotted as a function of the normalized effective flow stress, $(\sigma - \sigma_y)/\mu$, for both pure Al and CC alloys; the yield stress (σ_y) is chosen at the onset of the Lüders deformation for the alloys. The initial work hardening rate of the alloy, equal approximately to $\mu/10$, is of a factor of almost two higher than the work hardening rate of pure Al, of the order of $\mu/20$. This is being observed for all temperatures and within the broad range of the flow stresses,

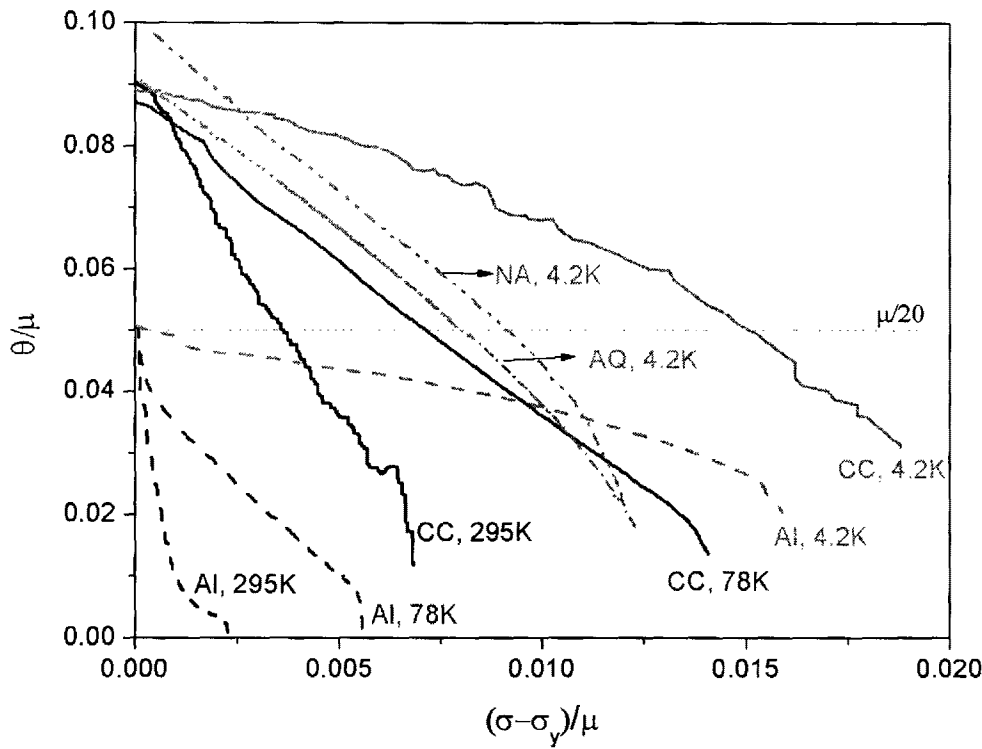


Figure 4.5: Normalized by temperature dependent shear modulus work hardening characteristics as a function of reduced flow stress. CC and Al denote the CC alloy and pure Al, respectively. NA and AQ denote the natural aged and the as-quenched Al-Zn-Mg alloys, respectively, for comparison from the literature [133]

indicating that more effective dislocation storage is taking place during deformation of the alloys compared to pure Al. For pure Al, the work hardening decreases very fast at 295K and 78K, which indicates that the intensive dynamic recovery is taking place during plastic flow. At 4.2K, dynamic recovery is suppressed; the rate of work hardening decrease is much slower than at higher temperatures, indicating that more effective dislocation storage occurs in the substructure. Figure 4.5 shows that the alloy exhibits a qualitatively similar behaviour of work hardening with respect to the deformation temperature, i.e. the work hardening rate decreases faster as temperature increases, suggesting that dynamic recovery processes operate more effectively at

higher temperatures in the CC material. At 4.2K, the work hardening rate of the alloy remains at an unusually high level, above $\mu/20$, for an extended range of plastic flow. It is seen, however, that the hardening rate decreases faster in the CC alloy than in pure Al, suggesting that more intensive dynamic recovery operates in the CC material. It has been reported in the literature that Al-Mg-Zn alloys deformed at 4.2K exhibit an abnormally high hardening rate [133]. For comparison with present results, Figure 4.5 also shows work hardening behaviours of naturally aged, solution-treated and quenched Al-Mg-Zn alloys from Deschamps et al. [133]. It is seen that the CC alloy exhibits an even higher work hardening rate than the Al-Mg-Zn system both in aged and quenched states within a broad range of flow stress.

4.1.2 Strain Rate Sensitivity Measurements

The experimental data of strain rate sensitivity measurements are analyzed by plotting $\left. \frac{\Delta\sigma}{T\Delta\ln\dot{\epsilon}} \right|_{T,\Sigma}$ against $(\sigma - \sigma_y)$, as suggested by Haasen [135]. Here $\Delta\sigma$ is the change in stress due to the instantaneous change of strain rate, and σ , σ_y , $\dot{\epsilon}$, T and Σ represent the applied stress, yield stress, strain rate, temperature and structure, respectively. It is well known that two important parameters determined from the above analysis are: (i) the thermodynamic strain rate sensitivity (SRS) of a material obtained as the slope of a given characteristic and (ii) a thermal component of the flow stress given by the intercept of a plot with the vertical axis. Figure 4.6 shows Haasen plots for both pure Al and CC alloys obtained in this work; for comparison, results for supersaturated solid solution (SSS) and precipitation hardened AA6111 alloys available in the literature [134] are also included in the graph. For the clarity of the figure, we present the strain sensitivity results obtained in the jump tests from higher to lower strain rate, as schematically shown in Figure 3.1. Quantitatively the same strain rate sensitivity characteristics were obtained in the jump tests from

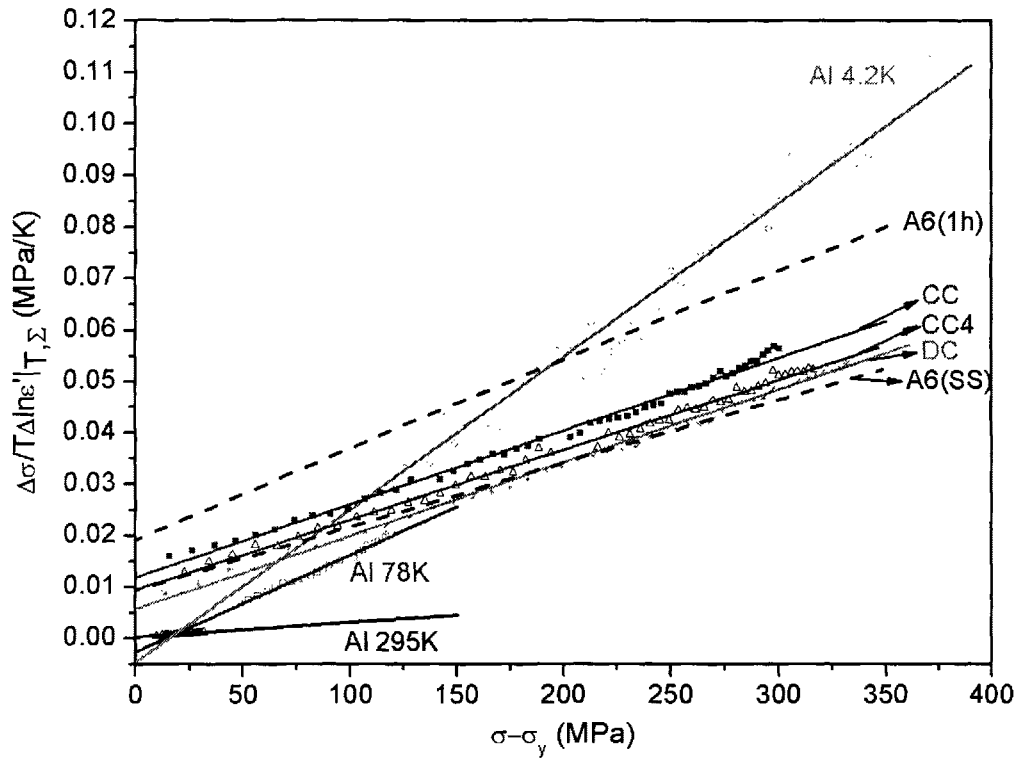


Figure 4.6: Haasen plot characteristics obtained from strain rate sensitivity tests with rate changes between 10^{-4} and $10^{-5} s^{-1}$. CC and CC4 denote continuous cast alloys annealed for 2 hours at $350^{\circ}C$ and $450^{\circ}C$, respectively; DC, direct chill cast alloy; Al, pure Al. For comparison with the present data, strain rate sensitivity results for AA6111 are replotted from Esmacili et al [134]. A6(1h) represent AA6111 material aged for 1 hour at $180^{\circ}C$, and A6(SS) represents the supersaturated solid solution AA6111.

lower to higher strain rate, as shown in Appendix F. Similarly, a negligible difference in the strain rate sensitivity results obtained from the jump test with the increase and decrease of the strain rate was reported by other authors for the supersaturated solid solution AA6111 [134]. It is seen that CC alloys exhibit strain rate sensitivity similar to those of AA6111 materials, with a value of about $1.4 \times 10^{-4} (K^{-1})$. The alloy annealed at $350^{\circ}C$ has a slightly higher positive intercept than the one annealed at $450^{\circ}C$. The intercept of the CC alloy is close to that of SSS AA6111, whereas aged

AA6111 exhibits a higher intercept. The graph also presents data for the DC AA5754 alloy tested in this work, with the same nominal composition as CC alloys but higher contents of iron, i.e. 0.2 wt% Fe in the DC material versus 0.09 wt% Fe in the CC alloy (Table 3.1). It is seen that DC data shows the lowest Haasen intercept among all systems considered, which also has positive value.

Strain rate sensitivity (SRS) of pure Al increases as temperature decreases; the SRS values are equal to 2.98×10^{-4} , 1.88×10^{-4} and 0.29×10^{-4} (K^{-1}) at 4.2K, 78K and 295K, respectively. Figure 4.6 shows that the intercept of pure Al data on the Haasen plot is equal to zero at room temperature, whereas it is slightly negative at lower temperatures. The reasons behind this behaviour will be discussed later.

During the plastic flow of a material, dislocations overcoming the obstacles move from a stable state (static equilibrium) to an unstable state (second equilibrium). The apparent activation area, Δa , swept by a dislocation segment during the glide between the unstable and stable equilibrium states at a given stress is evaluated from the following equation [51, 136]:

$$\Delta a = \frac{MkT}{b} \left. \frac{\partial \ln \dot{\epsilon}}{\partial \sigma} \right|_{T, \Sigma} = \frac{MkT}{mb(\sigma - \sigma_y)} \quad (4.1)$$

where k is the Boltzmann constant; M , the Taylor factor; b , Burger's vector; and m , the strain rate sensitivity in the engineering definition.

Figure 4.7 shows the activation volume, $V' = b\Delta a$, for the CC alloy and pure Al as a function of effective flow stress on a log scale, where b is Burgers vector ($\sim 0.28nm$) and Δa is the activation area. It is seen that pure Al exhibits an activation area with a strong temperature dependence. For example, at the effective flow stress of 25MPa, the activation areas have been determined to be approximately $10nm^2$, $30nm^2$, and $175nm^2$ at 4.2K, 78K and 295K, respectively. For a given flow stress, the activation area increases as temperature increases due to the higher contribution from the thermal energy. At a constant temperature, the activation area decreases

as the flow stress increases (Figure 4.7). The presence of solute atoms reduces the activation area of a material; the activation area of CC alloy at 78K decreases from approximately 9nm^2 to 2.5nm^2 , close to the values observed for pure Al at 4.2K (Figure 4.7).

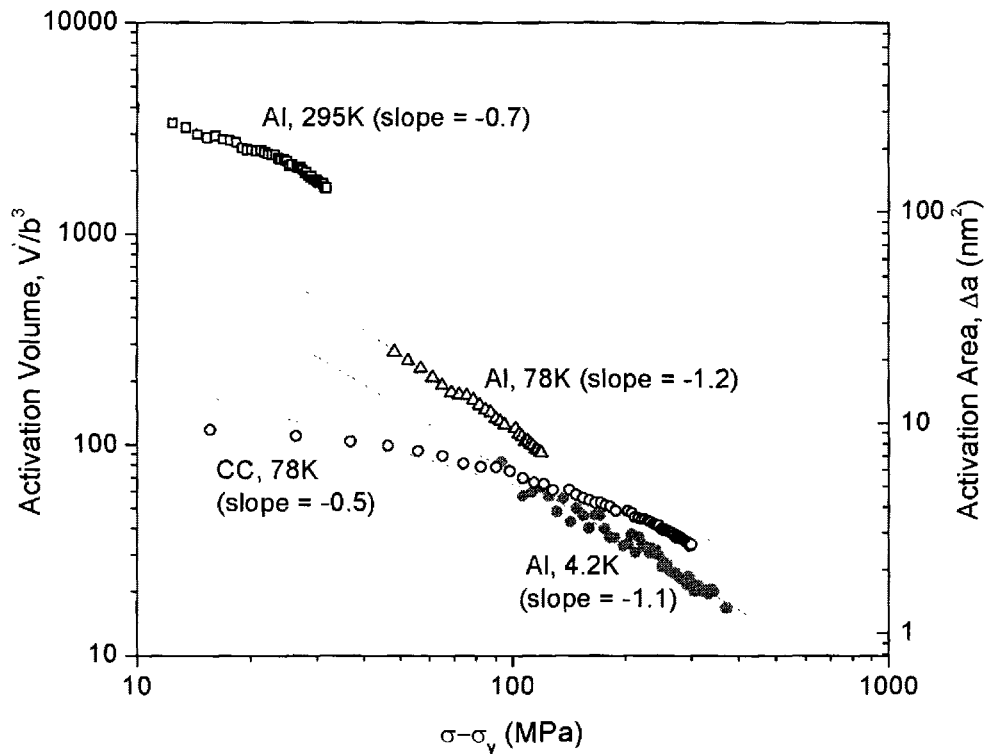
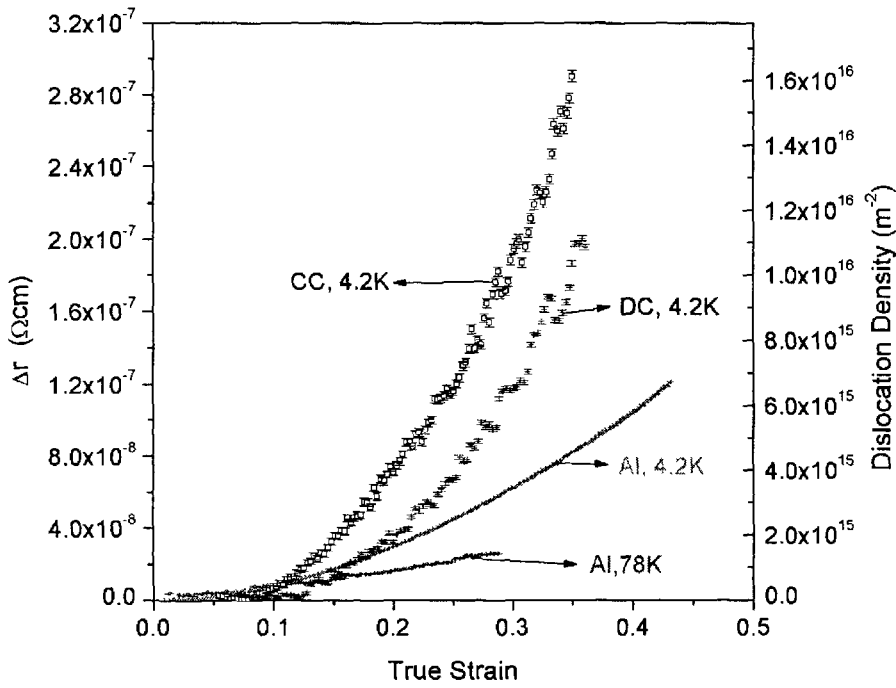


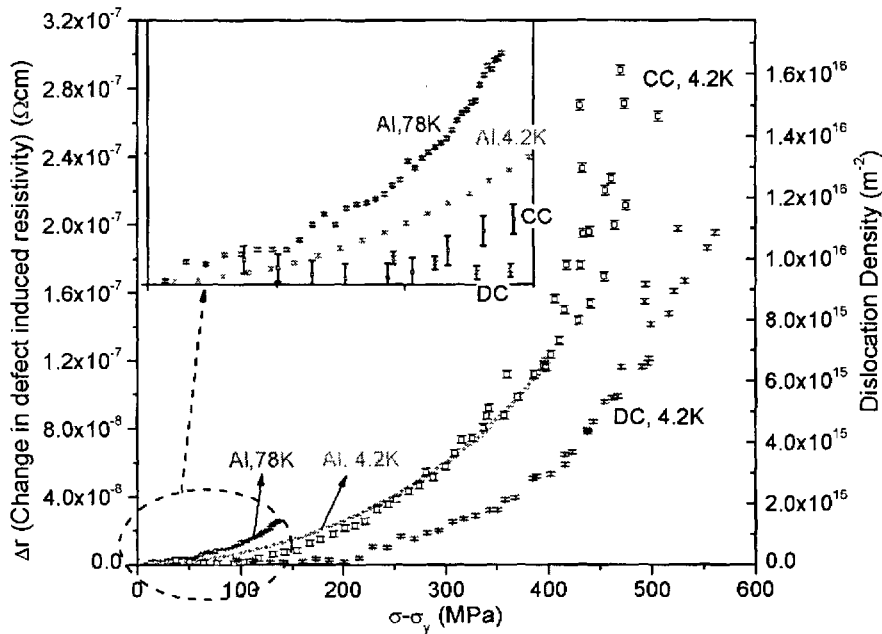
Figure 4.7: Activation volume as a function of the effective flow stress on a log scale for the CC alloy and pure Al. Activation area is given on the right axis.

4.1.3 Electrical Resistivity

Figure 4.8(a) shows raw data of deformation induced resistivity over the residual resistivity value as a function of the true strain for Al, CC and DC alloys deformed at 4.2K. The high purity of Al used in this work enabled us to measure change in



(a)



(b)

Figure 4.8: Evolution of defect induced resistivity change during deformation as a function of (a) true strain and (b) the effective flow stress for the CC alloy and pure Al

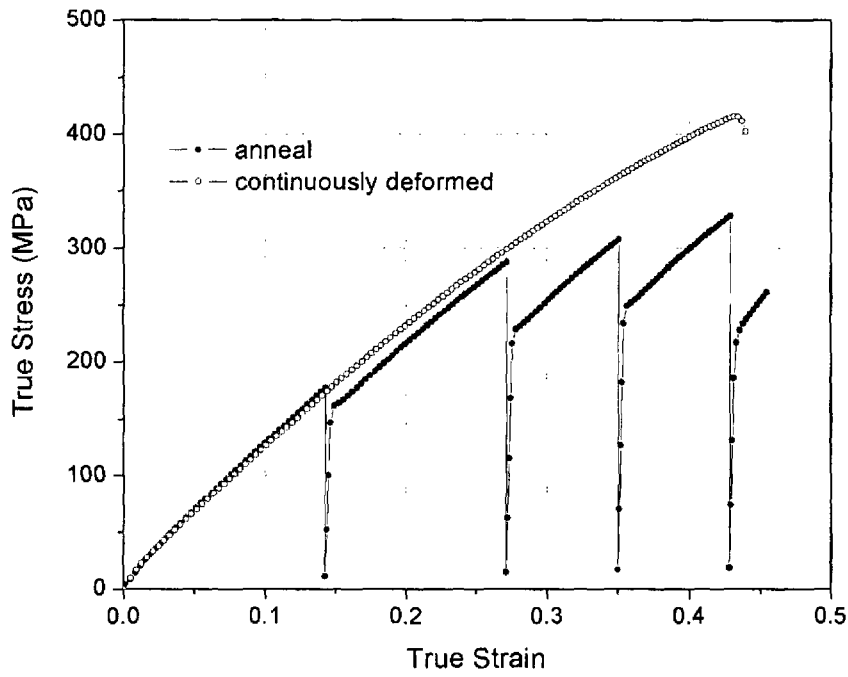
electrical resistivity in this material during deformation at 78K, which is included in the graph. It is seen that, in every case, the resistivity increases parabolically with the strain, indicating that deformation is homogeneous on the macroscopic scale. Compared to pure Al, the alloys show higher scattering in resistivity data due to the contribution from solute and impurity scattering. Assuming that all deformation induced defects are dislocations, the electrical resistivity is recalculated into dislocation densities, using the value of $1.8 \times 10^{-25} \Omega m^3$ for specific resistivity per unit length of dislocation in Al [137]. The data in Figure 4.8(a) can thus be interpreted as the evolution of dislocation density during plastic deformation for both pure Al and Al alloys. It is seen that pure Al accumulates in average about $7 \times 10^{15} m^{-2}$ dislocation density before the fracture. The total dislocation density stored in the CC alloy before the fracture is higher and is of the order of $1.5 \times 10^{16} m^{-2}$ - $1.6 \times 10^{16} m^{-2}$. The DC material accumulates in average $1.1 \times 10^{16} m^{-2}$ dislocation density before the fracture.

Figure 4.8(b) shows deformation induced resistivity as a function of effective flow stress for all materials studied. For pure Al, resistivity increases roughly parabolically with the flow stress up to the point of fracture. The resistivity characteristics for alloys show appreciable scattering of data points; the scattering increases as the flow stress increases. This reflects the unstable deformation due to adiabatic shearing of the lattice, which contributes to the scattering of the flow stress at the same dislocation content. Figure 4.8(b) shows that the resistivity evolution as a function of stress for the CC alloy follows closely the characteristic of pure Al. It is seen that, for a given flow stress level, resistivity of the DC alloy is lower than that of pure Al or the CC material in a broad range of stresses. As previously shown, the resistivity data can be recalculated into dislocation densities. This data shows that, at the same flow stress level, pure Al deformed at 78K produces the highest dislocation densities among all materials studied.

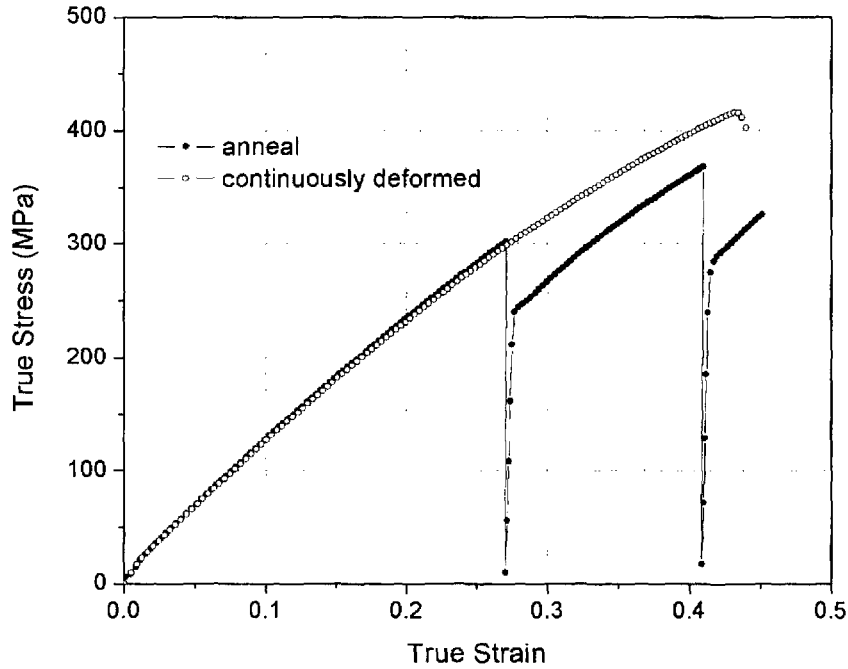
4.1.4 Intermittent Annealing Experiments

Figure 4.9 shows true stress - true strain curves of pure Al for a continuously deformed specimen as well as for specimens that were intermittently annealed four and two times at room temperature and then re-cooled down to 4.2K to resume deformation. A significant influence of annealing on flow stress is observed; (i) the stress drops 20 - 30% when the specimen is annealed at room temperature and deformed again at 4.2K and (ii) the magnitude of the stress drop increases with increasing strain and is independent of the number of intermediate anneals, which implies that it is independent of the anneal history (Figure 4.10). Generally, intermittently annealed specimens show larger deformation before the fracture than continuously deformed specimens.

Figures 4.11 and 4.12 show the variation of total change in resistance, Δr , of a sample deformed as a function of true strain and true stress, respectively. It is seen that the resistivity increases quadratically during deformation. The resistivity measurements of continuously deformed and intermittently annealed samples at the early stage of deformation demonstrate the reproducibility and consistency of data; the increase in resistance of the continuously deformed sample is almost identical to the one of the annealed sample up to the first anneal. Each anneal resulted in a decrease in resistivity of 65 - 75% and the annealed resistivity is independent of the number of anneals. The magnitude of the decrease in resistivity for the present materials is remarkably higher than that for the copper single crystals previously reported by Niewczas and co-workers [59]. The copper does not show a stress drop on reloading after an anneal. Resumed deformation at 4.2K after anneal at room temperature results in a re-increase in resistivity with increasing strain, which follows a path approximately parallel to that for the continuously deformed sample (Figure 4.11).



(a)



(b)

Figure 4.9: True tensile stress vs. true strain of continuously deformed and annealed samples of pure Al: (a) four intermittent anneals and (b) two intermittent anneals

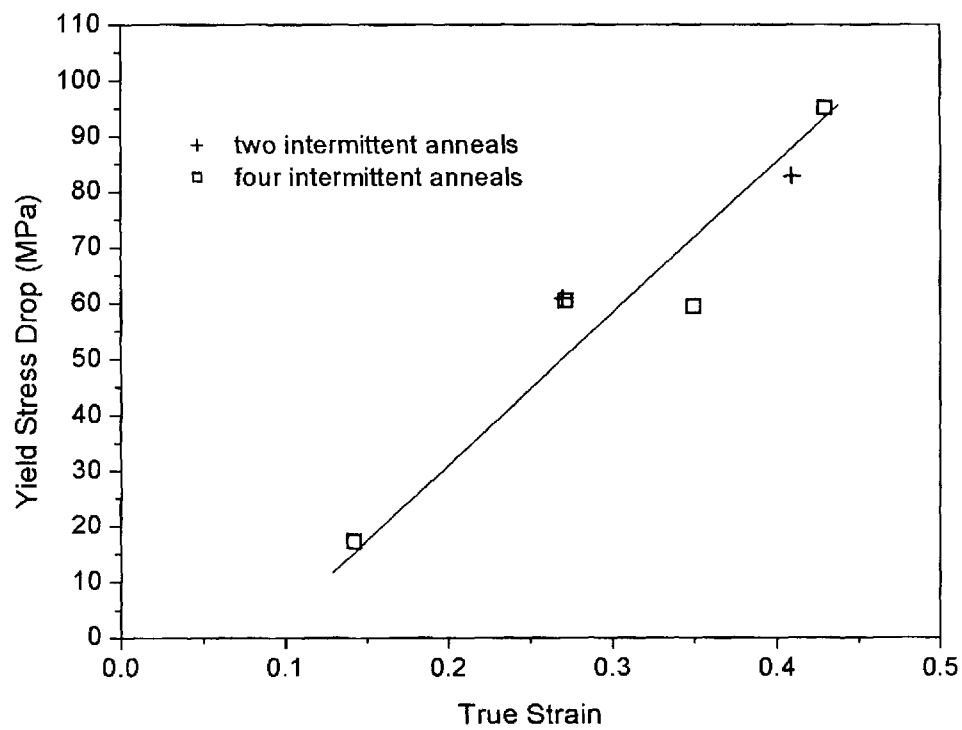
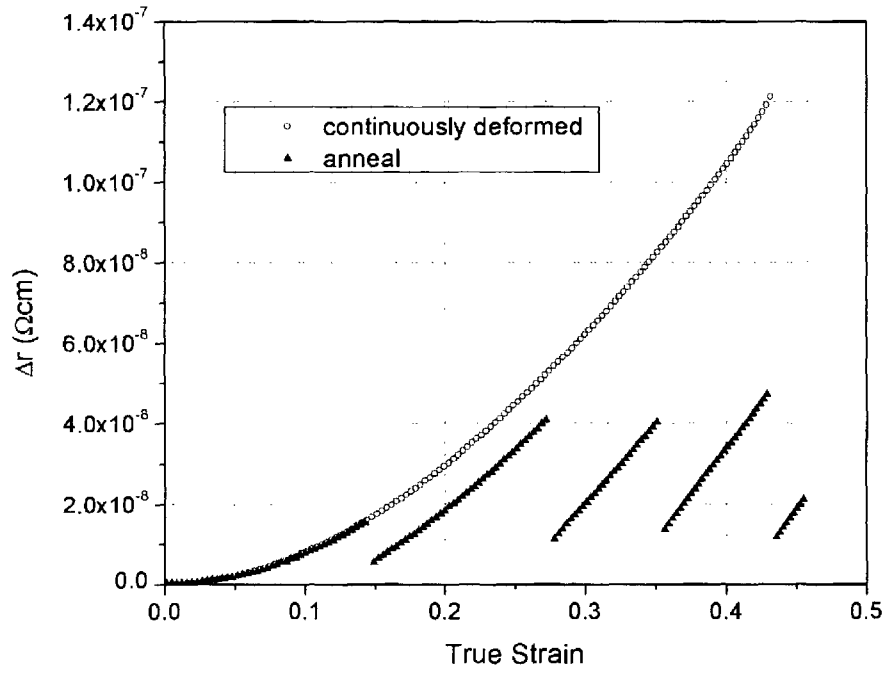
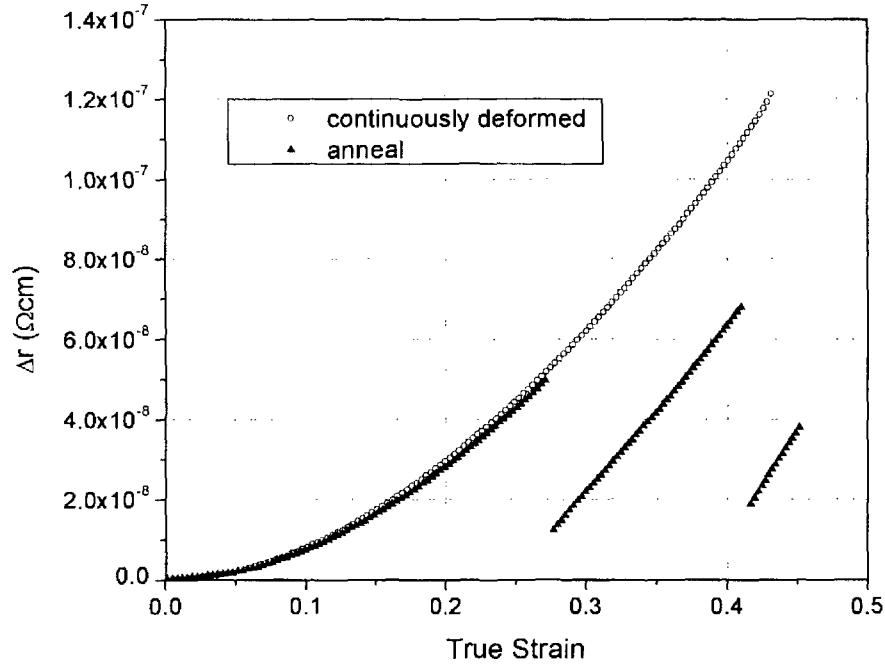


Figure 4.10: Yield stress drop induced by annealing during deformation

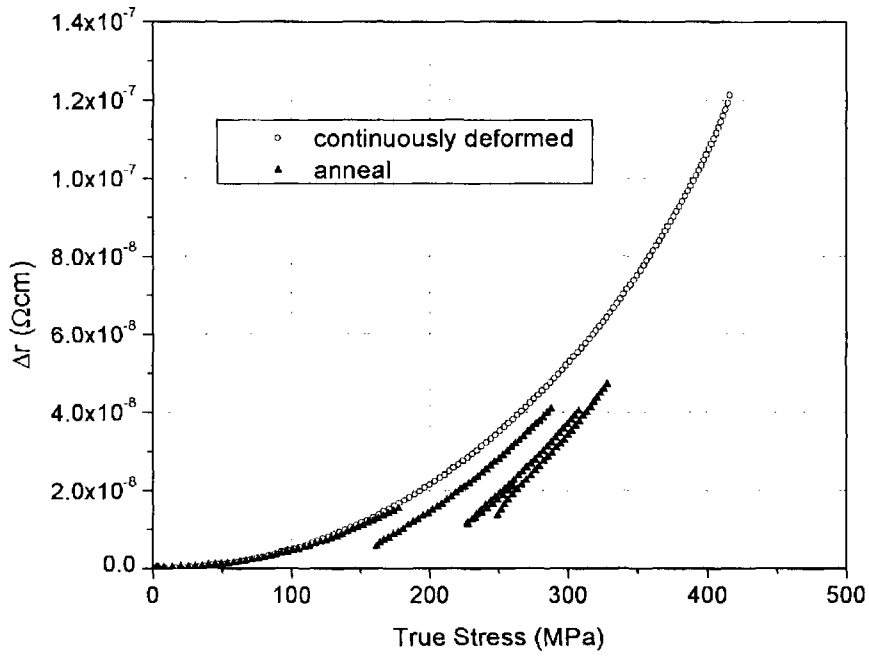


(a)

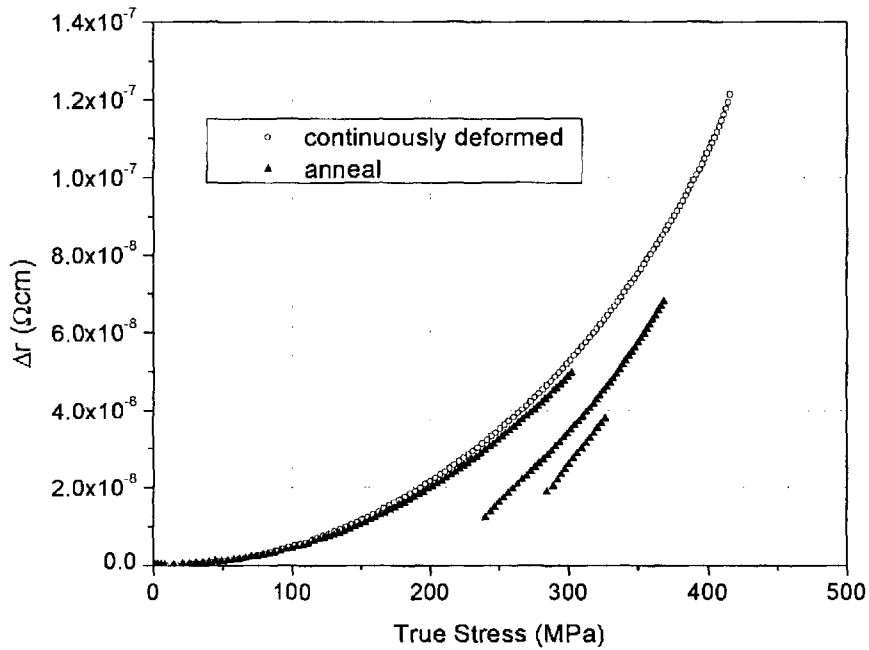


(b)

Figure 4.11: Increase in resistivity as a function of tensile strain: (a) four intermittent anneals and (b) two intermittent anneals



(a)



(b)

Figure 4.12: Increase in resistivity as a function of true stress: (a) four intermittent anneals and (b) two intermittent anneals

Figure 4.13 shows the recoverable and unrecoverable components of the resistivity change as a function of true strain for samples intermittently annealed at room temperature. The recoverable component increases parabolically while the unrecoverable portion increases linearly with the strain. Tables 4.1 and 4.2 give fitting parameters of power and linear equations used to fit experimental data. The characteristics show that the recoverable resistivity is of a factor of seven larger than the unrecoverable fraction of resistivity at the point of failure. A similar propensity of recoverable and unrecoverable resistivity components is observed as a function of true stress. Figure 4.14 shows these characteristics and it is seen that, as in previous case (Figure 4.13), recoverable resistivity increases parabolically with the flow stress, whereas the unrecoverable resistivity shows a linear relationship. The increase of recoverable resistivity is substantially larger than that of the unrecoverable, suggesting that recoverable defects are produced at a much higher rates and that their production increases as deformation proceeds. Figures 4.13 and 4.14 also provide information about the dislocation densities as a function of either true strain or tensile stress with the assumption that both resistivity components arise from line defects (dislocations) and the specific resistivity per unit length of dislocation is taken as $1.8 \times 10^{-25} \Omega m^3$ in Al [137]. Fitting parameters for the dislocation density data obtained in this way are also shown in Tables 4.1 and 4.2.

Table 4.1: Fitting parameters for recoverable defects with $y = a \cdot x^b$ equation

Criterion, y	Independent Variable, x	Constant	
		a	b
Resistivity Change (Ωcm)	True strain	6.20×10^{-7}	2.08
	True stress (MPa)	3.49×10^{-15}	2.86
Dislocation Density (m^{-2})	True strain	3.45×10^{16}	2.08
	True stress (MPa)	4.36×10^8	2.72

Table 4.2: Fitting parameters for unrecoverable defects with linear equation $y = c \cdot x$

Criterion, y	Independent Variable, x	Constant, c
Resistivity Change (Ωcm)	True strain	3.83×10^{-8}
	True stress (MPa)	3.74×10^{-11}
Dislocation Density (m^{-2})	True strain	2.13×10^{15}
	True stress (MPa)	2.08×10^{12}

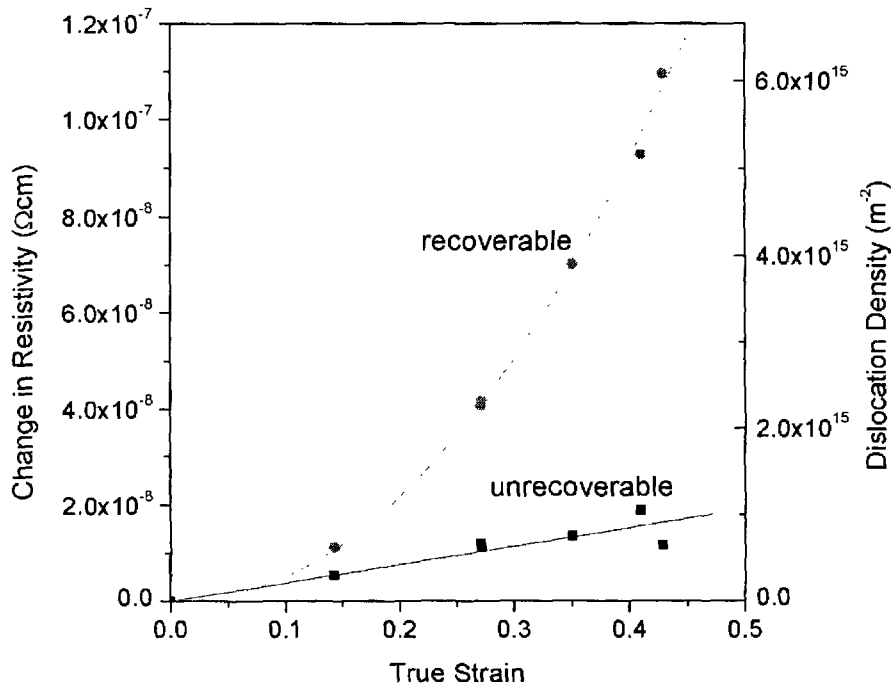


Figure 4.13: Changes in recoverable and unrecoverable resistivity as a function of true strain for intermittently annealed samples

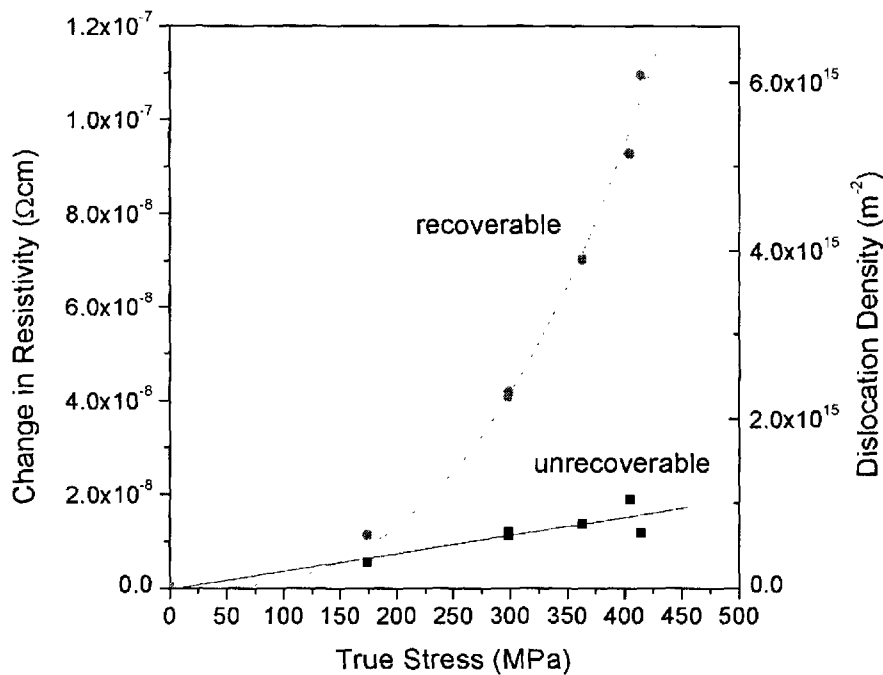


Figure 4.14: Changes in recoverable and unrecoverable resistivity as a function of true stress for intermittently annealed samples

Figure 4.15 shows isochronal annealing data for pure Al deformed at 4.2K. Open symbols in the figure were obtained by warming a deformed sample to a given temperature followed by cooling it back to 4.2K, where change of the resistance of the sample was measured. This procedure was repeated by increasing the anneal temperature up to 300K. In contrast, the closed symbols were obtained by annealing a deformed sample directly at a given temperature and cooling it back to 4.2K to measure its resistance. The figure shows that two points (open and closed symbols) at a given temperature are very close to each other. This indicates that the fraction of deformation-induced resistivity remaining in a sample is determined by the final annealing temperature, not by the number of intermittent anneals at lower temperatures.

Figures 4.16, 4.17 and 4.18 show true stress - true strain curves of pure Al for a continuously deformed specimen as well as for specimens that were intermittently

annealed at 100K, 200K and 260K, respectively, and then re-cooled down to 4.2K to resume deformation. In order to investigate the effect of relaxation of the substructure during unloading, one sample was unloaded and reloaded at 4.2K, which is denoted by “A” on Figures 4.16, 4.19 and 4.22. The anneal test was then resumed as denoted by “B” on the figures. The relaxation of the substructure during unloading followed by the annealing at 100K does not influence the flow stress (Figure 4.16), although the anneal results in a decrease in resistivity by 30%. A slight decrease (less than 1.0%) in resistivity is observed during unloading (Figures 4.19 and 4.22). On the other hand, 3% and 8% stress drops are observed when the specimen is annealed at 200K and 260K, respectively (Figures 4.17 and 4.18). In these cases, the anneal decreases the resistivity by 57% and 69% at 200K and 260K, respectively (Figures 4.20, 4.21, 4.23 and 4.24).

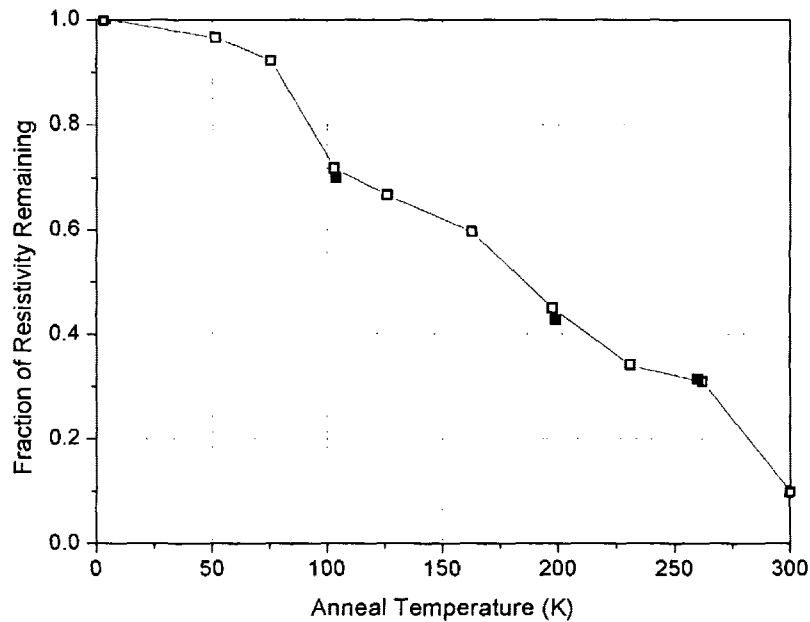


Figure 4.15: Isochronal annealing curve for pure Al deformed 37% (380MPa) at 4.2K. Open symbols represent the fraction of deformation-induced resistivity remaining in the structure as a function of anneal temperature. The closed symbol shows the resistivity remaining when an equivalently deformed sample is annealed by warming directly to a given temperature.

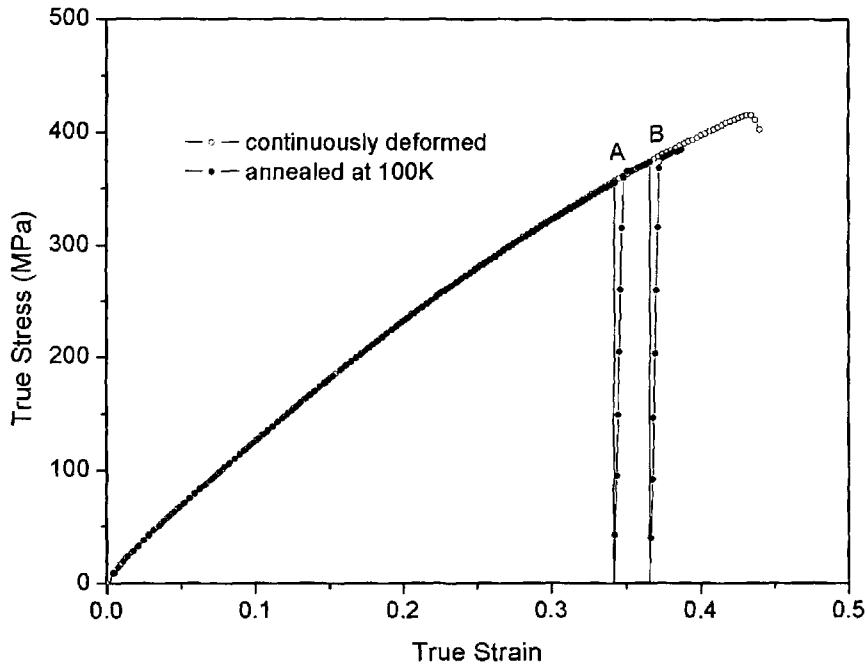


Figure 4.16: True tensile stress vs. true strain characteristics continuously deformed and annealed samples of pure Al at anneal temperature of 100K.

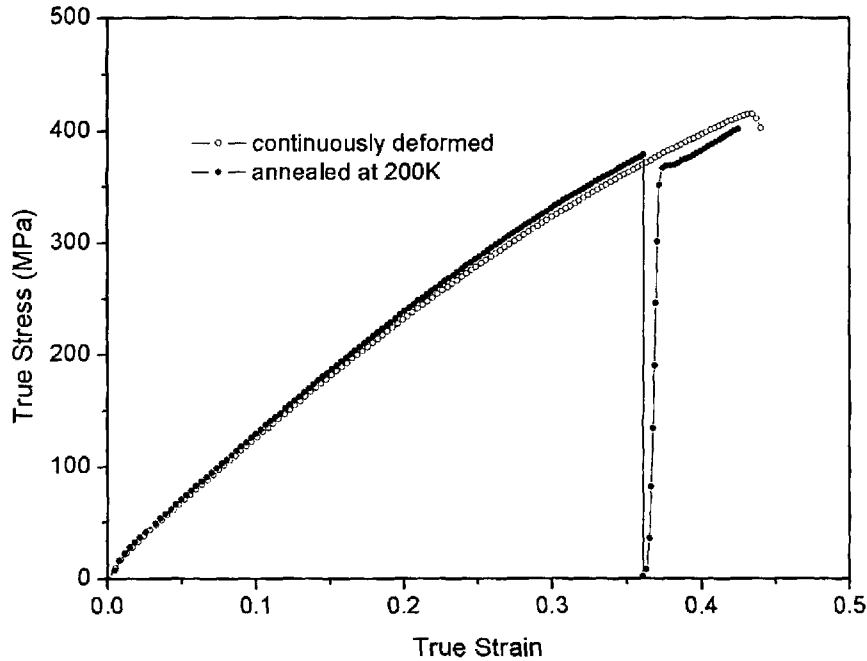


Figure 4.17: True tensile stress vs. true strain characteristics continuously deformed and annealed samples of pure Al at anneal temperature of 200K

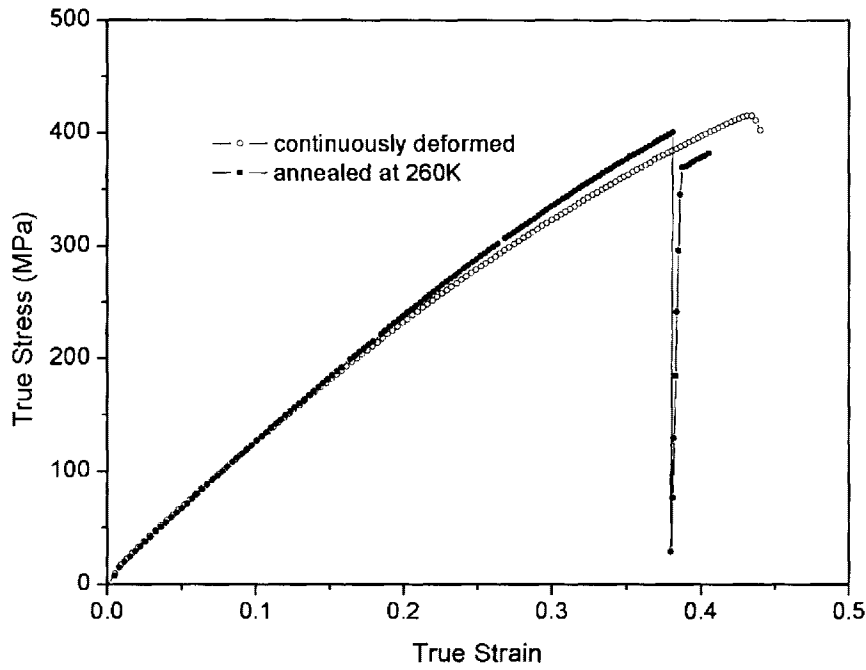


Figure 4.18: True tensile stress vs. true strain characteristics continuously deformed and annealed samples of pure Al at anneal temperature of 260K

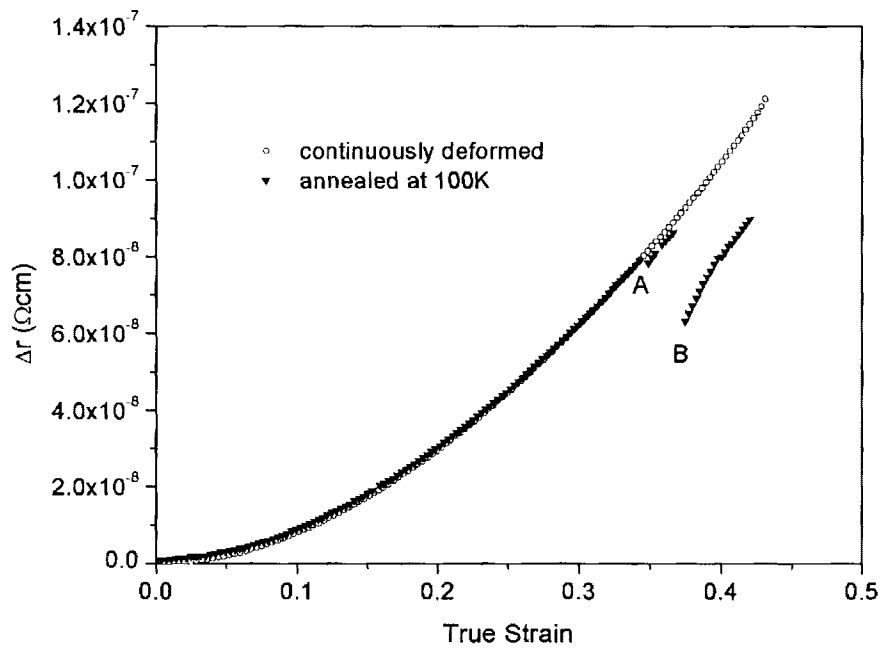


Figure 4.19: Increase in resistivity as a function of true strain at anneal temperature of 100K

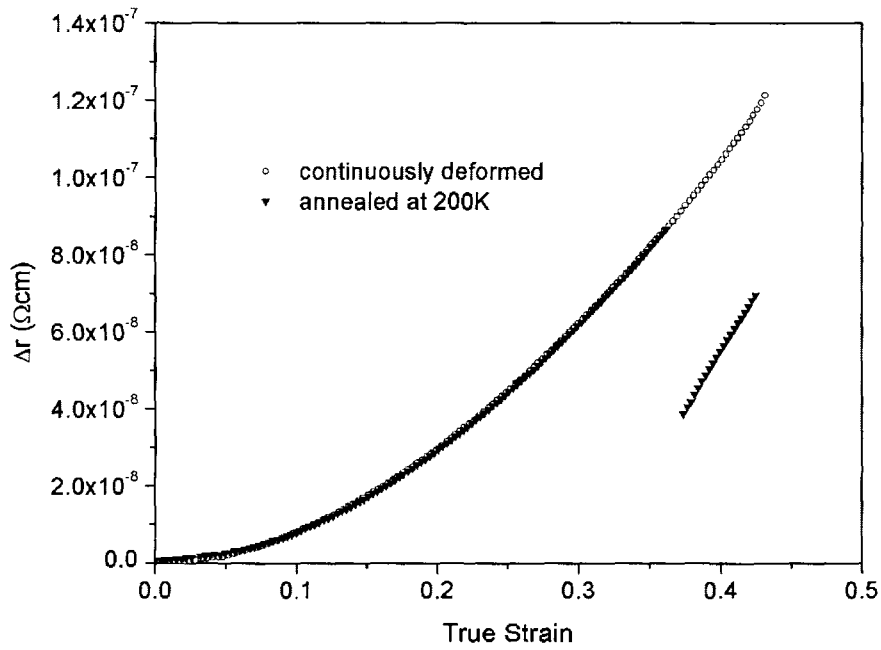


Figure 4.20: Increase in resistivity as a function of true strain at anneal temperature of 200K

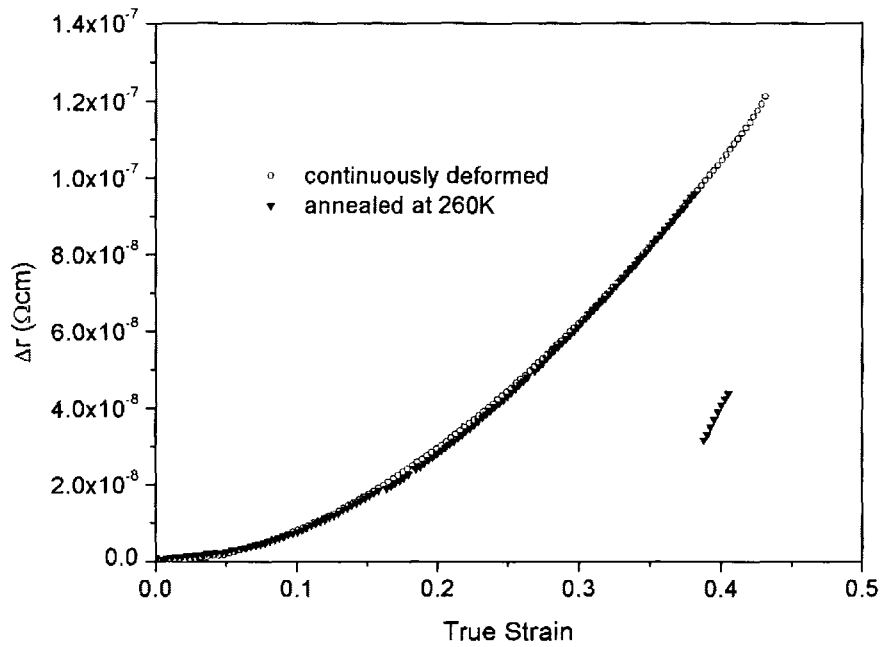


Figure 4.21: Increase in resistivity as a function of true strain at anneal temperature of 260K

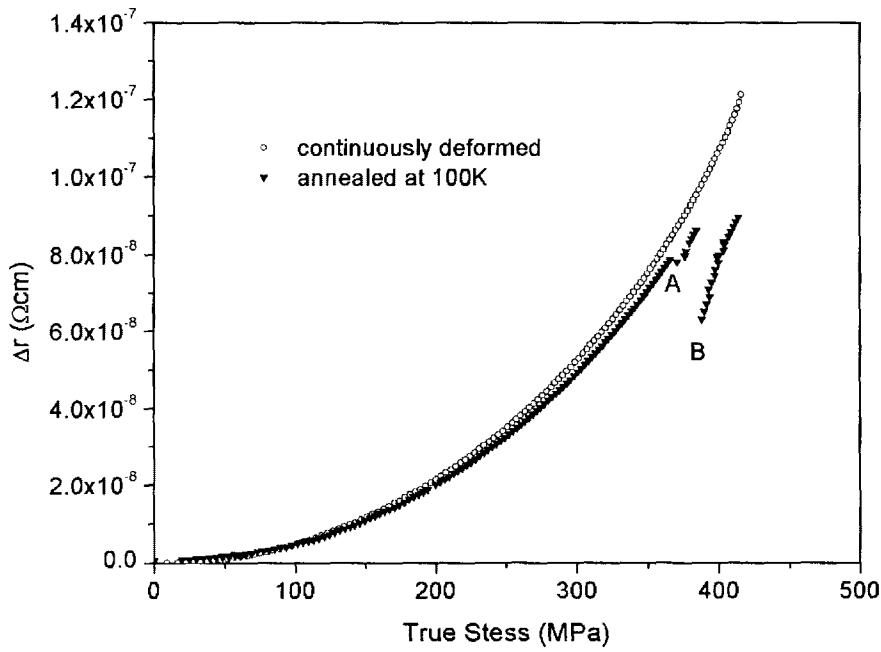


Figure 4.22: Increase in resistivity as a function of true stress at anneal temperature of 100K

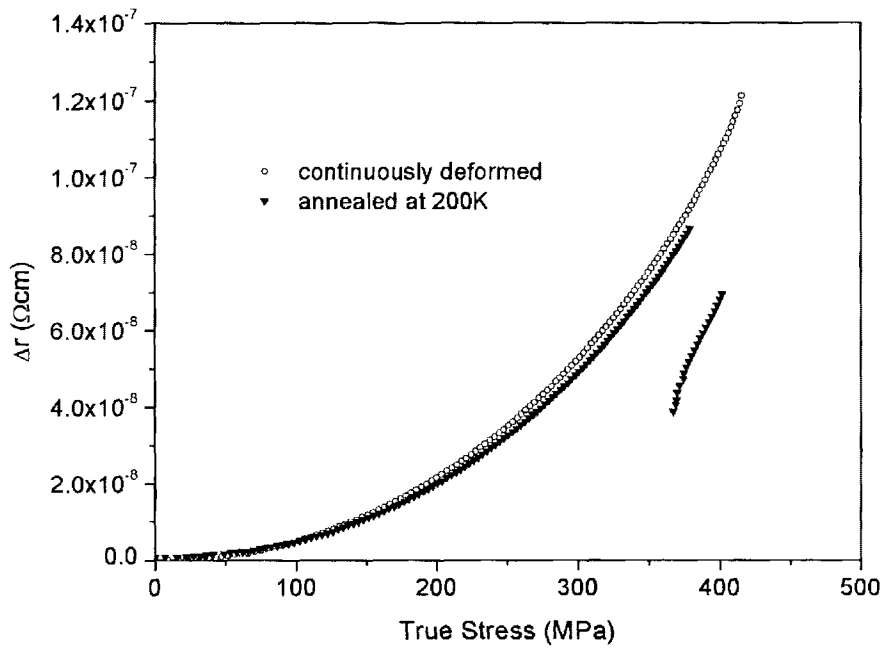


Figure 4.23: Increase in resistivity as a function of true stress at anneal temperature of 200K

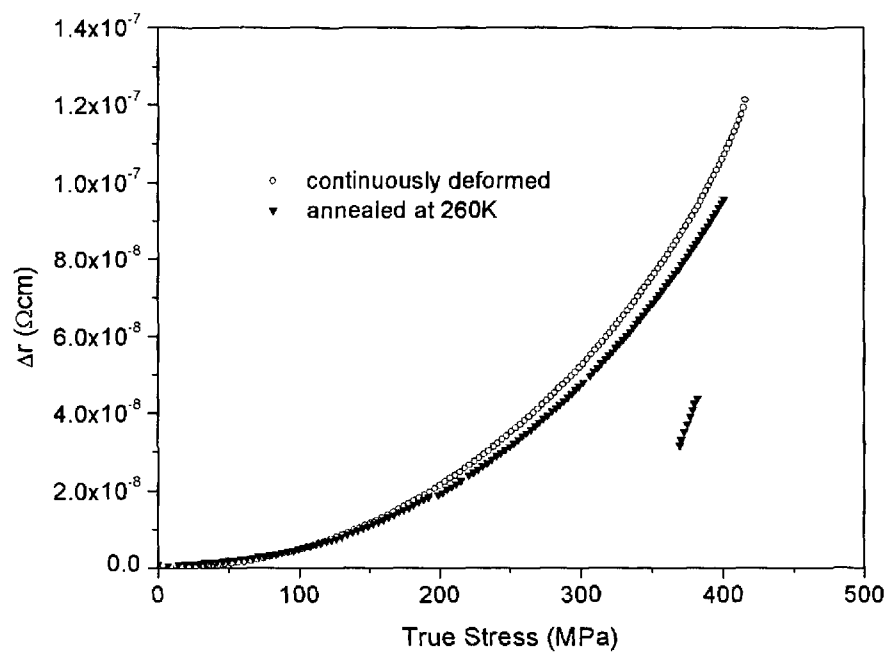


Figure 4.24: Increase in resistivity as a function of true stress at anneal temperature of 260K

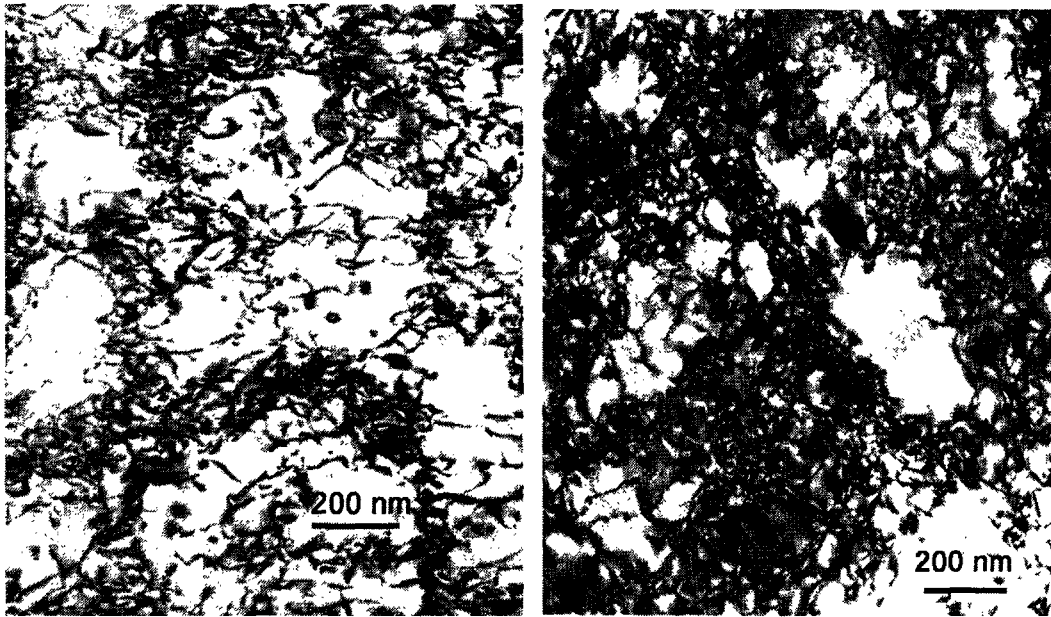
4.1.5 Structural Studies

Figure 4.25 shows the microstructure of the CC alloy before and after plastic deformation at different temperatures. The annealed CC material contains non-homogeneously distributed fine particles smaller than $1\mu\text{m}$ in diameter, produced during continuous casting of the alloy [6]. These particles are observed both in the form of strings aligned along rolling direction as shown in Figure 4.25 (a) and also in the form of random clusters distributed non-homogeneously in the Al-rich matrix.

Figure 4.25 (b) shows TEM observations of the microstructure in the CC material deformed 10% at room temperature. Dislocations are stored in the entire volume of the material and one can recognize a formation of characteristic cell structures with the higher dislocation density accumulated in the cell wall and a somewhat less dense cell interior. The average cell size of this structure is of the order of $0.5\text{-}0.7\mu\text{m}$. It is seen that the formation of these features is not associated with the second phase particles as no particles are found in this area. The alloy deformed 17% at 4.2K exhibits, on average, much higher dislocation densities. In some areas, as is shown in Figure 4.25 (c), dislocations form insulated cells with a size of the order of $0.2\text{-}0.5\mu\text{m}$. In highly deformed samples (Figure 4.25 (d)), the dislocations are stored quite homogeneously in the volume of the specimen, and there is no clear separation into higher and lower dislocation density areas, as was seen in the sample deformed at room temperature.

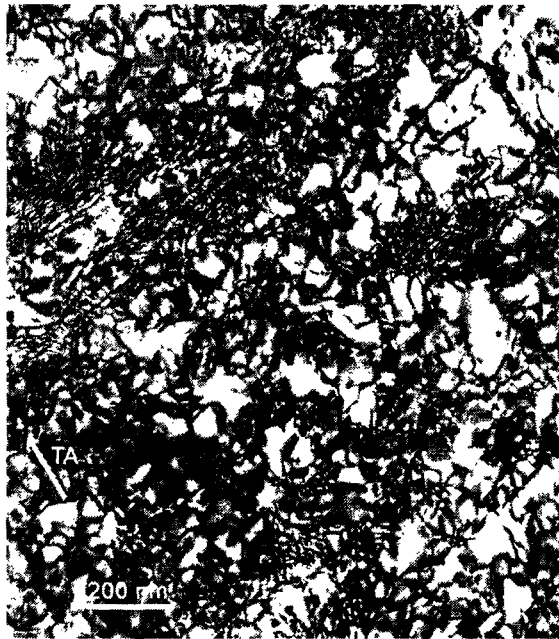


Figure 4.25: TEM observations of the microstructure of CC alloys: (a) prior to deformation, (b) the substructure developed after 10% of deformation at 295K at the flow stress of 130MPa, (c) dislocation substructure developed after 17% of deformation at 4.2K corresponding to the flow stress of 320MPa and (d) dislocation substructure developed in the CC sample deformed till fracture, i.e. after 33% of deformation at 4.2K corresponding to the flow stress of 520MPa (TA denotes the tensile direction.). (cont'd)



(b)

(c)



(d)

Figure 4.25: (cont'd)

Figure 4.26 shows examples of the dislocation substructure in pure Al deformed till fracture, i.e. 35%, 30% and 43% of strain at 295K, 78K and 4.2K, respectively. In comparison with the CC alloy, the substructure of pure Al is markedly different. In all cases, the micrographs show well-developed substructures with dislocation subboundaries separating areas of recovered cell interiors. There are substantially fewer defects found inside the subgrains than was observed in the CC alloy. Smaller cells are produced at lower temperatures. The scale of the subgrains ranges between 1-3 μm in material deformed at 295K, 0.6-1.7 μm in Al deformed at 78K and 0.2-0.7 μm in Al deformed at 4.2K.

TEM observations (Figures 4.25 and 4.26) show that the dislocation content and the nature of dislocations stored in CC material are different from these found in pure Al. Pure Al exhibits a strong tendency towards grain subdivision and development of low misoriented subboundaries within larger grains. This has not been observed in the CC alloy, which tends to form a relatively homogeneous network of dislocations, particularly at low temperatures.

4.1.6 Texture

Figure 4.27 shows $\{111\}$ pole figures recalculated from ODFs of the CC material in as-received state (Figure 4.27 (a)) and after annealing at 350°C and 450°C (Figures 4.27 (b) and (c)). The as-received CC material shows a typical rolling texture with a β fiber that extends from the copper $\{112\}\langle 111 \rangle$ to the brass $\{011\}\langle 211 \rangle$ orientation with the center at S orientation $\{123\}\langle 634 \rangle$. The CC specimens annealed at 350°C retain relatively strong components of the cold-rolled material (Figure 4.27 (b)) whereas samples annealed at 450°C develop the rotated cube texture as shown in Figure 4.27 (c). Figure 4.27 (d) shows a $\{111\}$ pole figure of the as-received DC alloy

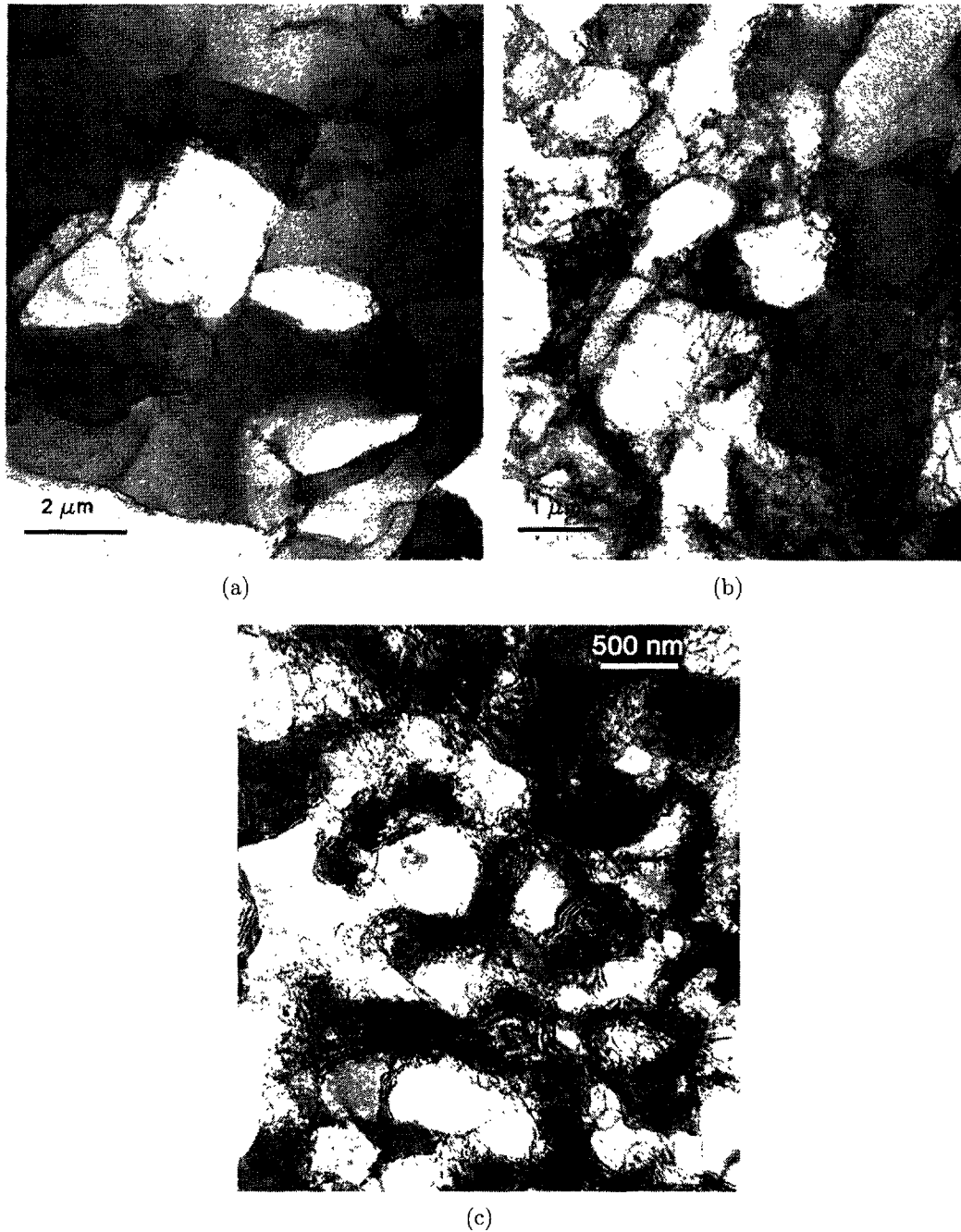


Figure 4.26: TEM observations of the microstructure of pure Al deformed till fracture at different temperatures, i.e., (a) 35% of deformation at 295K corresponding to a flow stress of 50MPa, (b) 30% of deformation at 78K at the flow stress of 150MPa, (c) 43% of deformation at 4.2K corresponding to a flow stress of 415MPa.

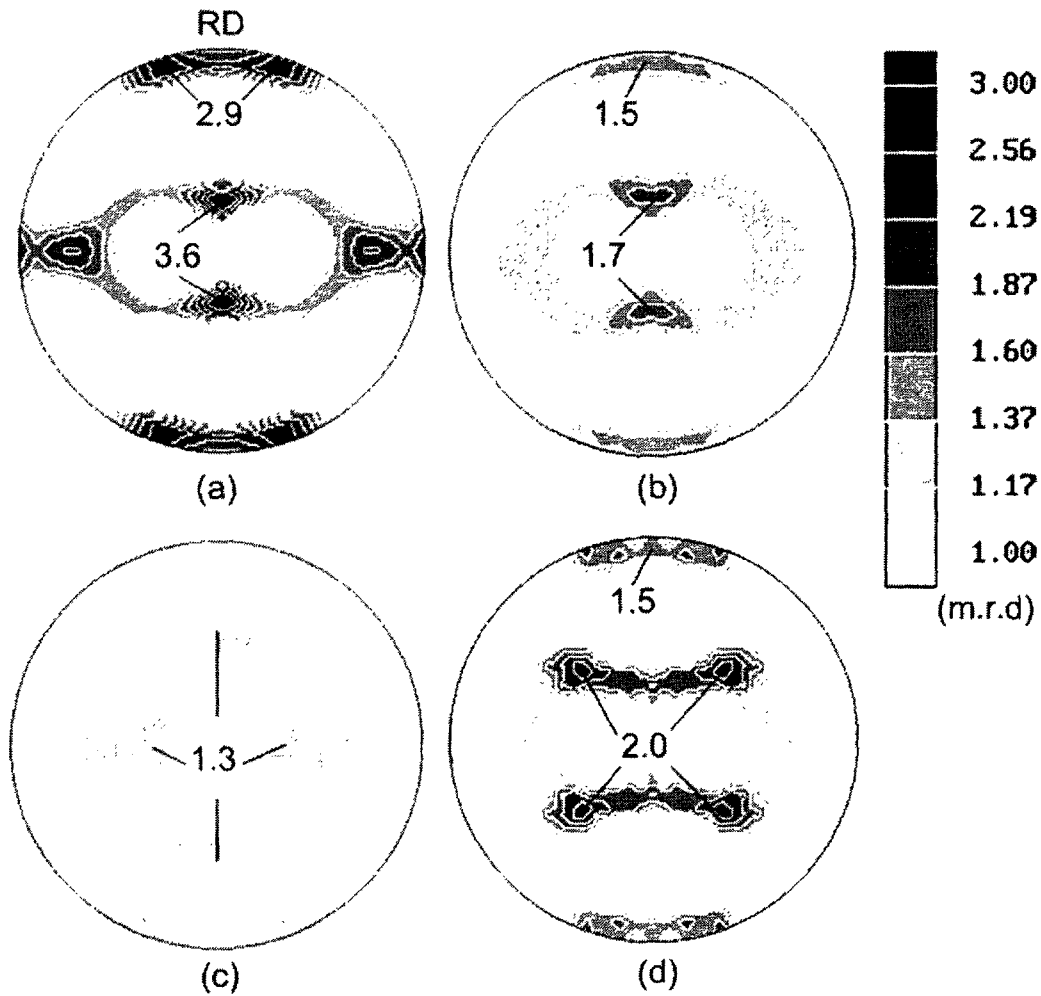


Figure 4.27: $\{111\}$ pole figures of: (a) the as-received CC alloy, (b) the CC alloy after annealing at 350°C for 2hrs, (c) the CC alloy after annealing at 450°C for 2hrs and (d) $\{111\}$ pole figures of the as-received DC alloy. RD represents the previous rolling direction of the samples.

in an annealed state. The DC material retains features of the deformation texture, but also shows components of the cube texture developed during the post-deformation annealing cycle, which are not observed in the annealed CC alloy (Figures 4.27 (b) and (c)).

With increasing tensile deformation, the tensile axis (TA) of DC and CC samples rotates towards $\langle 111 \rangle$, which is pronounced by the development of new peaks in the neighborhood of the north and south poles in the stereographic projections in Figure 4.28. The peaks became stronger after about 19% of strain.

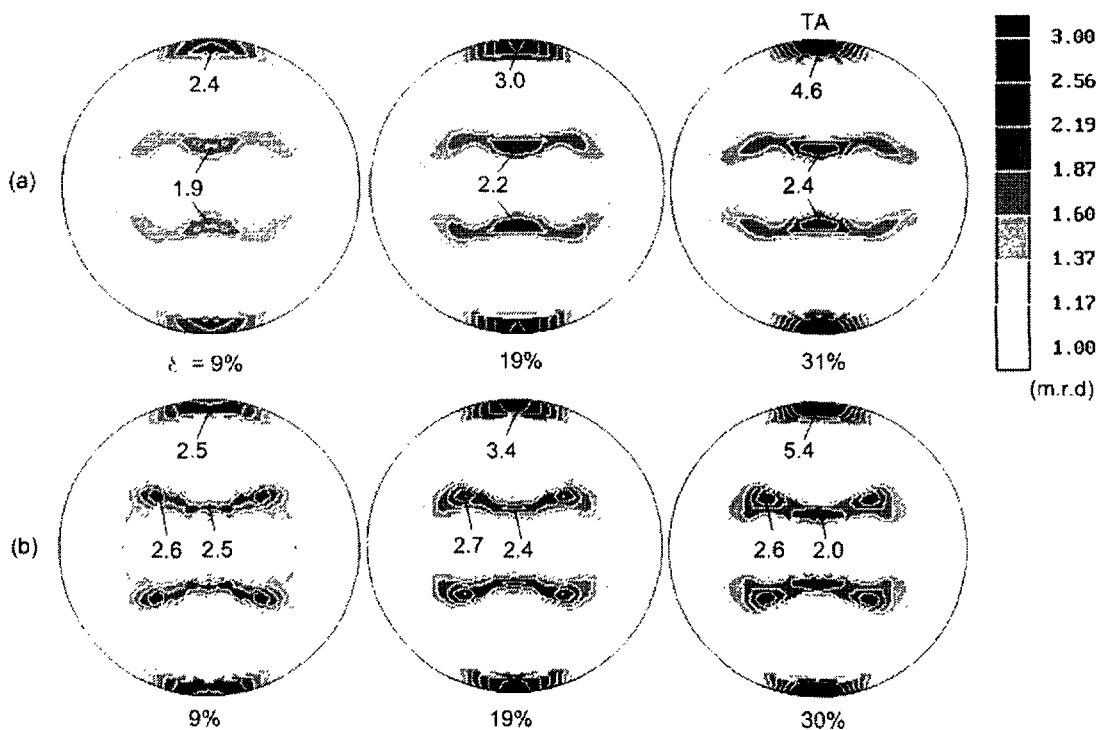


Figure 4.28: $\{111\}$ pole figures for (a) CC and (b) DC samples deformed at 4.2K to different strains given in the figure. Tensile axis is denoted as TA.

Figure 4.29 shows the effect of annealed texture (Figures 4.27 (b) and (c)) on the texture developed after 19% of strain at room temperature. It is seen that the

intensity of $\{111\}$ diffraction peaks is higher in samples previously annealed at 350°C than at 450°C ; however, the type of the texture is qualitatively identical in both specimens.

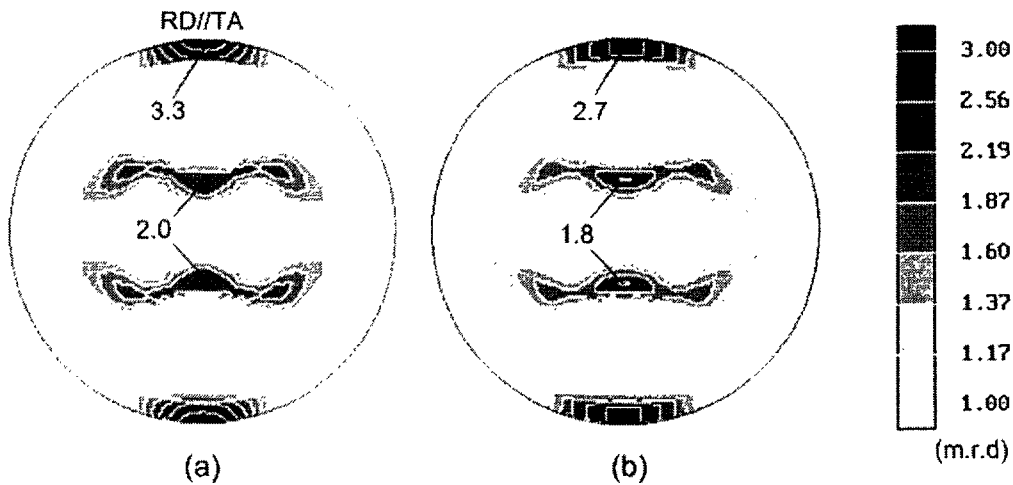


Figure 4.29: $\{111\}$ pole figures of CC specimens annealed at (a) 350°C and (b) 450°C after fracture (about 19% of strain) at room temperature.

Figure 4.30 shows ODF of the sample deformed to fracture at 4.2K at different Φ angles. The main texture components showing strong intensities of the diffraction peaks are marked on the figure. High intensities are observed mostly at $\langle 111 \rangle$ and $\langle 100 \rangle$ orientations indicating that the tensile axis for many grains rotate toward either $\langle 111 \rangle$ or $\langle 100 \rangle$ orientations. For example, at $\Phi = 65^\circ$, a new peak is formed at orientation $\{123\}\langle 111 \rangle$ in the neighborhood of the $\{123\}\langle 634 \rangle$ rolling texture component; at $\Phi = 90^\circ$, one observes the appearance of new peaks belonging to $\{001\}\langle 100 \rangle$ family as well as $\{011\}\langle 111 \rangle$ (Figure 4.30). It is being observed that the intensities of $\langle 111 \rangle$ peaks are generally higher than $\langle 100 \rangle$.

The evolution of the texture during plastic deformation is independent of the test temperature up to 19% of strain. Beyond this deformation, the peak intensity appears

to be more sensitive to deformation temperature; for example, it is seen in Figure 4.31 that at a strain of about 30%, the peak intensity at 78K is higher than observed at 4.2K.

The rotation of the tensile axis of the samples during tensile deformation can be visualized by plotting the orientation distribution function against one of the Euler angles as a function of deformation. As an example, Figure 4.32 shows orientation distributions at $\Phi = 65^\circ$ and $\theta = 35^\circ$ for CC material annealed at 350°C and deformed at 295K, 78K and 4.2K with the strain rate of $1.6 \times 10^{-4} \text{s}^{-1}$; ODF sections for the samples deformed until fracture at the strain rate of $1.6 \times 10^{-5} \text{s}^{-1}$ are also included for comparison. It is seen that the strong $\langle 111 \rangle$ texture is developed rapidly beyond 19% of strain. One observes that the intensity of the diffraction data in the sample deformed until fracture and previously annealed at 450°C is lower than in the reference sample annealed at 350°C and deformed the same amount (Figure 4.32 (a)). Samples deformed at 78K show higher orientation density compared to samples deformed at 4.2K beyond 19% of strain (Figures 4.32 (b) and (c)). Figure 4.32 also reveals that lowering the strain rate has no significant effect on either the nature of the orientation distribution or the peak intensity of texture components.

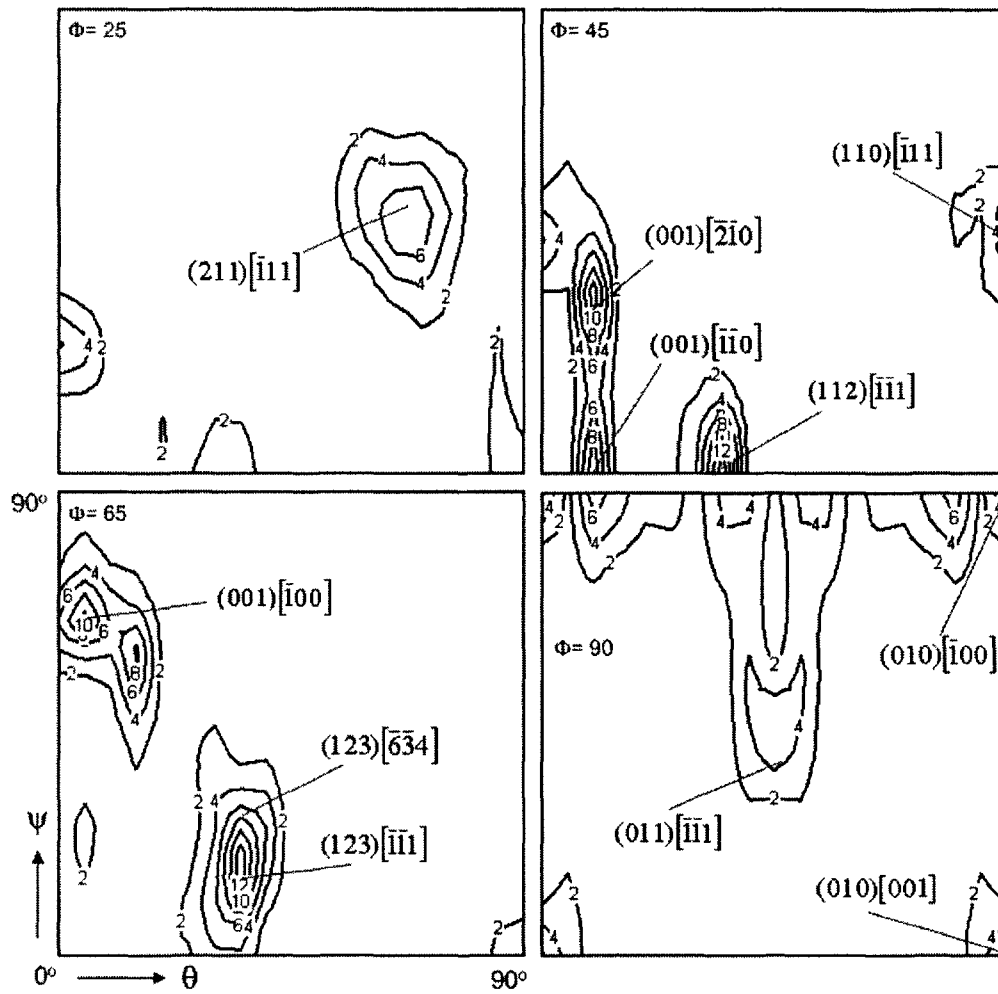


Figure 4.30: Selected sections of orientation distribution for the CC specimen deformed till fracture at 4.2K (32% of strain) at different Φ angles of 25° , 45° , 65° and 90°

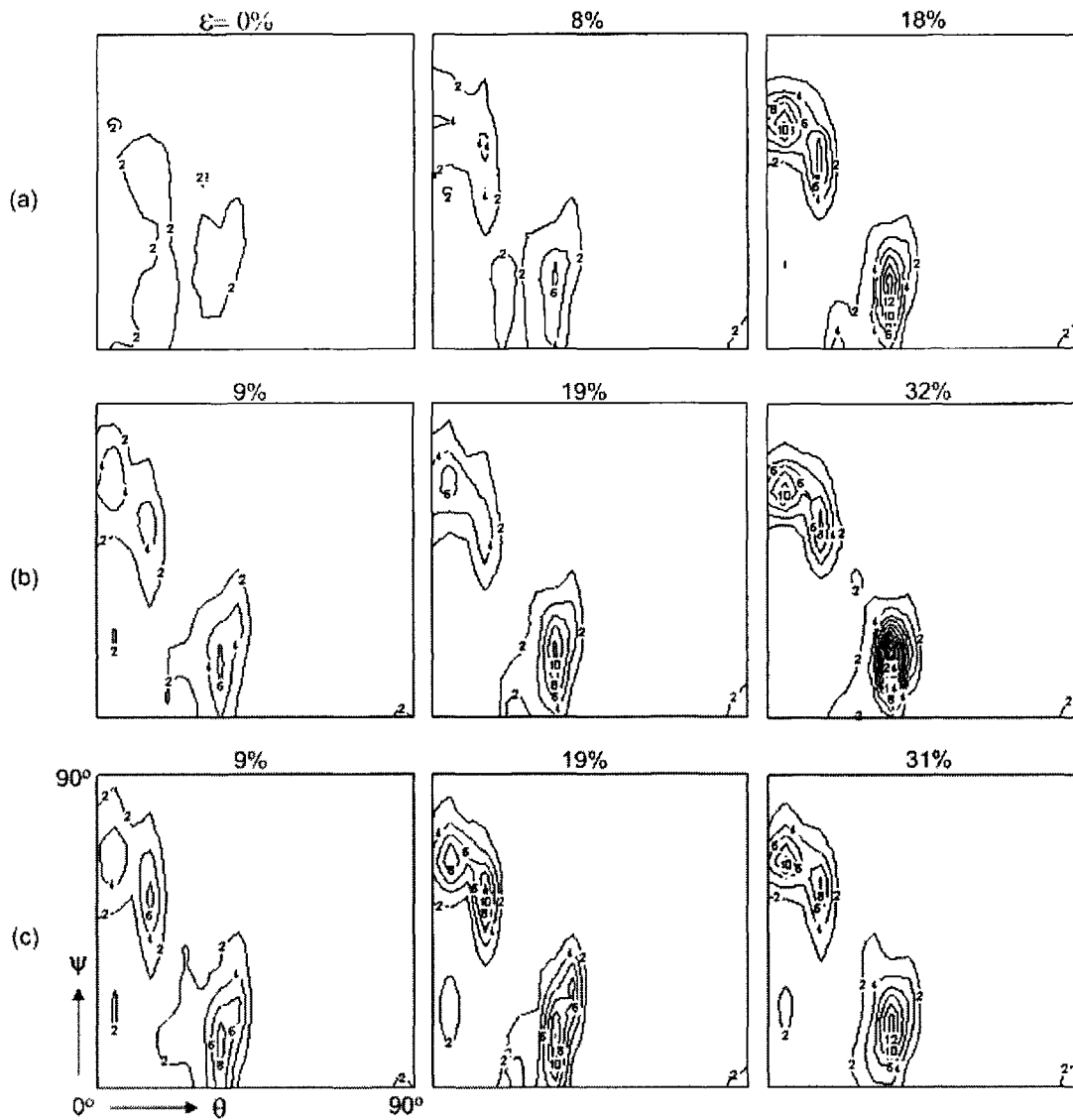
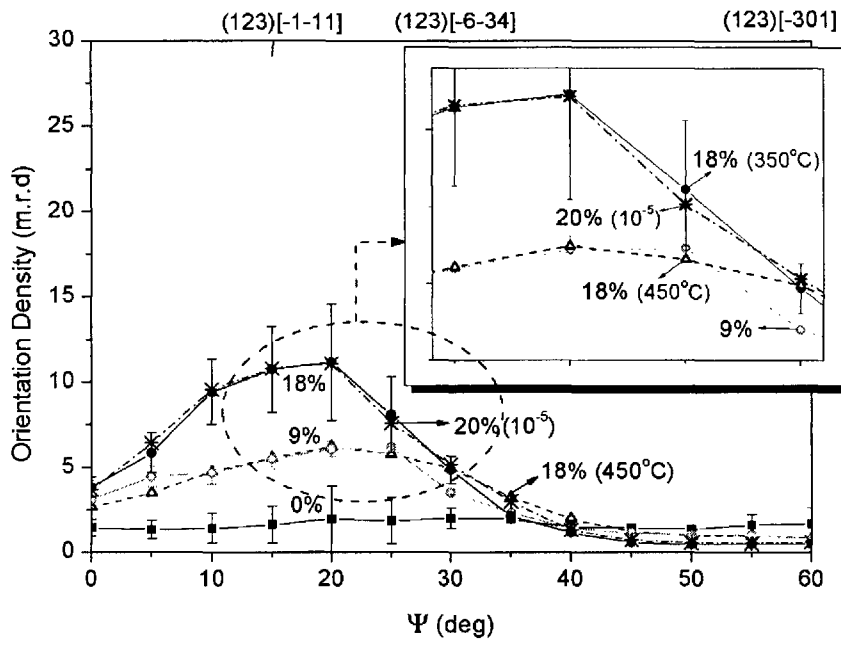
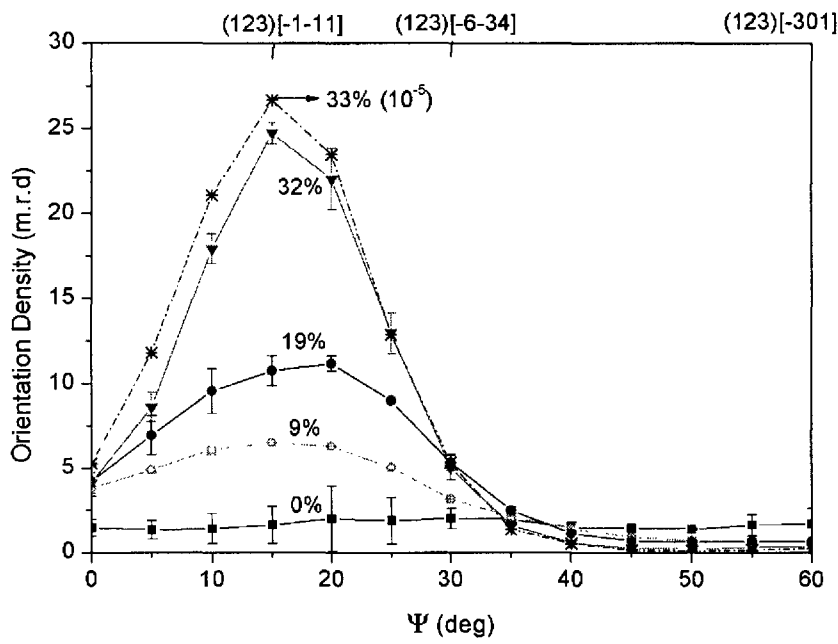


Figure 4.31: Orientation distributions function at a constant $\Phi = 65^\circ$ for CC samples deformed to different strains at temperature of (a) 295K, (b) 78K and (c) 4.2K

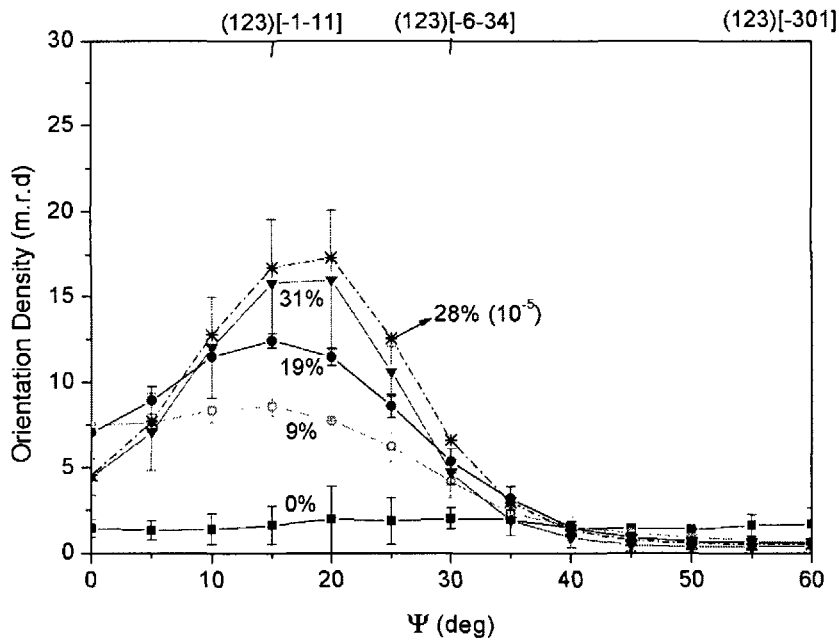


(a)



(b)

Figure 4.32: (cont'd)



(c)

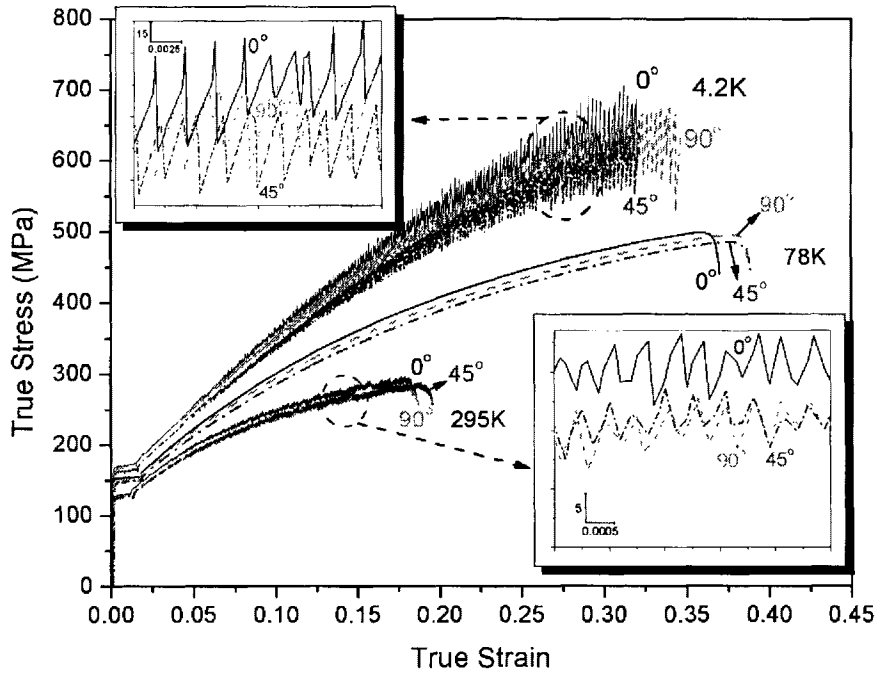
Figure 4.32: Orientation distributions of the CC material at $\Phi = 65^\circ$ and $\Theta = 35^\circ$ deformed at (a) 295K, (b) 78K and (c) 4.2K with the strain rate of $10^{-4}s^{-1}$. Figures show orientation distributions for the specimen annealed at 350°C and deformed to a given strain indicated on the graph; figure (a) shows the data for the specimen annealed at 450°C . Data for the samples deformed at the strain rate of $10^{-5}s^{-1}$ are included on the graphs for comparison. (cont'd)

4.2 Anisotropic Deformation

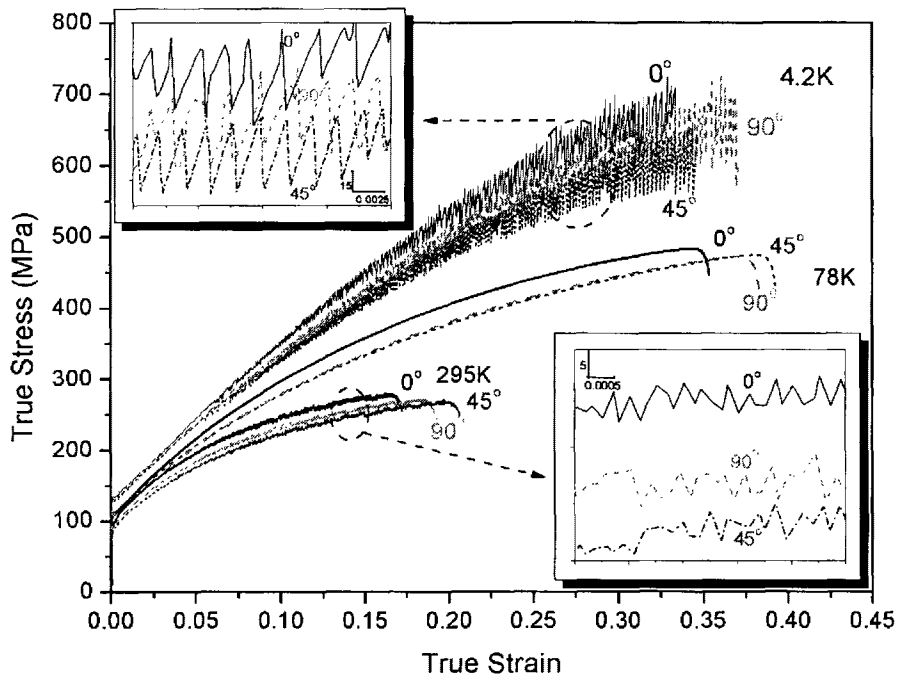
4.2.1 Tensile Behaviour

Serrated flow due to dynamic strain aging at room temperature and the adiabatic shear effects at 4.2K occur regardless of the tensile direction of samples. At 78K, the samples exhibit homogeneous deformation for every tensile direction (Figure 4.33). The anisotropy in tensile elongation and ultimate tensile strength is observed at every temperature (Figure 4.33). The homogeneous elongation at both 45° and 90° orientations is generally higher than in the 0° sample. The maximum tensile stress in the rolling (0°) direction is always the highest, and the one in the 45° direction is the lowest. The differences in tensile stress between these two specimens for the CC alloy at strain of 20% are approximately 3%, 5% and 7% for 295K, 78K and 4.2K, respectively. For DC samples, the differences are approximately 5%, 7% and 9% for 295K, 78K and 4.2K, respectively. At the strain of 30%, the differences in the tensile stress of CC samples are 5% and 9% at 78K and 4.2K, and 5% and 10% for the DC alloy at 78K and 4.2K, respectively.

The work hardening characteristics shown in Figure 4.34 allow the determination of when the anisotropy of the plastic flow begins. A significant difference in work hardening rate is observed in the early stage of deformation, and the work hardening rate in all directions become similar in the later stage of deformation. The work hardening rate in the 0° orientation is higher than that in other directions in the early stage of deformation (Figure 4.35).

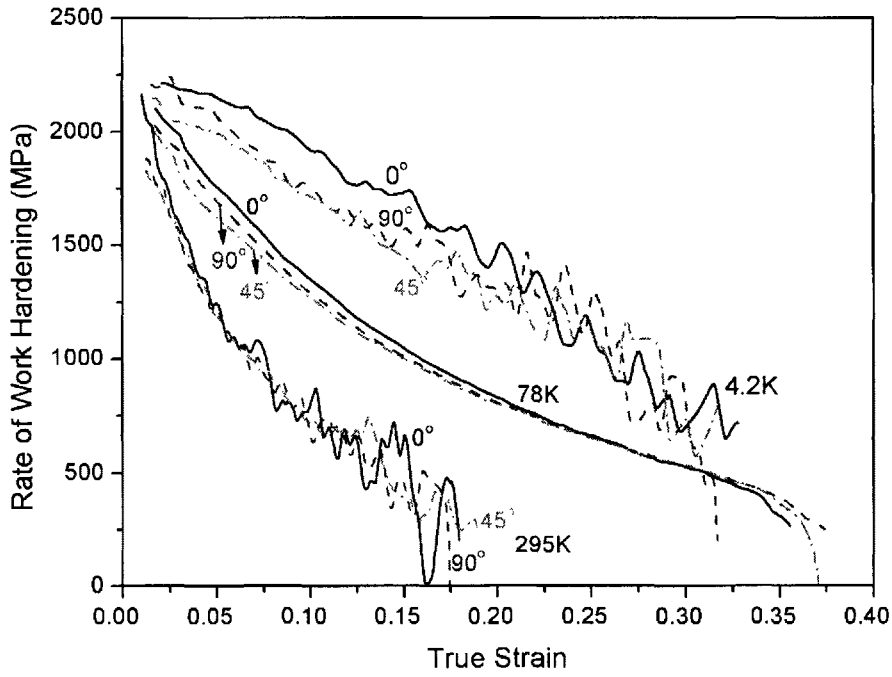


(a)

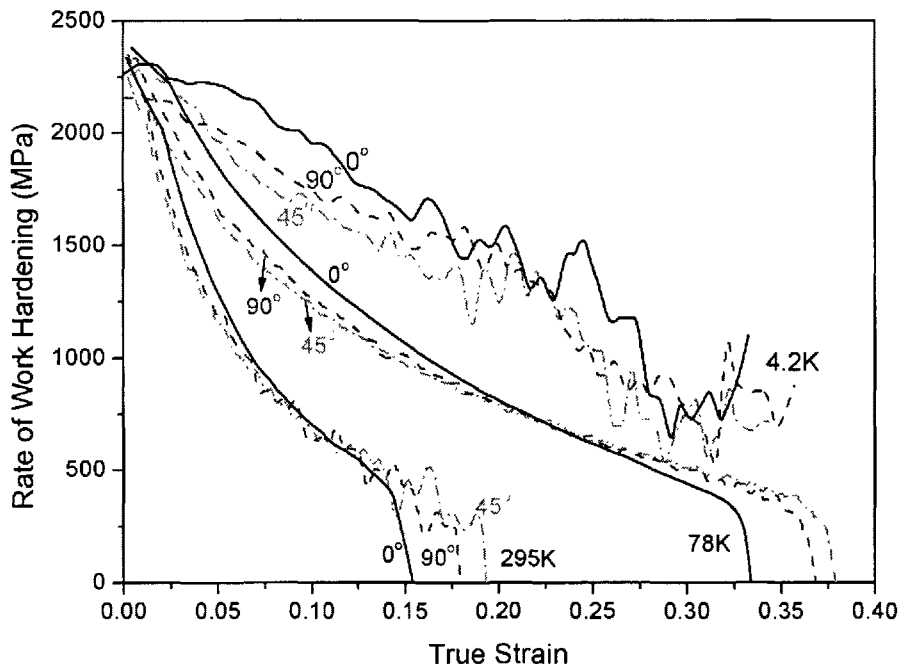


(b)

Figure 4.33: True stress vs. true strain curves for the (a) CC and (b) DC. Note: 0°, 45° and 90° are angles of the tensile axis to the rolling direction of the sheet.

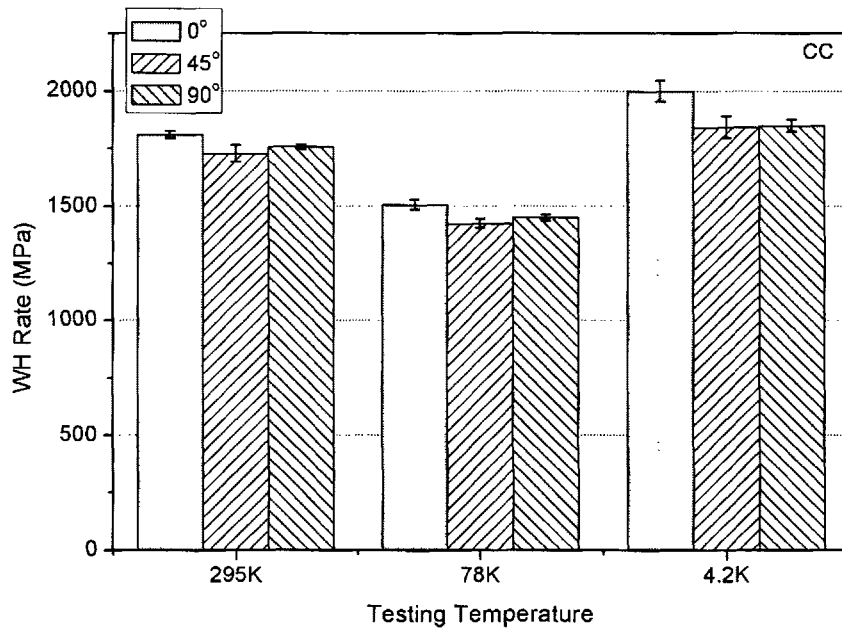


(a)

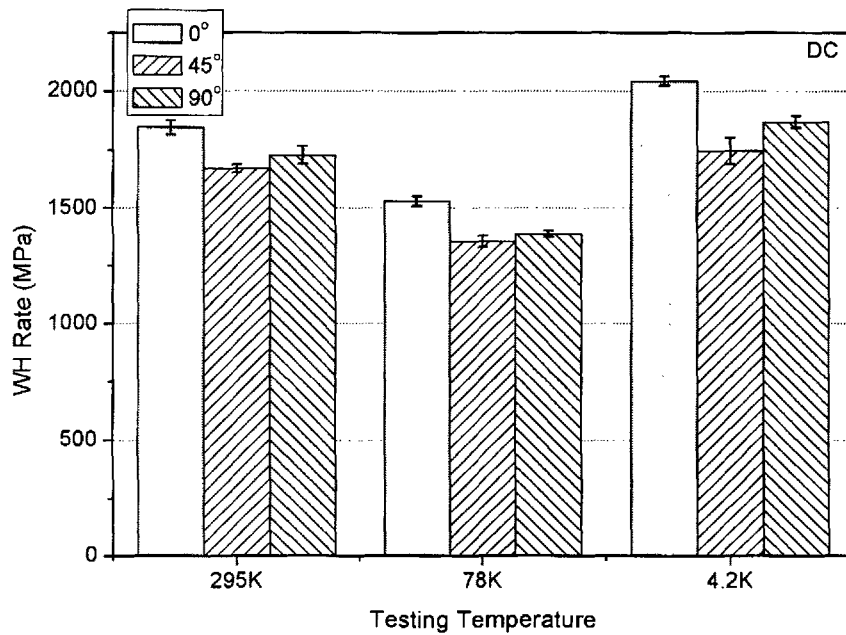


(b)

Figure 4.34: Behaviour of the work hardening rate for (a) CC and (b) DC alloys as a function of true strain



(a)



(b)

Figure 4.35: Work hardening (WH) rates at the early stage of deformation for (a) CC and (b) DC samples deformed to 3% of strain at 295K and 9% of strain at 78K and 4.2K

4.2.2 Strain Rate Sensitivity

The constituent particles present in the alloy can be responsible for the mechanical anisotropy, such as mechanical fibering [50, 67]. Since a rate sensitivity test provides powerful information on the nature of interactions between obstacles and dislocations, this analysis will give an insight into the effect of obstacle structure on the anisotropy in materials studies.

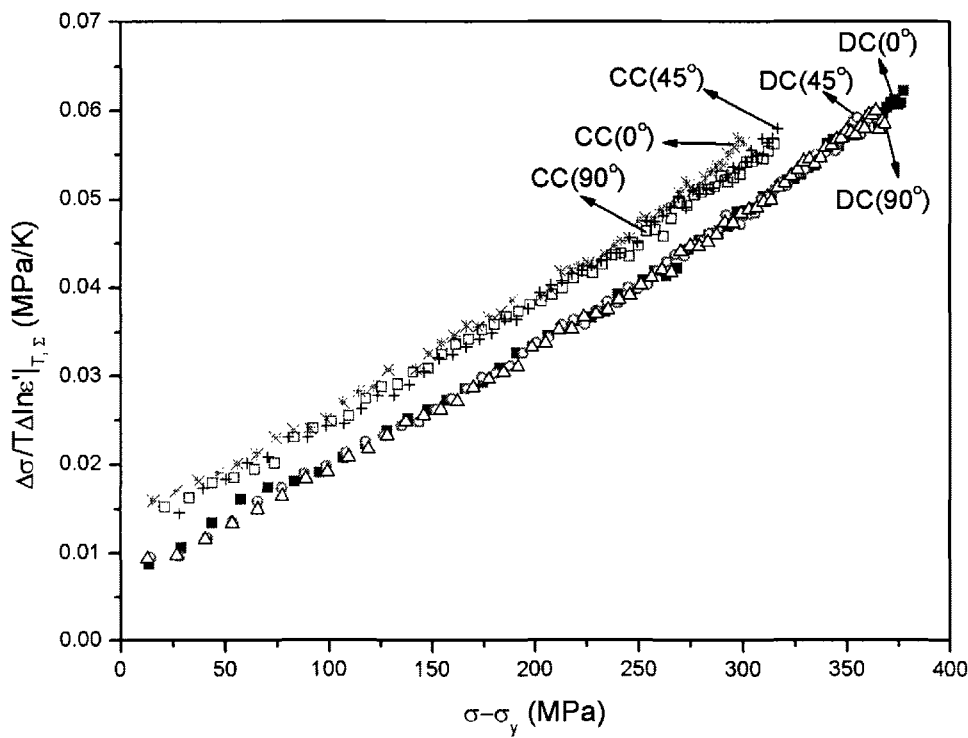
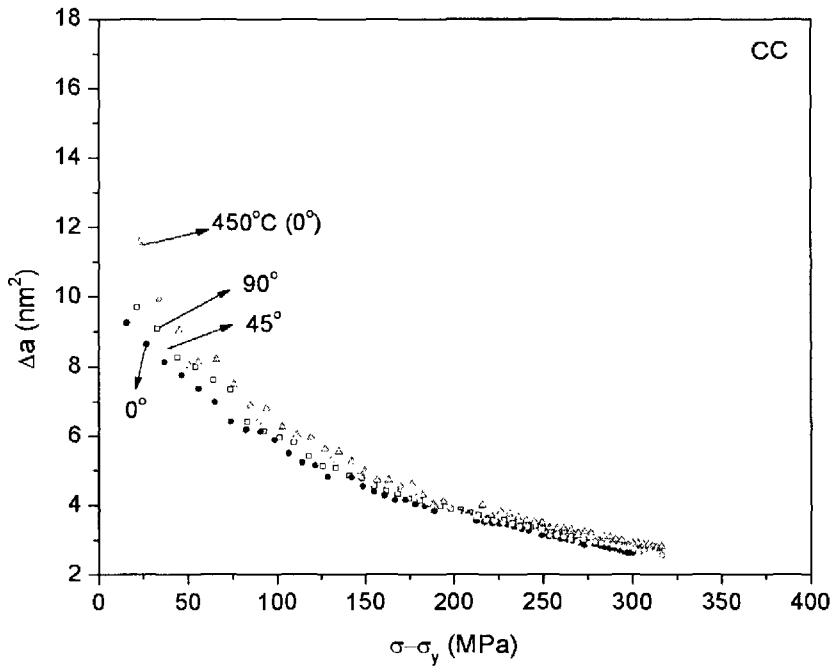


Figure 4.36: Haasen plot obtained from strain rate change tests at the test temperature of 78K for CC and DC alloys

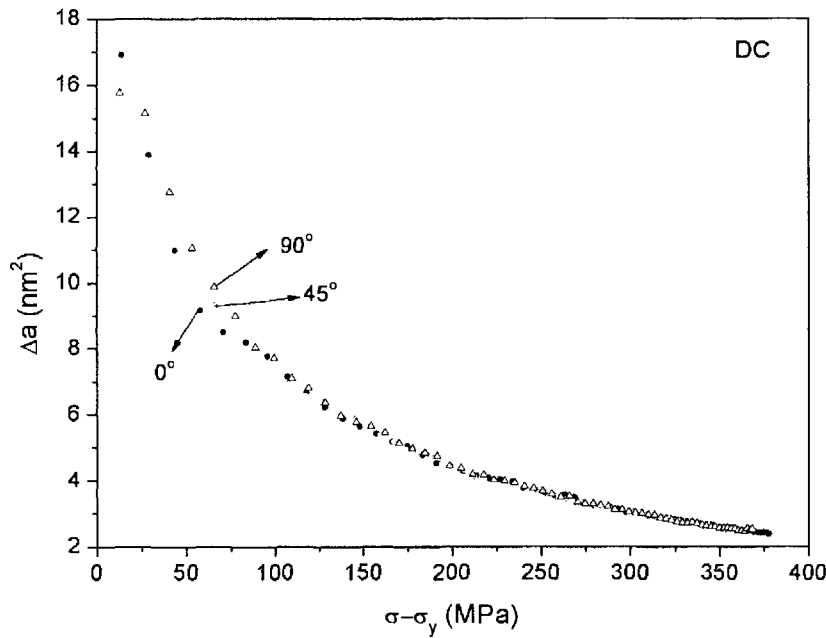
Figure 4.36 shows the Haasen plot produced from the rate sensitivity results with strain rate change between 10^{-4} and $10^{-5} s^{-1}$ at the test temperature of 78K for CC and DC alloys. At other temperatures, the Haasen plot could not be constructed due

to the extensive serration of the flow stress. The y-intercept of Haasen plot for the DC is lower than that for the CC alloy. This indicates that the substructure of the CC material provides a larger contribution of thermal component to the flow stress. This is attributed to (a) the larger grain size of the DC alloy and (b) the fact that more solute atoms precipitated out in the DC material during the thermomechanical process, which consequently resulted in less amount of solute atoms in the solution, giving a lower contribution of a thermal component in the DC material. However, no anisotropy of the strain rate sensitivity is observed in Haasen plot for both CC and DC materials; the y-intercepts and the slopes of curves for each tensile direction overlap each other (Figure 4.36).

The activation area is the area swept by a dislocation segment during activation between the unstable and the stable equilibrium states at a given stress. The activation area is evaluated based on the rate sensitivity data. In the initial stage of deformation, the activation area in the 0° orientation is slightly lower for both CC and DC alloys (Figure 4.37). The activation areas in all directions, however, become closer at the later stage of deformation, which is similar to the propensity of work hardening rate mentioned earlier. The activation area for the CC heat-treated at 450°C is higher than that for the CC heat-treated at 350°C (Figure 4.37 (a)). This is because the larger grain size of the 450°C heat-treated material makes the dislocation movement easier.



(a)



(b)

Figure 4.37: Activation area obtained from the rate sensitivity data at 78K for the (a) CC and (b) DC. 450°C denotes the CC material heat-treated at 450°C for 2 hours

4.2.3 Texture

4.2.3.1 Texture Evolution in Anisotropic Deformation

$\{111\}$ pole figures of the undeformed and deformed CC samples at 4.2K for different tensile directions with respect to the previous rolling direction (RD) are shown in Figure 4.38. Before deformation, the annealed CC specimen contains a reminiscence of the rolling texture (Figure 4.38 (a)). The DC material retains the cube texture as well as the rolling texture as shown in section 4.1.6.

The texture of the specimen deformed in the 0° direction can be approximately described by an ideal $(1\bar{1}2)[\bar{1}11]$ orientation, and the high intensities at the north and south poles of the pole figure indicate that the tensile axis (TA) rotates toward $\langle 111 \rangle$ orientation (Figure 4.38 (b)). When the TA is perpendicular to the RD, the texture can be described by a $(\bar{1}\bar{1}0)[1\bar{1}2]$ orientation, and two strong intensities observed at the periphery in the TA indicate that grains tend to orient their $\langle 111 \rangle$ direction parallel to the TA (Figure 4.38 (d)). For the sample deformed at 45° to the RD, the texture cannot be described by any low index ideal orientation (Figure 4.38 (c)). However, the presence of the high intensity maxima observed at the periphery is close to the TA, which also indicates a rotation of the $\langle 111 \rangle$ direction of grains toward the TA.

With increasing tensile strain, intensity maxima are developed at the periphery of the $\{111\}$ pole figure in the TA direction for the 0° , 45° and 90° samples; Figure 4.39 shows these results for 90° CC and DC samples deformed at 4.2K. The intensity increases more rapidly above 19% at the periphery close to the TA direction. This indicates that the TA tends to be aligned with $\langle 111 \rangle$ orientation and the rotation of grains to $\langle 111 \rangle$ occurs more rapidly after 19%. The same trend was observed at

other temperatures and other directions. Discussion of the underlying mechanisms of this phenomenon is offered in section 5.1.4.

The pole figures of 0° , 45° and 90° directions show different texture patterns with respect to low index ideal orientations; the texture of the 45° sample cannot be described by any low index ideal orientation. In addition to these ideal orientations, orientation distribution functions also reveal a rotation of individual main components contained in the initial texture. For 0° and 90° , high intensity maxima are observed near $\langle 111 \rangle$ and $\langle 112 \rangle$ orientations in the RD, respectively (Figure 4.40). This indicates that the main components of the initial textures are rotated during deformation, and $\langle 111 \rangle$ and $\langle 112 \rangle$ axes of grains become parallel to the RD for 0° and 90° , respectively. The intensity increase in these texture components is observed with increasing strain (Figure 4.41). For the 45° orientation, similar to the 90° samples, it is often observed that the $\langle 112 \rangle$ axis of grains becomes parallel to the RD (Figure 4.42).

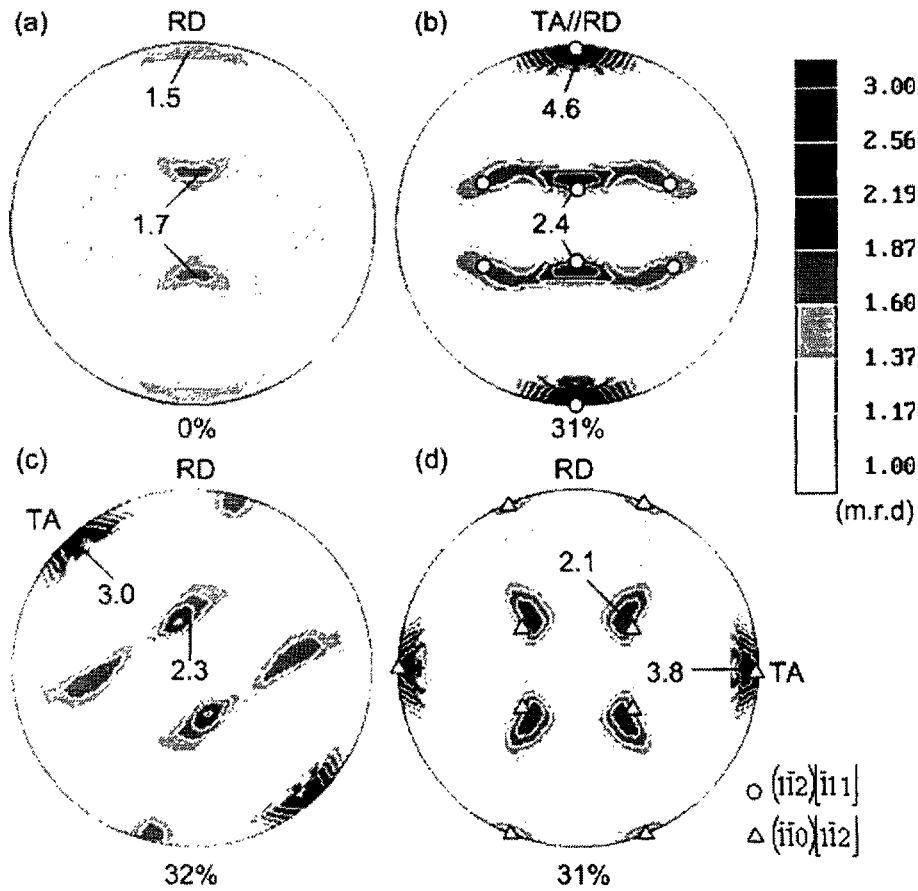


Figure 4.38: $\{111\}$ pole figures of CC samples undeformed (a) and deformed at 4.2K with the tensile axis TA at (b) 0° , (c) 45° and (d) 90° to the previous rolling direction RD

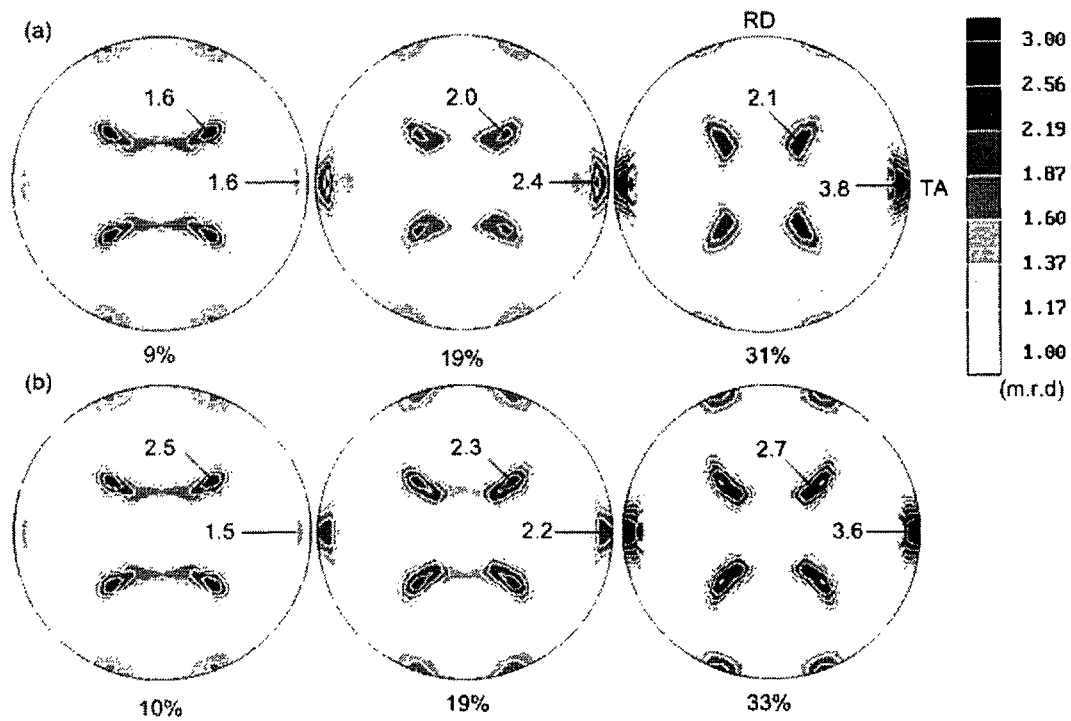


Figure 4.39: Evolution of $\{111\}$ pole figure during deformation at 4.2K for the (a) CC and (b) DC for the tensile axis at 90° to the previous RD

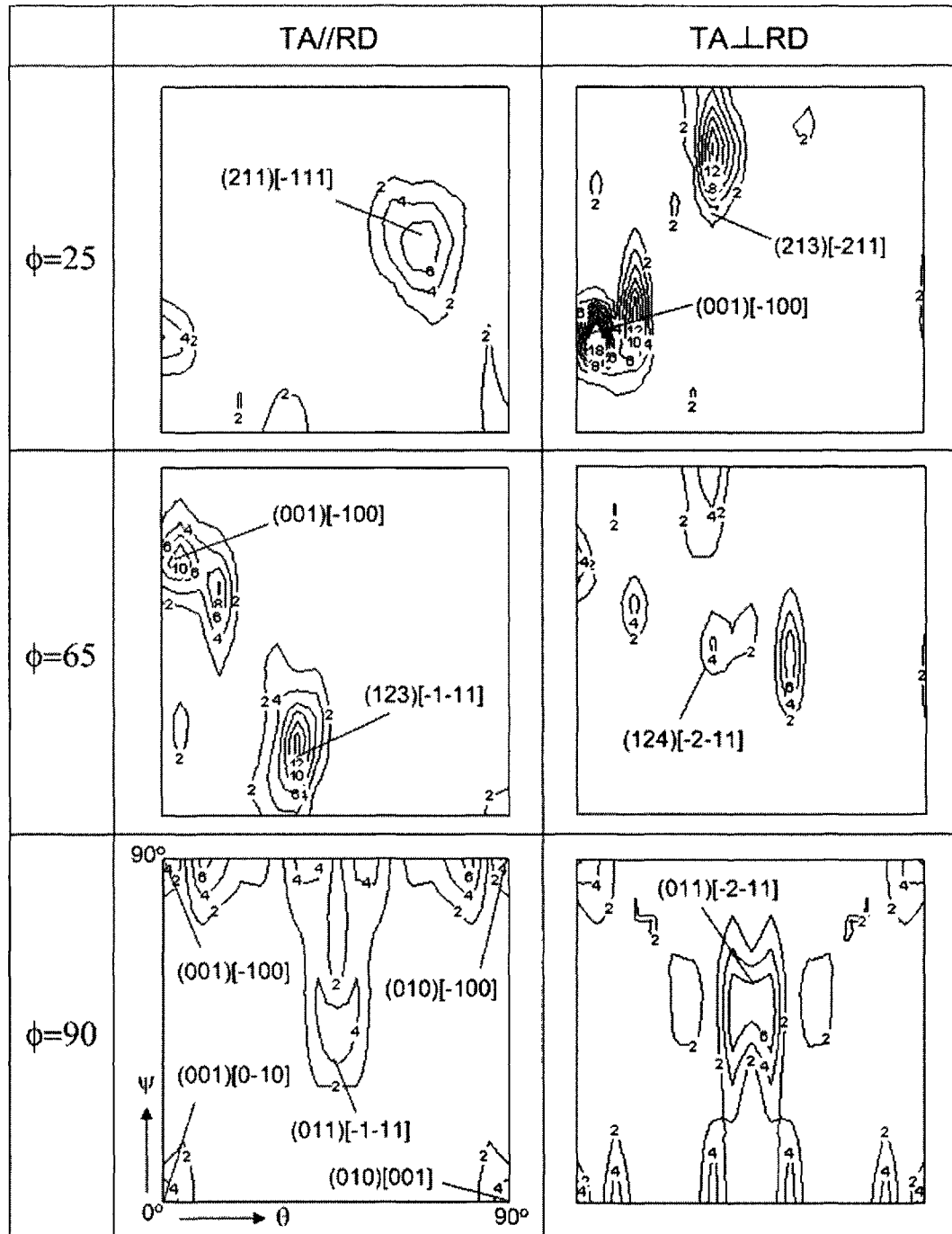
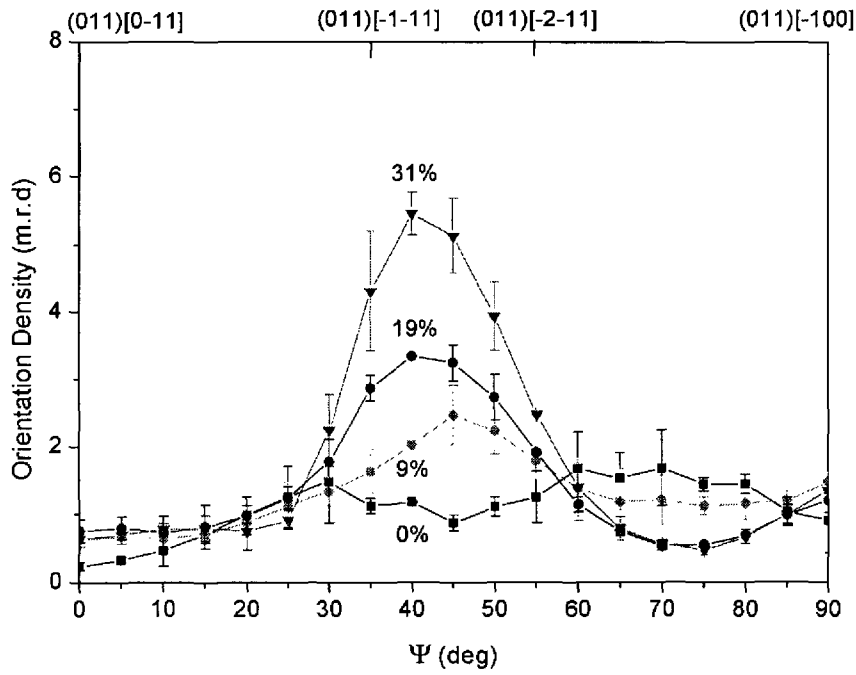
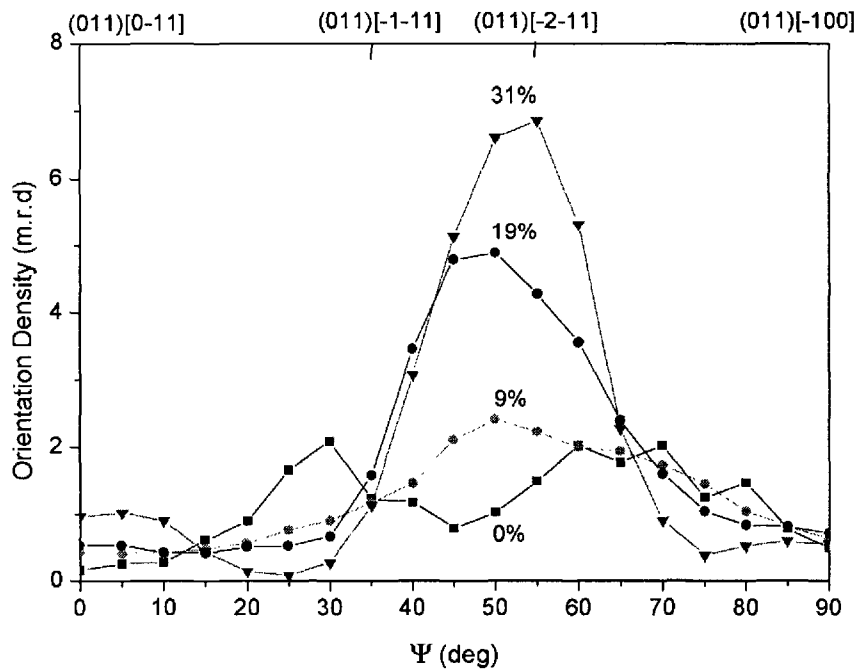


Figure 4.40: Selected sections ($\Phi = 25, 65$ and 90) of orientation distribution for the CC specimen after 31% deformation at 4.2K for the tensile axis at 0° and 90° to the previous RD



(a)



(b)

Figure 4.41: Orientation distributions at $\Phi = 90$ and $\Theta = 45$ for the tensile axis at (a) 0° and (b) 90° to the previous RD for CC specimens deformed at 4.2K

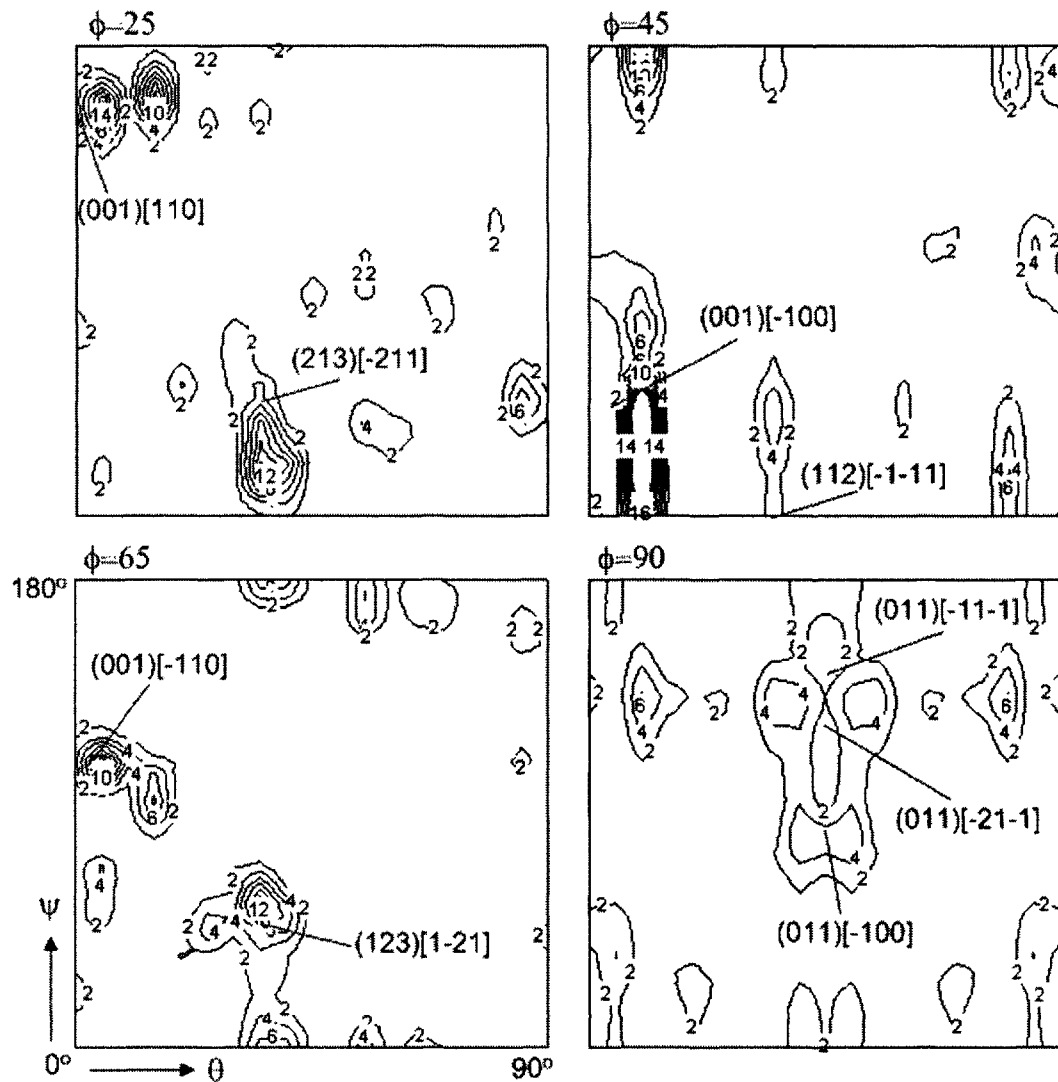


Figure 4.42: Selected sections ($\Phi = 25, 45, 65$ and 90) of orientation distribution for the tensile axis at 45° to the previous RD for CC specimens deformed 32% at 4.2K

4.2.3.2 Effect of Texture on Mechanical Anisotropy

Crystallographic texture is one of the major factors producing the mechanical anisotropy. It is well known that the tensile stress, σ , is related to a critical resolved shear stress, τ_c , through the Taylor factor, M :

$$\sigma = M\tau_c \quad (4.2)$$

A sheet material generally has non-random textures (i.e., the value of M varies), which results in directionality in yield stress and flow stress. In terms of the yield stress, the present materials do not exhibit a strong anisotropy, although they show the slightly lower yield stress in the 45° orientation. However, the directionality in flow stress is significant (Figure 4.33). In order to investigate the contribution of texture evolution to the directionality in flow stress, Taylor factors at various levels of strain (Figure 4.43) were calculated from experimental texture measurements using the Los Alamos Polycrystal Plasticity (LApp) code [138].

The evolution of the Taylor factor at every tensile direction shows very slow, or no, increase at the beginning of deformation and rapid increase at the later stage of deformation, where the microstructure is stable. This behaviour is related to the texture evolution mentioned in sections 4.1.6 and 5.1.4. Taylor factors for the 45° and 90° directions are lower than that for the 0° direction due to the effect of the initial texture. Detailed texture analyses will be presented in the following chapter. The measured flow stresses at strain of 20% show directionality at all temperatures (Figure 4.44 (a)). Normalizing these flow stresses at a strain of 20% with corresponding Taylor factors results in a constant flow stress independent of the tensile direction for 295K and 78K (Figure 4.44 (b)). This is verified statistically by the variance (Anova) analysis; details of Anova analysis are presented in Appendix A. These results strongly indicate that the anisotropy in flow stress between 0° , 45° and 90° directions arise solely from the differences in the texture for the 295K and 78K tests.

However, the normalization procedure does not completely account for the anisotropy observed at 4.2K, although one may expect that the crystallographic texture is also a major factor of the anisotropy at 4.2K.

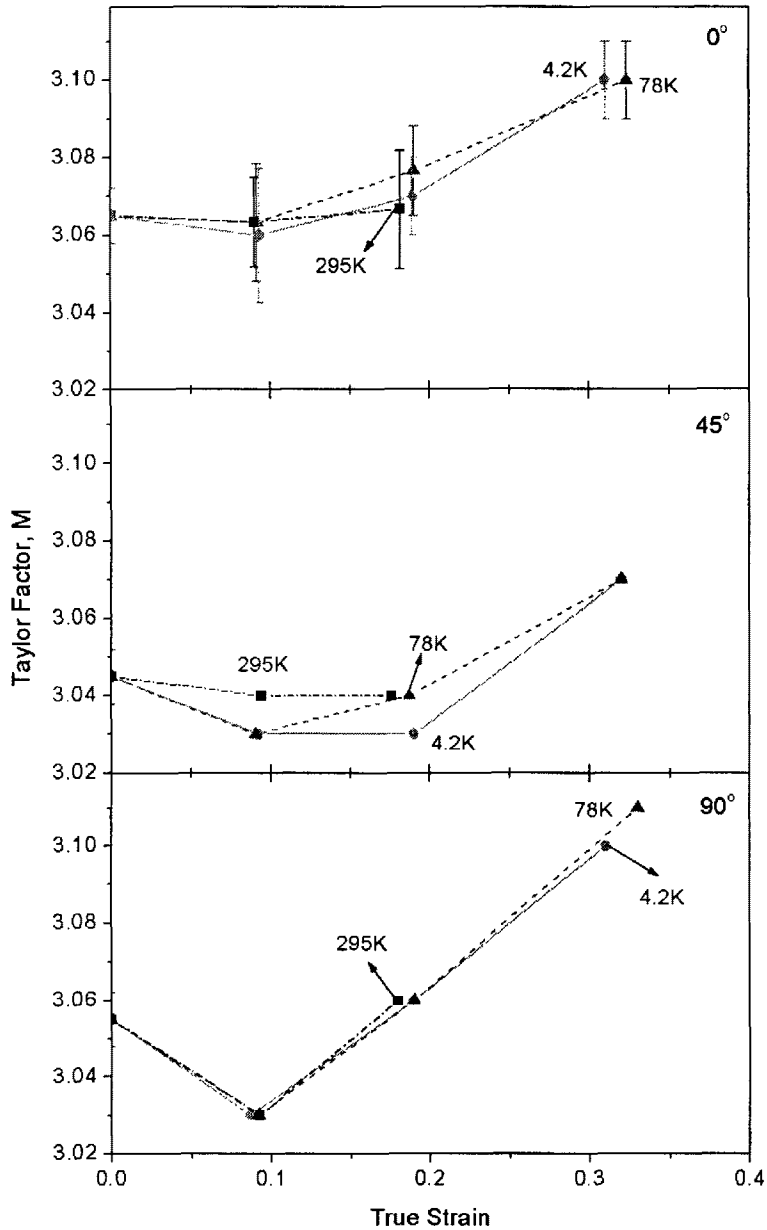
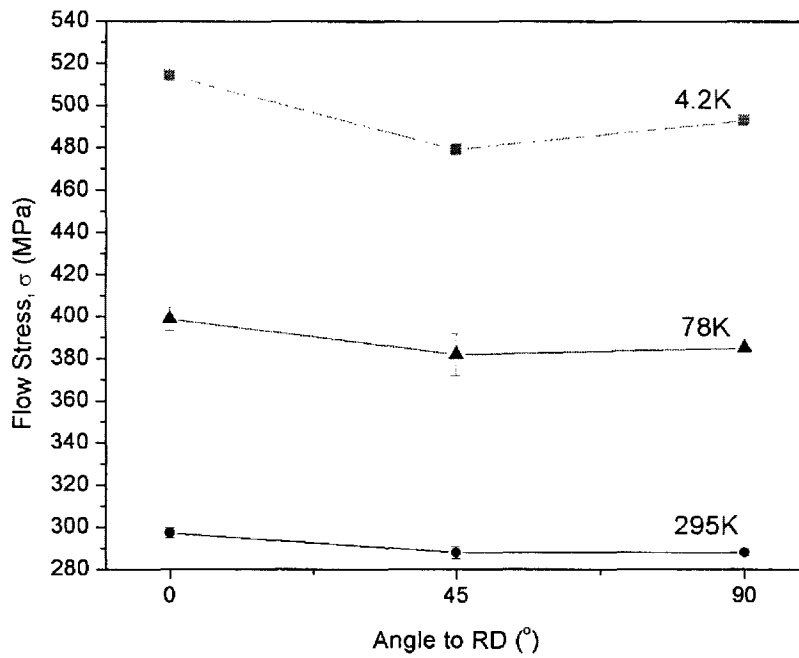
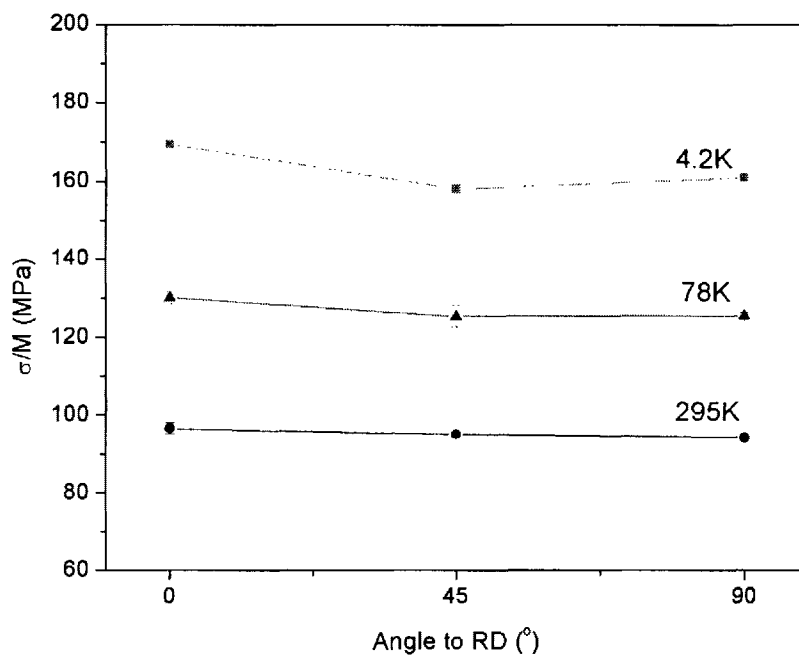


Figure 4.43: Evolution of Taylor factor during deformation for the CC at 0°, 45° and 90° angles to the previous rolling direction RD, respectively



(a)



(b)

Figure 4.44: Effect of the preferred crystallographic orientation on the flow stress: (a) angular variation of the flow stress σ and (b) the flow stress normalized by the corresponding Taylor factor (σ/M) at strain of approximately 20% for the CC alloy

Chapter 5

Discussion

5.1 Continuous Deformation

5.1.1 Mechanical Properties

Continuous cast aluminum alloys deformed at 4.2K and 295K exhibit plastic flow instabilities associated with two different processes operating during tensile deformation of the material. At room temperature, Portevin-LeChatelier (PLC) deformation is responsible for the serrated plastic flow of CC alloys. The magnitude of the serrations increases as strain increases. The PLC instabilities are classified into five different types A, B, C, D, and E [139]. The CC alloy shows B-type serrations through most of the plastic flow at 295K, with a small onset of type A instabilities observed at the early stage of deformation (Figures 4.1 and 4.2). As the strain rate decreases, more solute atoms diffuse to dislocations and the magnitude of stress drops (oscillation) increases (Figure 4.1). Present results agree with other studies of the Portevin-LeChatelier effect in Al alloys, published in the literature, e.g. [130].

Load instabilities at 4.2K arise from the thermomechanical instability in the substructure occurring during adiabatic shearing of the lattice. These processes have been studied in detail for various systems in the 1950's and 60's including pure metals [140, 141] and Al alloys [131, 132, 142]. When shear deformation initiates at low

temperatures due to the low thermal conductivity of the material, the heat generated during this process is localized in a small volume of the deformed specimen. Basinski [132] measured that during adiabatic deformation, the temperature of pure copper increases locally to 60K. One can expect that the local increase of the temperature in the CC sample during adiabatic shearing can be at least of this order of magnitude or higher. The localized heating produces softening of the substructure along the deformation path and leads to the shear localization on the length scale crossing a number of grain boundaries. The adiabatic deformation produces load drop instabilities associated with characteristic sound clicks and affects the work hardening behaviour of the material at 4.2K.

The adiabatic shear localization can also be initiated at a very high strain rate, where the time for the thermal diffusivity is short and the generated heat can not be dissipated in the volume of the material [143,144]. In samples deformed at a low strain rate, the heat per unit time generated by moving dislocations is lower and the local temperature increases slowly. Hence, the alloy deformed at 4.2K with a lower strain rate exhibits less frequent stress drops, whereas it shows extensive serrations with a high frequency of load drop at 295K, due to PLC deformation (Figure 4.1 (b)).

In comparison with Al alloys, pure Al shows a stable deformation at 4.2K because of the better thermal conductivity, which allows fast dissipation of the heat produced during the slip event. This is also reflected in work hardening characteristics of both materials (Figure 4.5), showing that the work hardening rate of the CC alloy at 4.2K decreases faster than that of pure Al, suggesting that the recovery rate is higher in alloy than pure metal. Such behaviour of the work hardening results from the adiabatic localized heating causing softening of the substructure and inducing shear localization, which increases the apparent recovery rate in CC alloy. In the absence

of adiabatic deformation, one can expect that the recovery rate in the CC material should be lower.

Present results reveal that a CC alloy deformed at 4.2K exhibits a remarkably high strength of the order of 700MPa just before the fracture (Figure 4.1). This is comparable to the strength level achieved in precipitation-hardened materials [133, 134]. Compared to those age-hardenable Al-Mg and Al-Zn-Mg alloys, the hardening rate of CC alloy at 4.2K is much higher in the wide range of flow stresses (e.g. Figure 4.5). It has been suggested that, in non-heat-treatable alloys, solute atoms lower stacking fault energy, therefore reducing dynamic recovery and enhancing work hardening capacity [78]. The strong hardening of CC alloy must be attributed to the influence of alloying elements present in the solid solution and it is evident, from the results shown in Figure 4.5, that this influence is particularly effective at low temperatures. Lloyd [73] studied mechanical properties and work hardening behaviours of a 5xxx series of Al-Mg alloys down to 85K and concluded that out of all elements present in these systems Mg inserts the strongest effect on the hardening behaviour through the solute drag contribution, which inhibits dislocation rearrangement and increases hardening rate.

With the exception of 4.2K, which will be discussed later, the work hardening decreases approximately at the same rate for both materials at 78K and slightly faster in pure Al than the CC at 298K (Figure 4.5), indicating that the solute atoms and impurities do not change substantially the kinetics of dynamic recovery processes at this temperature range. Thus, these processes must be governed by dislocation-dislocation interactions. As discussed previously, the higher recovery rate in the CC material at 4.2K compared to pure Al is a direct consequence of the adiabatic shear deformation, which produces substantial softening of the microstructure on the macroscopic scale and affects the work hardening behaviour of the alloy. To provide a

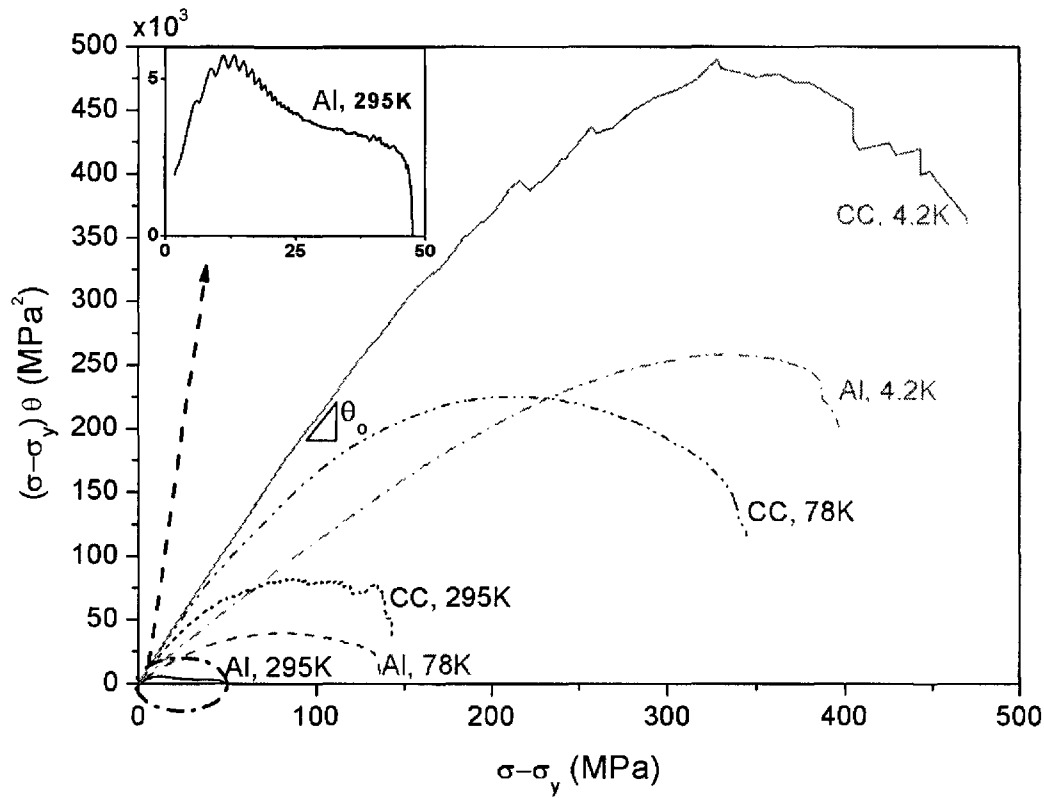


Figure 5.1: The effect of dislocation storage on the strain hardening of the CC alloy and pure Al, respectively. θ_0 is defined as the slope of a straight line through the origin in the region of linearity (see text for details).

more detailed picture of the storage mechanisms operating during deformation of CC alloy in comparison with pure Al, Figure 5.1 shows characteristic of $(\sigma - \sigma_y)d\sigma/d\varepsilon$ plotted as a function of effective flow stress, $\sigma - \sigma_y$. In the Kocks-Mecking description [38], the strain hardening rate is expressed in terms of two competing mechanisms: athermal storage of dislocations and dynamic recovery,

$$\theta = \theta_0 - \theta_r(\dot{\gamma}, T) = \theta_0 - k\tau \quad (5.1)$$

where θ is the macroscopic hardening rate, θ_0 is the athermal storage term of the strain hardening rate, θ_r is the dynamic recovery term, $\dot{\gamma}$ is the shear rate, T is

temperature, k is constant and τ is the shear stress. The rate of the work hardening decrease is proportional to k representing the rate of dynamic recovery. In the case of deformation of polycrystalline materials, one can write by application of the Taylor factor [38]:

$$(\sigma - \sigma_y) \theta = (\sigma - \sigma_y) [\theta_0 - \theta_r(\sigma, \dot{\epsilon}, T)] \quad (5.2)$$

where σ is the true tensile stress, σ_y is the yield stress, and $\dot{\epsilon}$ is the strain rate. The initial slope of the relationship (5.2) represents the athermal storage of dislocations, whereas deviation from linearity occurring at higher stresses indicates the onset of a dynamic recovery process. In the present experiments, θ_0 for Al is equal to about 1.3 (GPa), whereas for the CC alloy θ_0 is found to be equal to approximately 2.2 (GPa). θ_0 is thus almost exactly equal to $\sim E/50$ for pure Al and $\sim E/32$ for the CC alloy. The athermal storage term, θ_0 , is larger for the CC alloy than pure Al. This indicates that the CC alloy more effectively accumulates dislocations in the structure.

The athermal-storage contribution θ_0 is related to the dislocation mean free path, l , and dislocation density, ρ , through equation (5.3) [38]:

$$\theta_0 = \frac{\alpha \mu}{2l\sqrt{\rho}} \quad (5.3)$$

where μ is the shear modulus and α is constant. Referring back to Figure 5.1 and data at 4.2K, the CC alloy characteristically deviates from the linearity at the effective flow stress of approximately 70MPa-80MPa, whereas pure Al does so at about 80MPa-100MPa, corresponding to average stored dislocation densities of approximately $5 \times 10^{13} m^{-2}$ and $3 \times 10^{14} m^{-2}$, respectively (Figure 4.8 (b)). TEM observations reveal independently that at this deformation stage both materials develop a relatively homogeneous dislocation substructure. One can estimate that the average dislocation mean free path calculated based on the equation (5.3) is approximately equal to $0.3 \mu m$ for pure Al and $0.6 \mu m$ for the CC alloy. This is much smaller than the initial grain size of these materials ($600 \mu m$ Al and $14 \mu m$ CC alloy) and much larger than the

average distance between solute atoms in the glide plane of the CC alloy $\sim 1.5\text{nm}$. In case of pure Al, the dislocation mean free path corresponds rather closely to the size of the cell structure produced after large deformation. More detailed discussion of this aspect of the present work will be provided later in section 5.1.3. However, based on the above estimate, one can conclude that the dislocation-dislocation interactions (not dislocation-grain boundaries or dislocation-particle or dislocation-solute interactions) are important in the dislocation storage in these materials. The dislocation mean free path corresponds relatively closely to the size of the observed cell structure in pure Al, which indicates that dislocation storage occurs on cell walls, and therefore processes occurring within the cell walls determine the rate of the dynamic recovery in this metal at least at the low temperature regime.

After a certain amount of plastic deformation, $(\sigma - \sigma_y)d\sigma/d\varepsilon$ curves (Figure 5.1) develop a negative curvature. At 4.2K, the downward curvature occurs at approximately the same flow stress of about 350MPa for both pure Al and the CC alloy, corresponding to average dislocation density of approximately $5 \times 10^{15} m^{-2}$ (Figure 4.8). Although not confirmed, it is unlikely that the point at which these curves turn down is associated with the development of any form of damage process, because it occurs relatively far below the ultimate tensile strength of these materials. The alternate possibility is that some accelerated recovery is taking place in the substructure, initiated at a dislocation density of the order of $4 \times 10^{15} m^{-2}$. It is noted that at higher temperatures (e.g., 78K) dynamic recovery occurs much earlier in pure Al than the CC alloy. This implies that the CC material is more resistant to this process, which intensifies after more advanced deformation than in pure Al.

TEM observations reveal that, at the flow stress of 300-350MPa, Al develops a well defined cell structure whereas the CC produces a relatively homogeneous, Taylor-like dislocation arrangement. It is estimated that the relative volume fraction of the cell

walls to the cell interiors in pure Al is approximately 30% to 70%, whereas the density of dislocations stored in the walls relative to the dislocation density inside the cell is in the ratio 10:1 (Figure 4.26 (c)). Assuming that the simple rule of mixture applies i.e.:

$$\rho_T = f\rho_w + (1 - f)\rho_i \quad (5.4)$$

where ρ_T is the total dislocation density stored in the material, ρ_w is the dislocation density stored in the wall, ρ_i is the dislocation density stored in the cell interior and f is the volume fraction occupied by the cell walls. One can estimate that the downward curvature of $(\sigma - \sigma_y)d\sigma/d\varepsilon$ curves or the accelerated dynamic recovery occurs in Al when the dislocation density in the wall and the cell interior are approximately: $\rho_w = 1.1 \times 10^{16} m^{-2}$ and $\rho_i = 1.1 \times 10^{15} m^{-2}$. As mentioned previously for CC alloys, this process occurs at the average dislocation densities $\sim 4 \times 10^{15} m^{-2}$. These figures correspond to the average dislocation spacing in the CC alloy of the order of 16nm and approximately 10nm and 30nm in the wall and inside the cell of pure Al, respectively. It is seen that the dynamic recovery intensifies when the spacing between dislocations approaches 10-15nm, indicating that similar fundamental processes operate for the dislocation annihilation in pure Al and the CC alloy.

It will be of interest to apply the same approach to estimate the average dislocation spacing in both materials at the point of fracture. In this case, the dislocation densities are approximately $\rho_w = 1.9 \times 10^{16} m^{-2}$ and $\rho_i = 1.9 \times 10^{15} m^{-2}$ in the cell wall and the cell interior of pure Al and $\sim 1.5 \times 10^{16} m^{-2}$ in the CC alloy. This represents the average dislocation spacing in the CC alloy of the order of 8nm and approximately 7nm and 23nm in the wall and inside the cell of pure Al, respectively. It is striking that the average dislocation spacing in the CC alloy and in highly dislocated walls of Al correspond very well to each other. This may indicate that, independent of the composition of the system, the fracture is initiated by some form of dislocation

collapse occurring in the areas where the dislocation densities approach a critical level or a critical spacing for spontaneous annihilation. It is estimated that this spacing for Al and the CC alloy is between 7-8nm at 4.2K.

In pure Al deformed at 78K, the total dislocation density at the fracture is $\sim 1.8 \times 10^{15} m^{-2}$ (Figure 4.8). The volume fraction of the cell walls to the cell interiors is approximately 20% to 80%, and the similar 10:1 ratio is taken for the density of dislocations stored in the wall relative to cell interior in Al deformed at 78K (Figure 4.26 (b)). The dislocation densities, ρ_w and ρ_i , are thus approximately: $\rho_w = 6.4 \times 10^{15} m^{-2}$ and $\rho_i = 6.4 \times 10^{14} m^{-2}$, which represents an average dislocation spacing of 12nm and 39nm in the wall and inside the cell of pure Al at 78K. It is not attempted to evaluate these figures for Al deformed at 295K or for alloys as they would be subjected to a large error.

5.1.2 Mechanism of Plastic Deformation

Haasen characteristics show that one mechanism of plastic deformation operates during deformation of pure metal and also in the Al alloys studied in this work (Figure 4.6). A Haasen plot of pure Al deformed at room temperature passes through the origin, suggesting that the flow stress is determined by dislocation-dislocation interactions and obeys the Cottrell-Stokes law, which is also confirmed by Figure 4.7. A good linear relationship between the activation volume and the effective flow stress (Figure 4.7) indicates that Cottrell-Stokes law holds at low temperatures as well as room temperature because it implies that $\tau_e V'$, where τ_e is the effective flow stress and V' is the activation volume, is independent of strain, which is known as the modified Cottrell-Stokes law [145]. The deviation from the linearity for the alloy in Figure 4.7 is usually attributed to the effect of impurities on the short-range stress

which gives rise to a high solute-dislocation component [48]. Pure Al shows a slightly negative intercept at lower temperatures in the Haasen plot (Figure 4.6), which again suggests that its substructure provides a more strain rate sensitive component for the flow stress than forest dislocation interactions. This athermal component may arise from the nature of the dislocation substructure produced at low temperatures, characterized by the higher volume (fraction) of the cell walls, comprising a higher dislocation content and larger misorientations across the walls.

The y-axis intercepts of the Haasen plot for alloys are always higher than for pure Al, due to the presence of solute atoms in the aluminum matrix, which provide a larger thermal component to the flow stress. If more solutes precipitate as in the case of DC alloy, the thermal contribution decreases and the value of y-intercept is lower. This will also suppress or eliminate Lüders deformation as observed experimentally in Figure 4.1 (c). Therefore, it is not surprising that the CC alloy, containing more alloying contents in the solid solution than the DC alloy due to the effect of the thermomechanical process, shows the higher positive intercept on the Haasen plot. At the same time, the CC alloy annealed at 450°C, indicated as CC4 in Figure 4.6, shows a lower thermal component than our reference the CC material annealed at 350°C. It also shows the lower yield stress, but the work hardening behaviour of these two specimens is the same (Figure 4.2 and Section 5.1.5). This is attributed to two possible factors: one related to the grain size difference and the second to the composition of the matrix. The strain rate sensitivity of the material is very sensitive to the compositional change; small changes in the solid solution are immediately visible on the Haasen characteristic of the material [51]. However, optical observations reveal that, with the exception of the grain size, there is no substantial difference in the nature, the size or distribution of precipitates present in CC samples annealed at 450°C and 350°C. This suggests that the larger grain size of the sample annealed at a higher

temperature affects the yield stress and should lower the thermal component of the flow stress, as observed experimentally. It is also interesting to note that the y-axis intercept of CC alloys is close to the one of solution treated AA6111 [134]. This indicates that both materials are characterized by a similar strength of obstacles, which provides a similar thermal component to the flow stress during thermal activation. When fine precipitates are formed in aged AA6111, the thermal component is even larger than observed in solution treated material [134].

5.1.3 Electrical Resistivity and Microstructure

5.1.3.1 Continuous Deformation

Analyses of the electrical resistivity data for pure Al and Al alloys show that the following relationship between the effective flow stress and the total dislocation density holds up to large stresses:

$$\sigma - \sigma_y = M\alpha Eb\rho^n \quad (5.5)$$

where E is the Young modulus; b , the Burgers vector; M , the Taylor factor ~ 3.01 ; α , a constant; and n , another constant. Figure 5.2 plots log of the effective flow stress as a function of the log of the dislocation density, i.e. $f(\log(\sigma - \sigma_y)) = \log(\Delta\rho)$ for different materials. The slope of this figure gives a value of the exponent, n , in equation (5.5), which varies between pure Al, Al alloys and deformation temperature (Figure 5.2). The n values determined from the linear regression analysis are given in Table 5.1.

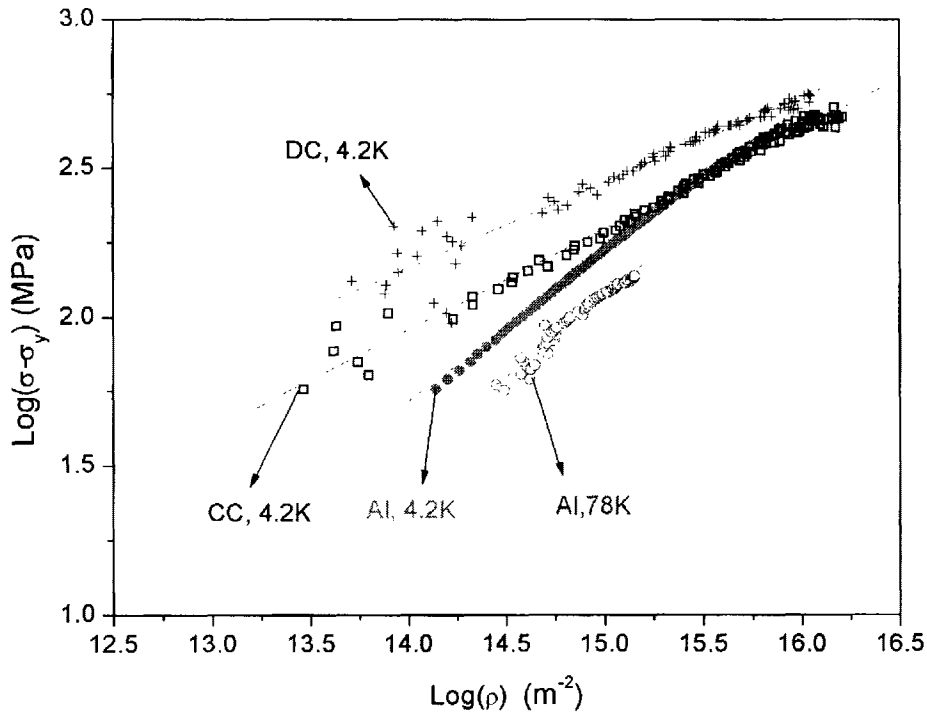


Figure 5.2: Flow stress as a function of the total dislocation density for Al, CC and DC alloys. Slopes of these relationships give values of the exponent n in relationship given by equation (5.5). The n values are 0.54, 0.5, 0.34, 0.29 for Al deformed at 78K and 4.2K, the CC alloy deformed at 4.2K and the DC alloy deformed at 4.2K, respectively (see the text for details). Linear regression lines are also included in the figure.

Table 5.1: Values of the fitting parameters n , k_1 , and k_2 to equations (5.5) and (5.6)

Materials	Al(78K)	Al(4.2K)	CC(4.2K)	DC(4.2K)
n	0.54	0.5	0.34	0.29
k_1	2.52×10^8	4.22×10^8	8.12×10^8	7.07×10^8
k_2	2.24	1.10	0.40	0.10

Pure Al deformed at 4.2K shows that the flow stress is proportional to the square root of the total dislocation density, i.e. $\sigma \sim \rho^{1/2}$ (e.g. [40]). The CC and DC alloys exhibit substantial deviations from this relationship with the n exponent equal to 0.29 and 0.34 for DC and CC alloys, respectively (Table 5.1). It is important to emphasize that equation (5.5) reflects the relationship between the total dislocation density stored in the materials during deformation at 4.2K and the flow stress. It has been shown in section 4.1.4 that the total dislocation density produced during deformation at 4.2K has two components: one contributes to the flow stress and resistivity (unrecoverable defects) and the other contributes only to the electrical resistivity (recoverable defects) in the case of low temperature deformation of pure Al. One can thus expect that, after accounting for these two dislocation density components, n values that correspond to the relationship between the density of unrecoverable defects and the flow stress will be different from those given above. Basinski and Basinski [146], after compiling various data available in the literature, reported for pure copper the following relationship: $\tau \sim \rho^{0.43}$ between the flow stress and the dislocation density, which is attributed to the effect of other obstacles such as impurities on the flow stress.

Let us now discuss in more detail the evolution of electrical resistivity (total dislocation density) in pure Al. For a given flow stress, the resistivity change of Al at 4.2K is lower than at 78K (Figure 4.8 (b)). This indicates that, in order to support a given stress, a higher dislocation density must be stored in the material at higher temperatures (see also Figure 5.2). This reflects the strength of the obstacle structure that a given dislocation distribution exerts on the mobile dislocations during plastic flow. It is clear that the dislocation network produced at 78K provides weaker obstacles than the network developed at 4.2K, so that more defects are required to resist the glide of mobile dislocations at the same stress level.

The strength of the obstacle structure is reflected in the values of the activation area shown in Figure 4.7. It is seen that the activation area at 78K is larger than at 4.2K indicating that dislocations can more easily overcome the obstacles. On the other hand the activation area of the CC alloy at 78K resides close to the range of the one of pure Al at 4.2K, which suggests that, at the same temperature, the CC alloy develops stronger and more stable obstacle structure than Al, in agreement with mechanical characteristics.

The evolution of the dislocation mean free path in Al and Al alloys is obtained from the variation of dislocation density with strain (Figure 4.8 (a)) according to the expression $\bar{l} = \frac{M}{b \frac{d\rho}{d\varepsilon}}$, where M is the Taylor factor ~ 3.01 , b is the Burgers vector, ρ is density of dislocations and ε is the true strain [38]. Figure 5.3 shows the dislocation mean free path as a function of effective flow stress. For materials deformed at 4.2K the mean free path decreases exponentially, and for the DC and CC alloy, it stabilizes at the value of $0.1\mu\text{m}$ at the fracture. In the case of pure Al deformed at 4.2K and 78K, the mean free path at the point of fracture is equal to $0.4\mu\text{m}$ and $1.5\mu\text{m}$, respectively. It is interesting to note that at 78K the mean free path decreases roughly linearly with the stress, which suggests that plastic deformation of aluminum at 78K is controlled by different kinetics of storage and recovery than at 4.2K.

For comparison with the present results, Figure 5.3 includes the dislocation mean free path for a nominally pure Al with the grain size of $3.2\mu\text{m}$ deformed at 78K, as reported by other author [147]. It is seen that the initial dislocation mean free path for $3.2\mu\text{m}$ Al is approximately $1.6\mu\text{m}$, whereas our value is about $3.5\mu\text{m}$. Interestingly, the measured mean free path in the present study is a factor of only about 2 higher than the literature data, although the grain size of pure Al ($600\mu\text{m}$) in the present study is more than 180 times larger. This indicates that the dislocation mean free

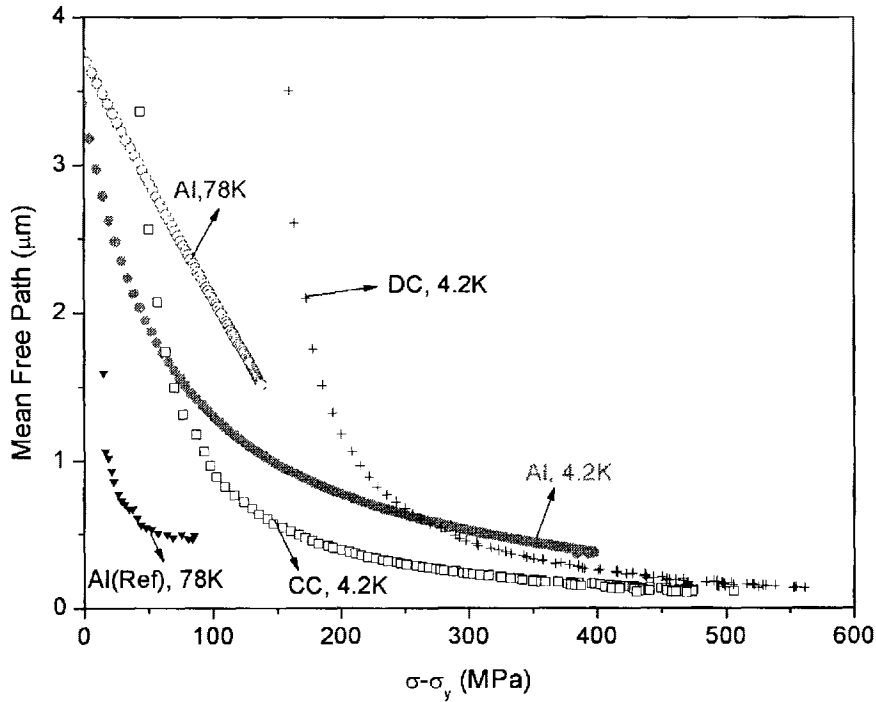


Figure 5.3: Evolution of the dislocation mean free path for CC and DC alloys deformed at 4.2K and Al deformed at 4.2K and 78K. Al(Ref) denotes the mean free path for nominally pure Al deformed at 78K, taken from the literature [147].

path of pure Al deformed at 78K is governed by dislocation-dislocation interactions and not by dislocation-grain boundary interactions.

The mean free path of dislocations determined from electrical resistivity measurements shows a very good agreement with the scale of the dislocation substructure produced during deformation as seen by TEM. In the case of pure Al deformed at 4.2K, the mean free path of $0.4\mu\text{m}$ at the fracture corresponds to the size of the cell structure, which indicates that cell boundaries provide a significant rate of dislocation storage. In Al alloys, on the other hand the dislocations are stored quasi-homogeneously in the volume and the mean free path reflects the spacing between obstacles, i.e. forest dislocations within the dislocation network.

As the mean free path decreases and the density of dislocation increases, dynamic recovery plays a more important role during plastic deformation. This process has been discussed in section 5.1.1 based on the behaviour of the work hardening rate, and it was concluded that at temperatures of 78K and 298K the kinetics of dynamic recovery of pure Al and Al alloy is very similar and that it seems to be controlled by the dislocation annihilation occurring within highly dislocated areas of the substructure. The electrical resistivity results can provide insight into these processes occurring at 4.2K. As known, the evolution of the dislocation density with strain has commonly been assumed to be represented by the sum of two contributions. One contribution is proportional to the square root of the dislocation density associated with the hardening storage rate, and another contribution is proportional to the dislocation density associated with the recovery rate. The rate of dislocation density change with strain is thus expressed as:

$$\frac{d\rho}{d\varepsilon} = k_1\sqrt{\rho} - k_2\rho \quad (5.6)$$

where k_1 is the constant representing the work hardening rate, and k_2 is another constant proportional to the rate of dynamic recovery. In the present work these contributions have been determined by fitting the relationship of $\frac{d\rho}{d\varepsilon} = f(\rho)$ with $k_1\sqrt{\rho} - k_2\rho$. The experimental data points and fits are shown in Figure 5.4, and constants k_1 and k_2 are given in Table 5.1. For pure Al, the constant k_1 increases as the temperature decreases from 78K to 4.2K and is higher for CC and DC alloys than pure Al. These results, in addition to the hardening characteristics discussed in section 5.1.1, give direct evidence that the work hardening component of the flow stress is larger in Al alloys than in pure Al. On the other hand, Table 5.1 shows that for pure Al, the k_2 value is larger at 78K than at 4.2K and that k_2 in Al alloys is lower than in pure metal. This indicates that annihilation of dislocations occurs with a higher rate at higher temperatures where the thermal energy is available, whereas

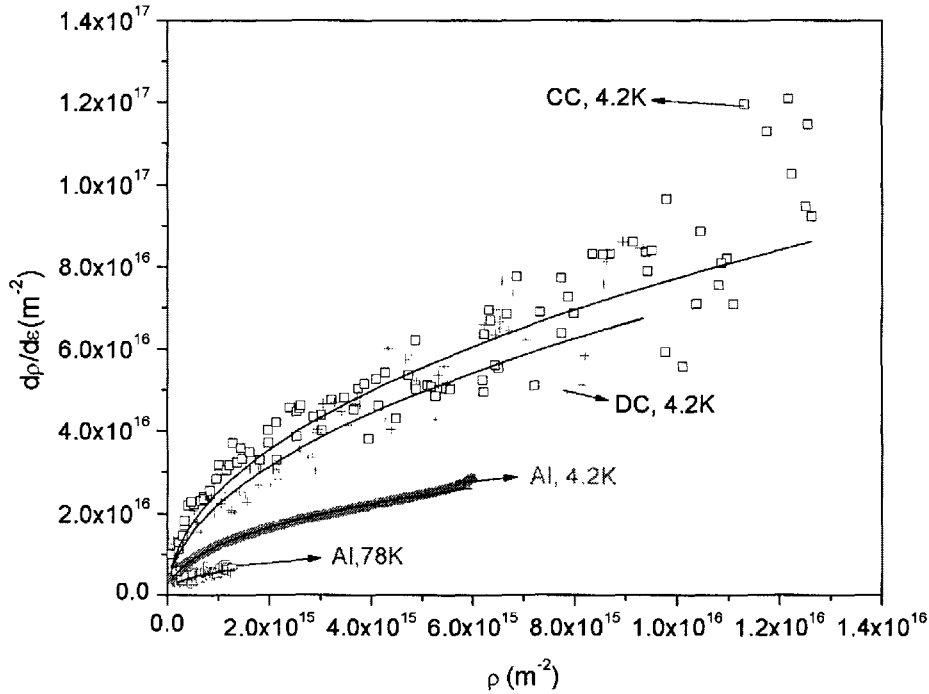


Figure 5.4: Rate of the dislocation density change with the strain $\frac{d\rho}{d\varepsilon}$ as a function of the dislocation density ρ . The characteristics are fitted to the rate equation $\frac{d\rho}{d\varepsilon} = k_1\sqrt{\rho} - k_2\rho$ with k_1 and k_2 constants given in Table 5.1. Both the experimental data points (symbols) and the fitting curves (lines) are shown in the graph.

these processes are slowed down in Al alloys. This is attributed to the effect of solute atoms, which increase the dislocation storage capacity and suppress dynamic recovery, possibly through their influence on the stacking fault energy, affecting the nature of the dislocation structure produced in these materials. It should be emphasized here that the above analysis reflects changes occurring entirely within the dislocation substructure without regard to the macroscopic deformation behaviour of the materials. As discussed in section 5.1.1, the work hardening characteristic of the CC alloy at 4.2K (Figure 4.5) gives a higher apparent recovery rate than in pure Al, as a result of adiabatic deformation. One can see that electrical resistivity data are insensitive

to this effect, as the signal arises from the integrated defect content in the sample, which does not decrease during adiabatic shearing.

5.1.3.2 Fracture

In all materials studied, fracture occurs reproducibly within a narrow range of strength, work hardening rate, dislocation density and the dislocation mean free path characteristic for a given material and deformation temperature. The fracture surface observations reveal that all materials undergo ductile fracture by the nucleation and growth of voids. In the case of Al alloys, failure is not particle-stimulated and particles seem to have a weak influence on ductility. From the work hardening characteristics (Figure 4.5), it can be deduced that, at 4.2K, fracture in Al alloys occurs far before the work hardening capacity is exhausted, i.e. before the Considere criterion is met. Therefore, there must be a mechanism that triggers the nucleation of voids and leads to the material failure. In section 4.1.1, it was shown that CC samples exhibit the largest elongation at 78K where both Portevin-LeChatelier and adiabatic deformation are suppressed. This suggests that these processes facilitate the premature necking and fracture of samples. The literature provides a considerable amount of data suggesting that PLC deformation has a detrimental effect on ductility, e.g. [24, 148, 149].

There is much less data available regarding the effect of adiabatic deformation on deformation behaviour and fracture. Present results reveal that the adiabatic deformation affects the macroscopic work hardening rate of the alloys, and although it may aid in nucleating strain localization, adiabatic shear is not a primary cause of the fracture. This is concluded from the fact that the homogeneous elongation of the sample deformed with a higher strain rate, where the adiabatic deformation

operates very intensively, is not lower than the elongation of samples deformed at a lower strain rate (Figure 4.1).

TEM observations show that there are significant differences in the nature of the dislocation substructure developed in Al and Al alloys. The intriguing feature is that the average spacing between dislocations within highly dislocated areas at the point of fracture is represented by the same figure in both Al and Al alloys. Thus, it seems that the failure occurs when a certain dislocation density limit or a critical dislocation spacing is achieved in the substructure to allow for spontaneous annihilation of dislocations and global collapse of the dislocation network in these areas. Estimated is a critical dislocation spacing of about 8nm in Al and Al alloys at 4.2K and \sim 12nm in pure Al at 78K. These figures correspond well to Brown's theoretical estimations of critical height for the athermal collapse of dislocation dipoles in copper [150].

Destabilization of the dislocation substructure at stresses, as these developed before the fracture, will cause persistent flow localization in softened volumes of the material and will lead to nucleation of voids, their growth and eventually necking and failure. Assuming that voids form in highly dislocated areas (e.g. cell walls in Al), this should produce a fracture surface with a high density of small dimples at low temperatures as there are many places where voids will nucleate. In contrast, the coarser scale of the substructure developed at higher temperatures provides less potential sites for the void nucleation. Thus there will be fewer voids formed; consequently, a few voids with the large size eventually dominate in the fracture surface. This is reflected in the nature of the fracture surface produced in Al and Al alloys at 295K, which is filled up predominantly with a few large dimples (Figures 4.3 and 4.4).

5.1.3.3 Intermittent Annealing

Resistivity measurements in samples deformed at 4.2K and annealed at room temperature show that the total resistivity consists of recoverable and unrecoverable components (Figures 4.13 and 4.14). The amount of resistivity annealed out at a given strain is independent of the number of anneals; i.e., the amount of resistivity of a specimen annealed out by one intermediate anneal to a given strain is the same as the total resistivity annealed out by several intermediate anneals to the given strain. It is also observed that the resistivity after anneal increases at the same rate as the resistivity increase of the continuously deformed sample without an intermediate anneal (Figures 4.11 and 4.12). This implies that defects responsible for the total annealable resistivity are generated at the same rate during deformation, regardless of whether or not those defects are removed by intermediate anneals.

The other salient feature of these results is that up to 30% yield stress drops are observed when the deformation resumes after an anneal at room temperature (Figure 4.9). The magnitude of the flow stress drop is independent of the number of anneals (Figure 4.10). This indicates that the defects which are removed during anneal contribute both to electrical resistivity and also partially to the flow stress, and they are created at the same rate independently of whether they are produced continuously or periodically removed by an intermediate anneal. The most widely accepted explanation of the nature of annealable defects is that these are point defects; for example, it was argued that short vacancy dipoles annealed out by pipe diffusion account for annealable resistivity in Cu single crystals [59]. However, the flow stress is not influenced by the annealable defects in Cu, in contrast to what is being observed in Al. The isochronal annealing curve (Figure 4.15) shows that almost 60% of deformation induced resistivity anneals from the substructure below 200K. This suggests

that short-circuit diffusion is responsible for this annealable resistivity, because bulk vacancies are immobile below 200K [59].

Both the recoverable and the unrecoverable fractions of the total resistivity increase; the former increases parabolically with the true strain/stress, and the latter increases linearly. The fraction of the recoverable resistivity in the total resistivity is approximately 90% at the fracture, which is much larger than reported fraction of 40-60% in Cu single crystal [59]. Although the results of this work on Al and previous results on Cu single crystals [59] cannot be quantitatively compared, present observations indicate that the point defects are not the only species contributing to the annealable portion of electrical resistivity in aluminum when it is annealed at room temperature. The anneal of only point defects is not sufficient to account for the large flow stress drop (up to 30%) and increase in ductility. Thus, more than 30% of recoverable resistivity, which anneal out between 4.2K and 295K, must be attributed to other defects or processes such as annihilation of debris and possibly also recrystallization. This conclusion is supported by the following arguments; if one assumes that recoverable resistivity arises only from vacancies which anneal out from the structure, the vacancy concentration generated at higher strains would be of the order of 6.7×10^{-4} (1% of vacancies in the unit volume of the material contributes $\sim 1.5 \times 10^{-6} \Omega cm$ to resistivity [151], then $1 \times 10^{-7} \Omega cm$ in Figure 4.13 gives a concentration of vacancies $C_V \sim 6.7 \times 10^{-4}$). This is even larger than the concentration of vacancies in liquid Al, which indicates that other defects and phenomena must be taken into consideration.

TEM observations reveal evidence of recrystallization occurring in pure Al during annealing at room temperature. Figure 5.5 shows the microstructure of the sample with two intermittent anneals up to the point of fracture (approximately 45% of strain). Recrystallization is occasionally observed near grain boundaries; e.g. the

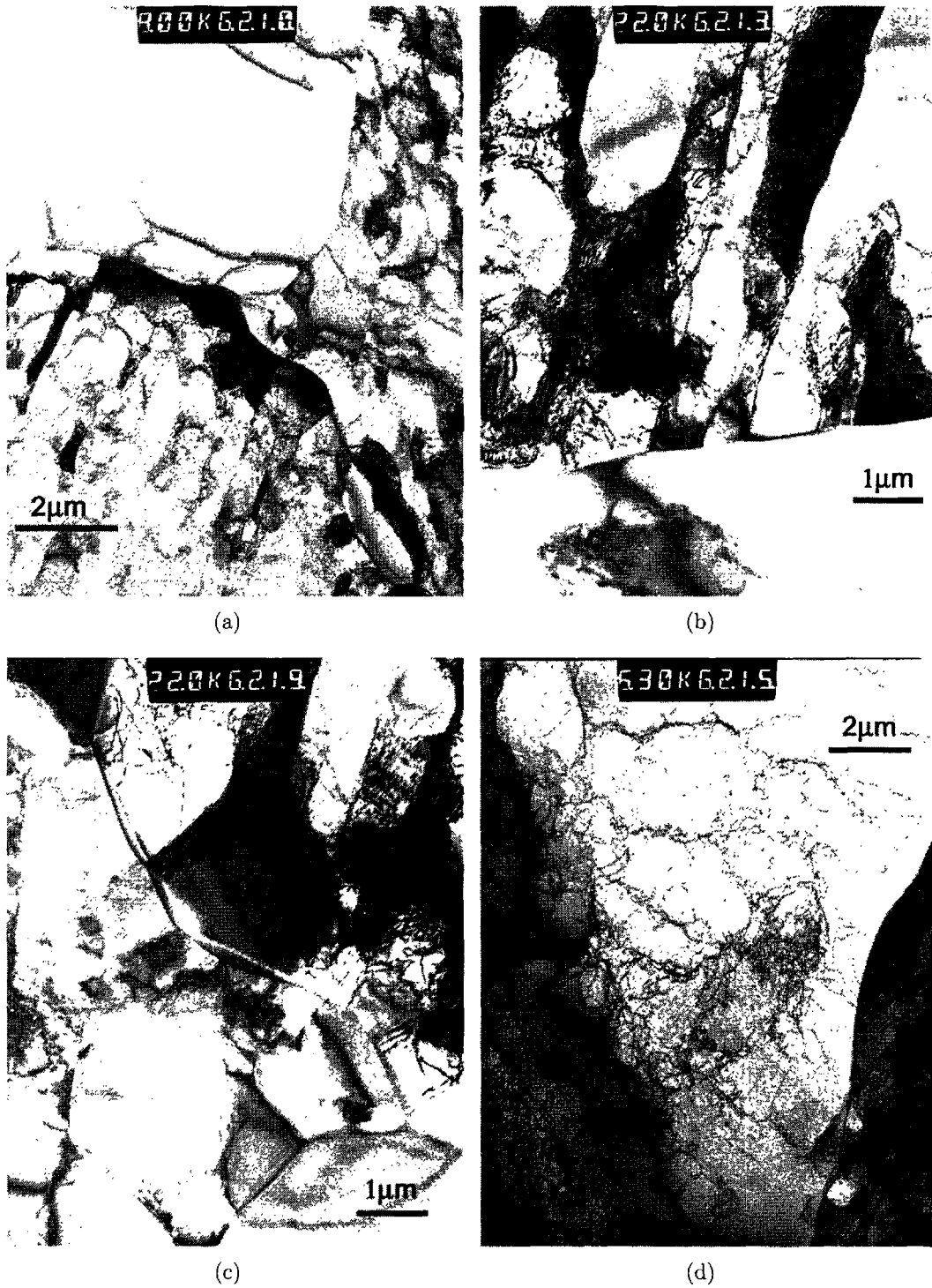


Figure 5.5: Microstructure of the two intermittent annealed sample of pure Al (after fracture)

grain in the top left hand corner in Figure 5.5 (a), the bottom grain in Figure 5.5 (b), the grain in the bottom left hand corner in Figure 5.5 (c), and the left side of Figure 5.5 (d) show features of static recrystallization. Since annealing and reloading were repeated on the sample, new cell structures developed on reloading are occasionally observed inside the recrystallized grains (Figure 5.5 (b), (c), and (d)). The size of dislocation cells verifies that the dislocation cells inside the recrystallized grain are developed after reloading. The cells range from 1.5 to 3.5 μm and are larger than those produced during continuous deformation. For the continuous deformation, the scale of the subgrains ranges between 0.2-0.7 μm for 43% deformed pure Al at 4.2K (Figure 4.26). The size of the cell structure generally decreases as mentioned in chapter 2; e.g. it reduces from 2 μm to 1.3 μm when Al is strained from 10% to 30% at room temperature [83]. Static recovery of the dislocations in both the cell walls and cell interiors occurring during annealing at room temperature contributes to the development of the cell structure, which is much larger than the one observed in the continuous deformation at the equivalent strain and temperature (Figure 5.5).

Based on microstructural observations, one can conclude that the large flow stress drops observed in Al in this study are caused by the recrystallization that occurs during an anneal. The flow stress drop after an anneal was also observed in pure Mg by other authors [152]. The homologous temperature, $T_h = T/T_m$, (T is the annealing temperature and T_m is the melting temperature) for Al is equal to 0.32. It is 45% higher than that for Cu for which $T_h=0.22$; T_h of Mg is close to the one of Al. Although $T_h = 0.32$ is considered to be below the recrystallization temperature of materials, one observes that the static recrystallization occurs in Al (presumably also in Mg) during the annealing process at room temperature. This indicates that the dislocation density, which is stored in the structure at 4.2K, is sufficient to de-

velop a driving force to induce grain boundary motion at room temperature, in effect, producing not only the flow stress drop but also the increase in ductility (Figure 4.9).

5.1.4 Texture

5.1.4.1 Initial Texture

Texture of undeformed CC and DC alloys reflects their thermomechanical processing history, which includes continuous or direct chill casting, hot and cold rolling and subsequent annealing. These processes influence the formation of precipitates [153], and the size and distribution of these precipitates determine the annealing texture in AA5457 alloys [6]. It has been reported that materials containing fine (below $1\mu\text{m}$) precipitates do not develop recrystallization (annealing) texture, but rather inherit components of previous deformation (rolling) texture after annealing. This process is called “continuous recrystallization” to reflect the fact that there is no abrupt change of texture during annealing. On the contrary, materials with coarse precipitates generally produce cube or rotated-cube textures, resulting from particle-stimulated recrystallization, termed “discontinuous recrystallization” [6, 75].

TEM observations reveal that a CC material in an undeformed state contains a low volume fraction, less than 3%, of relatively small precipitates/particles of random distribution, occasionally agglomerated in strings along rolling direction (Figure 4.25). During annealing, the CC alloy undergoes the “continuous recrystallization” preserving components of deformation texture inherited from the previous cold-rolling process (Figure 4.27 (a)). However, the character of the texture changes if the annealing temperature is higher. This is evident by comparing textures of the CC sample annealed at 350°C and at 450°C . It is seen that specimens annealed at 350°C show

relatively strong reminiscence of previous deformation texture (Figure 4.27 (b)). On the other hand, specimens annealed at 450°C exhibit features of the rotated cube texture, in transition from deformation to annealing texture (Figure 4.27 (c)).

TEM observations, not shown here, reveal that the DC material contains larger particles than the CC alloy. However, overall particle density is low in DC alloys. These large particles act as nucleation sites for “discontinuous recrystallization” and promote development of a cube or rotated cube texture, a common feature of annealed DC materials [6]. Because the volume fraction of the second phase particles is low and the annealing temperature was not sufficiently high, the texture of DC samples does not transform fully to annealing texture (Figure 4.27 (d)). As a result, the material inherits a mixture of two texture components, i.e. deformation texture and the cube, or near cube, components of annealing texture (Figure 4.27 (d)).

5.1.4.2 Texture Evolution

Diffraction data reveal that the tensile axis of deformed CC and DC samples rotates towards either $\langle 111 \rangle$ or $\langle 100 \rangle$ orientation during plastic deformation. The development of $\langle 111 \rangle$ and $\langle 100 \rangle$ fiber textures in the CC material deformed at 4.2K is clearly seen on inverse pole figures calculated from the ODF in Figure 5.6. Savoie and co-workers [121] have shown that the strength of these two texture components after deformation depends on the orientation density of the initial texture; the higher initial intensity at $\langle 111 \rangle$ and/or $\langle 100 \rangle$ produces the higher resultant intensity at these orientations after deformation. Present results agree with these studies and show that the CC alloy annealed at 450°C develops relatively low intensity of $\langle 111 \rangle$ orientation after deformation at room temperature. On the other hand CC samples preserving stronger components of the rolling texture after annealing at 350°C develop the strong

intensity of $\langle 111 \rangle$ peaks after the same amount of tensile deformation (Figure 4.29). These effects are clearly visible in a local orientation distribution (Figure 4.32(a)) showing that the intensity of $(123)[\bar{1}\bar{1}1]$ in the sample annealed at 450°C is lower than in sample annealed at 350°C .

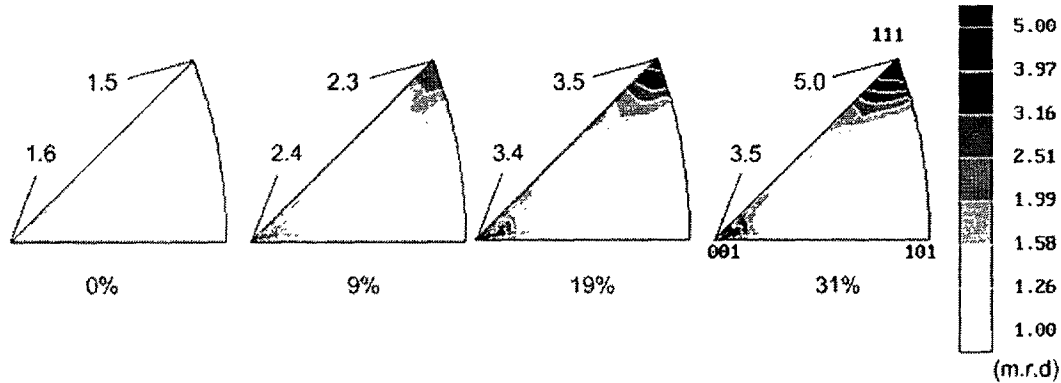


Figure 5.6: Inverse pole figures for tensile axis of the CC specimen deformed at 4.2K after different amount of deformation, revealing a rotation of tensile axis to either $\langle 111 \rangle$ or $\langle 001 \rangle$ orientation.

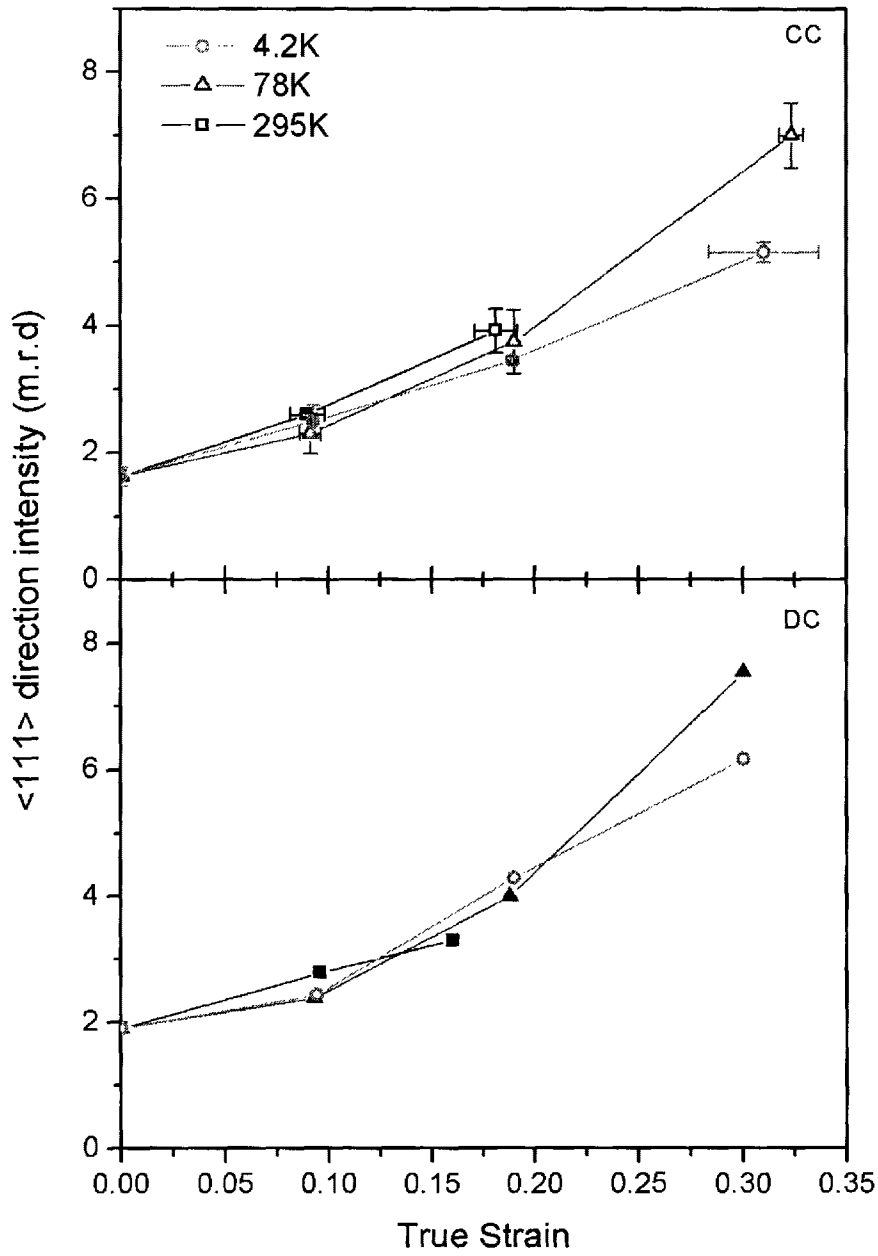
In section 4.1.6, it was shown that in both CC and DC alloys texture changes rapidly after about 19% of the tensile strain (Figures 4.28, 4.31, and 4.32). During the early stage of the plastic flow, the dislocations are stored quasi-homogeneously in the volume of a sample, and the dislocation mean free path decreases rapidly [78,79]. Homogeneous deformation of a polycrystalline aggregate requires that different grains deform in a compatible way and are subjected to relatively homogeneous shape and dimensional changes. As deformation proceeds, larger misorientations develop in the substructure and the texture evolution becomes more sensitive to the nature of the dislocation structure produced in a material [104]. Other authors have shown that the type of texture produced in pure Al depends upon the size and the morphology of dislocation cells, which provide boundaries limiting the dislocation glide [124]. Indeed it is seen that the size of the cell structure in pure Al is closely related to the dislocation

mean free path (section 5.1). Al-Mg alloys develop relatively homogenous dislocation substructures at 4.2K, 78K and 295K. The dislocation mean free path is determined by the spacing between forest dislocations within the dislocation network; for the CC alloy deformed at 4.2K and 78K to larger strains, the dislocation mean free path has been estimated approximately $0.6\mu\text{m}$ (section 5.1.3). In the present experiments, the fast evolution of texture in CC and DC materials initiates at the stage where the dislocation mean free path after initial decrease attains a pseudo-plateau. At 4.2K this occurs at the effective stress of approximately 300MPa - 400MPa and strain of about 20% (section 5.1.3). Results of electrical resistivity measurements (section 5.1.3) show that, at this stage of deformation, more dislocations are generated per unit time and consequently they contribute to faster texture changes.

Figure 5.7 shows the evolution of intensities determined from inverse pole figures (e.g. Figure 5.6) for both $\langle 111 \rangle$ and $\langle 100 \rangle$ orientations as a function of true strain at three different temperatures. The results indicate that the intensity increase scales with amount of deformation experienced by the material, and the intensity increase is faster in $\langle 111 \rangle$ than $\langle 100 \rangle$ orientation. DC and CC samples deformed to larger strains at 4.2K exhibit generally lower intensity of $\langle 111 \rangle$ and/or $\langle 100 \rangle$ peaks, and this indicates that rotation of the lattice is slower than in material deformed at higher temperatures.

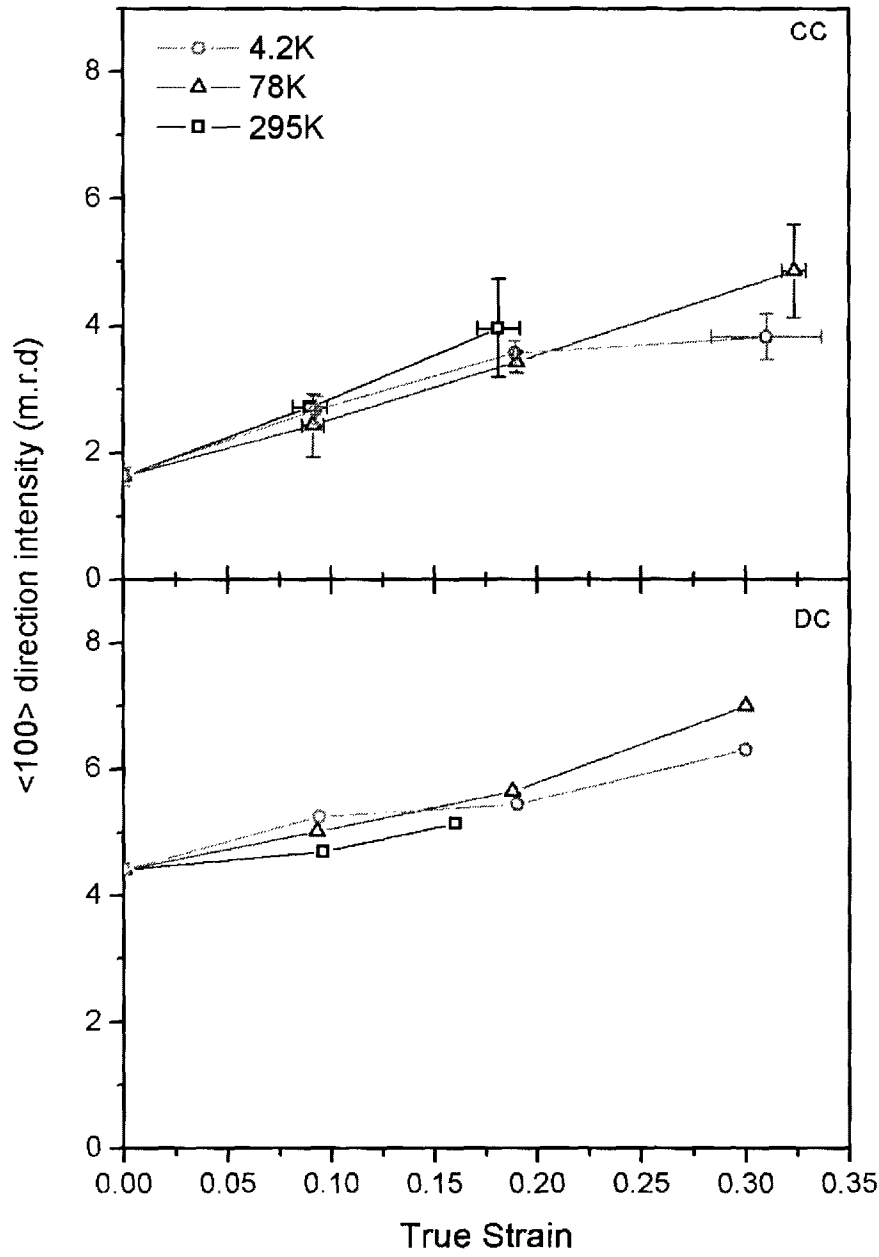
To examine the effect of the dislocation substructure on the peak intensity, the strengths of $\langle 111 \rangle$ and $\langle 100 \rangle$ orientations at different temperatures are plotted as a function of the effective flow stress ($\sigma - \sigma_y$), as shown in Figure 5.8. It is seen that the intensity increase of $\langle 111 \rangle$ orientation is substantially larger than this observed in $\langle 100 \rangle$ peaks. This and the characteristic observed in Figure 5.7 indicate that $\langle 111 \rangle$ orientation is the stable end orientation formed during tensile deformation whereas $\langle 100 \rangle$ is the metastable one. Other results showed that $\langle 111 \rangle$ is the characteristic

end orientation also in pure Al, whereas non-heat-treatable Al-4.4%Mg (AA5182) alloys develop relatively both $\langle 111 \rangle$ and $\langle 001 \rangle$ stable end orientations during tensile deformation [124]. As discussed earlier, after recrystallization during annealing, the DC material develops a cube texture with the intensity of $\langle 100 \rangle$ orientations much higher than $\langle 111 \rangle$ (Figures 4.38, 5.7, and 5.8); it is seen in Figures 5.7 and 5.8 that the initial intensity of $\langle 100 \rangle$ is much higher than $\langle 111 \rangle$. However, even in this case the intensity of $\langle 100 \rangle$ peaks after deformation is lower than $\langle 111 \rangle$, which supports the view that $\langle 100 \rangle$ is the metastable end orientation formed during tensile deformation of this alloy.



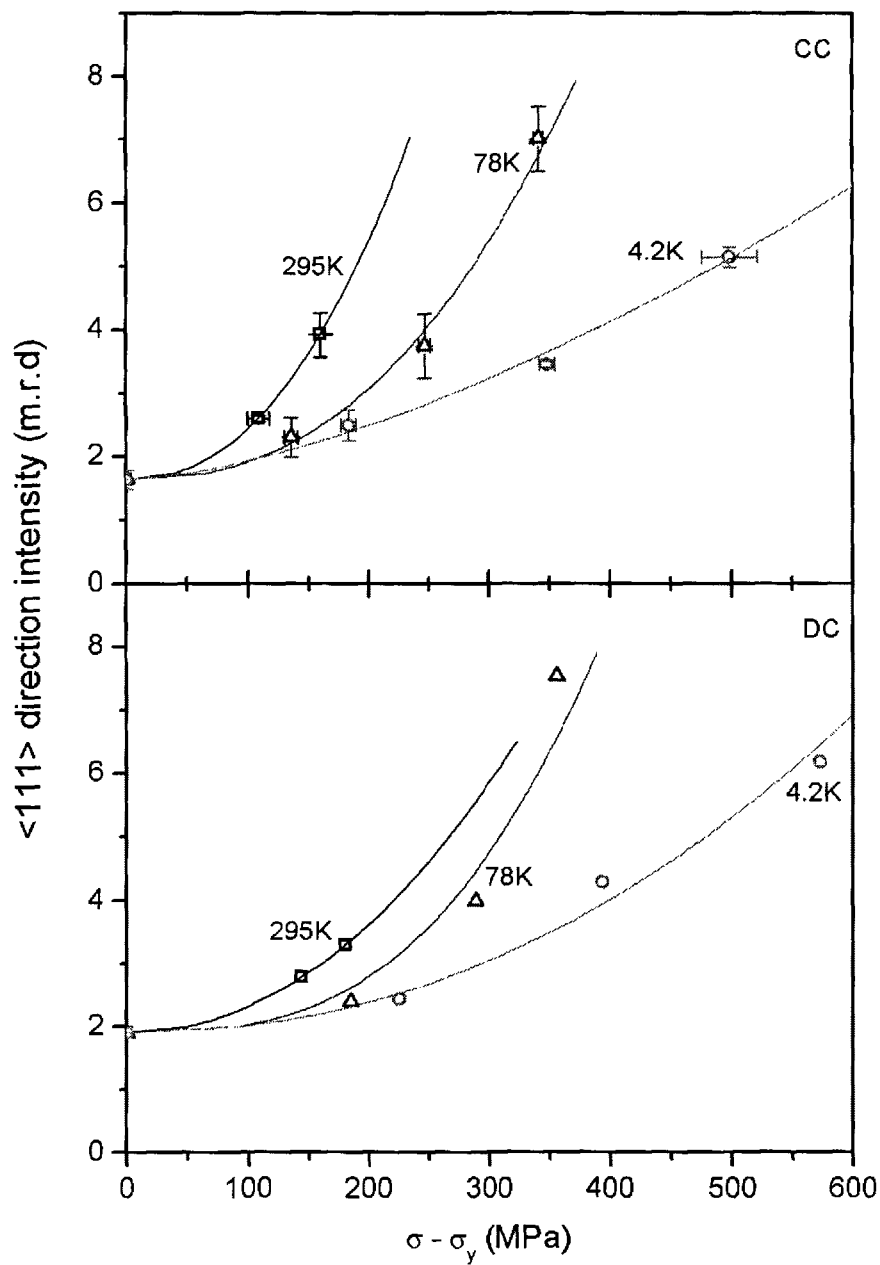
(a)

Figure 5.7: Effect of temperature on intensities of (a) $\langle 111 \rangle$ and (b) $\langle 001 \rangle$ peaks parallel to the tensile axis of CC and DC samples as a function of true strain (cont'd)



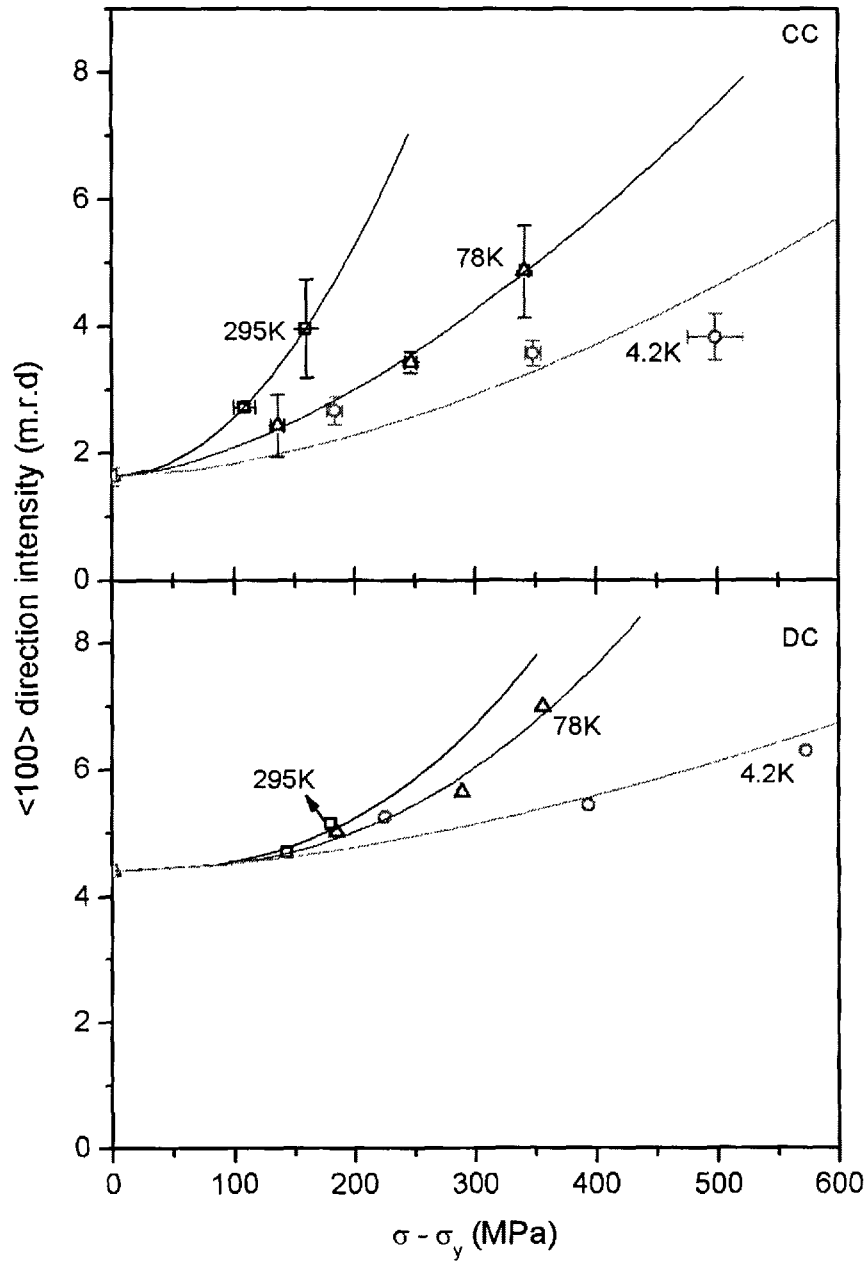
(b)

Figure 5.7: (cont'd)



(a)

Figure 5.8: Effect of temperature on intensities of (a) $\langle 111 \rangle$ and (b) $\langle 001 \rangle$ peaks parallel to the tensile axis of CC and DC samples as a function of effective stress. The fitting curves are also included on the graphs (cont'd)



(b)

Figure 5.8: (cont'd)

5.1.4.3 Stable End Orientation

Dependence of the intensity on the flow stress shown in Figure 5.8 suggests that the intensity of the stable orientations should correlate with the dislocation density and also with the work hardening of the material. The experimental data in Figure 5.8 are fitted to the polynomial equation of type:

$$\sigma - \sigma_y = \beta(I - I_o)^w \quad (5.7)$$

where $(\sigma - \sigma_y)$ is the effective flow stress, I is the intensity of the stable end orientation, I_o is the initial intensity of the stable end orientation, both β and w are constants. The fitting curves are shown in Figure 5.8 for CC and DC alloys and fitting parameters are given in Table 5.2. It is seen that constants w are in the range of 0.40 - 0.65. For many Al alloys deformed at room temperature, the flow stress and the dislocation density satisfy the well known relationship [38, 41]:

$$\sigma - \sigma_y = M\alpha_1\mu b\rho^{1/2} \quad (5.8)$$

Table 5.2: I_o , β , and w values in equation (5.7) used to fit experimental data in Figure 5.8

			$I_o(\text{m.r.d})$	β	w	R^2
$\langle 111 \rangle$	CC	295K	1.63	110	0.45	1.0
		78K	1.63	172	0.42	0.998
		4.2K	1.63	221	0.65	0.997
	DC	295K	1.9	153	0.49	1.0
		78K	1.9	195	0.40	0.976
		4.2K	1.9	281	0.47	0.996
$\langle 100 \rangle$	CC	295K	1.63	104	0.51	1.0
		78K	1.63	164	0.63	0.999
		4.2K	1.63	258	0.60	0.944
	DC	295K	4.41	215	0.40	0.991
		78K	4.41	245	0.42	0.995
		4.2K	4.41	360	0.60	0.963

where σ_y , ρ , μ and b are the yield stress, dislocation density, shear modulus and the Burgers vector, and α_1 is the constant. Comparing equation (5.8) with equation (5.7) at 295K, one can see that the intensity increase of $\langle 111 \rangle$ and $\langle 100 \rangle$ orientations scales approximately proportionally to the dislocation density ρ , or more precisely as $\sim \rho^{1.11}$ and $\sim \rho^{1.02}$ for $\langle 111 \rangle$ of the CC and the DC, respectively. For the particular case of deformation of CC and DC materials at 4.2K, it was found from electrical resistivity measurements (section 5.1) that the flow stress of the CC alloy is expressed in terms of dislocation density as: $\sigma - \sigma_y = M\alpha_1\mu b\rho^{0.34}$, whereas, for the DC alloy, $\sigma - \sigma_y = M\alpha_1\mu b\rho^{0.29}$. Taking appropriate values of w from Table 5.2 at 4.2K, one finds an intensity increase of $\langle 111 \rangle$ peaks scales as $\sim \rho^{0.52}$ and $\sim \rho^{0.62}$ for CC and DC alloys. The same estimation reveals that intensity of $\langle 100 \rangle$ peaks scales as $\sim \rho^{0.57}$ and $\sim \rho^{0.48}$ for CC and DC alloys, respectively. If the relationship between intensity of the diffraction peaks, I , of the stable orientations and the dislocation density ρ is expressed by the power equation of the form: $I \sim \rho^n$, the above figures suggest that the exponent n in this equation increases as deformation temperature increases. It would be interesting to investigate if a similar trend is also preserved at temperatures higher than 300K.

Now discussed is the effect of deformation temperature on the behaviour of the stable end orientation. Present results show that, as the deformation temperature decreases, an equivalent level of intensity at $\langle 111 \rangle$ and/or $\langle 100 \rangle$ peaks corresponds to a higher value of the flow stress, which is achieved after approximately the same amount of tensile deformation experienced by the material (Figure 5.8). At the initial stage of plastic flow specimens deformed at different temperatures show the same intensity change of main texture components, suggesting that the texture evolves with the same rate. On the other hand, at larger deformations, the texture produced at 78K or 295K is sharper than that developed at 4.2K; this is evident by inspecting Fig-

ures 4.31, 4.32, 5.7, and 5.8. This indicates that the rotation of the tensile axis of the sample toward the stable orientation induced by the crystallographic slip is somewhat suppressed at lower temperatures. This feature must be related to the nature of the dislocation substructure produced at low temperatures, its strength as an obstacle structure for other dislocations, and its resistance to recovery both under dynamic and static conditions. Hansen and co-workers [104] reported that the misorientation across the geometrically necessary boundaries forming a cell-block structure increases as strain increases. Such structures promote inhomogeneous deformation inside individual grains; different slip systems are activated in different cell-blocks producing local misorientations and texture scattering between grains, so that no sharp texture is formed.

CC and DC alloys deformed at 4.2K develop substructure consisting of dislocations with different Burgers vectors generated by multislip, which form stable Taylor-like dislocation networks, a typical configuration of materials with low stacking fault energy [79,154]. This substructure provides strong forest obstacles for new dislocations, which attempts to cut through this network but are immediately trapped in the lattice. This suppresses the rate of the lattice rotation induced by the slip systems operating in individual grains. On the other hand, the very high density of dislocations stored in the material introduce substantial bending of the lattice planes, which contributes to the broadening of the intensity distribution of the diffraction peaks and results in development of less sharper texture, as observed in samples deformed at low temperatures.

The behaviour of the work hardening of CC and DC alloys (Figure 4.5) supports above arguments. It has been observed that due to more effective dynamic recovery, the rate of decrease of work hardening in these materials occurs faster at higher temperatures. In order to maintain the constant strain rate, the annihilation of

mobile dislocations must be balanced by the generation of new dislocations during plastic flow. These dislocations operate on the larger length scale and are stored in less homogeneous fashion in the structure, producing sharper texture at higher temperatures.

5.1.5 Texture Modeling

In an attempt to validate the experimental results and to study the work hardening behaviour in response to crystallographic orientations of grains, a viscoplastic self-consistent (VPSC) simulations [13] were performed using a discretized form of the experimental texture as input containing 1022 orientations; the detailed methodology of VPSC modeling is described in Appendix C. In order to predict the macroscopic stress-strain behaviour based on the given orientations of a polycrystal, the modified Voce hardening equation of single crystal was used as follows:

$$\tau = \tau_0 + (\tau_1 + \theta_1 \Gamma) \left(1 - \exp \left(-\frac{\theta_0 \Gamma}{\tau_1} \right) \right) \quad (5.9)$$

where τ is the critical resolved shear stress (CRSS) for $\langle 111 \rangle \langle 110 \rangle$ and Γ , τ_0 , $(\tau_0 + \tau_1)$, θ_0 and θ_1 are the applied strain, the initial CRSS, the back-calculated CRSS, the initial hardening rate and the asymptotic hardening rate, respectively. These parameters can be directly related to the macroscopic stress-strain behaviour [155]. First, the relation between the macroscopic stress S and the critical shear stress τ is given using the Taylor factor M :

$$S = \overline{M\tau} \quad (5.10)$$

where bar denotes averaging the grains overall.

Then, the hardening behaviour is obtained by taking the derivative of equation (5.10) with respect to the macroscopic strain E :

$$\frac{dS}{dE} = \overline{\frac{dM}{dE} \tau} + M \overline{\frac{d\tau}{dE}} \quad (5.11)$$

substituting the macroscopic strain increment dE in the equation (5.11) with the sum of shears per grain $d\Gamma$:

$$dE = \frac{\overline{d\Gamma(E)}}{\bar{M}} \quad (5.12)$$

and the equation (5.11) becomes:

$$\frac{dS}{dE} = \theta \bar{M}^2 \quad (5.13)$$

where θ is the strain hardening rate for grains.

From equations (5.10) and (5.13), the yield stress, the back-calculated stress, the initial work hardening rate and the asymptotic hardening rate in the macroscopic stress-strain curve can be directly related to the microscopic hardening law in equation (5.9), and expressed by $\tau_0 \bar{M}_{(0)}$, $(\tau_0 + \tau_1) \bar{M}_{(\infty)}$, $\theta_0 \bar{M}_{(0)}^2$ and $\theta_1 \bar{M}_{(\infty)}^2$, respectively ([155], appendix C).

For the simulation of the tensile deformation of alloys used in this study, published data of single crystal hardening parameters [156] were adjusted in order to fit to the experimental tensile curves at 295k, 78K and 4.2K. Figures 5.9 and 5.10 show the experimental and simulated stress-strain responses, the single-crystal parameters used for these simulated curves are given in Table 5.3.

Table 5.3: Single crystal hardening parameters of the modified Voce hardening equation used to fit experimental data with VPSC methodology (units of MPa)

Material	Test Temp. (K)	τ_0	τ_1	θ_0	θ_1
CC	295 (450°C anneal)	48	90	520	18
	295 (350°C anneal)	54	90	520	18
	78	59	90	627	125
	4.2	70	100	627	220
DC	295	48	90	630	20
	78	55	90	627	125
	4.2	62	100	617	230

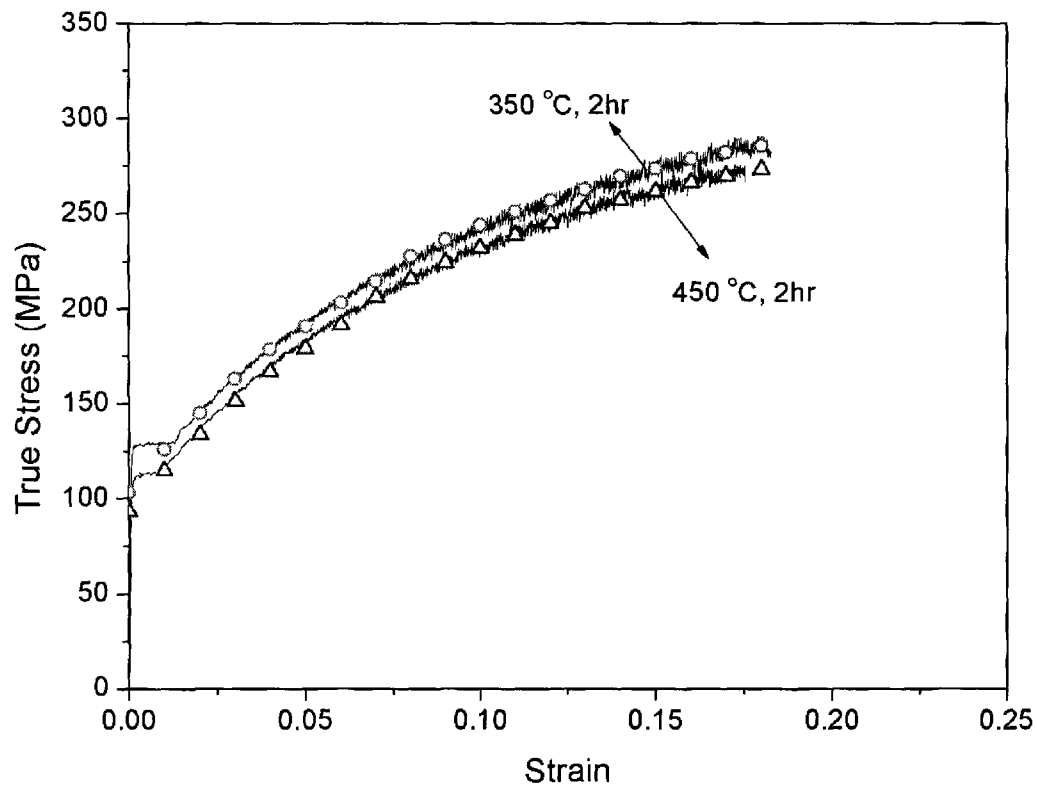
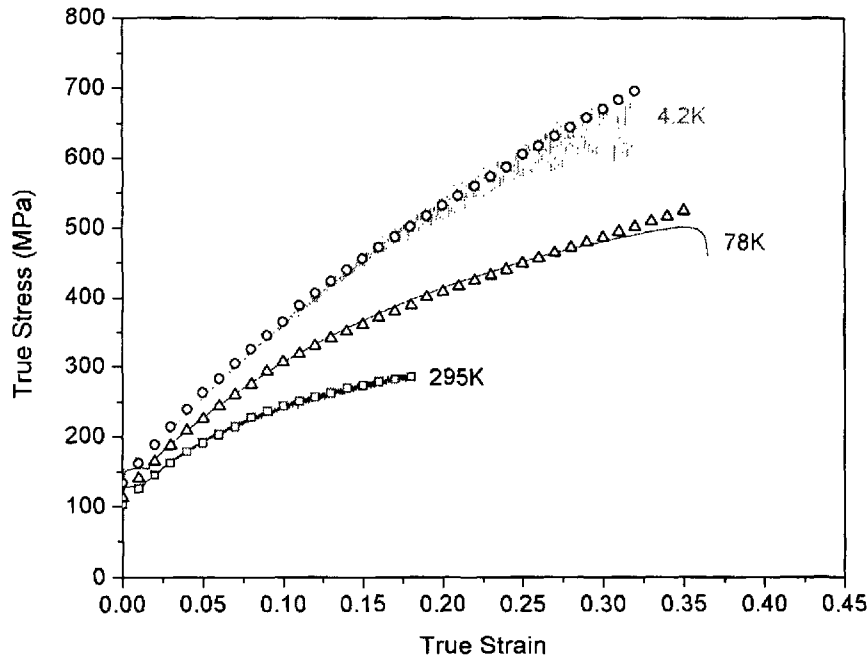
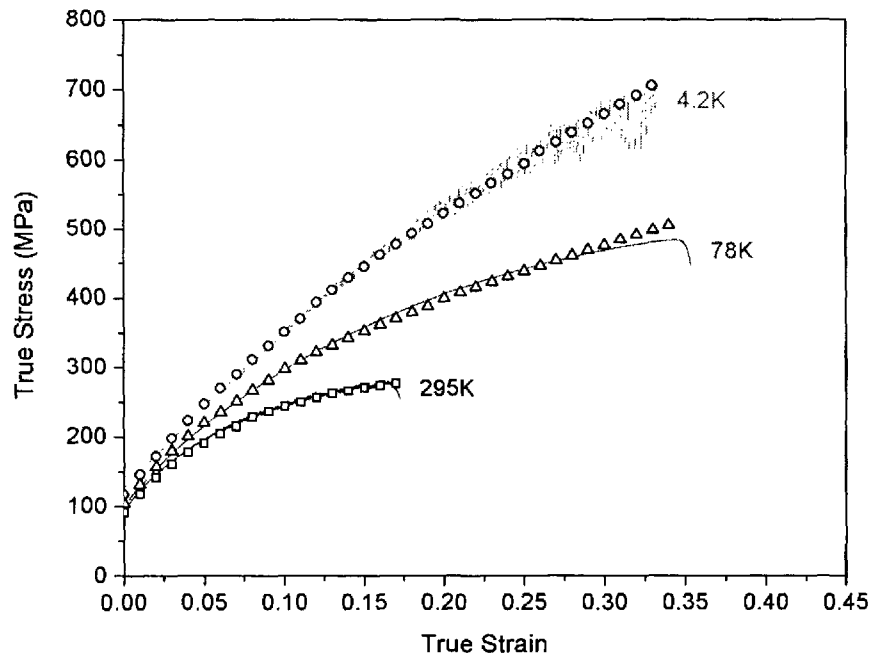


Figure 5.9: Comparisons of experiments (lines) and simulations (symbols) of deformation at room temperature for CC materials annealed for 2 hours at 350°C and 450°C



(a)



(b)

Figure 5.10: Comparisons of experimental (lines) and simulated (symbols) true stress - true strain curves for CC (a) and DC (b) alloys

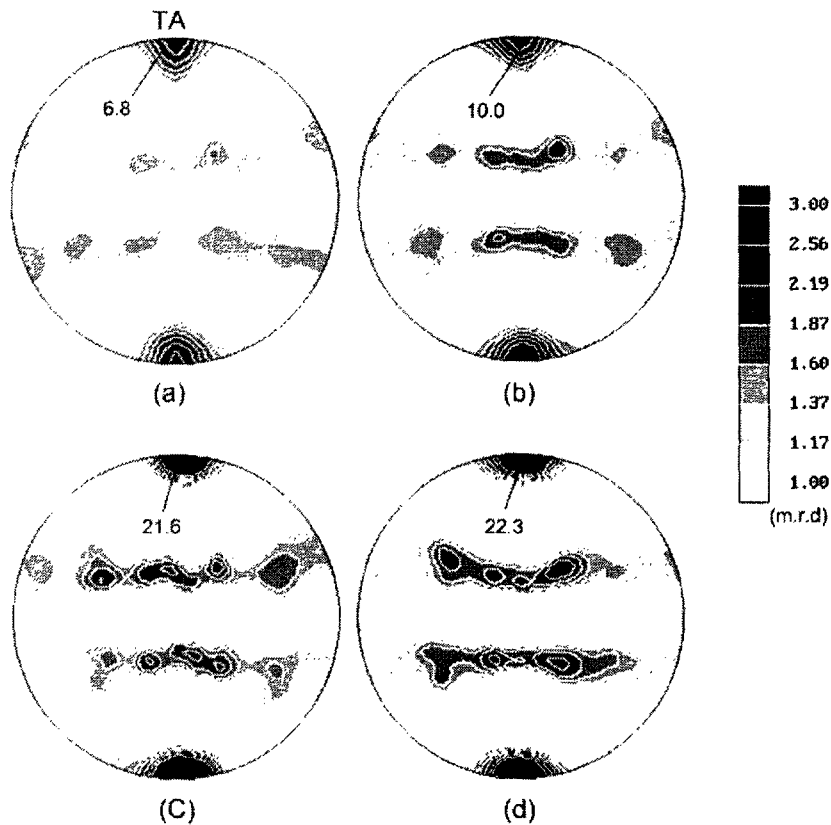


Figure 5.11: $\{111\}$ pole figure obtained from deformation simulation for CC materials: 18% strain at room temperature with CC materials annealed at 450°C (a) and 350°C (b) and 33% strain at 4.2K for CC (c) and DC (d) materials

In Table 5.3, the sample annealed at 350°C has the initial CRSS (τ_0) of 54MPa compared to 48MPa for specimens annealed at 450°C, whereas the values of other parameters are the same. The simulated textures of these specimens in Figure 5.11 show a similar propensity as the experimental textures in Figure 4.29. The intensity at $\langle 111 \rangle$ orientation for CC specimen annealed at 350°C is higher than the one annealed at 450°C due to the effect of the initial texture as mentioned earlier. This indicates that work hardening behaviours of these two specimens are identical and the work hardening mechanism is not altered by two different anneals and the subsequent

change of the initial texture. Sections 4.1 and 5.1 show that differences in the yield stress and the work hardening behaviour of these two annealed CC materials are attributed to the combined effect of the grain size difference and the composition of matrix. It can be further concluded that the initial texture has little influence on the work hardening behaviour, at least in this case, probably due to the weak initial texture, although the intensities of this texture components are strong enough to observe the effect of the initial texture on the resulting texture.

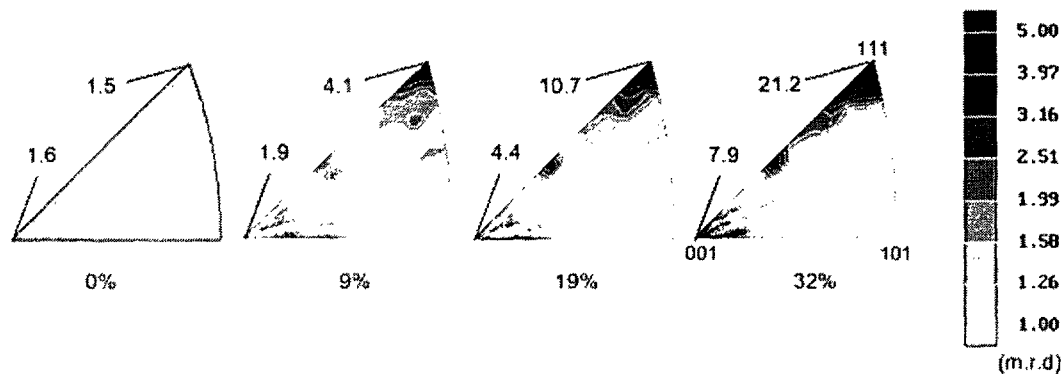
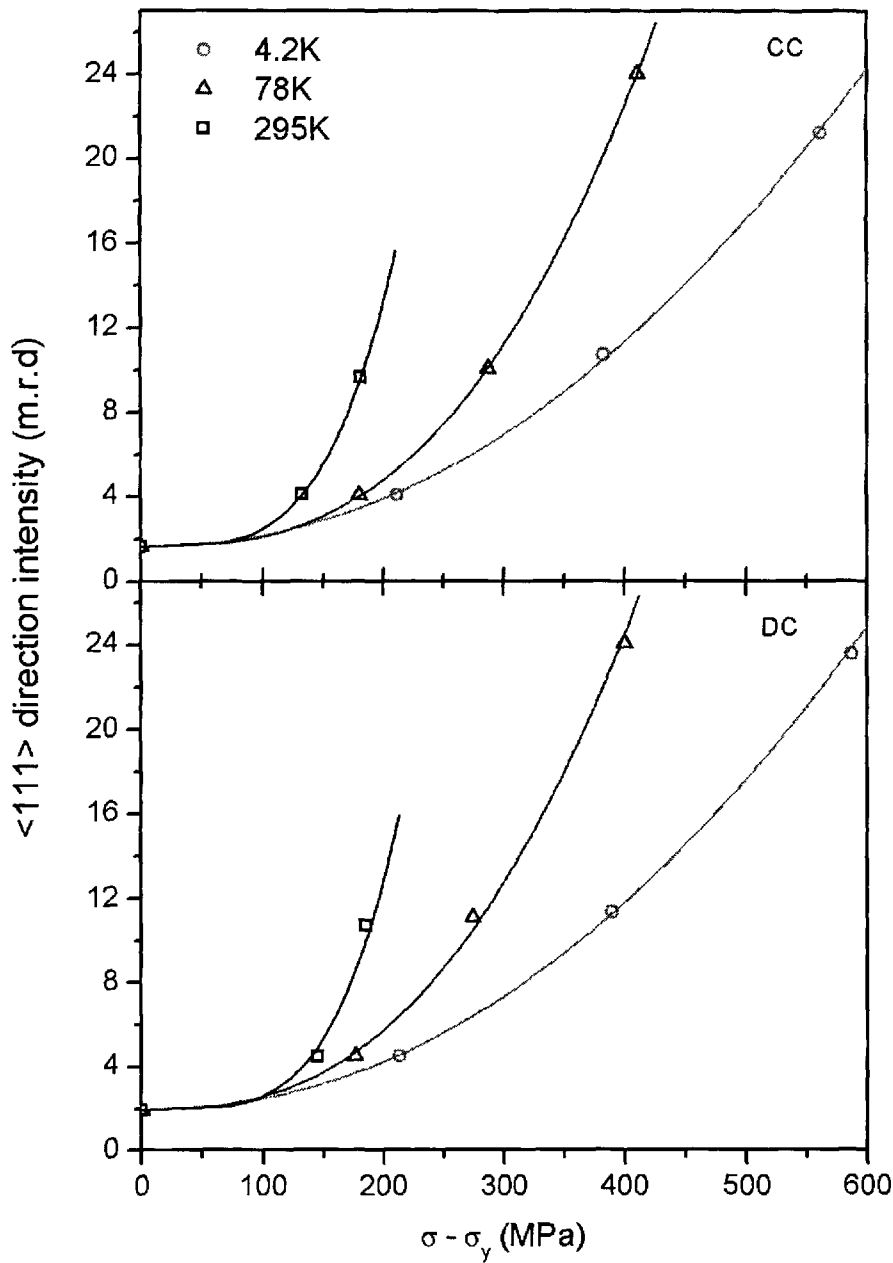


Figure 5.12: Simulated inverse pole figures for tensile axis of CC specimen deformed at 4.2K after different amount of deformation, revealing a rotation of tensile axis to either $\langle 111 \rangle$ or $\langle 001 \rangle$ orientation.

The simulated texture patterns of CC and DC materials at other test temperatures (e.g., Figures 5.11 (c) and (d)) are in good agreement with the experimental results. The characteristic of the simulated intensity variation at the stable end orientation with stress (Figure 5.13 (a)) also agrees with the experimental observations (Figure 5.8). Figures 5.12 and 5.13 plot strengths at $\langle 111 \rangle$ orientation of the simulated inverse pole figure (e.g., Figure 5.12) of the tensile axis. The character of the simulated inverse pole figures (Figure 5.12) is in good agreement with experiments (Figure 5.6); the strength at $\langle 111 \rangle$ and $\langle 100 \rangle$ orientations increases with strain. Figure 5.13 confirms that the intensity variation of the stable end orientation is a parabolic function of the

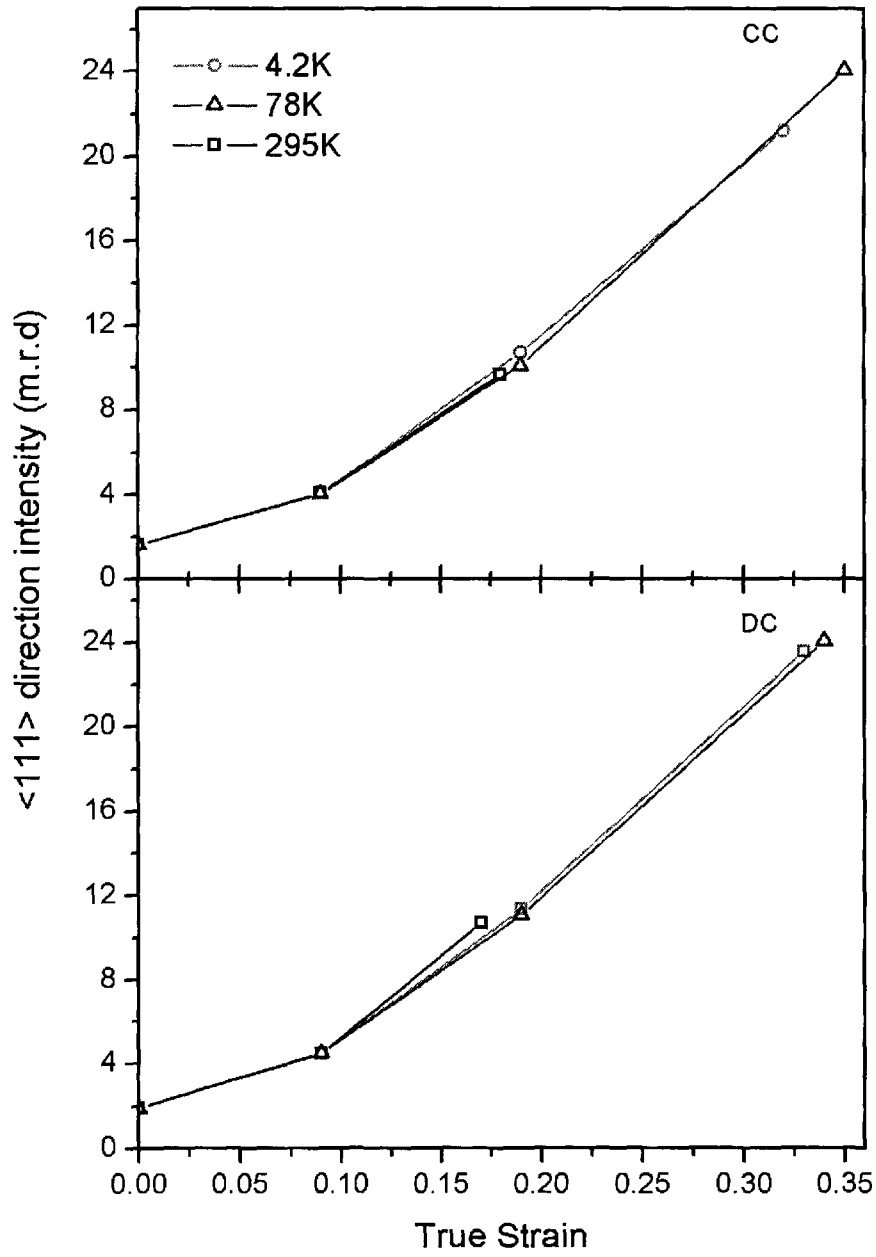
flow stress as experimentally shown in section 5.1.4. The simulated intensity variation of the stable end orientation as a function of strain is close to a linear relationship, but the slope increases at the later stage of strain due to the specific nature of the dislocation structure developed during deformation as discussed earlier (Figure 5.13 (b)).

The simulation results of CC and DC materials with experimental initial textures, indicate that the asymptotic hardening rate (θ_1) in Table 5.3 increases noticeably to approximately 1100% with decrease in test temperature, while other parameters vary within 30%. This indicates that the test temperature has a significant effect on the work hardening rate at the later stage of deformation. This is attributed to the suppressed dynamic recovery at a lower temperature; the accumulated dislocations undergo more intensive dynamic recovery at the later stage of deformation which reduces the work hardening rate. However, the suppressed dynamic recovery at a lower temperature results in more effective dislocation storage in the substructure, as discussed in earlier sections, and in the higher asymptotic hardening rate (θ_1).



(a)

Figure 5.13: Simulated intensities of <111> axes lying parallel to the tensile axis as a function of effective stress (a) and true strain (b) (cont'd)



(b)

Figure 5.13: (cont'd)

5.2 Anisotropic Deformation

5.2.1 Mechanical Properties

For both CC and DC materials, samples oriented 45° and 90° to rolling direction show larger tensile strain (homogeneous deformation) before the necking, compared to samples deformed parallel to the rolling direction (Figure 4.33). The homogeneous deformation may vary in samples deformed at 4.2K, due to the adiabatic shear instability. This anisotropy in elongation is associated with the anisotropy of the work hardening behaviour and the point at which the instability condition is met (Figure 4.34).

The latent hardening, inhomogeneous microstructure, particle distribution and the crystallographic texture have usually been considered as the source of the anisotropy of the work hardening rate [9, 14–18, 115–119]. However, the present results reveal that the anisotropy of the flow stress and the work hardening rate observed in this work cannot be explained by the latent hardening concept [14]. It is also known that the effect of latent hardening is insignificant in aluminum [9]. Microstructural inhomogeneities may be in the form of a variable grain structure, with regard to both the grain size and the grain shape. It was reported that both, the grain size and shape as well as the microstructural anisotropy in the form of an inhomogeneous particle distribution, are not controlling factors of directionality of the work hardening rate in AA5754 alloy [115]. Haasen analysis, which gives a measure of thermal barriers to dislocation glide, indirectly indicates the insignificant effect of solute and grain on the work hardening anisotropy for CC and DC alloys; the difference in slope and y-intercept for each tensile direction is minimal in Haasen plot (Figure 4.36). Also, as the effect of the second phase particle on plastic deformation is not significant in this

material (section 5.1), it is concluded that the particles themselves and the particle distribution are not the primary factors of the work hardening anisotropy. Another noticeable characteristic of the tensile curve of the present alloy is the serrated plastic flow occurring at every tensile direction at room temperature due to dynamic strain aging (Figure 4.33). It has been reported by other researchers that inhomogeneous deformation due to the Portevin-Le Chatelier effect is not a source of the anisotropy [115].

The above arguments, then, suggest that crystallographic texture is the major factor of the work hardening anisotropy in these materials. Taylor analysis (Figure 4.44) and VPSC simulation results (section 5.2.3) strongly support these conclusions. The work hardening rate in the early stage of deformation is higher in samples oriented parallel to the rolling direction than along any other direction (Figures 4.34 and 4.35). This is attributed to the effect of the initial texture on deformation behaviour. For the 0° tension, the tensile axis of many grains is initially parallel to the $\langle 111 \rangle$ stable end orientation, and thus the high initial work hardening rate is determined by multiple slip. This results in a faster decrease of the work hardening rate during later stage of deformation observed in 0° samples, due to the intensive dynamic recovery occurring in this highly dislocated substructure (Figure 4.34).

The tensile axis of samples oriented at 45° to rolling direction is initially located inside the $\langle 001 \rangle$ - $\langle 011 \rangle$ - $\langle 111 \rangle$ stereographic triangle, corresponding to the easy glide region of the single crystal. Thus, the sample work-hardens less during the initial stage until the TA reaches the stable end orientation at the later stage of deformation. The work hardening behaviour for 90° samples can be explained using above arguments. The evolution of the tensile axis for this sample orientation will be discussed in detail in the following section.

In the case of the DC material, the work hardening rate of 0° samples decreases faster than the 45° and 90° samples at the later stage of deformation; the curves cross over and the work hardening rates for 45° and 90° remain on a higher level especially at 78K and 295K (Figure 4.34 (b)). Such features of the hardening behaviour are not observed for the CC material (Figure 4.34 (a)) although 0° samples also show the faster decrease of the work hardening rate due to the effect of crystallographic orientation, as mentioned previously. This indicates that more intensive dynamic recovery occurs in 0° samples of DC alloy. This is presumably caused by the difference in microstructure between DC and CC materials. As the DC material contains larger particles than CC material, more dislocation debris accumulate around these particles. For 0° samples of the DC alloy, the more intensive accumulation of dislocation begins earlier than in other orientations, and the dynamic recovery is intensified around large particles. This consequently accelerates the decrease of the work hardening rate at the later stage.

This geometric effect of crystallographic orientation is shown in the variation of the activation area for both CC and DC materials. In the initial stage of deformation, the activation area in the 0° samples is the lowest (Figure 4.37), because the material work-hardens more effectively in the early stage and restricts the movement of dislocation.

The Taylor normalization (Figure 4.44) accounts for the anisotropy of mechanical properties of samples deformed at higher temperatures and supports the view that crystallographic texture is the major cause of the anisotropy. However, the Taylor model (Figure 4.44) and the simulation of deformation behaviour (section 5.2.3) do not reproduce the magnitude of the anisotropy of the flow stress at 4.2K, although the modeling results agree qualitatively well with the experiment. This discrepancy may be caused by the effect of the microstructure observed at 4.2K. It is believed that the

well-defined planar dislocation structure may be a source of anisotropy of mechanical properties, and the development of such structures is often determined by the crystallographic orientation of the samples [14]. This can explain the anisotropic behaviour of the flow stress at low temperatures, since the microstructure shows evidence of the planar arrangement and the banded substructure (section 4.1.5). Figure 5.14 shows typical misorientations in the range of 1-3 degrees across dislocation bands, measured by means of convergent beam electron diffraction (CBED).

As seen in Figure 5.14, the dislocation bands are highly directional. It is known that the occurrence of the banded structure is favorable for certain textures and deformation conditions. For example, banding is much less frequently observed in cube textured material deformed parallel to the rolling direction [14]. Therefore, the occurrence of the banded structure most likely enhances the plastic anisotropy of the material, and results in the quantitatively larger deviation of the flow stress in samples not parallel to the tensile direction at the low temperatures.

5.2.2 Texture

5.2.2.1 *Rotation Path of the TA*

High intensities developed at the periphery of the $\{111\}$ pole figure for the 0° , 45° and 90° samples (Figure 4.38) indicate that the $\langle 111 \rangle$ orientation is the stable end orientation in this alloy, regardless of the initial orientation of the tensile axis. However, the rotation path of the tensile axis toward the $\langle 111 \rangle$ orientation varies depending on the initial tensile axis direction. The main components of the texture for each tensile direction show the rotation path of the tensile axis during deformation. Rauno and Gonzalez [126] studied deformation of Al-5%Ca-5%Zn alloy by means of

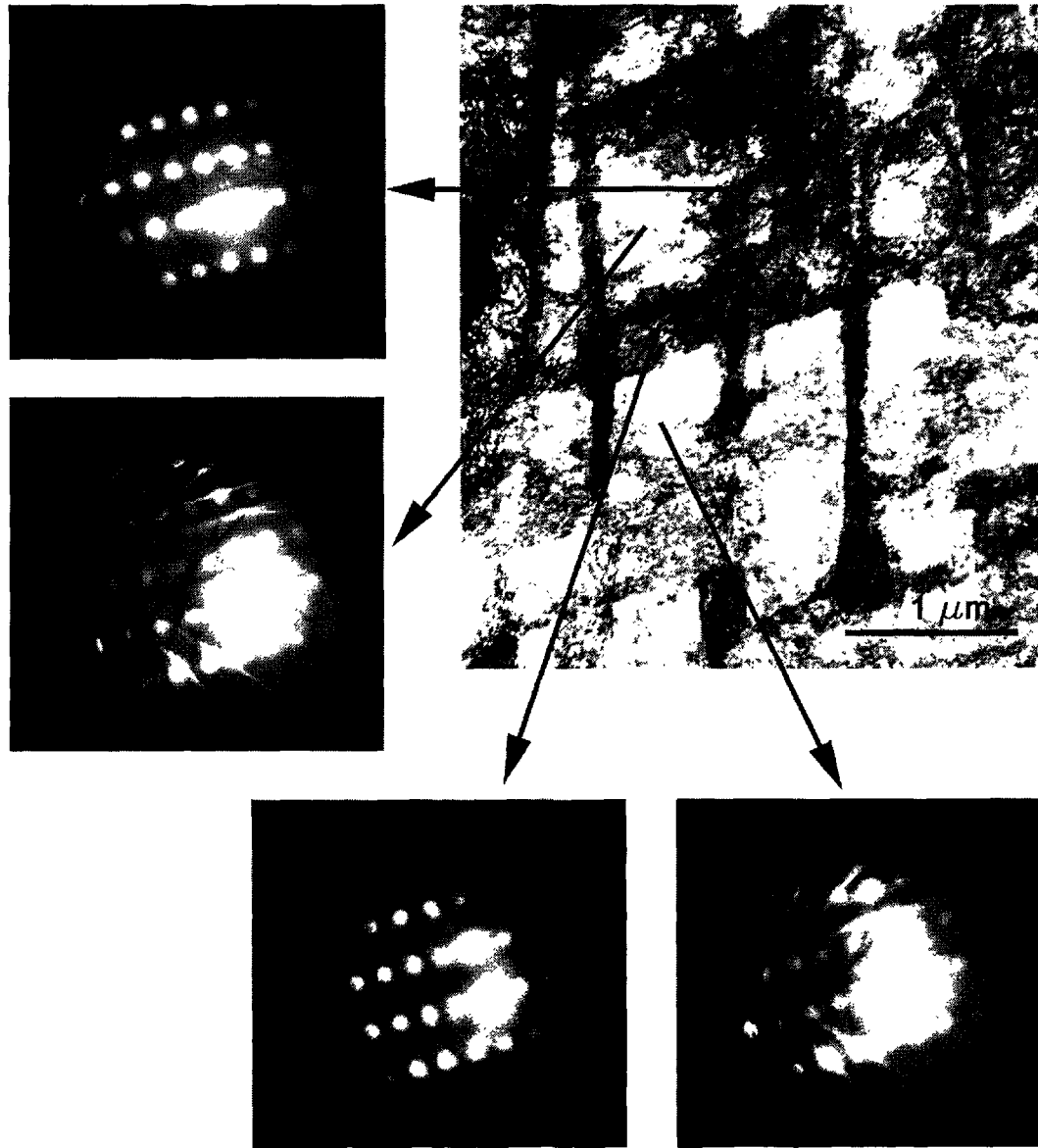


Figure 5.14: Misorientation across the banded structure for the CC material tested at 78K. Kikuchi diffractions reveal misorientations across bands

tensile tests at 400°C at a strain of $10^{-2} s^{-1}$, and analyzed the rotation of the TA on the $[001] - [011] - [\bar{1}11]$ unit stereographic triangle. It was shown that the tensile axis rotates from $\langle 011 \rangle$ through $\langle \bar{1}12 \rangle$ to $\langle \bar{1}11 \rangle$ when the TA was perpendicular to the RD.

In the present work, when the TA of the samples is parallel to the RD, the TA of many grains is initially located close to $\langle 111 \rangle$. Since the $\langle 111 \rangle$ orientation is the stable end orientation, the TA does not rotate further and the material is subjected to multiple slip, which results in the higher work hardening rate. Hence, no significant change of orientation is observed after deformation (Figures 4.38 (a) and (b)). For the case of the tensile axis perpendicular to the rolling direction, the intensity maxima at $\langle 112 \rangle$ orientation in the RD (Figures 4.38(d) and 4.40) indicate that the tensile axis passes through $\langle 112 \rangle$ and eventually reaches $\langle 111 \rangle$ orientation. For the 45° direction, the ideal orientation is not directly observed from the pole figure (Figure 4.38 (c)). However, it can be inferred from the orientation distribution in Figure 4.42 that the TA first approaches $\langle 112 \rangle$ and rotates toward $\langle 111 \rangle$ like in the case of the 90° sample.

5.2.2.2 Stable End Orientation

The development of the stable orientation, $\langle 111 \rangle // TA$, in AA5754 alloy can be illustrated with inverse pole figures of the TA in the same way as discussed in section 5.1.4. Figure 5.15 clearly shows the typical development of $\langle 111 \rangle // TA$ fiber texture with increasing strain for the TA perpendicular to the previous RD for CC materials tested at 4.2K. It is seen that the intensity increases also in $\langle 100 \rangle$ orientation with increasing strain, which was reported as the metastable end orientation in section 5.1.4. In order to evaluate the behaviour of the stable end orientation for each tensile direction, $\langle 111 \rangle$ intensities in the inverse pole figures are plotted against the effective

flow stress, $\sigma_y - \sigma_o$, (Figure 5.16) and the true strain (Figure 5.17). The experimental data of intensity changes with flow stress are fitted to the polynomial equation discussed in section 5.1.4. The fitting curves are shown in Figure 5.16 for each tensile direction of CC and DC alloys, and the fitting parameters are given in Table 5.4. It is seen that the intensities of the 45° and 90° samples are lower than the 0° sample at every flow stress level (Figure 5.16). This indicates that the number of grains whose $\langle 111 \rangle$ orientation is aligned with the TA is always the highest for the 0° sample, before and after deformation.

Table 5.4: I_o , β , and w values in equation (5.7) and the fitting curves are shown in Figure 5.16

		CC			DC		
		295K	78K	4.2K	295K	78K	4.2K
0°	I_o	1.63	1.63	1.63	1.9	1.9	1.9
	β	110	172	221	153	195	281
	w	0.45	0.42	0.65	0.49	0.40	0.47
	R^2	1.0	0.998	0.997	1.0	0.976	0.996
45°	I_o	0.79	0.79	0.79	0.69	0.69	0.69
	β	164	222	299	177	256	324
	w	0.50	0.39	0.56	0.50	0.36	0.5
	R^2	0.988	0.984	0.996	0.997	0.953	0.962
90°	I_o	1.14	1.14	1.14	1.5	1.5	1.5
	β	158	190	287	219	295	440
	w	0.50	0.40	0.52	0.30	0.30	0.35
	R^2	0.984	0.938	0.981	0.960	0.996	0.846

The Visco-Plastic Self Consistent (VPSC) modeling experiments verify these experimental observations. Details of the simulation procedure are presented in section 5.1.5 and in the subsequent section. The simulated texture patterns for each tensile direction well represent the experimental measurements (Figure 5.18). The simulation results (Figure 5.19) also indicate that the initial low intensity of the 45° and 90°

samples at the stable end orientation results in the low intensity at every flow stress level, as observed experimentally (Figure 5.16).

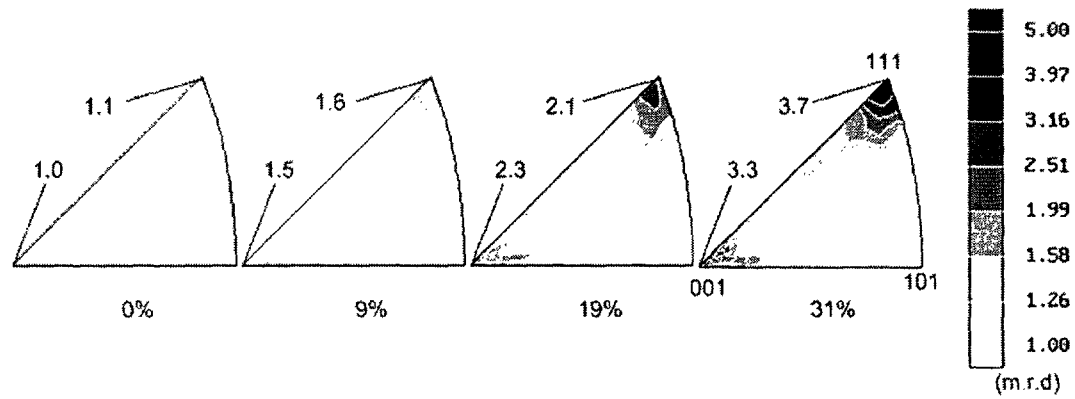


Figure 5.15: Inverse pole figures of the TA perpendicular to the previous RD for the CC specimen tested at 4.2K

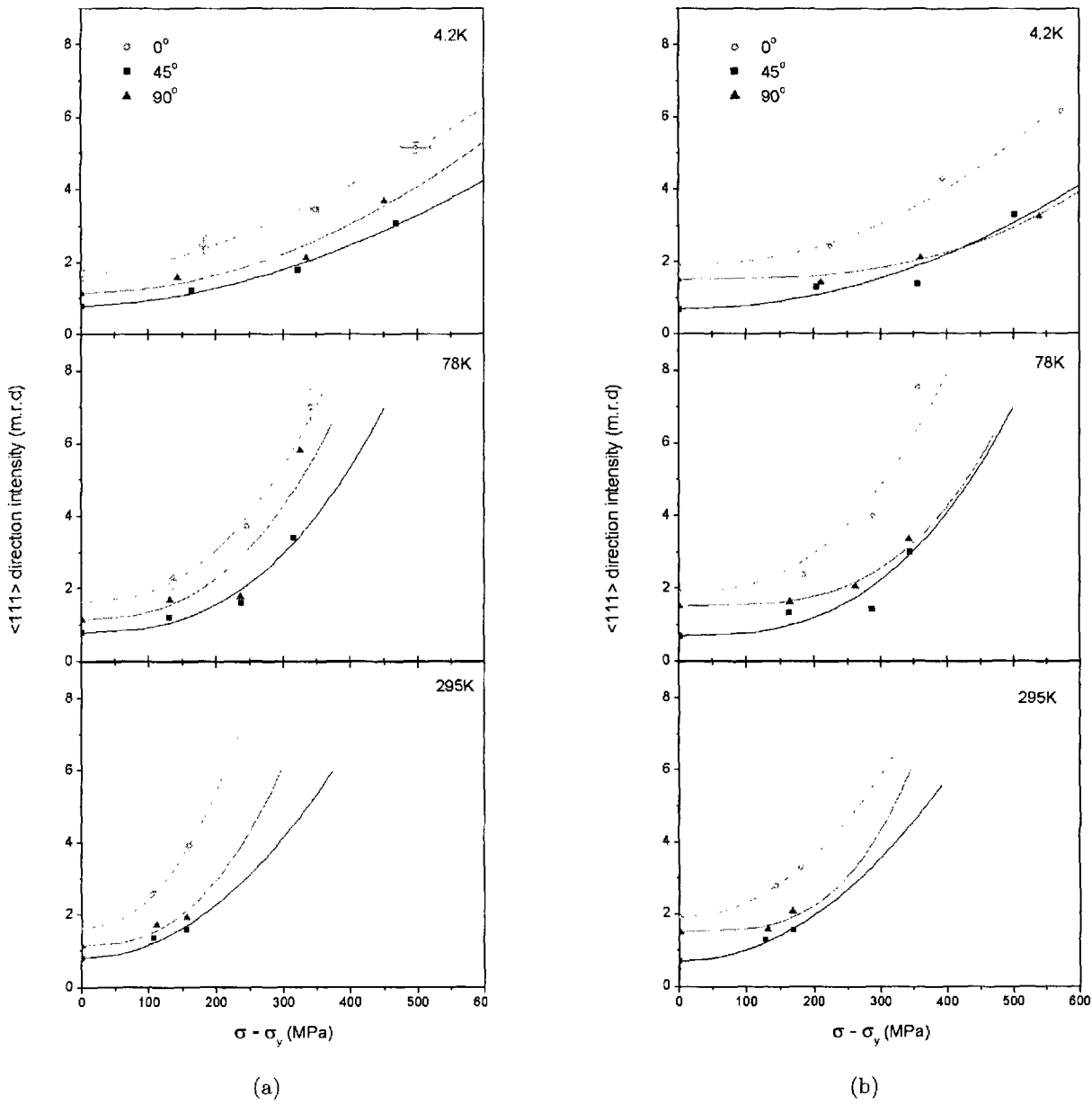


Figure 5.16: Behaviour of the stable end orientation as a function of effective flow stress for the tensile axes at 0° , 45° and 90° to the previous RD for the CC (a) and DC (b). The y-axis represents the intensity of $\langle 111 \rangle$ axis parallel to the tensile direction.

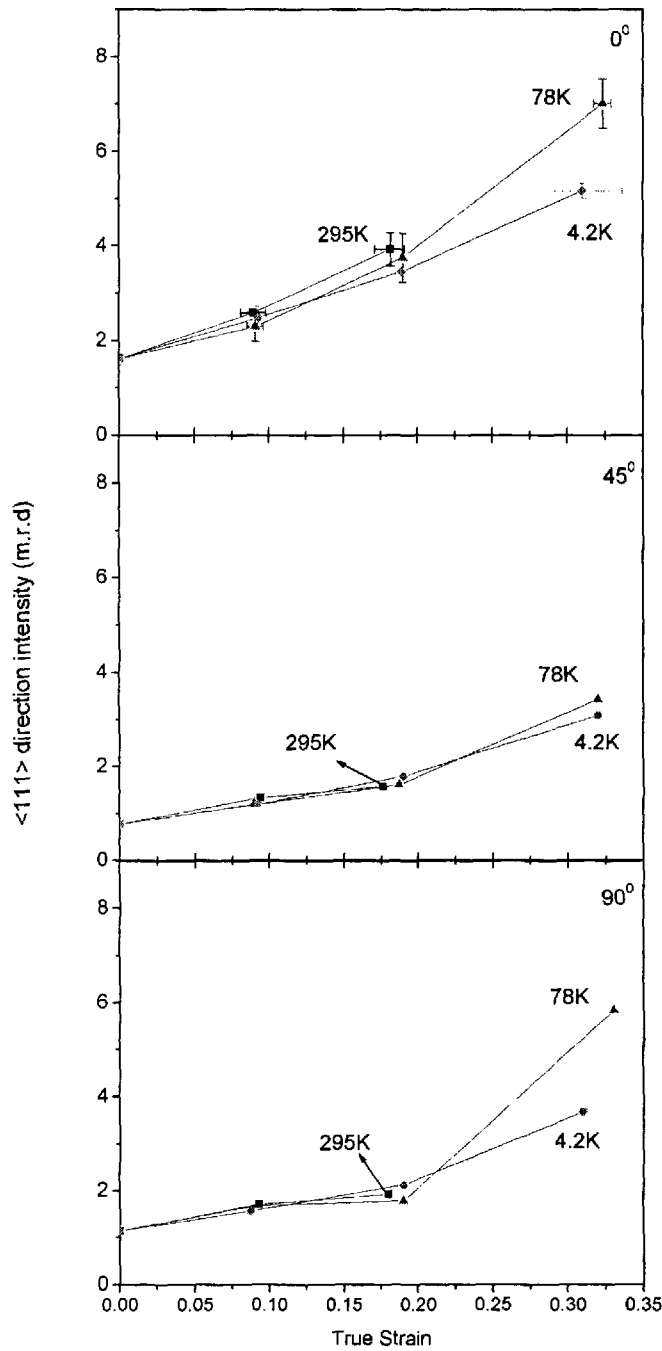


Figure 5.17: Behaviour of the stable end orientation as a function of strain for the tensile axes at 0°, 45° and 90° to the previous RD for the CC alloy. The y-axis represents the intensity of <111> axis oriented parallel to the tensile direction.

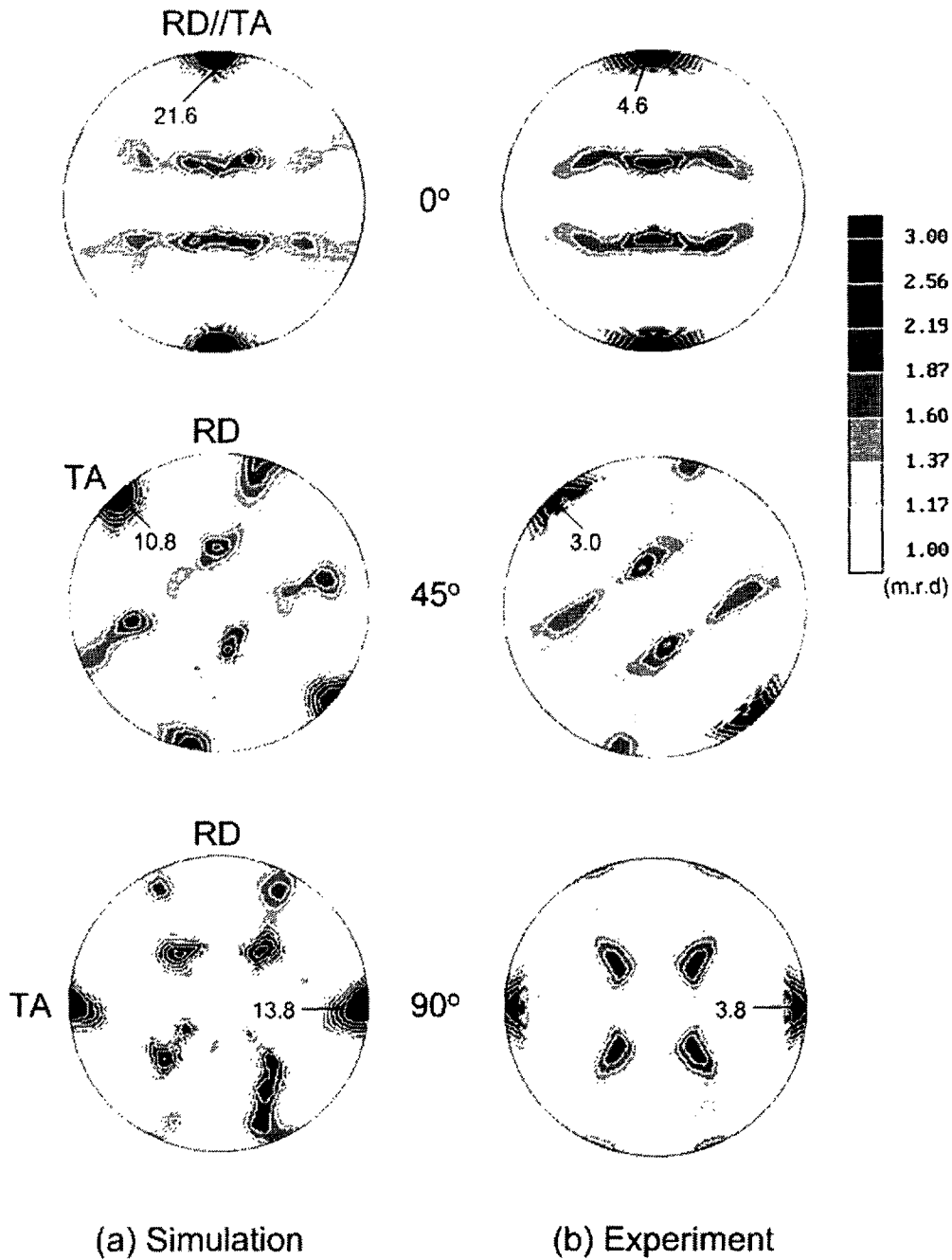


Figure 5.18: Comparisons of simulated and experimental $\{111\}$ pole figures after 33% straining of CC specimens at 4.2K

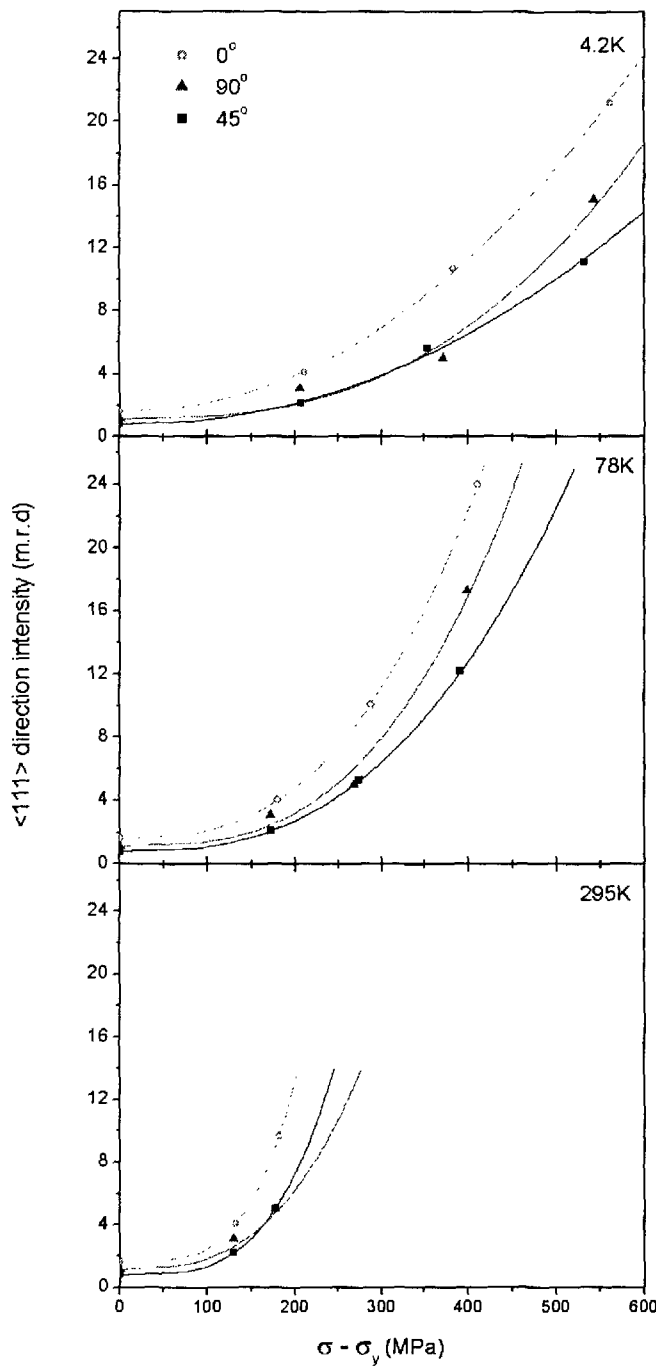
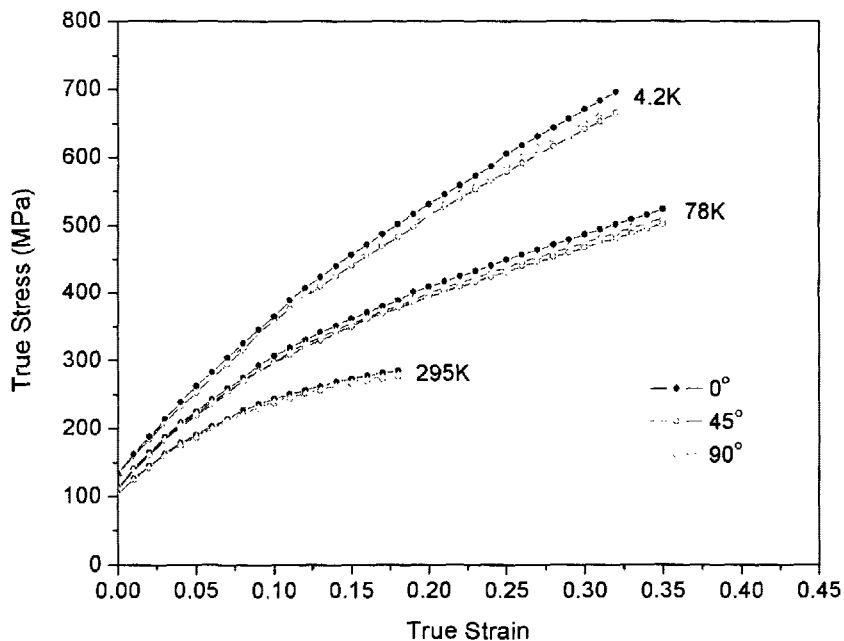


Figure 5.19: Simulated results of the stable end orientation as a function of effective flow stress for the tensile axes at 0° , 45° and 90° to the previous RD for the CC alloy

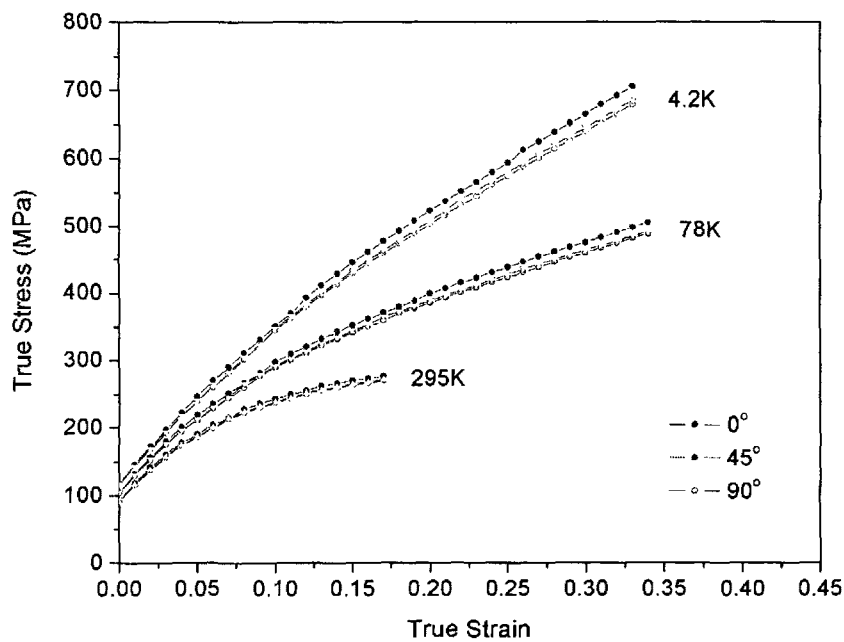
5.2.3 Modeling

In section 5.1.5, the tensile tests are simulated for the tensile axis parallel to the previous rolling direction using a VPSC code [13]. In an attempt to further investigate the effect of texture on the anisotropic deformation, VPSC simulations are performed for samples oriented at 45° and 90° to the rolling direction with the initial experimental texture data as input parameters (Figure 5.20).

The simulation results show very good agreement with experimental data and reproduce the behaviour of the flow stress and the yield stress well (Figure 5.20). No significant anisotropy of the yield stress is observed in modeling experiments, which agrees with the measurement results. The behaviour of the flow stress obtained from the simulation is also very similar to that observed in the experiment. The pole figures from the simulation are quite close to the experimental results as well (Figure 5.18). The magnitude of the anisotropy of the flow stress is not fully reproduced, especially for samples deformed at 4.2K (Figure 5.20). The difference in maximum flow stress between the 0° and 45° orientations obtained from the simulation of the CC material is about 30MPa, but it is 50MPa from the experiment. Thus, the modeling does not reproduce the anisotropy of the flow stress for samples deformed at 4.2K, like does the Taylor analysis discussed in the previous section. This is attributed to the fact that the simulation methodology does not include the effect of the directionality of the dislocation substructure in the form of the band structure observed in the material deformed at low temperature (section 4.1.5 and section 5.2.1). It was shown by other researchers that the dislocation substructure may be another source of anisotropy [14]. Present results suggest that the band structure enhances the plastic anisotropy of CC and DC materials under real deformation conditions.



(a)



(b)

Figure 5.20: Simulation of the flow stress for (a) CC and (b) DC alloy samples with different orientations marked on the graphs. In the analysis, initial experimental texture corresponding to the respective tensile directions was used.

Chapter 6

Summary and Conclusions

Work hardening behaviour, microstructure and texture evolution during tensile deformation in pure Al, continuous cast and direct chill cast AA5754 Al alloys have been studied between 4.2K and 295K. The focus is on the low temperature regime where mechanical properties of these materials have not been sufficiently explored. Al alloys show two kinds of flow instabilities, resulting from dynamic strain aging known as Portevin-LeChatelier effect at 295K and adiabatic deformation at 4.2K. At 78K, the flow instability is suppressed and these materials exhibit a homogeneous deformation. Plastic deformation of high purity Al is governed mainly by dislocation-dislocation interactions, and a stronger athermal component of the flow stress observed at lower temperatures arises from the nature of the dislocation cell structure produced in this material. Al alloys exhibit a larger thermal component of the flow stress due to the presence of solute atoms in the matrix.

Electrical resistivity measurements reveal that all materials exhibit different kinetics of dislocation storage and recovery, which is reflected both in the constitutive relationship between flow stress and the total dislocation density and in the way these materials approach fracture. The results reveal that the CC alloy deformed at 4.2K exhibits a remarkably high work hardening capacity, with the work hardening rate of the order of $\mu/20$ for most of the plastic flow, attaining eventually the strength of 700MPa just before the fracture. The work hardening capacity of the CC alloy

at 4.2K is more effective than in precipitation-hardened materials probably due to a higher dynamic recovery component in heat-treatable alloys.

The evolution of the dislocation mean free path shows a good agreement with TEM observations of the substructure and suggests that dislocations are accumulated within the cell walls in pure Al and quasi-homogeneously in the volume of Al alloys. Particles have small or no influence either in the process of dislocation storage or during the fracture.

Direct measurements of the evolution of the defect content during deformation at 4.2K suggest that the rate of dynamic recovery occurring within a dislocation network is slower in Al alloys than in pure Al. However, adiabatic deformation, which operates during plastic flow, affects the macroscopic work hardening behaviour of alloys and gives the higher apparent recovery rate than observed in pure metal. Dislocation density variations and their analyses show that fracture occurs when dislocation density approaches a critical level locally in highly dislocated areas. Dislocation density figures give an estimate for the critical spacing between dislocations in these areas to trigger spontaneous annihilation. At 4.2K this figure is ~ 8 nm for all materials, whereas at 78K it has been estimated only for Al and is ~ 12 nm. The weakening of the substructure, arising from the collapse of the dislocation network under the high stresses, forces the flow localization, the nucleation of voids, and fracture.

Texture measurements at various strains show that $\langle 111 \rangle$ is the stable end orientation in CC and DC AA5754 alloys deformed in tension between 4.2K and 295K. The $\langle 100 \rangle$ is the meta-stable end orientation that is developed alternatively during plastic flow. Depending upon the intensity of the initial texture of the material, both orientations may exhibit stronger or weaker intensity after uniaxial deformation. The rapid texture enhancement occurs at the later stage of deformation after about 20% of strain, when dislocation substructure evolves to the configuration that favors dis-

location storage on approximately constant length scale. The results clearly indicate that the intensity level of the $\langle 111 \rangle$ stable end orientation increases parabolically with the flow stress, which reflects the rate of grain rotations during plastic deformation induced by the operating slip systems. The results suggest a power relationship between the intensity of $\langle 111 \rangle$ peak and the dislocation density, i.e., $I \sim \rho^n$. The exponent n in this equation increases as temperature increases from 0.52 at 4.2K to 1.11 at 295K for the CC alloy; from 0.62 at 4.2K to 1.02 at 295K for the DC alloy. One observes a significant effect of deformation temperature on texture evolution. In general, texture formed at lower temperatures is weaker than this produced at higher temperatures. At a lower temperature, the same level of $\langle 111 \rangle$ peak intensity is achieved at higher flow stress, suggesting that lattice rotation is suppressed as deformation temperature decreases. This has been interpreted in terms of the effect of dislocation substructure and the processes of dislocation storage and recovery occurring during the deformation of these materials, which promote development of a homogeneous and stable dislocation network associated with higher degree of texture scattering between individual grains.

The anisotropy studies indicate that the crystallographic texture is the major factor responsible for the different tensile behaviour of the alloys, depending on the location of the initial tensile direction of the sample with respect to the rolling direction. However, the differences in mechanical properties are relatively small. As the tensile axis (TA) rotates toward $\langle 111 \rangle$ orientation, the texture changes. Different rotation paths of the TA affect the operating slip systems activated during tensile deformation and consequently the work hardening rate. The results reveal that the work hardening rate is greatly influenced by the orientation of the tensile axis; the initial work hardening rate is always the highest when the TA is parallel to the previous rolling direction, as many grains with $\langle 111 \rangle // \text{TA}$ are oriented for multiple slips

right from the beginning of deformation. The texture results show that a low initial intensity at the stable end orientation results in a low resultant intensity at this orientation after the deformation.

The Visco-Plastic Self Consistent modeling experiments have been carried out to predict mechanical properties of AA5754 alloys and to provide insight into operating mechanisms of plastic flow. These modeling studies confirm that the work hardening behaviour of CC alloys annealed at 350°C and 450°C are identical, and are not affected by annealing conditions and their initial textures. The annealing treatment affects the yield stress and the ultimate tensile stress and this is attributed to the effect of the grain size. The results also show that a low initial intensity of texture components produces a low intensity of resultant texture components after deformation. The variation of the intensity of the stable end orientation obtained from simulation is described as a function of the true stress, i.e. $I \sim \rho^n$ as observed in the experiments. The simulation results show that the asymptotic hardening rate (θ_1) increases up to approximately 1100% with decrease in test temperature while other parameters vary within 30%. This indicates that test temperature significantly affects the work hardening behaviour, particularly at the later stage of deformation. This is attributed to the suppressed dynamic recovery and the more effective dislocation storage in the substructure in samples deformed at low temperatures. At higher temperatures, more intensive dynamic recovery affects the storage process and effectively reduces the work hardening rate at the later stage of deformation.

Bibliography

- [1] Miller, W. S., Zhuang, L., Bottema, J., Wittebrood, A. J., De Smet, P., Haszler, A., and Vieregge, A. (2000) *Mater. Sci. and Eng.* **A280**, 37–49.
- [2] Taub, A. I., Krajewski, P. E., Luo, A. A., and Owens, J. N. (2007) *JOM* **59(2)**, 48–57.
- [3] Liu, J. and G., M. J. (2003) *Metall. and Mat. Trans. A* **34A**, 951–966.
- [4] Yu, X. F., Zhao, Y. M., Wen, X. Y., and Zhai, T. (2005) *Mat. Sci. and Eng.* **A394**, 376–384.
- [5] Cheng, X. M. and Morris, J. G. (2000) *Scripta Mater* **43**, 651–658.
- [6] Cheng, A. M. and Morris, J. G. (2002) *Mater. Sci. and Eng.* **A323**, 32–41.
- [7] Zandrahimi, M., Platias, S., Price, D., Barrett, D., Bate, P. S., Roberts, W. T., and Wilson, D. V. (1989) *Metall. Trans.* **20A**, 2471–2482.
- [8] Van Houtte, P. and Aernoudt, E. (1976) *Mater. Sci. and Eng* **23(1)**, 11–22.
- [9] Juul Jensen, D. and Hansen, N. (1990) *Acta metall. mater.* **38(8)**, 1369–1380.
- [10] Zhou, Y., Neale, K. W., and Toth, L. S. (1993) *Int. J. Plast.* **9(8)**, 961–978.
- [11] Ceccadi, D., Yale, F., Baudin, T., Penelle, R., Royer, F., and Arminjon, M. (1994) *Int. J. Plat.* **10(6)**, 643–661.
- [12] Molinari, A., Canova, G. R., and Ahzi, S. (1987) *Acta Metall* **35(12)**, 2983–2994.
- [13] Lebensohn, R. A. and Tome, C. N. (1993) *Acta metall. Mater.* **41(9)**, 2611–2624.

- [14] Li, F. and Bate, P. S. (1991) *Acta metall. mater.* **39(11)**, 2639–2650.
- [15] Lloyd, D. J. and Sang, H. (1979) *Metall. Trans. A* **10**, 1767–1772.
- [16] Martin, P., Baudelet, B., Esperance, G. L., Korbel, A., and Schmitt, J. H. (1988) In P. O. Kettunen, T. K. Lepisto, and M. E. Lehtonen, (ed.), Proc. 8th Int. Conf. on the Strength of Metals and Alloys, Oxford(eds by P.O. Kettunen, T.K. Lepisto and M.E. Lehtonen, Oxford: . pp. 403–408.
- [17] Eardley, E. S., Humphreys, F. J., Court, S. A., and Bate, P. (2002) *Mat. Sci. Forum* **396-402**, 1085–1090.
- [18] Eardley, E. S., Soulet, A., Court, S. A., Humphreys, F. J., and Bate, P. S. (2003) *Materials Science Forum* **426-432**, 363–368.
- [19] Jin, H. and Saimoto, S. (2002) *Scripta Materialia* **46**, 275–279.
- [20] Jin, H. and Saimoto, S. (2004) *Scripta Materialia* **50**, 1319–1323.
- [21] Spencer, K., Corbin, S. F., and Lloyd, D. J. (2002) *Mater. Sci. and Eng.* **A325**, 394–404.
- [22] Spencer, K., Corbin, S. F., and Lloyd, D. J. (2002) *Mater. Sci. and Eng.* **A332**, 81–90.
- [23] Sarkar, J., Kutty, T. R. G., Conlon, K. T., Wilkinson, D. S., and Embury, J. D. (2001) *Mater. Sci. and Eng.* **A316**, 52–59.
- [24] Kang, J., Wilkinson, D. S., Jain, M., Embury, J. D., Beaudoin, A. J., Kim, S., Mishra, R., and Sachdev, A. (2006) *Acta Mater.* **54**, 209–218.
- [25] Liu, W. C., Wen, X. Y., and Morris, J. G. (2001) *Advances in the Metallurgy of Aluminum Alloys* pp. 406–415.
- [26] Liu, J. and G., M. J. (2004) *Metall. and Mat. Trans. A* **35A**, 265–277.
- [27] Birol, Y. (2006) *Mat. Sci. and Tech.* **22(8)**, 987–994.

- [28] Tikhovskiy, I., Raabe, D., and Roters, F. (2007) *Mater. Proc. Tech.* **183**, 169–175.
- [29] Lamontagne, C., Worswick, M. J., and Martin, P. (1996) *Aluminum and Magnesium for Automotive Applications* pp. 105–121.
- [30] Kawazoe, M., Shibata, T., Mukai, T., and Higashi, K. (1997) *Scripta Materialia* **36(6)**, 699–705.
- [31] Reynolds, A. P. and Li, Q. (1996) *Scripta Materialia* **34(11)**, 1803–1808.
- [32] Kim, S. S., Haynes, M. J., and Gangloff, R. P. (1995) *Mat. Sci. and Eng* **A203(1-2)**, 256–271.
- [33] Gil-Sevillano, J., vanHoutte, P., and Aernoudt, E. (1980) *Prog. Mater. Sci.* **25**, 69–417.
- [34] Rollet, A. D., Kocks, U. F., and Doherty, R. D. (1987) In A. K. Sachdev and J. D. Embury, (ed.), TMS-AIME, Philadelphia, USA: . p. 211.
- [35] Zehetbauer, M. and Seumer, V. (1993) *Acta Metall. Mater* **41**, 577–588.
- [36] Gil-Sevillano, J. (1993) In R. W. Cahn and E. J. Kramer, (ed.), *Materials Science and Technology: A comprehensive treatment v6*, : Weinheim pp. 19–88.
- [37] Mecking, H. and Estrin, Y. (1987) In S.I.Andersen et al, (ed.), Riso National Laboratory, Roskilde, Denmark: . pp. 123–145.
- [38] Kocks, U. F. and Mecking, H. (2003) *Prog. Mat. Sci.* **48**, 171–273.
- [39] Nes, E. (1998) *Prog. Matr. Sci.* **41**, 129–193.
- [40] Nabarro, F. R. N., Basinski, Z. S., and Holt, D. B. (1964) *Adv. Phys.* **13(50)**, 193–323.
- [41] Kuhlmann-Wilsdorf, D. (2004) *Metall. Mater. Trans.* **A35**, 369–418.

- [42] Mecking, H. (1979) In P. Haasen, V. Gerold, and G. Kostorz, (ed.), *Strenght of Metals and Alloys(ICSMA-5) v3*, Pergamon Press: . pp. 1573–1594.
- [43] Narutami, T. and Takamura, J. (1991) *Acta Metall et Materialia* **39(8)**, 2037–2049.
- [44] Caceres, C. H. and Blake, A. H. (2007) *Mat. Sci. and Eng A* **462(1-2)**, 193–196.
- [45] Mecking, H. and Kocks, U. F. (1981) *Acta Metall.* **29**, 1865–1875.
- [46] Cottrell, A. H. and Stokes, R. J. (1955) *Proc. Roy. Soc. A* **233**, 17–34.
- [47] Basinski, Z. S. (1974) *Scripta metall.* **8(11)**, 1301–1307.
- [48] Saimoto, S. and Sang, H. (1983) *Acta metal.* **31(11)**, 1873–1881.
- [49] Bochniak, W. (1993) *Acta metall. mater.* **41(11)**, 3133–3140.
- [50] Dieter, G. E. (1986) *Mechanical Metallurgy*, McGraw-Hill, New York, .
- [51] Diak, B. J., Upadhyaya, K. R., and Saimoto, S. (1998) *Prog. Mat. Sci.* **43**, 223–363.
- [52] Basinski, S. J. and Basinski, Z. S. (1966) *ASM, Metal Park, Ohio* pp. 1–44.
- [53] Basinski, Z. S., Dugdale, J. S., and Howie, A. (1963) *Phil. Mag.* **8**, 1989–97.
- [54] Basinski, Z. S., Sahoo, M., and Saimoto, S. (1977) *Acta metal.* **25**, 657–665.
- [55] Basinski, Z. S. and Saimoto, S. (1967) *Can. J. Phys.* **45(3)**, 1161–1176.
- [56] Basinski, Z. S. and Dugdale, J. S. (1985) *Phys. Rev. B* **32**, 2149–2155.
- [57] Broom, T. (1954) *Advances in Physics* **3(9)**, 26.
- [58] Blewitt, T. H., Coltman, R. R., and Redmann, J. K. (1955) In Kettuneeu P. O., T. Lepisto, and M. E. Lehtonem, (ed.), *Proceeding of the conference on defects in crystalline solids*, : Bristol, London: Physical Society p. 369.
- [59] Niewczas, M., Basinski, Z. S., Basinski, S. J., and Embury, J. D. (2001) *Phil. Mag. A* **81(5)**, 1121–1142.

- [60] Miura, Y. and Ihara, K. (2004) *Mat. Sci. and Eng.* **A387-389**, 651–654.
- [61] Miura, Y. and Ihara, K. (2004) *Mat. Sci. Forum* **449-452**, 31–36.
- [62] Stanford, N., Dunne, D., and Ferry, M. (2003) *Acta Materialia* **51(3)**, 665–676.
- [63] Nakashima, H. and Yoshinaga, H. (1987) *Creep and Fracture of Engineering Materials and Structures* pp. 15–28.
- [64] Embury, J. D., Poole, W. J., and J., L. D. (2006) *Materials Science Forum* **519-521**, 71–78.
- [65] Takaai, T., Tatsumi, T., and Tamura, T. (1986) In *Strength of Metals and Alloys (ICSMA 7)*, Proceedings of the 7th International Conference Montreal, Que, Can: . pp. 135–139.
- [66] Saji, S., Senda, S., and Hori, S. (1986) In *Strength of metal and alloys (ICSMA7)*; proceedings of the 7th international conference on the strength of metals and alloys Montreal, Canada: . pp. 471–476.
- [67] Vasudevan, A. K. and Doherty, R. D. (1998) *Aluminum Alloys-Contemporary Research and Applications, Treatise on Materials Science and Technology v21*, Academic Press, Boston.
- [68] Ryen, O., Laukli, H. I., Holmedal, B., and Nes, E. (2006) *Met. and Mat. Trans. A* **37A**, 1–7.
- [69] Burger, G. B., Gupta, A. K., Jeffrey, P. W., and Lloyd, D. J. (1995) *Mater. Charact.* **35(1)**, 23–39.
- [70] Hammad, A. M., Ramadan, K. K., and Nasr, M. A. (1989) *Zeitschrift fuer Metallkunde* **80(3)**, 173–177.
- [71] Rollet, A. D., Kocks, U. F., Embury, J. D., G., S. M., and Doherty, R. D. (1988) In P. O. Kettunen, T. Lepisto, and M. E. Lehtonen, (ed.), *Proc. Of*

- the Int. Conf. On the Strength of Metals and Alloys (ICSMA8), Pergamon Press, Oxford: . pp. 433–438.
- [72] Lloyd, D. J. and Court, S. A. (2003) *Mater. Sci. and Techn* **19**, 1349–1354.
- [73] Lloyd, D. J. (2006) *Mat. Sci. Forum* **519-521**, 55–61.
- [74] Lloyd, D. J. (1980) *Metall. Trans. A.* **11A**, 1287–1294.
- [75] Humphreys, F. J. and Hatherly, M. (1995) *Recrystallization and Related Annealing Phenomena*, Elsevier Applied Science, Barking, UK.
- [76] Bay, B., Hansen, N., Hughes, D. A., and Kuhlmann-Wilsdorf, D. (1992) *Acta metall. mater.* **40(2)**, 205–219.
- [77] Hansen, N. (1990) *Mat. Sci. and Tech.* **6**, 1039–1047.
- [78] Hughes, D. A. (1993) *Acta metall. Mater.* **41(5)**, 1421–1430.
- [79] Kuhlmann-Wilsdorf, D. (1989) *Mat. Sci. and Eng.* **A113**, 1–41.
- [80] Hansen, N., Bay, B., Juul Jensen, D., and Leffers, T. (1985) *Strength of Metals and Alloys (ICSMA7), Proc. Of the 7th Int. Conf.* pp. 317–322.
- [81] Hansen, N. and Huang, X. (1998) *Acta mater.* **46(5)**, 1827–1836.
- [82] Liu, Q., Juul Jensen, D., and Hansen, N. (1998) *Acta Mater.* **46(16)**, 5819–5838.
- [83] Barker, I., Ralph, B., and Hansen, N. (1988) In Kettunen P. O., T. Lepisto, and M. E. Lehtonen, (ed.), *Proc. Of the Int. Conf. On the Strength of Metals and Alloys (ICSMA8)*, : Pergamon Press, Oxford pp. 277–282.
- [84] Young, C. T., Headley, T. J., and Lytton, J. L. (1986) *Mater. Sci. Eng.* **81**, 391–407.

- [85] Hansen, N. (1996) In J. G. Morris, S. K. Das, and H. S. Goodrich, (ed.), Aluminum alloys for packing II, : The mineral, metals, and materials society pp. 11–26.
- [86] Kuhlmann-Wilsdorf, D. and Hansen, N. (1991) *Scripta metal. et mater.* **25**, 1557–1562.
- [87] Liu, Q. and Hansen, N. (1995) *Scripta metal. mater.* **32**, 1289–1295.
- [88] Driver, J. H., Juul Jensen, D., and Hansen, N. (1994) *Acta metall. mater.* **42**, 3105–3114.
- [89] Theyssier, M. C., Chenal, B., Driver, J. H., and Hansen, N. (1995) *Phys. Stat. Sol. (b)* **149**, 367–378.
- [90] Xing, Q., Huang, X., and Hansen, N. (2004) *Mat.Sci. Forum* **467-470**, 209–216.
- [91] Baxter, G. J., Furu, T., Zhu, Q., Whiteman, J. A., and Sellars, C. M. (1999) *Acta mater.* **47(8)**, 2367–2376.
- [92] Chu, D. and Morris, W. J. (1996) *Acta Mater.* **44(7)**, 2599–2610.
- [93] Kral, R. (1996) *Phys. Stat. Sol. (a)* **157**, 255–263.
- [94] Korbel, A., Embury, J. D., Hatherly, M., Martin, P. L., and Erbsloh, H. W. (1986) *Acta metall.* **34(10)**, 1999–2009.
- [95] Driver, J. H. and Papazian, J. M. (1985) *Mater. Sci. Eng.* **76(1-2)**, 51–56.
- [96] Verdier, M., Janecek, M., Brechet, Y., and Guyot, P. (1998) *Mat. Sci. and Eng* **A248**, 187–197.
- [97] Nakayama, Y. and Morii, K. (1987) *Acta Metall* **35(7)**, 1747–1755.
- [98] Morii, K., Mecking, H., and Nakayama, Y. (1985) *Acta Metall* **33(3)**, 379–386.
- [99] Roopchand, B. J. and Morris, J. G. (1973) *Scr. Metall.* **7(8)**, 839–845.
- [100] Fujita, H. and Tabata, T. (1977) *Acta matall.* **25**, 793–800.

- [101] Robinson, J. M. and Shaw, M. P. (1994) *Mat. Sci. and Eng.* **A174**, 1–7.
- [102] Endou, S. and Inagaki, H. (2003) *Z. Metallkd.* **94**, 1206–1216.
- [103] Field, D. P. and Weilnad, H. (1994) *Mat. Sci.For.* **157-162**, 1181–1188.
- [104] Hansen, N., Juul Jensen, D., and Hughes, D. A. (1994) *Mat. Sci. Forum.* **157-162**, 693–700.
- [105] Westengen, H. (1982) *Z. Metallkunde* **73**, 360–368.
- [106] Hollingsworth, E. G., Frank, G. R., and Willett, R. E. (1962) *Trans. Met. Soc. AIME* **224**, 188–189.
- [107] Zaidi, M. A. and Wert, J. A. (1989) In A. K. Vasudevan and R. D. Doherty, (ed.), Aluminum alloys-contemporary research and applications, Treatise on Materials Science and Technology v21, Academic press, Boston: . pp. 137–170.
- [108] Sandstrom, R. (1980) In N Hansen and T Leffers, (ed.), First Riso Symposium on Metallurgy and Materials Science, Riso Natianal Laboratory, Roskilde, Denmark: . pp. 45–49.
- [109] Nes, E., Ryum, N., and Hunderi, O. (1985) *Acta Metall* **33**, 11–22.
- [110] Parker, B. A. (1989) In A. K. Vasudevan and R. D. Doherty, (ed.), Aluminum alloys-contemporary research and applications, Treatise on Materials Science and Technology v21, Academic press, Boston: . pp. 539–562.
- [111] Lutjering, G. and Weissman, S. (1970) *Acta Metall.* **18**, 785–795.
- [112] Prince, K. C. and Martin, J. W. (1979) *Acta Metall.* **27**, 1401–1406.
- [113] Liu, Y. S., Cheng, X. M., Liu, J. T., and Morris, J. G. (2000) *Mater. Sci. Forum* **331-337**, 191–196.

- [114] Jin, H., Li, J., Seki, F., and Saimoto, S. (2000) *Mat. Sci. Forum* **331-337**, 745–750.
- [115] Johnson, C. and Lloyd, D. J. (2000) *Materials Science Forum* **331-337**, 715–726.
- [116] Bate, P. S. (1993) *Metall. Trans.* **24A**, 2679–2689.
- [117] Bate, P., Roberts, W. T., and Wilson, D. V. (1981) *Acta metall.* **29**, 1797–1814.
- [118] Takahashi, H., Motohashi, H., and S., T. (1996) *Int. J. Plast.* **12(7)**, 935–949.
- [119] Lopes, A. B., Rauch, E. F., and Gracio, J. J. (1999) *Acta mater.* **47(3)**, 859–866.
- [120] Taylor, G. I. (1938) *J. Inst. Metals* **62**, 307–324.
- [121] Savoie, J., Zhou, Y., Jonas, J. J., and Macewen, S. R. (1996) *Mater. Sci. and Eng.* **44(2)**, 587–605.
- [122] Baczynski, G. J., Guzzo, R., Ball, M. D., and Lloyd, D. J. (2000) *Acta. Mater.* **48**, 3361–3376.
- [123] Ohtani, S. and Inagaki, H. (2002) *Materials Science Forum* **V408-412**, 1483–1488.
- [124] Ohtani, S. and Inagaki, H. (2003) *Z. Metallkd.* **94**, 983–992.
- [125] Hirsch, J. and Lucke, K. (1988) *Acta Metall.* **36(11)**, 2863–2882.
- [126] Ruano, O. A. and Gonzalez, G. (1985) *Scripta Metall.* **19**, 27–31.
- [127] Bruker Advanced X-ray Solutions (AXS) Inc., General Area Detector Diffraction System (GADDS) user manual, 4 edition (1999).
- [128] Matthies, S. and Vinel, G. W. (1982) *Phys. Stat. Sol. (b)* **112**, K111–114.

- [129] Kocks, U. F. (1988) In J. S. Kallend and G. Gottstein, (ed.), Proc. 8th International Conference on Textures of Materials (ICOTOM8), Warrendale, USA: Met. Soc. AIME. pp. 31–36.
- [130] Wen, W. and Morris, J. G. (2003) *Mater. Sci. and Eng.* **A354**, 279–285.
- [131] Basinski, Z. S. (1957) *Proc. R. Soc. Lond.* **A240**, 229–242.
- [132] Basinski, Z. S. (1960) *Aust. J. Phys.* **13**, 345–358.
- [133] Deschamps, A., Niewczas, M., Bley, F., Brechet, Y., Embury, J. D., Le Sinq, L., Livet, F., and Simon, J. P. (1999) *Phil. Mag. A.* **79(10)**, 2485–2504.
- [134] Esmaeili, S., Cheng, L. M., Deschamps, A., Lloyd, D. J., and Poole, W. J. (2001) *Mater. Sci. and Eng.* **A319-321**, 461–465.
- [135] Haasen, P. (1958) *Philos. Mag.* **3**, 384–418.
- [136] Kocks, U. F., Argon, A. S., and Ashby, M. F. (1975) Thermodynamics and Kinetics of Slip, Prog. Mater. Sci. 19, Pergamon Press, Oxford.
- [137] Watts, B. R. Dislocations in Solids pp. 175–419 Amsterdam: North-Holland (1989).
- [138] Kocks, U. F., Canova, G. R., Tome, C. N., Rollett, A. D., and Wright, S. I. (1998) Compute Code LA-CC-88-6, Los Alamos National Laboratory Los Alamos, NM, USA.
- [139] Rodriguez, P. (1984) *Bull. Mater. Sci.* **6(4)**, 653–663.
- [140] Hosford, W. F., Fleischer, R. L., and Backofen, W. A. (1960) *Acta Metall.* **8**, 187–199.
- [141] Chin, G. Y., Hosford, W. F., and Backofen, W. A. (1964) *Trans. AIME* **230**, 437–449.

- [142] Chin, G. Y., Hosford, W. F., and Backofen, W. A. (1964) *Trans. AIME* **230**, 1043–1048.
- [143] Burns, T. J. and Davies, M. A. (2002) *Int. J. Plasticity* **18(4)**, 487–506.
- [144] Molinari, A., Musquar, C., and Sutter, G. (2002) *Int. J. Plasticity* **18(4)**, 443–459.
- [145] Tanoue, K. (1991) *Scripta metall. mater.* **25**, 565–569.
- [146] Basinski, S. J. and Basinski, Z. S. (1979) *Dislocations in Solids (Amsterdam: North Holland)* **4**, 261–362.
- [147] Saimoto, S. (2006) *Phil. Mag.* **86(27)**, 4213–4233.
- [148] King, J. E., You, C. P., and Knott, J. F. (1981) *Acta Metall.* **29**, 1553–1566.
- [149] Kubin, L. P. and Estrin, Y. (1985) *Acta Metall.* **33**, 397–407.
- [150] Brown, L. M. (2002) *Phil. Mag. A* **82(9)**, 1691–1711.
- [151] Simmons, R. O. and Balluffi, R. W. (1963) *Phys. Rev.* **129**, 1533.
- [152] Bhattacharya, B. Plastic deformation of Mg in the temperature range between 4.2K and 300K, Phd dissertation, McMaster University Hamilton, ON, Canada (2006).
- [153] Suzuki, Y., Hashimoto, T., and Muramatsu, T. (2000) *Mater. Sci. Forum* **331**, 811–816.
- [154] Hughes, D. A., Kassner, M. E., Stout, M. G., and Vetrano, J. S. (1998) *JOM* **50(6)**, 16–21.
- [155] Tome, C. N., Canova, G. R., Kocks, U. F., Christodoulou, N., and Jonas, J. J. (1984) *Acta metall* **32**, 1637–1653.
- [156] Tome, C. N., Lebensohn, R. A., and Necker, C. T. (2002) *Met. and Mater. Trans. A* **33A**, 2653–2648.

-
- [157] Tome, C. N. and Lebensohn, R. A. (2003) *Manual for Visco-Plastic Self-Consistent (VPSC), version 6.*
- [158] Kocks, U. F., Kallend, J. S., Wenk, H. R., Rollett, A. D., and Wright, S. I. (1995) Compute Code LA-CC-89-18, Los Alamos National Laboratory Los Alamos, NM, USA.

Appendix A

Anova Analysis

An Anova analysis of variance, is a statistical measure on the difference between the means of groups, which is often termed “F test”. An F value gives information on whether there is a significant difference between groups or not. That is, it tells if the difference of the means between groups comes from sampling errors, or groups are significantly different from each other (true difference). The analysis starts from the null hypothesis which is the assumption that there is no true difference between groups. If the computed value for F is greater than the critical F value, the null hypothesis is rejected.

In order to quantitatively examine the significance of the effect of crystallographic orientation on the anisotropic behaviours as shown in Figure 4.44, Anova analysis is performed. Table 6.1 shows that the measured flow stresses at a strain of 20% are significantly different depending on the tensile direction; the computed values for F are greater than the critical F values at all three temperatures of 4.2K, 78K and 295K due to the anisotropy. However, after normalizing the flow stresses by the measured Taylor factors, the computed F values become smaller than the critical F values at 78K and 295K (Table 6.2). This implies that the crystallographic orientation is the major factor for the anisotropy of this material at 78K and 295K, although it still shows the anisotropic characteristic at 4.2K.

Table 6.1: Anova analysis results with $\alpha = 0.05$ for Figure 4.44 (a): comparisons of flow stresses between difference tensile directions at strain of 20%

For 4.2K

Source of Variation	SS	df	MS	F	P-value	F crit
Between Groups	2614.89	2	1307.44	16.46	0.00367	5.14
Within Groups	476.67	6	79.44			
Total	3091.56	8				

For 78K

Source of Variation	SS	df	MS	F	P-value	F crit
Between Groups	534	2	267	7.026	0.04910	6.94
Within Groups	152	4	38			
Total	686	6				

For 295K

Source of Variation	SS	df	MS	F	P-value	F crit
Between Groups	139.56	2	69.78	10.13	0.01193	5.14
Within Groups	41.33	6	6.89			
Total	180.89	8				

Note: SS, df, MS, and P-value represent the total sum of squares, degrees of freedom, the mean squares and the probability value, respectively.

Table 6.2: Anova analysis results with $\alpha = 0.05$ for Figure 4.44 (b): comparisons of flow stresses normalized by corresponding Taylor factors between difference tensile directions at strain of 20%

For 4.2K

Source of Variation	SS	df	MS	F	P-value	F crit
Between Groups	206.36	2	103.18	11.80	0.00832	5.14
Within Groups	52.44	6	8.74			
Total	258.80	8				

For 78K

Source of Variation	SS	df	MS	F	P-value	F crit
Between Groups	36.27	2	18.14	5.40	0.07299	6.94
Within Groups	13.43	4	3.36			
Total	49.70	6				

For 295K

Source of Variation	SS	df	MS	F	P-value	F crit
Between Groups	8.26	2	4.13	4.48	0.06449	5.14
Within Groups	5.53	6	0.92			
Total	13.79	8				

Note: SS, df, MS, and P-value represent the total sum of squares, degrees of freedom, the mean squares and the probability value, respectively.

Appendix B

Roughness

Band-type surface markings at approximately 45° to the tensile axis were visible with the naked eye on the surface of the specimen deformed at 295K, which are frequently observed during the PLC effect. These bands extend across the specimen (Figure 6.1) and are critical to the application of automotive exterior panels. At other temperatures, these bands were not observed with the naked eye or stereoscopes. In order to investigate the variation of roughness during deformation, the roughness of each specimen deformed to various stages of deformation was studied. 6.4x1.35mm area of specimens was scanned using a white light interferometer, Zygo, with the lateral camera resolution of $2.82\mu\text{m}$. The vertical z-scan measurement ranges from 0.1nm to $15000\mu\text{m}$. The optical observations of surface of specimens have been validated by this roughness measurement (Figure 6.2). The average roughness, Ra, is used to express the surface roughness of specimens. The Ra is the area between the roughness profile and its mean line or the integral of the absolute value of the roughness profile height over the evaluation length. The average roughness is also known as arithmetic average (AA), center line average (CLA), and arithmetical mean deviation of the profile. It is seen that the specimen deformed at room temperature become rougher with the degree of deformation (Figure 6.2). The variation of the roughness is slightly larger at 4.2K than 78K. This is presumably attributed to the effect of adiabatic shear deformation.

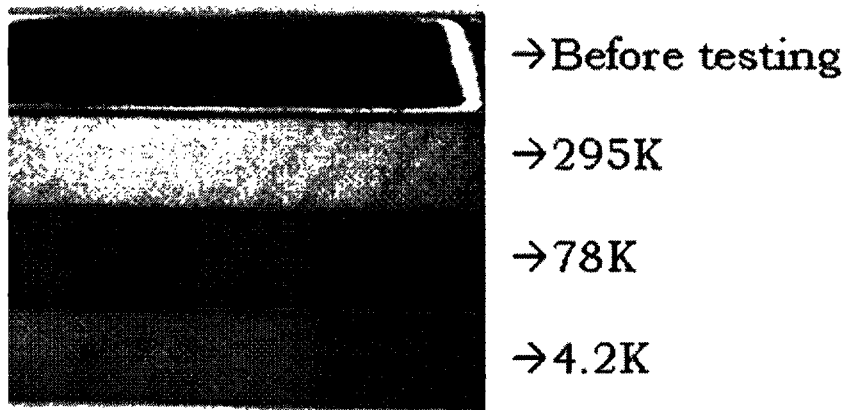
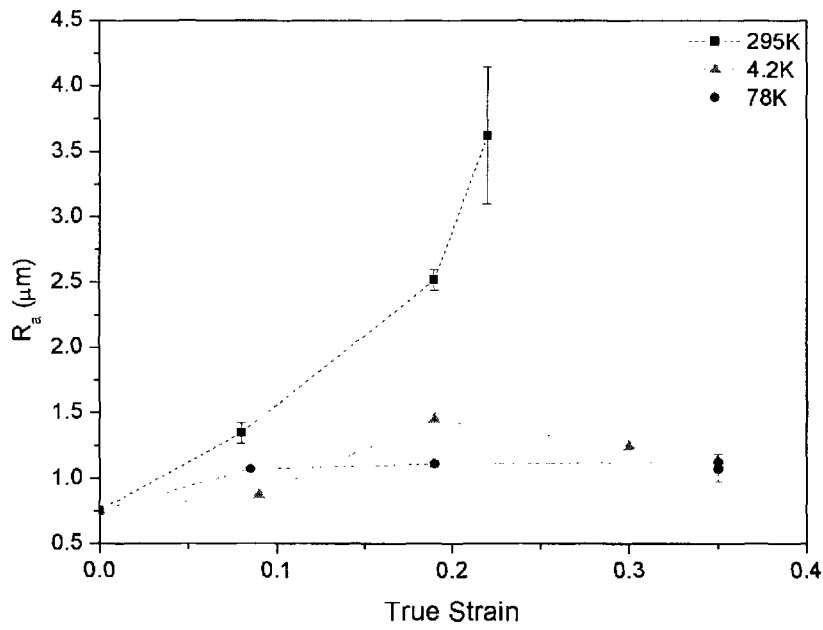
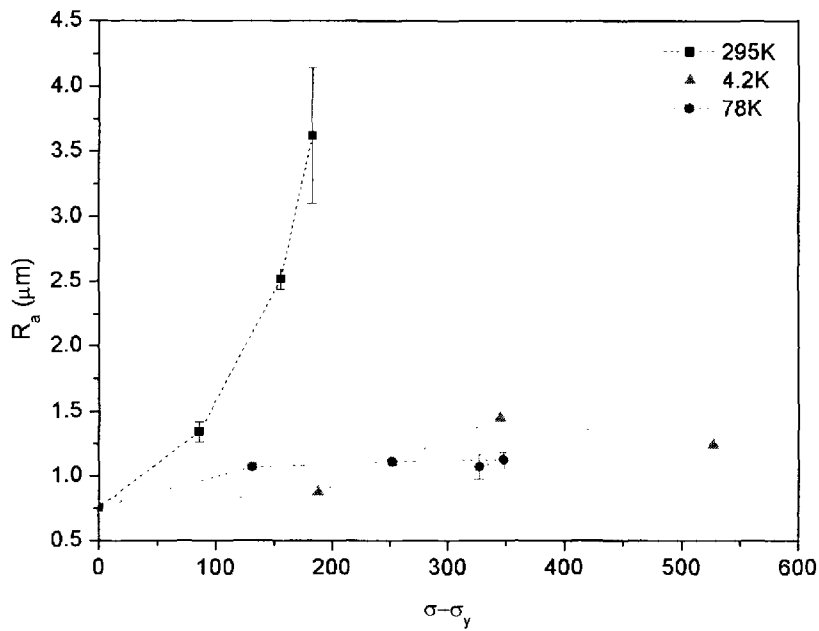


Figure 6.1: Surface observation with stereoscopes. Lüders-like bands are clearly visible at temperature 295K. The picture has been enlarged.



(a)



(b)

Figure 6.2: Roughness measurements for CC materials

Appendix C

Methodology of VPSC Modeling

The present appendix briefly describes the concept, constitutive equations, and work hardening parameters used in the Visco-Plastic Self-Consistent (VPSC) model. Also discussed will be how the simulation results in this present study were obtained using the experimental texture data.

The VPSC model treats each grain as an ellipsoidal visco-elastic inclusion embedded in an effective visco-plastic medium (surrounding grains). Plastic deformation occurs by crystallographic slip activated at the critical value of the resolved shear stress acting on a particular slip system, and the stress equilibrium is solved by the Eshelby solution. The visco-plastic response of the inclusion (single crystal) is described by the rate sensitive constitutive law:

$$D_{ij}^c = \dot{\gamma}_0 \sum_s m_{ij}^s \left(\frac{m^s : \sigma}{\tau^s} \right)^n = \dot{\gamma}_0 \sum_s \frac{m_{ij}^s m_{kl}^s}{\tau^s} \left(\frac{m^s : \sigma}{\tau^s} \right)^{n-1} \sigma_{kl} = M_{ijkl}^c \sigma_{kl} \quad (6.1)$$

where D^c is the strain rate in the grain, s denotes each slip system, m^s is the geometric Schmid tensor, τ^s is a threshold stress controlling the activation of the system, and n is the inverse of the rate sensitivity. Detailed constitutive equations used in the VPSC code are found in the VPSC manual [157].

For strain hardening, the code adopts the modified Voce hardening law, which is described by an evolution of threshold stress with accumulated shear strain in each grain:

$$\tau = \tau_0 + (\tau_1 + \theta_1 \Gamma) \left(1 - \exp\left(-\frac{\theta_0 \Gamma}{\tau_1}\right) \right) \quad (6.2)$$

where τ is the critical resolved shear stress (CRSS) for (111)<110> and Γ , τ_0 , $(\tau_0 + \tau_1)$, θ_0 and θ_1 are the applied strain, the initial CRSS, the back-calculated CRSS, the initial hardening rate and the asymptotic hardening rate, respectively (Figure 6.3(a)). These parameters are related to macroscopic stress-strain (S-E) curves as shown in Figure 6.3(b); detailed descriptions and derivations of the relations are presented in section 5.1.5. For the simulation of the results presented in this work, the published data of single crystal hardening parameters for AA5754 Al alloys were adjusted to fit to the experimental (macroscopic) tensile curves of the samples oriented parallel to the rolling direction at 295K, 78K and 4.2K, respectively. For the analyses of the samples 45 and 90 angles oriented from the RD at each temperature, only the initial texture data were changed corresponding to the experimental measurements. .

In order to incorporate textures of polycrystals, the VPSC code requires a set of weighted orientations, i.e. grains and their associated volume fractions as an input, and in turn produces a set of weighted orientations with mechanical responses as an analysis result in the simulation. The popLA package [158] is used to discretize texture data obtained from the experimental measurements of undeformed samples. The discrete texture data are described by densities in 1022 orientation spaces. On the other hand, the simulation results of weighted orientations from the VPSC were converted into continuous distributions using the popLA for the texture analyses and for the presentation of the pole figures and inverse pole figures.

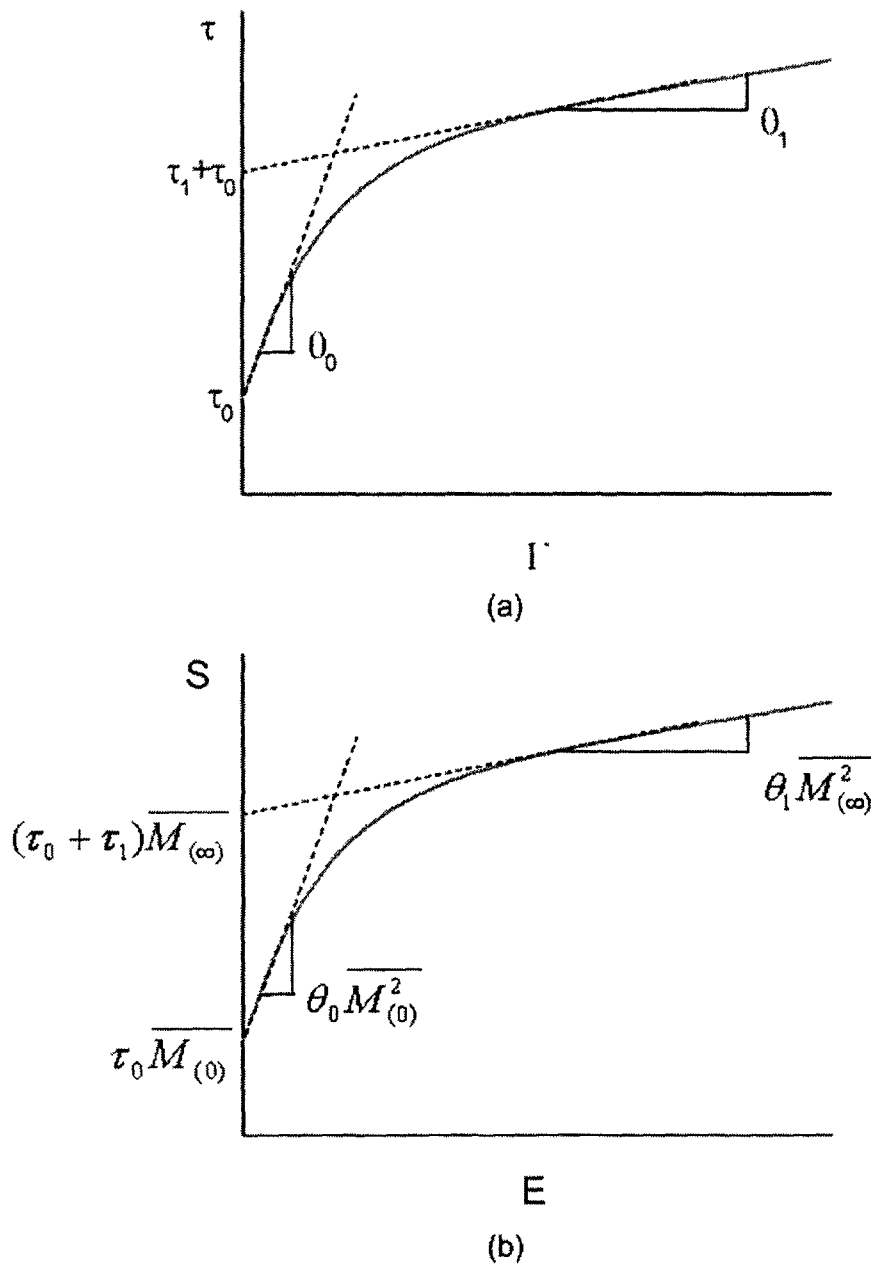


Figure 6.3: Schematic of the strain hardening model incorporated in VPSC code: (a) parameters of the empirical Voce law for a single crystal on the critical stress τ vs. the microscopic shear Γ curve and (b) their relation with a macroscopic stress-strain (S-E) curve (after Tome et al [155]) (see section 5.1.5 for detailed descriptions of parameters and relations.)

Appendix D

Resistivity Measurement

In-situ resistivity measurements in the present study are based on other experiments by Niewczas et al. [59], in which the methodology and the instruments are detailed. Figure 6.4 shows the schematic of the electrical potential difference measurement across the sample, which is based on the four point resistance measurement method, adopted in this study. The measured l and the cross-section area (s) of the sample within the gauge length were used with the measurement of potential difference (V) to compute the resistivity (ρ) as described in Equation 2.20. The resistivity was calculated assuming uniform deformation of the sample within the gauge length. The resistivity measurement was carried out by flowing the current (I) of 1A and 0.5A at 4.2K and higher temperatures, respectively, using a Hewlett-Packard precision power supply (6114A) operated at 12V. The flow of current was repeatedly reversed in order to cancel thermal electromotive forces occurred due to a difference in temperature between 4.2K and room temperature along the circuit, and the differences in pairs of readings of potential difference were used. The current was reversed approximately 60 times per second during the experiments, with a 20 nano-second delay time between the reversals; the reversal of current was delayed to remove the additional resistance generated by an eddy current. The potential differences were measured using a Hewlett-Packard digital voltmeter (HP-3456A) with a resolution of 10nV. In order to measure the potential change of the specimen smaller than 10^{-9} V,

the signal was amplified by a factor of 10^3 using a low-noise pre-amplifier. The data obtained from 10^4 readings gave a standard deviation of approximately $0.4n\Omega$.

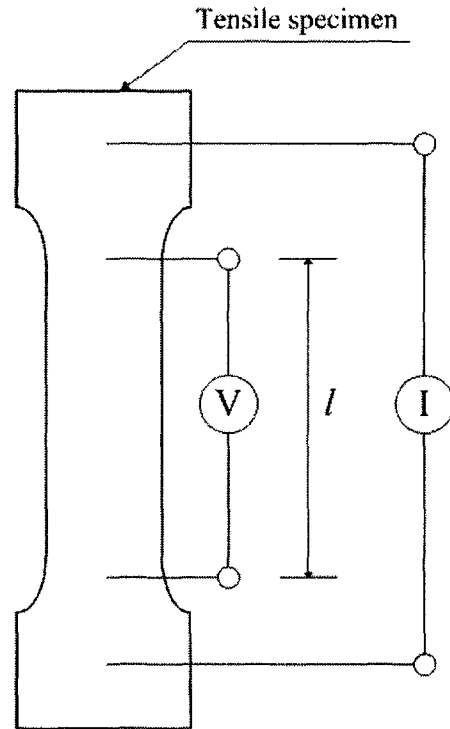


Figure 6.4: Schematic of the *in-situ* resistivity measurement setup. l represents the length of the specimen across which the potential difference is measured. l and the cross-section area (s) of the sample are used to compute the resistivity (ρ) as described in Equation 2.20.

Appendix E

Mean Free Path

Figure 6.5 shows the log of the mean free path, which is presented in a linear scale as shown in Figure 5.3. This log plot has often been adopted by other researchers [147].

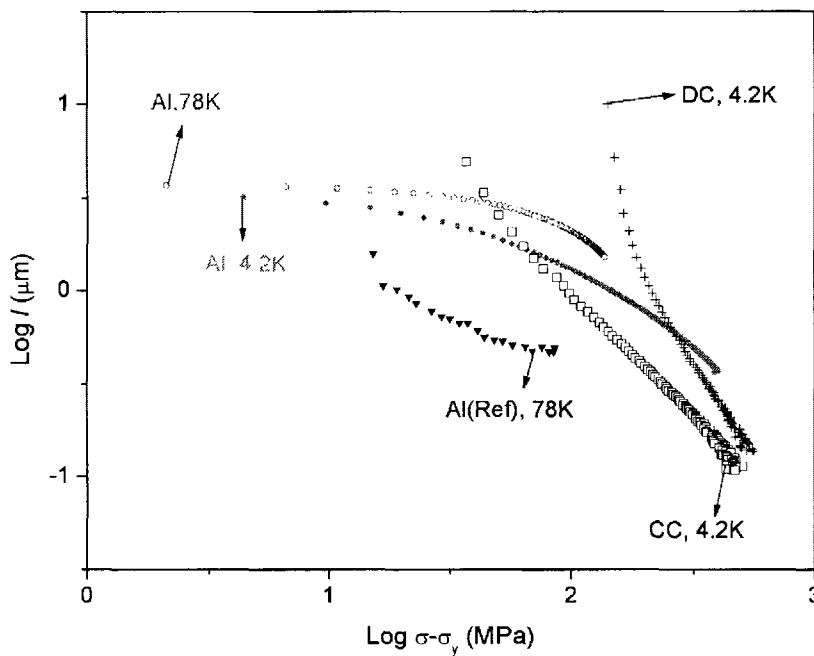


Figure 6.5: Evolution of the dislocation mean free path for CC and DC alloys deformed at 4.2K and Al deformed at 4.2K and 78K: Log(mean free path) vs. Log($\sigma - \sigma_y$). Al(Ref) denotes mean free path data for pure Al deformed at 78K taken from the literature [147]. Details are found in Figure 5.3 and section 5.1.

Appendix F

Strain Rate Sensitivity - Haasen plot

The figures in this section present the strain rate sensitivity data obtained in the jump tests with increasing and decreasing strain rate, associated with Figure 4.6. Figures 6.6 - 6.10 show quantitatively the same characteristics independently whether the stress difference is evaluated from the jump test with increasing or decreasing strain rate.

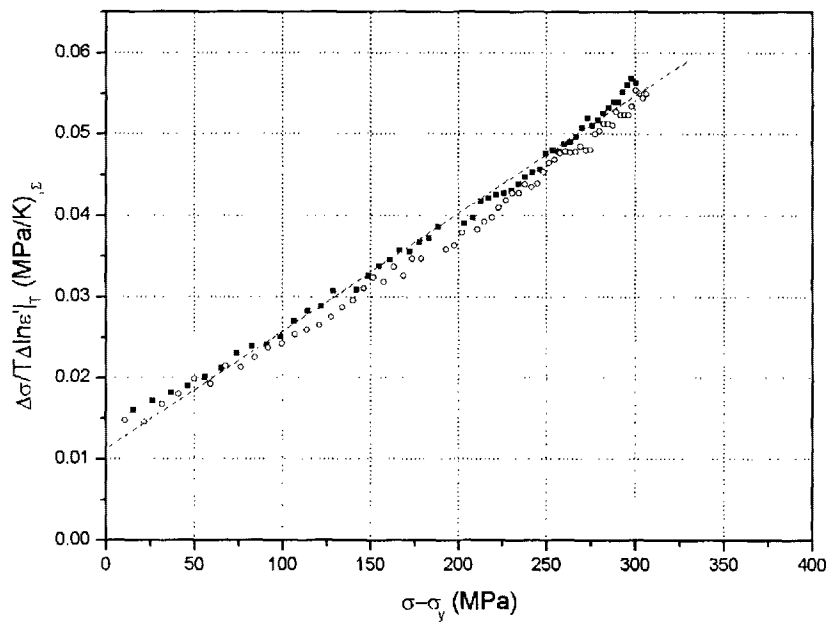


Figure 6.6: Haasen plot characteristics obtained from strain rate sensitivity tests for CC tested at 78K. Open symbols represent data obtained by an increase of strain rate, and closed symbols represent data obtained by a decrease of strain rate.

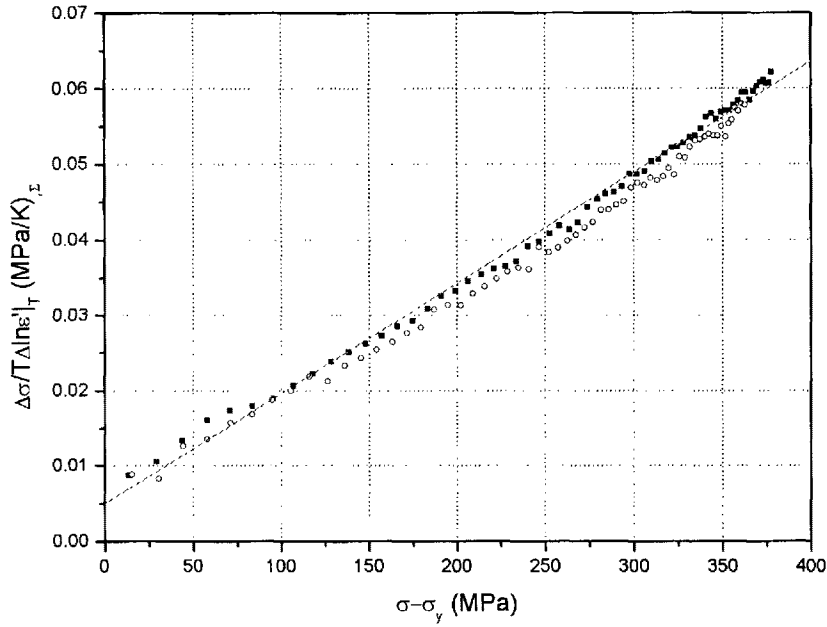


Figure 6.7: Haasen plot characteristics obtained from strain rate sensitivity tests for DC tested at 78K. Open symbols represent data obtained by an increase of strain rate, and closed symbols represent data obtained by a decrease of strain rate.

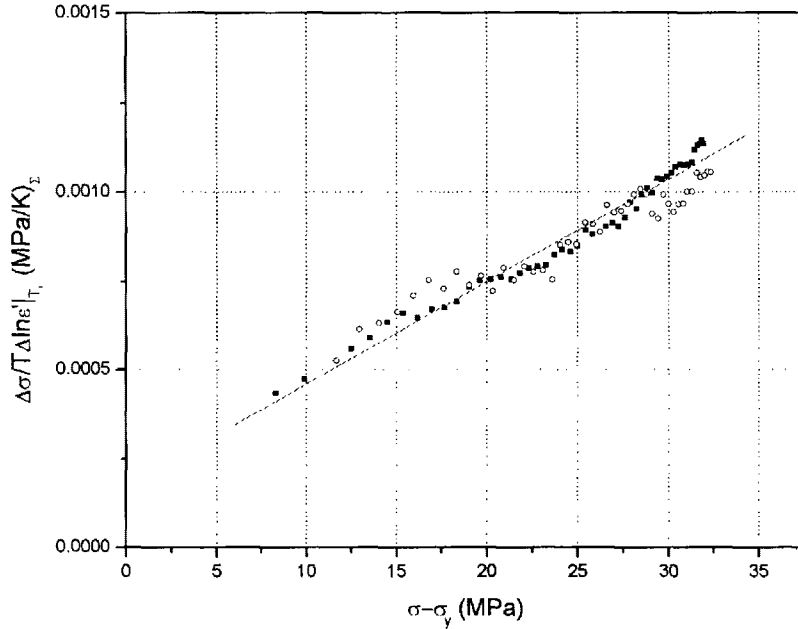


Figure 6.8: Haasen plot characteristics obtained from strain rate sensitivity tests for pure Al tested at 295K. Open symbols represent data obtained by an increase of strain rate, and closed symbols represent data obtained by a decrease of strain rate.

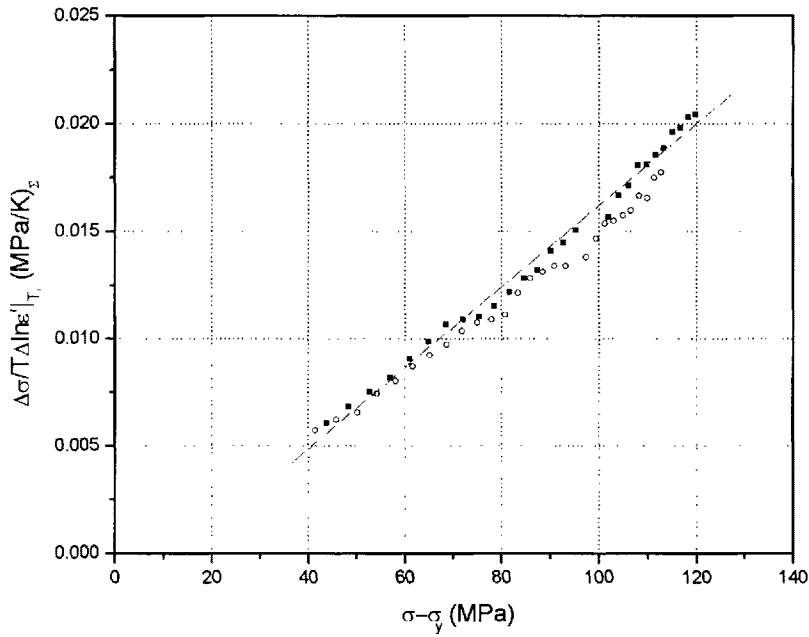


Figure 6.9: Haasen plot characteristics obtained from strain rate sensitivity tests for pure Al tested at 78K. Open symbols represent data obtained by an increase of strain rate, and closed symbols represent data obtained by a decrease of strain rate.

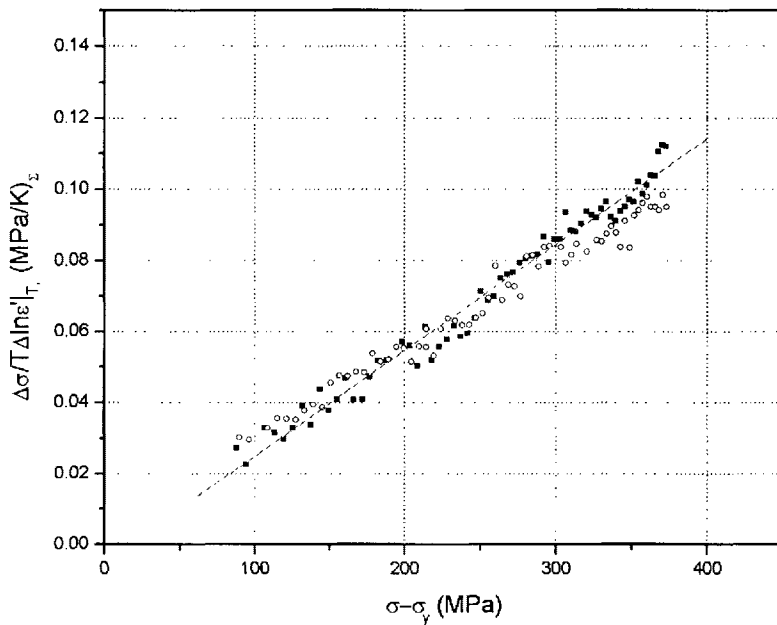


Figure 6.10: Haasen plot characteristics obtained from strain rate sensitivity tests for pure Al tested at 4.2K. Open symbols represent data obtained by an increase of strain rate, and closed symbols represent data obtained by a decrease of strain rate.